

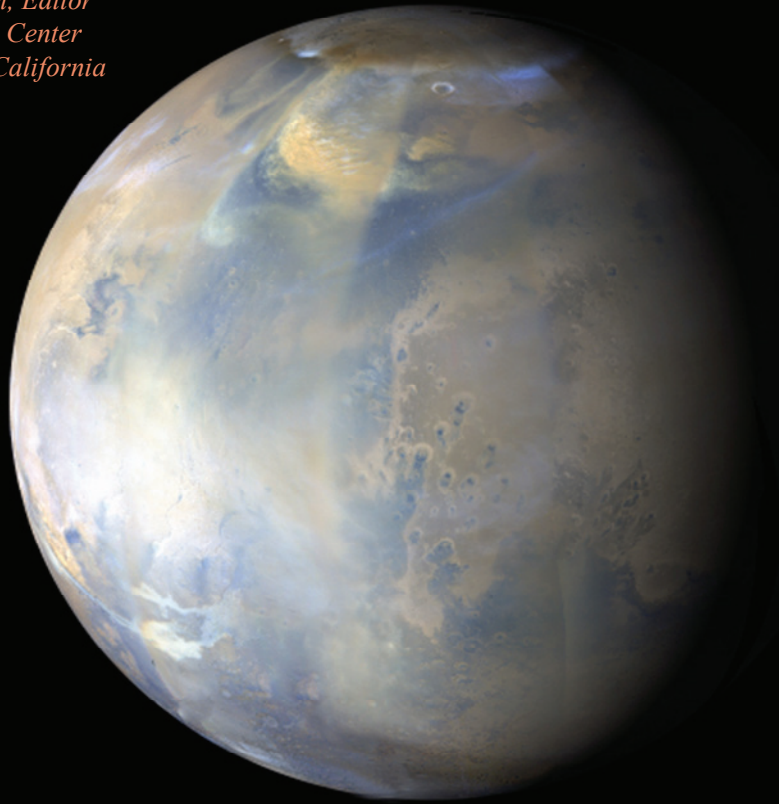
**NASA/CP-2010-216377**



## **Mars Dust Cycle Workshop**

**Ames Research Center  
September 15–17, 2009**

*Robert M. Haberle, Chairman and Convener  
Sandra J. Owen, Editor  
Ames Research Center  
Moffett Field, California*



<http://humbabe.arc.nasa.gov/MarsDustWorkshop/DustHome.html>

*Above image courtesy of Bruce Cantor, Malin Space Science Systems*

## The NASA STI Program Office . . . in Profile

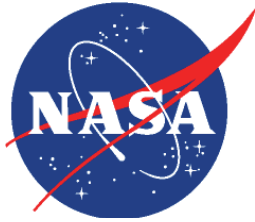
Since its founding, NASA has been dedicated to the advancement of aeronautics and space science. The NASA Scientific and Technical Information (STI) Program Office plays a key part in helping NASA maintain this important role.

The NASA STI Program Office is operated by Langley Research Center, the Lead Center for NASA's scientific and technical information. The NASA STI Program Office provides access to the NASA STI Database, the largest collection of aeronautical and space science STI in the world. The Program Office is also NASA's institutional mechanism for disseminating the results of its research and development activities. These results are published by NASA in the NASA STI Report Series, which includes the following report types:

- **TECHNICAL PUBLICATION.** Reports of completed research or a major significant phase of research that present the results of NASA programs and include extensive data or theoretical analysis. Includes compilations of significant scientific and technical data and information deemed to be of continuing reference value. NASA's counterpart of peer-reviewed formal professional papers but has less stringent limitations on manuscript length and extent of graphic presentations.
  - **TECHNICAL MEMORANDUM.** Scientific and technical findings that are preliminary or of specialized interest, e.g., quick release reports, working papers, and bibliographies that contain minimal annotation. Does not contain extensive analysis.
  - **CONTRACTOR REPORT.** Scientific and technical findings by NASA-sponsored contractors and grantees.
  - **CONFERENCE PUBLICATION.** Collected papers from scientific and technical conferences, symposia, seminars, or other meetings sponsored or cosponsored by NASA.
  - **SPECIAL PUBLICATION.** Scientific, technical, or historical information from NASA programs, projects, and missions, often concerned with subjects having substantial public interest.
  - **TECHNICAL TRANSLATION.** English-language translations of foreign scientific and technical material pertinent to NASA's mission.
- Specialized services that complement the STI Program Office's diverse offerings include creating custom thesauri, building customized databases, organizing and publishing research results . . . even providing videos.
- For more information about the NASA STI Program Office, see the following:
- Access the NASA STI Program Home Page at <http://www.sti.nasa.gov>
  - E-mail your question via the Internet to [help@sti.nasa.gov](mailto:help@sti.nasa.gov)
  - Fax your question to the NASA Access Help Desk at (301) 621-0134
  - Telephone the NASA Access Help Desk at (301) 621-0390
  - Write to:  
NASA Access Help Desk  
NASA Center for AeroSpace Information  
7115 Standard Drive  
Hanover, MD 21076-1320



**NASA/CP-2010-216377**



**Mars Dust Cycle Workshop  
Ames Research Center  
September 15–17, 2009**

*Robert M. Haberle, Chairman and Convener  
Sandra J. Owen, Editor  
Ames Research Center, Moffett Field, California*

National Aeronautics and  
Space Administration

Ames Research Center  
Moffett Field, California 94035-1000

---

**March 2010**

Available from:

NASA Center for AeroSpace Information  
7115 Standard Drive  
Hanover, MD 21076-1320  
(301) 621-0390

National Technical Information Service  
5285 Port Royal Service  
Springfield, VA 22161  
(703) 487-4650

Mars Dust Cycle Workshop  
NASA/Ames Research Center  
September 15-17, 2009

The Martian climate system is characterized in terms of the seasonal cycles of dust, water, and CO<sub>2</sub>, which are coupled and driven by the general circulation. Recent workshops on the Martian climate system have focused on the water and CO<sub>2</sub> cycles, but a workshop focused on the dust cycle, perhaps the most complex component of the climate system overall, has not been held since the post Viking data analysis programs of the 1980's. Given the enormous volume of data acquired since then, as well as the advances in modeling and laboratory methods, the time seemed right to hold a workshop focused on dust cycle.

Such a workshop was held at NASA/Ames Research Center on September 15-17, 2009. Nearly 70 people from around the world attended the 3-day workshop whose overall objective and primary theme was to understand the processes responsible for the lifting, transport, and removal of dust in the Martian atmosphere in the present climate system. This objective required the exchange of ideas from the geological and atmospheric science communities. Researchers working on similar topics for the Earth's climate system also attended. Consequently, the workshop attracted a wide variety of interested parties including students, post-docs, engineers, and university and government researchers.

To facilitate communication between the various communities the workshop was structured to provide ample time for individual presentations, follow-up discussions, and poster viewing. Topics touched on observational, modeling, and ongoing laboratory and fieldwork and these generated considerable cross-disciplinary discussion. Thus, the workshop was very successful in meeting its objectives.

A unique feature of the workshop was the two-step process for publishing the abstracts. Submitted abstracts were limited to a single paragraph with no figures, tables, or references. These abstracts were used to develop the program. After the workshop, participants were given the opportunity to revise their initial abstracts in order to add details, figures, references, etc., as well as to incorporate comments based on workshop discussions. Most participants took advantage of this opportunity. These "Extended Abstracts" are the main product of the workshop and are included here in the pages that follow.

Robert M. Haberle  
NASA/Ames Research Center  
January 2010



# Mars Dust Cycle Workshop

*September 15-17, 2009  
NASA Ames Research Center  
Space Science Auditorium  
Moffett Field, California*

## **Convener**

Robert Haberle  
*NASA Ames Research Center*

## **Scientific Organizing Committee**

Robert Haberle, Chair  
*NASA Ames Research Center*

Melinda Kahre  
*Bay Area Environmental Research Institute, NASA Ames Research Center*

Franck Montmessin  
*CNRS Service d'Aéronomie*

Claire Newman  
*California Institute of Technology*

Nilton Renno  
*University of Michigan*

Michael Smith  
*NASA Goddard Space Flight Center*

Mike Wolff  
*Space Science Institute*

## **Local Organizing Committee**

*Robert Haberle, NASA Ames Research Center  
Sandra Owen, NASA Ames Research Center  
Diana Frontella, NASA Ames Research Center  
Melinda Kahre, BAERI, NASA Ames Research Center*



---

## Table of Contents

---

### **Session One - General Overviews**

Zurek, R.W. ....	Page 3
<a href="#"><i>The Martian Dust Cycle Revisited</i></a>	
Murphy, J.R. ....	Page 4
<a href="#"><i>Modeling Dust in the Martian Atmosphere: A Process Driven Cycle</i></a>	
Clancy, R.T. and Wolff, M.J. ....	Page 5
<a href="#"><i>Recent Measurements of the Radiative and Physical Properties for Mars Dust</i></a>	

### **Session Two - Global Dust Storms**

Hale, A.S., Kass, D.M., Schofield, J.T., Kleinböhl, A., McCleese, D.J., and the MCS Team. ....	Page 11
<a href="#"><i>MCS Views of Atmospheric Dust During the 2009 Planet Encircling Dust Event</i></a>	
Kass, D.M., Snyder Hale, A., Schofield, J.T., Kleinböhl, A., McCleese, D.J., and the MCS Team. ....	Page 15
<a href="#"><i>MCS Views of Atmospheric Thermal Structure During the 2009 Planet Encircling Dust Event</i></a>	
Elteto, A., and Toon, O.B. ....	Page 20
<a href="#"><i>New Analysis of Mars Global Surveyor Thermal Emission Spectrometer Data from Global Dust Storm 2001A</i></a>	

### **Session Three - Distribution, Evolution, and Radiative Effects of Particle Sizes**

Goetz, W., Drube, L., Hecht, M.H., Hviid, S.F., Leer, K., Madsen, M.B., Parrat, D., Pike, W.T., Staufer, U., Sykulska, H., and Vijendran, S. ....	Page 25
<a href="#"><i>Martian Airborne Dust: How it Forms and Evolves. Near-Surface versus High-Altitude Properties.</i></a>	
Kleinböhl, A., Abdou, W. A., Schofield, J. T., Kass, D. M., McCleese, D. J. ....	Page 28
<a href="#"><i>Mars Climate Sounder Limb Retrievals of Dust and Water Ice Using Scattering Radiative Transfer: Implications for Particle Size</i></a>	
Heavens, N.G., Richardson, M.I., Kass, D.M., Kleinböhl, A., McCleese, D.J. ....	Page 32
<a href="#"><i>The Vertical Distribution of Dust in Mars' Atmosphere During Northern Spring and Summer: The Perspective from the Mars Climate Sounder</i></a>	
Forget, F. ....	Page 37
<a href="#"><i>Dust Vertical Distribution and Size as Simulated with the LMD General Circulation Model</i></a>	

## Table of Contents (cont.)

Madeleine, J.-B., Forget, F., Millour, E., and Wolff, M. J. ....	Page 42
<a href="#"><i>Dust Radiative Effects Experiments Using the LMD Mars General Circulation Model</i></a>	
<i>Poster Session Day One</i>	
Eluszkiewicz, J., Flittner, D.E., Moncet, J.-L., and Wolff, M.J. ....	Page 49
<a href="#"><i>Development of Limb-Scattering Radiative Transfer Models for Mars Remote Sensing and Data Assimilation</i></a>	
Esposito, F., Colangeli, L., Della Corte V., Palumbo, P., Merrison, J., Nørnberg, P., Lopez Moreno, J.J., Rodriguez-Gomez, J.F., Ventura, S. and the International MEDUSA Team .....	Page 50
<a href="#"><i>The Observations of Atmospheric Dust and Water Vapour Close to the Surface of Mars: The MEDUSA Experiment</i></a>	
Määttänen, A., Fouchet, T., Forni, O., Forget, F., Savijärvi, H., Gondet, B., Melchiorri, R., Langevin, Y., Formisano, V., Giuranna, M. and Bibring, J.-P. ....	Page 55
<a href="#"><i>Dust Properties from a Local Dust Storm Observed by OMEGA and PFS on Mars Express</i></a>	
Montmessin, F., Godefroy, M., Hamelin, M., Berthelier, J.J., Yahi, S., Aplin, K., Simoes, F., and Szago, K. ....	Page 58
<a href="#"><i>ARES: An In Situ Sensor to Characterize Mars Atmospheric Electricity</i></a>	
Mulholland, D.P., Read, P.L., and Lewis, S.R. ....	Page 62
<a href="#"><i>Variable Obliquity and Longitude of Perihelion Simulations with the UK Mars GCM</i></a>	
Ogohara, K. and Satomura, T. ....	Page 65
<a href="#"><i>Regionality of Dust Storm Expansion</i></a>	
Wolff, M.J., Clancy, R.T., Smith, M.D., and McConnochie, T. ....	Page 67
<a href="#"><i>Vertical Particle Size Variations: The TES Dataset</i></a>	

### ***Session Four - Lifting Overviews and Laboratory Studies***

Gillies, J.A., Etyemezian, V., and Nikolich, G. ....	Page 71
<a href="#"><i>Dust Entrainment on Earth and Mars</i></a>	
Neakrase, L.D.V., and Greeley, R. ....	Page 74
<a href="#"><i>Dust Devils in the Laboratory: Estimating Atmospheric Dust Contributions</i></a>	
Lacks, D.J., Forward, K.F., and Sankaran, R.M. ....	Page 77
<a href="#"><i>Particle-Size Dependent Electrostatic Charging of Martian Regolith Simulant</i></a>	



---

## Table of Contents (cont.)

---

### **Session Five - Lifting and Dynamics Associated with Small-Scale Systems**

Barth, E.L., Rafkin, S.C.R., and Farrell, W.M. ....	Page 83
<a href="#"><u>The Electrodynamics of Mars Dust Disturbances</u></a>	
Fuerstenau, S. ....	Page 86
<a href="#"><u>Some Observations on the Thermodynamics and Fluid Dynamics of Dust Devils on Mars</u></a>	
Fenton, L. K. and Michaels, T. I. ....	Page 88
<a href="#"><u>Characterizing the Sensitivity of Daytime Turbulent Activity on Mars with the MRAMS LES.</u></a>	
Spiga, A., Lewis, S.R. and Forget, F. ....	Page 93
<a href="#"><u>Atmospheric Dust and Mesoscale/Microscale Meteorology</u></a>	
Lee, S.W., Thomas, P.C., and Cantor, B.A. ....	Page 97
<a href="#"><u>Aeolian Redistribution of Dust on the Tharsis Volcanos: Seasonal and Episodic Variability</u></a>	

### **Session Six - Lifting and Dynamics Associated with Large-Scale Systems**

Hollingsworth, J.L., and Kahre, M.A. ....	Page 103
<a href="#"><u>Extratropical Cyclones, Frontal Waves and Mars Dust: Modeling and Considerations</u></a>	
Wilson, R.J. ....	Page 108
<a href="#"><u>The Role of Spatially Variable Surface Dust in GCM Simulations of the Martian Dust Cycle</u></a>	
Michaels, T.I. ....	Page 113
<a href="#"><u>In Search of More Realistic Model Parameterizations of Aeolian Processes on Mars</u></a>	
Poster Session Day Two:	
Hinson, D.P., and Wang, H. ....	Page 119
<a href="#"><u>Characteristics of Baroclinic Eddies and Their Influence on The Timing and Location of Regional Dust Storms</u></a>	
Newman, C.E., Richardson, M.I., and Toigo, A.D. ....	Page 120
<a href="#"><u>Simulating Dust Cycles and Storms in Mars WRF with Limited Surface Dust</u></a>	
Kahre, M.A., Wilson, R.J., Haberle, R.M., and Hollingsworth, J.L. ....	Page 125
<a href="#"><u>An Inverse Approach to Modeling the Dust Cycle with Two Mars General Circulation Models</u></a>	
Lorenz, R.D. ....	Page 130
<a href="#"><u>Power Law Distribution of Dust Devils on Mars and Earth</u></a>	
Rafkin, S.C.R. ....	Page 132
<a href="#"><u>Investigating Dust Storm Feedback Processes Under Realistic Conditions</u></a>	

---

## Table of Contents (cont.)

---

Wu, D., McConnell, J.C., Kaminski, J., and Akingunola, D. ....	Page 137
<a href="#"><i>Dust Lifting, Deposition, and Transport Processes in GM3</i></a>	

### **Session Seven - Polar Dust and Dynamical Processes**

Brown, A.J., and Wolff, M.J. ....	Page 143
<a href="#"><i>CRISM Observations of Atmospheric Dust in the Martian South Pole Region</i></a>	
James, P.B. ....	Page 148
<a href="#"><i>Effects of Global Dust Events on the CO<sub>2</sub> Polar Caps</i></a>	
McConnochie, T.M., Smith, M.D., and Wilson, R.J. ....	Page 152
<a href="#"><i>Dust in the MGS-TES Limb Sounding Data Set: Dust Advection by Thermal Tides, and the Dust-Free Winter Pole</i></a>	
Kuroda, T., Medvedev, A.S., Hartogh, P., and Takahashi, M. ....	Page 156
<a href="#"><i>Effects of Dust Storms to the Winter Polar Warmings in the Martian Middle Atmosphere</i></a>	

### **Session Eight - Near Surface Environment**

Whiteway, J. A., Dickinson, C., Komguem, L., Davy, R., and Taylor, P. ....	Page 163
<a href="#"><i>Phoenix Lidar Observations of Dust in the Atmosphere of Mars</i></a>	
Vaughan, A.F., Johnson, J.R., Sullivan, R., Herkenhoff, K.E., and Landis, G.A. ....	Page 166
<a href="#"><i>Pancam and Microscopic Imager Observations of Dust Movement and Morphology on the Spirit Rover</i></a>	
Sullivan, R., Herkenhoff, K., Johnson, J., Landis, G., and Vaughan, A. ....	Page 170
<a href="#"><i>Sand-Sized Dust Aggregates on Mars</i></a>	
Hébrard E., Coll P., Marticorena B., Bergametti G., Montmessin F., Forget F. and Millour E. ....	Page 174
<a href="#"><i>An Aerodynamic Roughness Length Map Derived from Martian Rock Abundance Data and its Effects on Aeolian Erosion Thresholds in a MGCM</i></a>	

***Session One***  
***General Overview***  
*Tuesday, September 15, 2009*  
*8:30 AM – 10:00 AM*



**THE MARTIAN DUST CYCLE REVISITED.** Zurek, R.W.

**PRESENTING AUTHOR:** Zurek, R.W., Jet Propulsion Laboratory, California Institute of Technology, Pasadena, CA

---

The recent program of exploration of Mars by a series of orbiters and landed craft have provided new insights into the nature and fate of dust suspended in its atmosphere. Even our terminology is evolving as new techniques are used to investigate that most Martian of phenomena, namely its dust storms, which range from local dust raising to global events. One particular advance is the developing quantification of the vertical distribution of dust suspended in the atmosphere and its interaction with the water cycle. Using the new extended record of atmospheric monitoring, we shall also re-examine the seasonal and interannual variation in occurrence of the largest dust storms and the nature of their origin.

*This talk is based in part on work carried out at the Jet Propulsion Laboratory, California Institute of Technology, funded by the National Aeronautics and Space Administration.*

## **MODELING DUST IN THE MARTIAN ATMOSPHERE: A PROCESS DRIVEN CYCLE.**

Murphy, J.R.

**PRESENTING AUTHOR:** Murphy, J.R., Department of Astronomy, New Mexico State University, Las Cruces, NM

---

The martian dust cycle, if in fact it is a cycle, depends upon the ability of dust to be raised from the surface in to the atmosphere, to then experience a long enough suspension lifetime to be horizontally transported to a location different from its surface source, and then to be returned to the surface either independently or in concert with the condensed phase of a gas. The ability to model this ‘cycle’ thus depends upon the capability of properly simulating each of the physical processes involved in emplacement, transport, and deposition. There is also the need to properly simulate other cycles (water, CO<sub>2</sub>, others?) with which dust interacts. In this presentation I will focus upon the understanding of and implementation of the relevant processes related to dust within the context of numerical models spanning global to local scales. I’ll conclude by attempting to assess which processes seem to be ‘in hand’ and which processes require additional investigation for proper implementation.

## RECENT MEASUREMENTS OF THE RADIATIVE AND PHYSICAL PROPERTIES FOR MARS DUST. Clancy<sup>1</sup>, R. T. and Wolff<sup>1</sup>, M. J., <sup>1</sup>Space Science Institute (P.O. Box 3370, Bald Head Island, NC 28461, (Clancy@spacescience.org).

**Introduction:** Significant advances in the quantitative definitions of Mars dust properties, radiative and physical, have resulted from Mars Global Surveyor (MGS), Mars Exploration Rovers (MER), Mars Express (MEX), and Mars Reconnaissance Orbiter (MRO) observations and analyses over the past decade. These include new definitions of visible, near-IR, and thermal-IR optical indices; as well as dust particle sizes, vertical distributions, and cloud microphysics. Such dust properties play critical roles in the radiative forcing and transport calculations of Mars global (GCM) and mesoscale dynamical simulations. An incomplete, biased review of recent advances in our understanding of Mars dust properties follows.

**Dust Optical Indices:** The radiative influence of dust in the Mars atmosphere may be characterized by two distinct wavelength regimes; the visible region (0.4-2  $\mu\text{m}$ ) where dust absorption of solar flux dominates atmospheric heating [1], and the thermal IR (7-40  $\mu\text{m}$ ) where dust radiation supplements atmosphere cooling by  $\text{CO}_2$  [2].

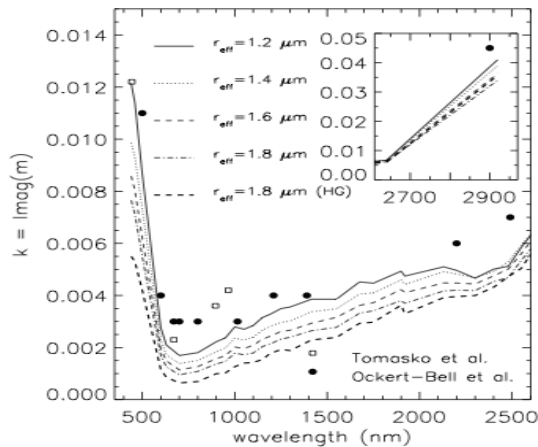


**Figure 1:** The 0.4-2.6  $\mu\text{m}$  spectral dependence for the imaginary refractive index of Mars dust is derived from CRISM EPF observations as a function of dust particle size (lines-[8]), and compared to previous Pathfinder [5] and Viking/Phobos [3,4] determinations. Figure reproduced from [8].

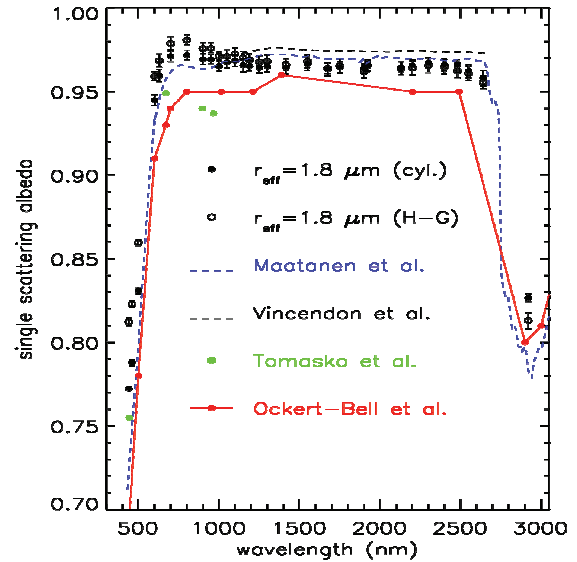


**Figure 2:** The 0.4-3.0  $\mu\text{m}$  spectral dependence of dust single scattering albedo (ssa) as retrieved from CRISM ([8], circle symbols for T-matrix cylinder and Henyey-Greenstein dust single scattering phase function models) and OMEGA [9,10] observations of the dusty Mars atmosphere. All of these CRISM/OMEGA analyses indicate substantially brighter dust than retrieved from Pathfinder [5] and Viking/Phobos [3, 4] observations. Figure reproduced from [8].

**Visible/Near-IR.** Dust solar absorption is specified by the dust single scattering albedo (ssa), which primarily depends on the dust imaginary optical index but also on dust particle size. Mars dust is not strongly absorbing in an absolute sense, with reported values for the solar band average ssa ranging from 0.86-0.89 [2,3,4,5] to 0.92-0.94 [6,7]. However, the dust absorption is proportional to  $1-\text{ssa}$  such that this range corresponds to a 30-40% disagreement in dust heating efficiency. Analyses of MRO CRISM [8] and MEX OMEGA [9,10] visible/near-IR spectral imaging observations over high dust loading conditions largely resolve this solar absorption discrepancy in favor of the higher ssa values, as well as providing visible and near-IR spectral dependences for dust ssa. The detailed radiative

transfer analysis of Wolff et al. [8] further yields the visible/near-IR spectral dependence of the dust imaginary and real optical indices as a function of dust particle size (figure 1, reproduced from [8]). A comparison of dust ssa values derived from the various spectrally resolved measurements is provided in figure 2 (reproduced from [8]). The effect of such lower ssa dust values, relative to values [3,4,5] currently employed in GCM and mesoscale simulations, has been demonstrated to significantly lower MGCM atmospheric temperatures, providing improved model simulations of atmospheric temperatures in the context of observed dust optical depths [9].

**Thermal-IR.** Analysis of Mariner 9 IRIS [10,11] and MGS TES [12] thermal IR spectra obtained during dust storm conditions in 1971 and 2001, respectively, have supported retrievals of dust optical indices over the 7-40  $\mu\text{m}$  spectral range. In addition, MER mini-TES spectra supported a separate analysis for dust thermal IR optical indices [13] such that dust optical indices over the 8-30  $\mu\text{m}$  wavelength range are particularly well determined. Figure 3 (reproduced from [12]) compares the IR spectral dependence of

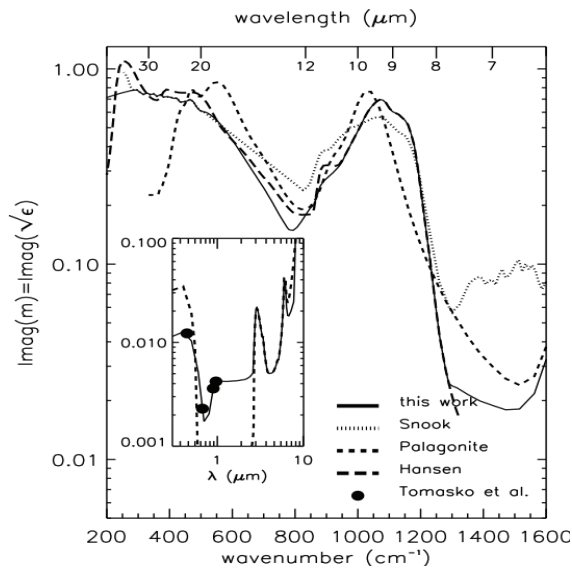


**Figure 3:** The 7-40  $\mu\text{m}$  spectral dependence for the imaginary refractive index of Mars dust is derived from analyses of Mariner 9 IRIS [10,11] and MGS TES [12] spectral observations of the dusty Mars atmosphere, and compared to the imaginary index of a Hawaiian palagonite sample [13]. The small insert compares index values over the visible/near-IR spectral range [8,13,14,5]. Figure reproduced from [12].

dust imaginary indices as retrieved from the TES [12], Mariner 9 IRIS [10,11] observations, and a terrestrial palagonite sample employed in modeling Mariner 9 IRIS dust spectra [13,14]. Si-O band absorptions near 9  $\mu\text{m}$  and longward of 18  $\mu\text{m}$ , lead to very low dust ssa values ( $<0.2$ ) and high cooling rates in the dusty and relatively warm lower atmosphere of Mars.

**Dust Single Scattering Phase Functions:** The single scattering phase function (sspf) specifies the angular distribution of light scattered as opposed to absorbed by the aerosol particle. Dust particle size and shape both strongly influence the dust sspf in complex fashions. Observational determinations of the Mars dust sspf include lander sky imaging [2,3,5] and orbiter emission-phase-function (EPF) sequence observations [6, 7], although the latter does not provide forward scattering angle coverage. All of these observations are limited to a few visible wavelengths and to the particular aerosol conditions (particle size and dust/ice composition) present at the time of the observations. The EPF observations demonstrate that ice clouds present variable sspf's that are quite distinct from the dust sspf [7]. Henyey-Greenstein 2-parameter sspf approximations [15] do not match observed dust scattering over visible to near-IR wavelengths (figure 4, reproduced from [8]), although they provide reasonable approximations at

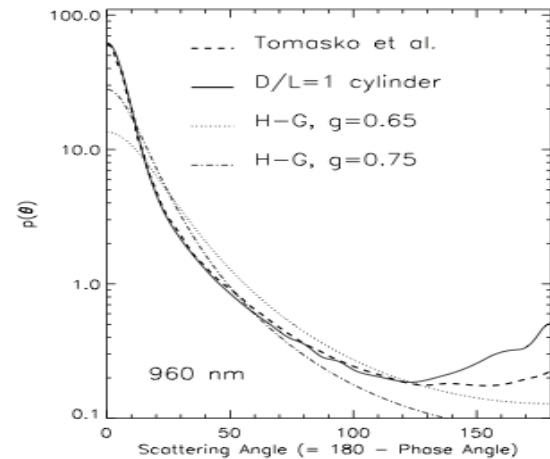


**Figure 4:** Dust single scattering phase functions (sspf) are presented for a wavelength of 960 nm; as derived from Pathfinder sky brightness observations [5], parameterized with Henyey-Greenstein [15] asymmetry factors ( $g$ ) of 0.65 and 0.75, and calculated from a T-matrix [16] solution for equant cylinders [8]. Figure reproduced from [8].



thermal IR wavelengths where forward scattering is muted [6]. Multi-wavelength, particle-size-dependent analyses, such as for MRO CRISM aerosol observations [8], have employed theoretical ssp<sub>f</sub>, generated from T-matrix numerical solutions for spheroid and cylindrical dust shapes [16]. Equant cylinder shapes provide reasonable approximations to the observed dust ssp<sub>f</sub>, except in the backscattering direction (figure 4).

The single scattering asymmetry parameter [ $g = \cos(\text{scattering angle})$  weighted  $4\pi$  steradian integral of the ssp<sub>f</sub>] specifies the average of forward versus backward scattering, which determines the degree to which the dust directs scattered solar flux to the surface versus back to space. Mars lander observations indicate  $g = 0.65$ - $0.68$  at visible wavelengths [3,5] versus values of  $0.5$ - $0.2$  calculated for  $9$ - $40 \mu\text{m}$  wavelengths [12].

**Dust Particle Sizes:** Dust particle size strongly influences the dust radiative properties (ratio of visible-to-IR optical depths, ssa, ssp<sub>f</sub>, and  $g$ ), dust lifting, and dust vertical distributions (through size dependent fall rates). Early analyses for Mars dust particle sizes indicated indicated cross-section weighted effective mean radii ( $r_{\text{eff}}$ ) in the range of  $2.5 \mu\text{m}$  [2,17]. Subsequent analyses [3,5,7,8,12,13,18] have returned significantly smaller dust particle sizes ( $r_{\text{eff}} = 1.4$ - $1.8 \mu\text{m}$ ), where the range may incorporate particle size variations in the Mars atmosphere.

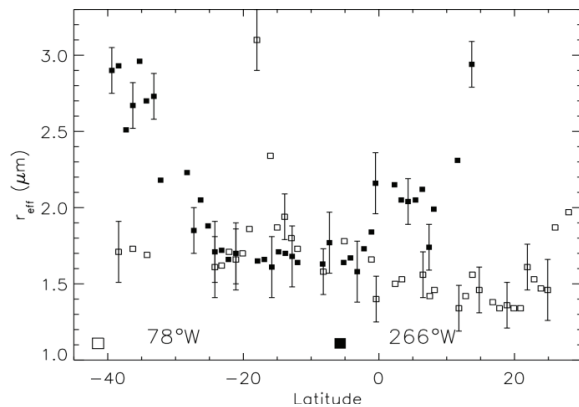


**Figure 5:** Dust particles sizes ( $r_{\text{eff}}$ ) retrieved from MGS TES observations of  $9$  and  $20 \mu\text{m}$  spectral absorptions during the 2001 global dust storm at  $L_s = 213^\circ$  [12]. Two Mars longitudes are presented, indicating substantial spatial variations in average dust particle sizes during this storm. Reproduced from [12].

Analyses of TES emission phase function (EPF) sequences, both for visible-to-IR opacity ratios [7] and the detailed dust IR spectral absorption [12], indicate that column average dust particle sizes increased to  $r_{\text{eff}} = 2$ - $3 \mu\text{m}$  over dust lifting regions during the 2001 dust storm (figure 5, reproduced from [12]).

Dust particle sizes would be expected to decrease with altitude, as affected by particle size dependent fall rates. Dust particle sizes of order  $r_{\text{eff}} \sim 1 \mu\text{m}$  at altitudes above  $20 \text{ km}$  have been observed within relatively quiescent dust lifting regimes [18, 19, figure 6]. It is also worth noting that water ice clouds often cap the vertical distribution of dust aerosols to altitudes below  $30 \text{ km}$  within minimum dust loading conditions [21].

In contrast, during global dust storm conditions larger dust particle sizes ( $r_{\text{eff}} = 1.5$ - $2.0 \mu\text{m}$ ) are modeled to extend to altitudes above  $40 \text{ km}$  [20]. Recent analysis of TES visible and thermal IR limb radiance profiles during the 2001 dust storm indicate such large dust sizes extended to  $50$ - $60 \text{ km}$  altitudes over regions of particularly intense dust lifting [19]. As indicated in figure 7 (reproduced from [19]), the global distribution of dust lifted to  $60 \text{ km}$  altitudes exhibits striking longitudinal variation. Bright regions correspond to peak dust opacity and particle sizes, dark regions reflect minimum dust opacity and particle sizes.

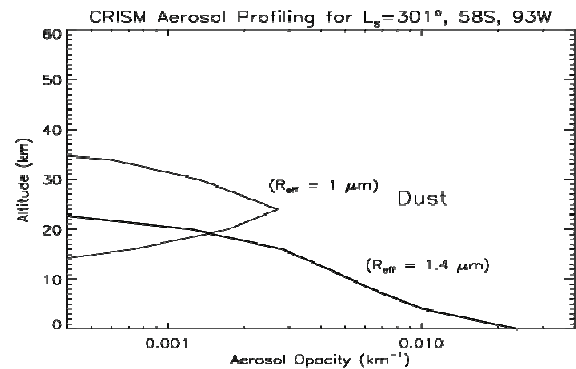


**Figure 6:** A vertical variation in dust particle size is retrieved from July 2009 CRISM limb observations, associated with the  $0.4$ - $4.0 \mu\text{m}$  spectral dependence of limb brightness versus limb tangent altitude. The period of observation corresponds to relatively limited dust lifting in the Mars southern hemisphere ( $\tau = 0.25$ ).

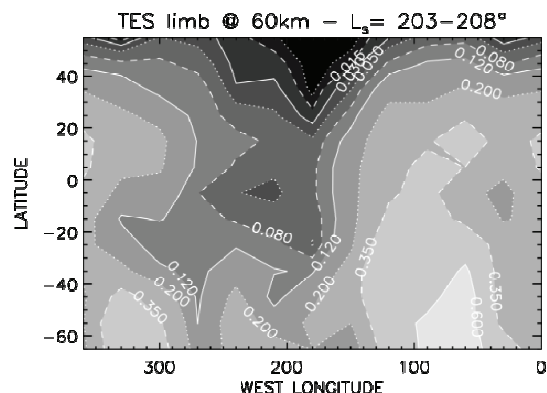


**Figure 7:** Global contour map of the TES solarband limb radiance at a tangent altitude of 60 km for the  $L_s$  range 203–208°, during the 2001 dust storm. Brightness units are  $500 \times$  TES units of  $W \cdot cm^{-2} \cdot sr^{-1} \cdot invcm^{-1}$ . Bright regions indicate scattering from  $r_{eff} = 1.5$  mm dust particles lifted to above 60 km altitudes. Figure reproduced from [19].

Currently, MRO MCS [22] and CRISM limb observations show the potential to characterize vertical profiles for dust particle size with global and seasonal coverages. Figure 6 presents the vertical opacity profiles for two dust particle size populations, as derived from spherical radiative transfer analysis of July 2009 CRISM limb spectra (0.4–4.0  $\mu m$ ) over 58S, 93W for  $L_s = 301^\circ$ . Dust lifting and cloud hazes are minimal at this time for the southern hemisphere of Mars.

**Dust Particle Composition:** The composition of Mars atmospheric dust was originally interpreted in terms of basalt, magnetite, and montmorillonite components on the basis of Mariner 9 IRIS spectra [17] and Viking lander imaging [2]. A less crystalline, palagonitic composition was later considered a more appropriate interpretation of the Mariner 9 IRIS observations [13] and Pathfinder lander imaging [23]. Recent TES and MER analyses favor a mechanically weathered product of surface basaltic rocks, with minimal chemical alteration [24, 25]. Such alteration appears limited to oxidation of a nanophase iron oxide component; the dust mineralogy includes pyroxene, olivine, and magnetite [25, 26]. Presumably, the iron oxide and magnetite components contribute to the solar absorption and the silicate components to the thermal IR absorption optical properties of the dust.

**Dust Particle Shapes:** Very little is known directly of the dust particle shapes, as MER and planned MSL microscope imaging resolution capabilities lie an order-of-magnitude above the dust particle sizes. The observed dust scattering phase function places limited constraints in that smooth, spheroid shapes are not preferred. MER microscopic imaging of Mars surface dust also suggests that individual dust particles form fluffy (under dense), sand-sized aggregates on the surface. Such loose aggregates could provide effective saltation grains that disintegrate into dust aerosols once lifted into the atmosphere [27].

**References:** [1] Gierasch P. J. and Goody R. M. (1972) *J. Atmos. Sci.*, 29, 400–402. [2] Pollack J. B. et al. (1979) *J. Geophys. Res.*, 84, 2929–2945. [3] Pollack J. B. et al. (1995) *J. Geophys. Res.*, 100, 5235–5250. [4] Ockert-Bell M. E. et al. (1997) *J. Geophys. Res.*, 102, 9039–9050. [5] Tomasko M. G. et al. (1997) *J. Geophys. Res.*, 104, 8987–9008. [6] Clancy R. T. and Lee S. W. (1991) *Icarus*, 93, 135–158. [7] Clancy R. T. et al. (2003) *J. Geophys. Res.*, 108(E9). [8] Wolff M. J. et al. (2009) *J. Geophys. Res.*, 114(E00D04). [9] Madeleine J.-B. et al. (2009) Mars Dust Cycle Workshop, NASA Ames. [10] Snook K. J. et al. (2000) *Bull. Amer. Astron. Soc.* 32, 51.08. [11] Hansen G. (2001) unpublished analysis. [12] Wolff M. J. and R. T. Clancy (2003) *J. Geophys. Res.* 108(E9), 5097. [12] Wolff M. J. et al. (2006) *J. Geophys. Res.* 111, E12S17. [13] Clancy R. T. et al. (1995) *J. Geophys. Res.* 100, 5251–5264. [14] Roush T. et al. (1991) *Icarus* 94, 191–208. [15] Henyey L. G. and Greenstein (1941) *Astrophys. J.* 93, 70–83. [16] Mishchenko M. I. et al. (1997) *J. Geophys. Res.* 102, 13,543–13,553. [17] Toon O. B. et al. (1977) *Icarus* 30, 663–696. [18] Chassigni E. et al. (1995) *J. Geophys. Res.* 100, 5525–5539. [19] Clancy R. T. et al. (2009) *Icarus*, accepted. [20] Kahre M. A. et al. (2008) *Icarus* 195, 576–597. [21] Clancy R. T. et al. (2007) *J. Geophys. Res.* 112(E04004). [22] Kleinböhl A. et al. (2009) Mars Dust Cycle Workshop, NASA Ames. [23] Morris R. V. et al. (2000) *J. Geophys. Res.* 105, 1757–1818. [24] Hamilton V. E. et al. (2005) *J. Geophys. Res.* 110(E12). [25] Madsen M. B. et al. (2009) *J. Geophys. Res.* 114(E06S90). [26] Goetz, W. (2009) Mars Dust Cycle Workshop, NASA Ames. [27] Sullivan R. et al. (2009) Mars Dust Cycle Workshop, NASA Ames.

**Session Two**  
***Global Dust Storms***  
*Tuesday, September 15, 2009*  
*10:30 AM – 12:00 PM*



## MCS VIEWS OF ATMOSPHERIC DUST DURING THE 2009 PLANET ENCIRCLING

**DUST EVENT.** Snyder Hale<sup>1</sup>, A., Kass<sup>1</sup>, D.M., Schofield<sup>1</sup>, J.T., Kleinböhl<sup>1</sup>, A., McCleese<sup>1</sup>, D.J., and the MCS Team. <sup>1</sup>Jet Propulsion Laboratory, Caltech, Mail Stop 169-237, 4800 Oak Grove Dr, Pasadena, CA 91109. ([Amy.S.Hale@jpl.nasa.gov](mailto:Amy.S.Hale@jpl.nasa.gov), [David.Kass@jpl.nasa.gov](mailto:David.Kass@jpl.nasa.gov), [John.T.Schofield@jpl.nasa.gov](mailto:John.T.Schofield@jpl.nasa.gov), [Armin.Kleinboehl@jpl.nasa.gov](mailto:Armin.Kleinboehl@jpl.nasa.gov), [Daniel.J.McCleese@jpl.nasa.gov](mailto:Daniel.J.McCleese@jpl.nasa.gov)).

**Introduction:** The Mars Climate Sounder (MCS) instrument on Mars Reconnaissance Orbiter (MRO) observed the dust activity in March through May of 2009 ( $L_s = 234^\circ$  to  $277^\circ$ ). MCS is a 9 channel filter radiometer (ranging from 0.3 to  $43\ \mu\text{m}$ ) with a 21 detector array oriented perpendicular to the limb of Mars for each channel. The primary use of the observations is for the retrieval of temperature, dust and water ice profiles [1], but radiances are measured and calibrated for all infrared detectors.

In this time period, most of the observed dust remained confined to the southern hemisphere, but was observed at all latitudes. Small amounts of dust were also observed in the middle atmosphere in the northern hemisphere soon after the growth of the southern activity. During the decaying phase, dust was also seen regionally at very high southern latitudes. This work is a companion piece to that of Kass et al. [2]. The Kass work presents atmospheric thermal structure in this time frame as seen by MCS, whereas this work presents dust height observations, as dust height is a quantity MCS can give us that other instruments cannot.

**Approach:** To map dust height in the atmosphere, we used the radiances from the A5 channel ( $22.1\ \mu\text{m}$ ), which is sensitive to dust opacity. The A5 channel's 21 individual detectors view different heights in the Martian atmosphere as MCS scans. The radiances from these detectors were then converted to brightness temperature. Areas with brightness temperatures over 120 K were considered to have dust present at a significant level. This value was chosen empirically based on brightness temperature profiles in the A5 channel like the one shown to the right (Figure 1).

This brightness temperature cutoff value was validated by comparing our calculated dust heights with retrieved dust profiles. The following figures show a retrieved profile and a dust height map generated with our method.

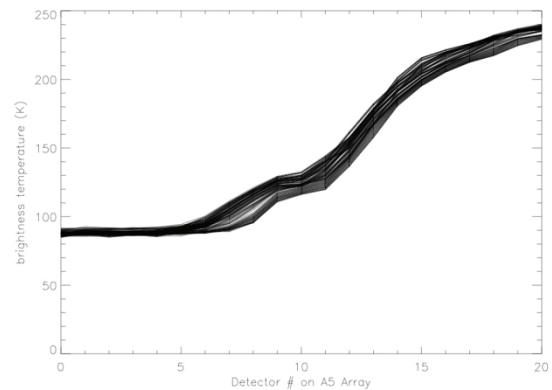


**Figure 1:** Brightness temperature profiles for the MCS A5 channel taken on April 1, 2009

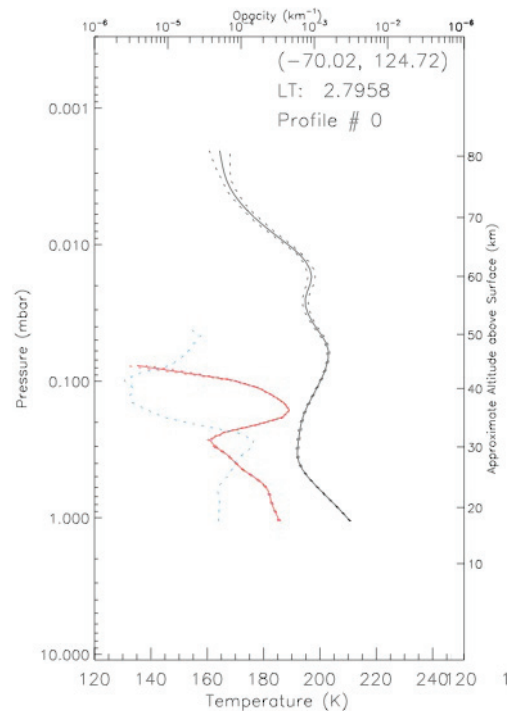


**Figure 2:** Dust profiles derived from MCS observations on taken on April 1, 2009. Dust is plotted on the red curve (solid line), water ice on the blue, and temperature on the black.

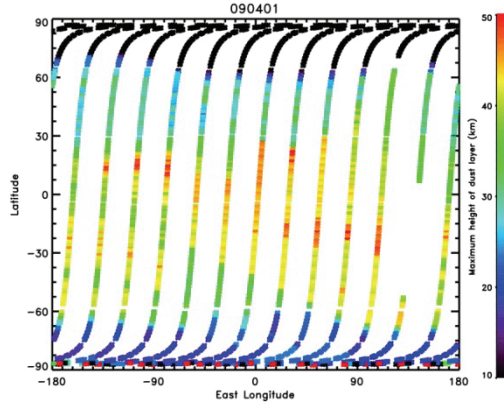


**Figure 3:** Dust heights mapped with our method for night time orbits on April 1, 2009. Dust layer height is relative to the areoid.

This profile shows a maximum dust opacity at a height of approximately 30 kilometers, which is what we see in our map. The maximum opacity for this profile is approximately  $2 \times 10^{-4} \text{ km}^{-1}$ ; inspection of other profiles indicates that this is the opacity value which corresponds to a brightness temperature in A5 of 120. Therefore, our maps are most accurately described as maps of the height at which the dust opacity is approximately  $2 \times 10^{-4} \text{ km}^{-1}$ . Obviously, some amount of dust may be present in the atmosphere at greater heights. Atmospheric height is calculated based on the spacecraft and instrument viewing geometry at the time of the observation and is relative to the areoid, not the actual surface. Therefore in places of pronounced topography, the calculated height will not be in close agreement with the actual height above the surface..

**Observations:** Dust heights were mapped for daytime (local time between 0900 and 2100) and nighttime orbits (local time between 2100 and 0900). Selected dates are shown below. The dates also correspond to the dates shown in the Kass et al. abstract, which explores atmospheric thermal structure during this same dust event.

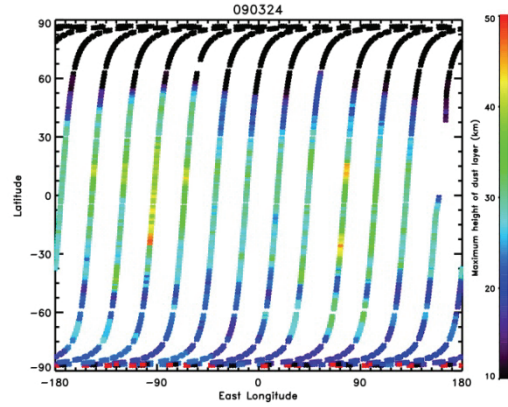
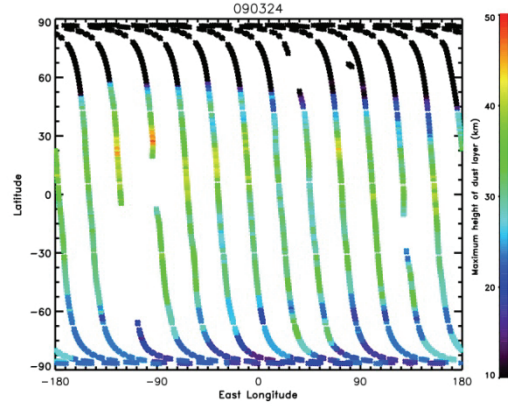


**Figure 4(a, b):** Dust heights for day (top) and night (bottom) on March 24, 2009, just before the start of the dust event.

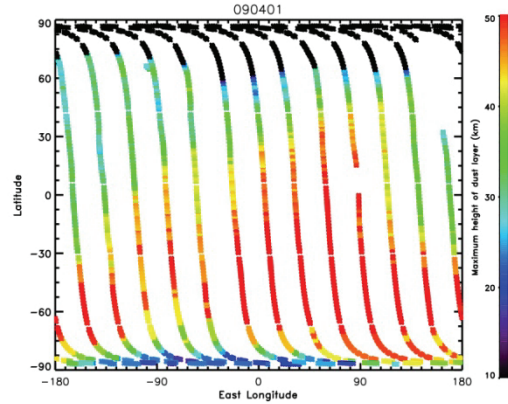


**Figure 5:** April 1, 2009 daytime orbits. Night orbits for the same day are shown in figure 3 and are not repeated here. This day is near the maximum of visible dust activity.



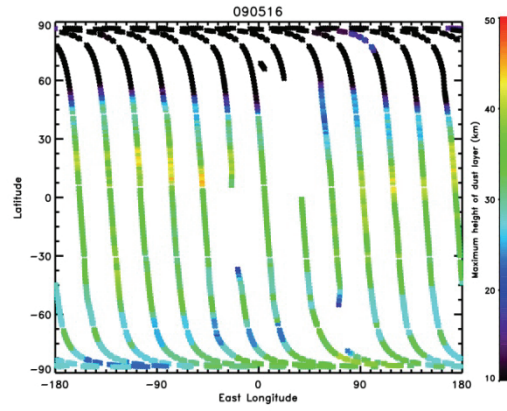
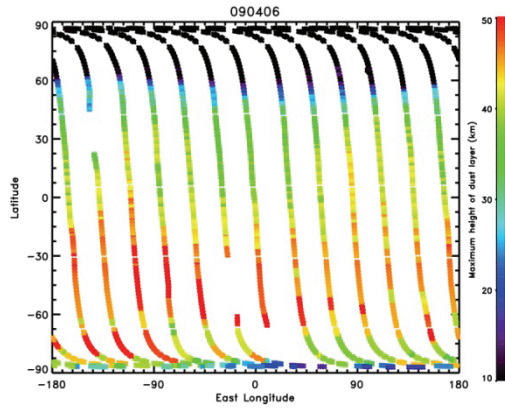


**Figure 6:** April 6, 2009 day (top) and night (bottom plots).

**Figure 7:** May 16, 2009 day (top) and night (bottom). Areas of dust at very high northern latitudes are likely polar hood clouds, not dust.

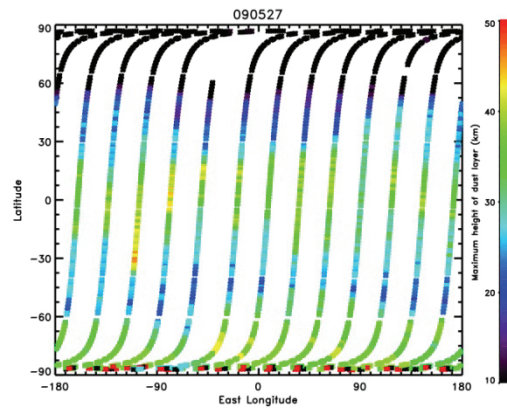
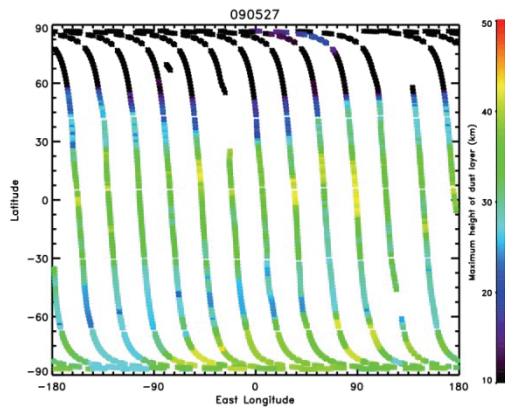
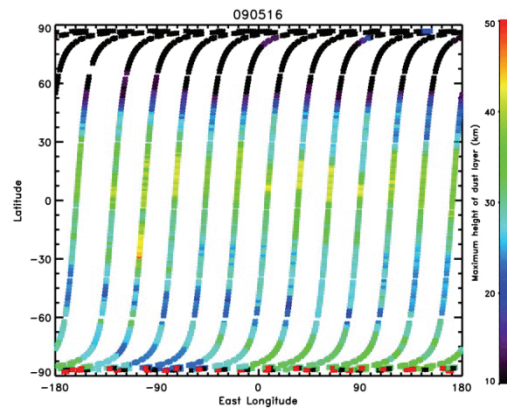
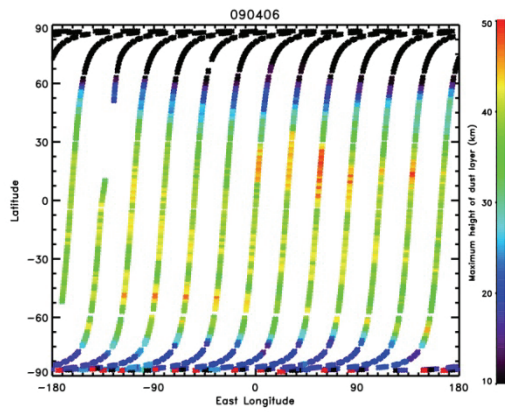


**Figure 8:** May 27, 2009 day (left) and night (right). Areas of dust at very high northern latitudes are likely polar hood clouds, not dust.

**Discussion:** The first observable dust activity for the 2009 dust storm/event occurred on March 25; the maps shown above of March 24 data are of a dust storm free atmosphere. Dust extent rapidly expanded over the next several days to all longitudes, though it remained confined to the southern hemisphere. Dust height in the atmosphere greatly and rapidly increased along with dust areal extent, with the most widespread and high dust being observed on and around April 1, 2009. After that, the dust heights began to decrease, though at a much slower rate than they had originally risen. April 6 observations show lower dust heights throughout the southern hemisphere, along with some localized high dust in low northern latitudes from approximately 0 to 180 east longitude. Throughout May, dust heights in the atmosphere continued to decrease, though in late May localized dust activity was observed at high southern latitudes; presumably this was a cap edge storm, and not directly related to the earlier dust event (see figure 8).

Maximum dust heights are generally observed to decrease at night relative to during the day at all time periods during the observed event. Localized areas of high dust may be in somewhat different locations at night as well (see figure 6 for an example of this).

Overall, the 2009 event as observed by MCS shows that the event had a quick onset, with dust becoming planet encircling and present high in the atmosphere within only a few days. Thereafter, the decay phase was much longer, taking place over nearly a Martian month. This is consistent with other observed Martian dust events. Differences in day and night dusts heights were also observed throughout the event.

**References:** [1] Kleinböhl A. et al. (2009), JGR, doi:10.1029/2009JE003358. [2] Kass, D.M. (2009), this meeting.

*This work was carried out at the Jet Propulsion Laboratory, California Institute of Technology under a contract with the National Aeronautics and Space Administration.*



## MCS VIEWS OF ATMOSPHERIC THERMAL STRUCTURE DURING THE 2009 PLANET ENCIRCLING DUST EVENT.

Kass<sup>1</sup>, D.M., Snyder Hale<sup>1</sup>, A., Schofield<sup>1</sup>, J.T., Kleinböhl<sup>1</sup>, A., McCleese<sup>1</sup>, D.J., and the MCS Team. <sup>1</sup>Jet Propulsion Laboratory, Caltech, Mail Stop 169-237, 4800 Oak Grove Dr, Pasadena, CA 91109. ([David.Kass@jpl.nasa.gov](mailto:David.Kass@jpl.nasa.gov), [Amy.S.Hale@jpl.nasa.gov](mailto:Amy.S.Hale@jpl.nasa.gov), [John.T.Schofield@jpl.nasa.gov](mailto:John.T.Schofield@jpl.nasa.gov), [Armin.Kleinboehl@jpl.nasa.gov](mailto:Armin.Kleinboehl@jpl.nasa.gov), [Daniel.J.McCleese@jpl.nasa.gov](mailto:Daniel.J.McCleese@jpl.nasa.gov)).

**Introduction:** Observations from the Mars Climate Sounder (MCS) [1] on the Mars Reconnaissance Orbiter (MRO) [2] provide a view of a planet encircling dust event in early 2009. MCS is a 9 channel filter radiometer (ranging from 0.3 to 43  $\mu\text{m}$ ) with a 21 detector array oriented perpendicular to the limb of Mars for each channel. The primary use of the observations is for the retrieval of temperature, dust and water ice profiles [3], but radiances are measured and calibrated for all infrared detectors.

In this work we focus on the thermal response of the atmosphere to the dust during the 2009 dust event. As discussed in the accompanying abstract (A. Snyder Hale [4]), the dust was planet encircling in the southern hemisphere, and while there was an increase in dustiness in the northern hemisphere, most of the dust was confined south of the equator.

**Analysis Approach:** To study the impact of the dust on the atmosphere, we primarily used the radiances from the lowest detector in the 15  $\mu\text{m}$  channel. The radiance was converted to a brightness temperature, which effectively provides the atmospheric temperature since the atmosphere is opaque. The measurement uncertainty is less than 1 K over the temperature ranges seen in the martian atmosphere [1].

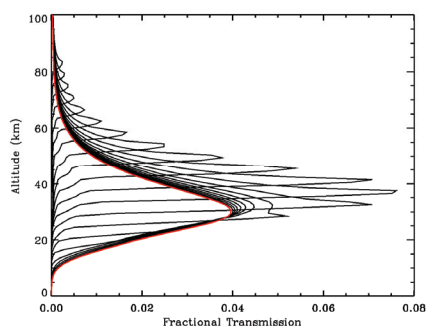


**Figure 1:** Weighting function for the MCS 15  $\mu\text{m}$  channel detectors when pointed at the limb. The red function is for the lowest detector, used in this study.

The lowest detector is nominally pointing at a tangent height 7.5 km below the surface, but the atmosphere is opaque at these wavelengths. The vertical weighting function is shown in figure 1. It is a broad, nadir-like weighting function which peaks at 30 km and primarily samples the atmosphere between 20 km and 40 km above the surface.

The weighting function has a  $\sim 60$  km in-track length (generally north-south, but east-west near the poles). It has a  $\sim 8$  km cross-track width. The location of the detector line of sight intersection with a 30 km altitude surface was used for mapping the observations. This takes into account the fact that the radiance does not come from the surface, but from the atmosphere.

**Observations:** Due to the rapidly evolving atmosphere, the observations were used to create daily maps and zonal averages (figures 2 through 7). For the maps the observations are interpolated, using the  $\sim 27^\circ$  longitude spacing of the MRO orbit [2].

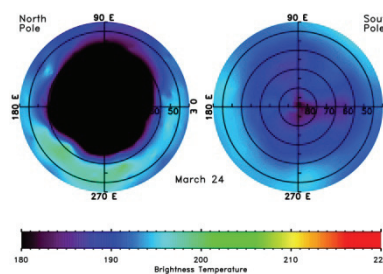


**Figure 2:** Atmospheric temperatures on March 24, 2009 ( $L_s = 233.3$ ). a) North and South polar projections of the 20 km to 40 km temperature. b) Zonal mean (solid), maximum (dashed) and minimum (dotted) temperatures. Gold is day and purple is night. The dotted bands are used for creating zonal time series (see figure 8).

In the maps, temperatures below 180 K (inside the winter polar vortex) are not shown to enhance the details in the rest of the atmosphere (MCS is sensitive to brightness temperatures down to  $\sim 90$  K in the  $15\ \mu\text{m}$  channel). Based on the observations, 180 K is a convenient cutoff for the edge of the vortex.

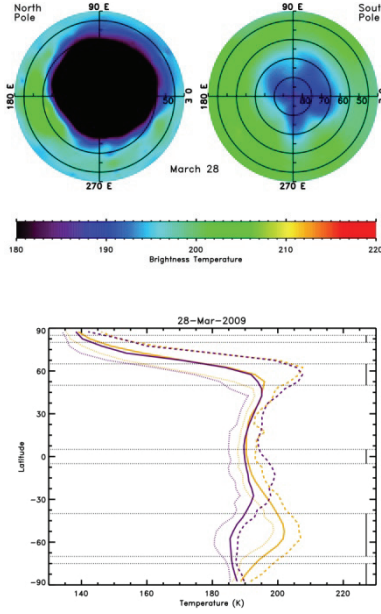


**Figure 3:** March 28, 2009 ( $L_s = 235.9$ ).

For both the maps and the zonal mean fields, the data is split in to day and night by local time to avoid mixing different local times together. Due to the MRO  $\sim 3$  pm orbit [2], we define daytime as 9 am to 9 pm. While we use a 12 hour window, the local time is near 3 am or 3 pm unless very near a pole. The 12-hour window, provides coverage at all latitudes without mixing local times at any latitude.

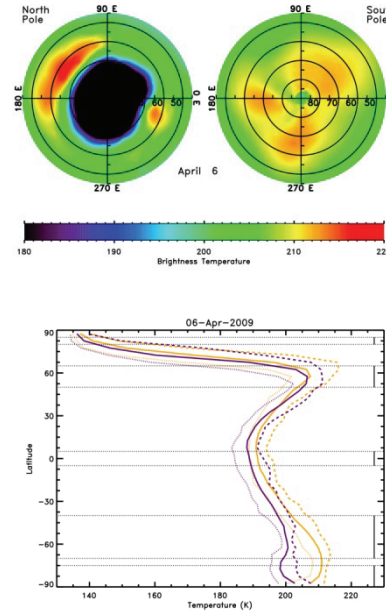


**Figure 5:** April 6, 2009 ( $L_s = 241.6$ ).

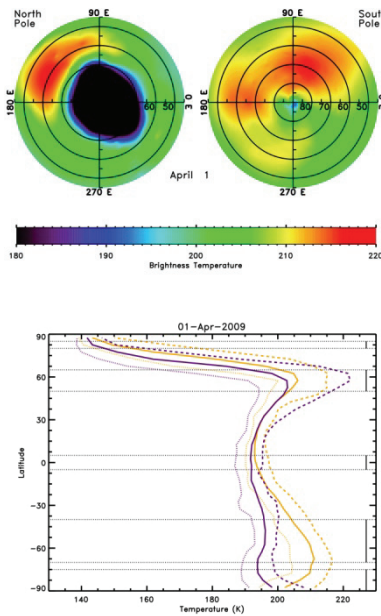


**Figure 4:** April 1, 2009 ( $L_s = 238.4$ ).

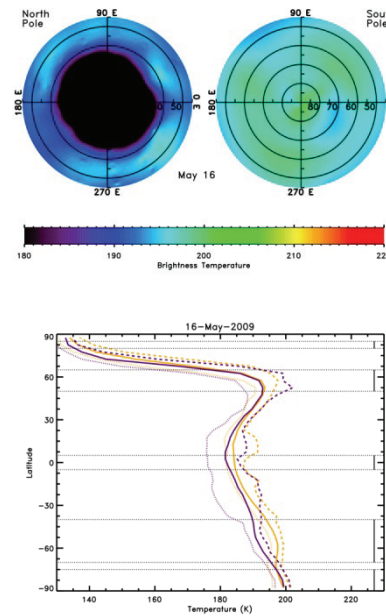


**Figure 6:** May 16, 2009 ( $L_s = 266.9$ ).

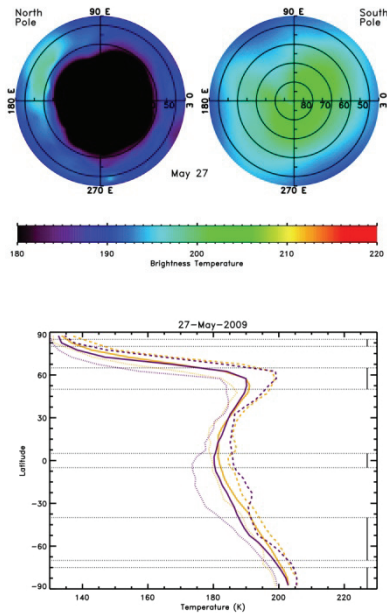


**Figure 7:** May 27, 2009 ( $L_s = 273.8$ ).

The zonal measurements were also binned in five discontinuous broader bins (shown on figure 2b) to produce time series of interesting latitude regions. Figures 8 through 12 show the day by day trends of the atmosphere in these bands.

**Dust Event Heating History:** The first changes in the atmospheric temperatures due to the storm, about 5K of warming at 30 km, appear on March 25<sup>th</sup>. Over the next three days, the heating intensifies and spreads to all longitudes.

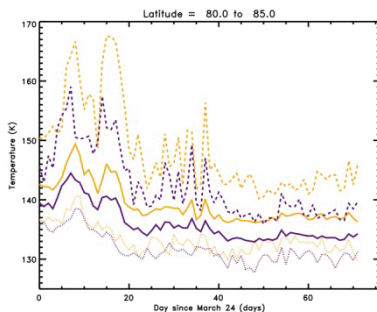


**Figure 8:** Time series of zonal mean (solid), minimum (dotted) and maximum (dashed) temperatures for the northern polar region (80N to 85N). Daytime is in gold and nighttime in purple.

The first of April shows the atmosphere during the peak of the heating. At this point, the core of the southern heating is moving poleward and the northern winter polar vortex has been compressed to its smallest areal extent. By April 6<sup>th</sup>, the temperatures have decreased in the south and are about to start decreasing in the north. In the south there are three longitudes with warm features that persist for the next 10 sols and do not circulate with the atmosphere. In the north, there are a number of brief warming episodes at various longitudes that last for one to two days.

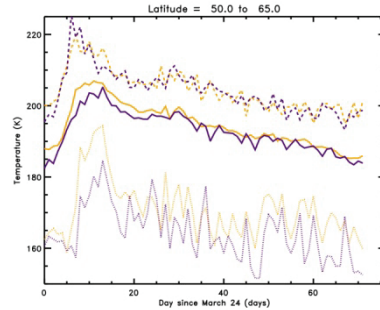


**Figure 9:** The peak of the northern heating (50N to 65N). Note the modified temperature scale

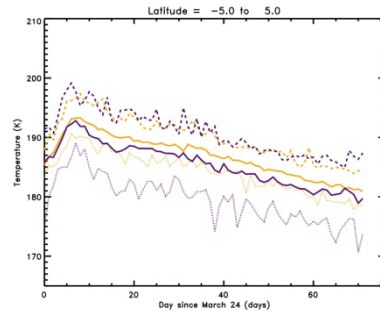


**Figure 10:** The equatorial regions (5S to 5N).

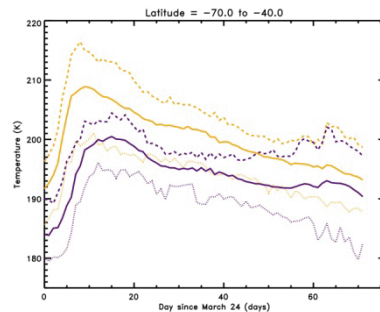


**Figure 11:** The peak dust activity (70S to 40S).

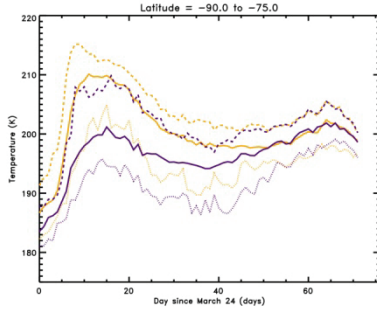


**Figure 12:** The southern polar region (90S to 75S).

The atmosphere continues to cool throughout the rest of April and the first half of May (through  $L_s$  267). At this point, the northern hemisphere is back to (or below) the pre-storm temperatures and the winter vortex has grown back to its original size. The May 16<sup>th</sup> maps show the start of a southern polar cap edge storm. This peaks around May 27<sup>th</sup> with modest daytime heating ( $< 10$  K). The nighttime temperatures do increase more (and start increasing earlier), although they reach similar temperatures. This southern heating has no impact on the northern hemisphere.

**Northern Hemisphere Response:** The response of the atmosphere in the northern hemisphere is quite complex. Figures 13, 14 and 15 show the retrieved temperature profiles early in the storm between 60N and 75N. These latitudes were selected to cover the region of maximum heating outside of the polar vortex.

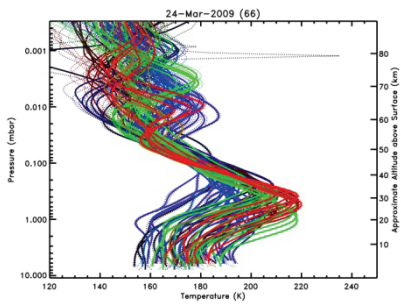


**Figure 13:** Afternoon retrieved temperature profiles between 60N and 75N on March 24, 2009 ( $L_s = 233.3$ ). They are color coded for longitude with 0E = Green, 90E = Blue, 180E = Black, -90E = Red.

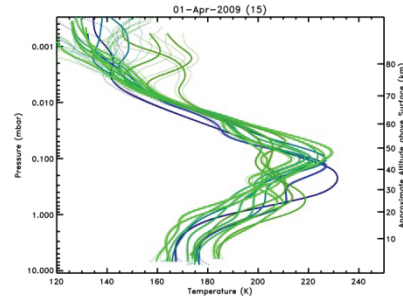


**Figure 14:** April 1, 2009 ( $L_s = 238.4$ ). Longitudes inside the polar vortex are not shown.

The dominant feature of the atmospheric profiles are the maxima in the middle atmosphere due to the descending branch of the Hadley circulation [5]. Prior to the start of the storm (figure 13), the atmosphere shows significant longitudinal variability. This is particularly noticeable near the surface. In the upper atmosphere (below 0.05 mbar), there is significant wave activity.

As the heating in the south develops and triggers a northern response, the atmosphere changes significantly. The maximum temperature due to the circulation increases from 220 K to 240 K while moving upward by up to 20 km (from 30 km to 50 km) and often broadening from 20 km deep to 40 km deep. At the same time, the longitudinal variability is reduced overall--despite the strong longitudinal variability seen in the temperature maps at 30 km. This is especially noticeable in the upper atmosphere where almost all of the pre-storm wave structure has disappeared.

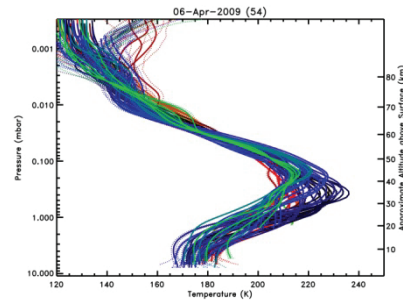


**Figure 15:** April 6, 2009 ( $L_s = 241.6$ ).

As this change in structure was occurring, the northern (winter) polar vortex was reduced to roughly half its size at an altitude of 30 km as the boundary moved from 60 N to 70 N (figure 2 versus figure 4).

**Conclusions:** It appears that large dust events, even when confined to the southern hemisphere, trigger a very fast change to the atmospheric temperatures globally. This includes even the core of the winter polar vortex in the opposite hemisphere.

These changes propagate very rapidly, often with the northern warming appearing within 24 hours of the start of the activity in the south. In some cases, it may even be as fast as 12 hours (based on looking at both daytime and nighttime changes). Due to a “focusing” effect, the largest temperatures changes, as well as the highest temperatures are in the northern hemisphere.

There are complex differences in the southern response when comparing the daytime and nighttime temperature changes. This is presumably a complex interaction between the solar driven dust heating, IR dust cooling, dynamical heating/cooling and modifications of the tide due to the global changes. The response also varies with latitude (as well as longitude), although this may be related to the distribution of the dust and/or the regions within the arctic circle.

**References:** [1] McCleese D. J. et al. (2007) JGR, 112, E05S06 doi:10.1029/2006JE002790. [2] Zurek R. W. and Smrekar S. E. (2007) JGR, 112, E05S01, doi:10.1029/2006JE002701. [3] Kleinböhl A. et al. (2009), JGR, doi:10.1029/2009JE003358. [4] Snyder Hale A. (2009), this meeting. [5] McCleese D.J. et al. (2008), Nature Geosci., 1, 745-749.

*This work was carried out at the Jet Propulsion Laboratory, California Institute of Technology under a contract with the National Aeronautics and Space Administration.*

---

## NEW ANALYSIS OF MARS GLOBAL SURVEYOR THERMAL EMISSION SPECTROMETER DATA FROM GLOBAL DUST STORM 2001A.

Elteto, A., Toon, O.B.  
Laboratory for Atmospheric and Space Physics, University of Colorado, Campus Box 392, Boulder, CO 80309-0392, 303-492-1534, Attila.Elteto@colorado.edu.

---

**Introduction:** Mars Global Surveyor's Thermal Emission Spectrometer (MGS TES) provided the best data coverage of the Martian atmosphere during a global dust storm to date in 2001. Despite this, analysis of this data has been either simplified [1] or limited in scope [2]. A global retrieval of dust effective radius, for example, has not been attempted before, despite the need for retrieval of this parameter to resolve a conflict between observations [2,3] and models [4,5]. In this work we revisit the TES data from the global dust storm of 2001 with a more up-to-date parameter retrieval algorithm in order to diagnose the dust storm's properties and effects, and learn about its significance in the Martian dust cycle.

**Methods:** Our retrieval algorithm uses Newtonian first-order sensitivity functions of the spectral response to variation in parameters to fit a model spectrum to the TES infrared data at selected TES channels at 499, 1099, and 1301  $\text{cm}^{-1}$ . The infrared spectrum is especially sensitive to variations in dust optical depth, effective radius, and surface temperature at these wavenumbers. After constructing an initial model spectrum using input of physical parameters from the TES archives [1], as well as assumed dust optical indexes [2], the retrieval iteratively fits the model to the data at all selected wavenumbers to simultaneously retrieve dust optical depth (referenced to 1075  $\text{cm}^{-1}$ ), geometric cross-section weighted effective radius, and surface temperature.

**Data selection:** We selected individual TES spectra at 5° latitude sampling increments of 0.2-1° width between 60°S and 60°N latitudes. We chose to retrieve in 10-20° areocentric longitude ( $L_s$ ) time increments, for 12 MGS orbits (about 1 Martian sol) of data at each time sample from  $L_s=175^\circ$  during the year of the global dust storm to  $L_s=296^\circ$  the next Martian year (MY25 and 26). We only selected daytime (about 1400-1500 hr local time) nadir viewing TES data with no appreciable presence of water ice ( $\tau_{875\text{cm}^{-1}} < 0.1$ ). We also filtered out data with low surface to atmosphere temperature contrast. Our retrieval algorithm produced meaningful results for 56878 individual TES spectra.

**Results and discussion:** We plotted our retrieved dust optical depths as a function of surface pressure (note: the surface pressure was not retrieved, but was acquired from the TES data archives [1], and is based on atmospheric models of Mars) using all results (indiscriminate of global location) from each time interval. We then calculated a linear fit ( $\tau = AP+B$ ) to retrieve the correlation ( $R^2$ , coefficient of determination) between dust optical depth and atmospheric column mass (as characterized by surface pressure). A global correlation between these parameters indicates global dust mixing processes. A lack of correlation indicates a lack of global mixing processes, when dust optical depth is determined by local dust lifting/mixing processes. We also calculated a global average dust optical depth at these times. However these averages should be taken only as first-order estimates because the data selection subject to our data filters, hence the latitudinal coverage, changed through the Martian seasons (for example: surface-to-air temperature contrast is low at high latitudes near the polar night). Our results are shown in Table 1.

Our results indicate that global dust mixing ( $R^2$ ) is low (less than about 0.1) except for periods during southern hemisphere spring and summer, subsequent to the increase in dust optical depth in both Martian years ( $L_s=214-357^\circ$ , and  $L_s=234-296^\circ$  respectively). This increase in a year with a global dust storm and one without one indicates that similar atmospheric mixing processes are present, and that global dust mixing is an expected part of the Martian dust cycle.

We also examined dust optical depth decay rates during the decay phase of the global dust storm between  $L_s=234-285^\circ$ . We calculated observed decay rates at various surface pressure bins (since our previous results show that dust was uniformly mixed during this time) and compared them to theoretical dust removal rates, assuming dust removal through gravitational sedimentation at the bottom of the atmospheric column subject to Stokes-Cunningham terminal velocities for the dust particles (Fig. 1). We found an agreement within about 50% (because of our simple, first-order approach to these calculations,



a statistically good fit) at all pressure bins until  $L_s=275^\circ$ , after which optical depth decay subsides, and new dust lifting/mixing processes return. These results are consistent with dust removal dominated by gravitational sedimentation of particles without the need for other processes, such as scavenging by the formation ice clouds.

Our work produced the first global retrieval of dust effective radius on Mars. Figure 2 a and b show our results for the global dust storm, as well as the corresponding season one Martian year later.

$L_s$ (degrees)	$R^2$	average $\tau$
175 (MY 25)	0.039	$0.20 \pm 0.07$
184	0.0486	$0.25 \pm 0.11$
194	0.0218	$1.11 \pm 0.26$
204	0.005	$1.52 \pm 0.28$
214	0.4091	$1.56 \pm 0.32$
224	0.4647	$1.38 \pm 0.26$
234	0.7854	NA
244	0.7884	$0.78 \pm 0.19$
255	0.7411	$*0.60 \pm 0.14$
265	0.6786	$0.48 \pm 0.11$
275	0.5723	$0.37 \pm 0.09$
285	0.5708	$0.29 \pm 0.08$
296	0.6103	$0.24 \pm 0.07$
316	0.5488	$0.22 \pm 0.08$
333	0.5405	$0.31 \pm 0.12$
357	0.4105	$0.19 \pm 0.06$
14 (MY 26)	0.0669	$0.16 \pm 0.05$
34	0.1086	$0.14 \pm 0.04$
58	0.026	$0.13 \pm 0.04$
75	0.0099	$*0.13 \pm 0.04$
93	0.0159	$*0.11 \pm 0.03$
115	0.00008	$*0.10 \pm 0.03$
134	0.033	$0.16 \pm 0.04$
154	0.249	$0.17 \pm 0.05$
175	0.0838	$0.21 \pm 0.08$
194	0.0926	$0.22 \pm 0.07$
214	0.1379	$0.31 \pm 0.14$
234	0.5432	$0.37 \pm 0.12$
255	0.6244	$0.33 \pm 0.09$
275	0.6023	$0.26 \pm 0.07$
296	0.2948	$0.22 \pm 0.08$

**Table 1:** the coefficient of determination ( $R^2$ ) of a linear fit to optical depth versus surface pressure of all results at each time interval. Also the global average dust optical depth. \* indicates results for which less than 50% of latitudes had retrieved optical depths to construct meaningful global averages. NA indicates that no latitudinal average optical depths were available.

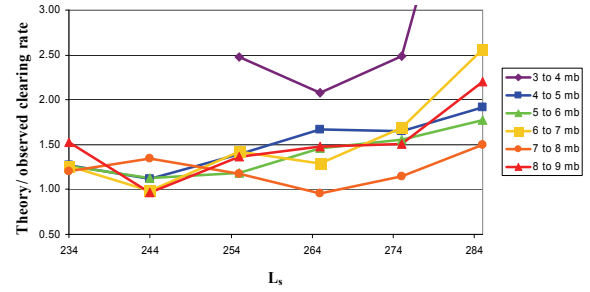


**Figure 1:** Theoretical (Stokes-Cunningham) dust clearing rates divided by observed clearing rates at various pressure bins. The 3-4mb bin had limited, uneven data coverage and hence is not reliable.

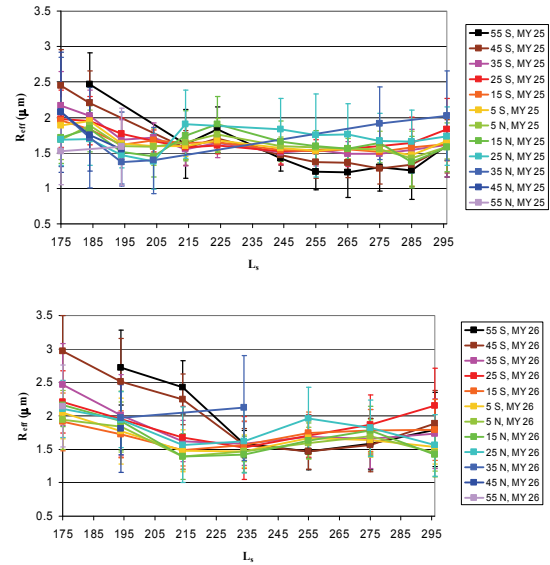


**Figure 2:** Retrieved zonally averaged dust effective radius for  $L_s=175-296^\circ$  in MY 25 (a) and 26 (b). The error bars represent the standard deviation of results in each latitude bin.

Zonally averaged dust effective radius was found to be statistically constant (within variability, as indicated by the standard deviation) at all locations except high southern latitudes ( $35^\circ$  and higher). The high southern latitudes had larger ( $>2 \mu\text{m}$ ) average effective radii around southern spring equinox ( $L_s=180^\circ$ ), and then smaller particles ( $<2 \mu\text{m}$ ). This behavior for high southern latitudes was also observed at northern spring equinox (not shown). The drop in dust particle size coincides with increase in dust opacity for both southern equinoxes.

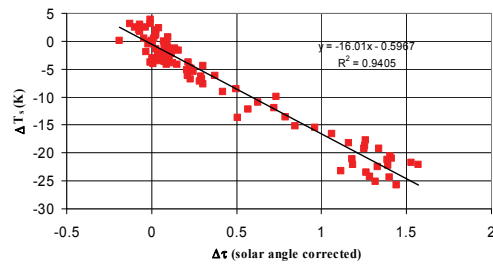


**Figure 3:** The difference in optical depth and surface temperature at all latitude and time bins between  $L_s=175$ - $296^\circ$  between MY 25 and 26.

The appearances of large average particle size coincide with observations of high latitude dust storms at these times and locations [6]. We suspect that these storms lift the larger particles observed in our retrievals. However, we did not observe increased zonally averaged dust effective radii at high northern latitudes at times when polar dust storms were observed in that hemisphere. This hemispheric asymmetry remains unexplained.

We also retrieved surface temperatures for the observation period in our data selection in order to quantify the climate effect of the global dust storm. We calculated the difference in dust optical depth and surface temperature between  $L_s=175$ - $296^\circ$  for each latitude and time bin between the two Martian years. Figure 3 shows our plot of  $\Delta T_s$  versus  $\Delta \tau$ .

There was a small amount of variability ( $\Delta T_s < 5K$ ,  $\Delta \tau < 0.3$ ) for conditions that were similar in both Martian years (for example, at  $L_s=175$ - $184^\circ$ , before the onset of the dust storm). These are probably due to slight changes in data coverage, as well as the variability of surface conditions, such as albedo, that determine surface temperature. However at larger optical depths a near-linear trend in surface temperature response to changes in optical depth emerges. This linear trend is similar to ones reported for soot ejected into Earth's atmosphere as a result of a theoretical global nuclear war [7].

**Conclusions:** We constructed a parameter retrieval algorithm for MGS TES data capable of simultaneously retrieving dust optical depth, effective radius, and surface temperature with global coverage. We used this algorithm to re-analyze TES data from Martian global dust storm 2001A, and discover new

clues to its place in the Martian dust cycle. These observations and discoveries should be considered by global circulation models as important global diagnostics in their analysis of the Martian dust cycle.

We found that dust is globally well-mixed subsequent to the rise in opacity associated with the dust storm. Global dust mixing is also present subsequent to the rise in opacity during southern hemisphere spring and summer the following Martian year when there was no global dust storm. Global dust mixing is low during northern spring and summer.

We found that dust clearing during the decay of the dust storm is consistent, to first order, with theoretical clearing due to gravitational settling of dust alone.

We discovered that latitudinal average dust effective radius is constant, within the standard deviation of results, at all latitudes except southern latitudes of  $35^\circ$  and higher. We observed larger average particle size at these locations around the two southern, and the one northern equinox within our observational period. The time and location of these larger particles coincides with observations of polar dust storms [6]. We did not observe large zonally averaged effective radii at northern latitudes, however.

We calculated the surface temperature response to increase in optical depth associated with the global dust storm. We discovered that the relation at larger optical depth is near-linear, similar to the response expected from a global nuclear war [7].

**References:** [1] Smith M. D. et al. (2000) JGR, 105, 9539-9552. [2] Wolff M. J. and Clancy R. T. (2003) JGR, 108, 5097. [3] Toon O. B. et al. (1977) Icarus, 30, 663-696. [4] Murphy J. R. et al. (1990) JGR, 95, 14,629-14,648. [5] Kahre M. A. et al. (2008) Icarus, 195, 576-597. [6] Cantor B. A. et al. (2006) JGR, 111, E12002. [7] Toon O. B. et al. (2008) Phys. Today, 61, 37-42.



# ***Session Three***

## *Distribution, Evolution, and Radiative Effects of Particle Sizes*

*Tuesday, September 15, 2009*

*2:00 PM – 5:00 PM*



## MARTIAN AIRBORNE DUST: HOW IT FORMS AND EVOLVES. NEAR-SURFACE VERSUS HIGH-ALTITUDE PROPERTIES.

Goetz<sup>1</sup>, W., Drube<sup>2</sup>, L., Hviid<sup>1</sup>, S. F., Leer<sup>2</sup>, K., Madsen<sup>2</sup>, M. B., Parrat<sup>3</sup>, D., Pike<sup>4</sup>, W. T., Stauffer<sup>5</sup>, U., Sykulska<sup>4</sup>, H., and Vijendran<sup>6</sup>, S.<sup>1</sup>Max Planck Institute for Solar System Research, Max Planck Strasse 2, 37191 Katlenburg-Lindau, Germany. <sup>2</sup>Niels Bohr Institute, University of Copenhagen, Juliane Maries Vej 30, 2100 Copenhagen OE, Denmark. <sup>3</sup>Jet Propulsion Laboratory, Caltech, 4800 Oak Grove Dr., Pasadena, CA 91109, USA. <sup>4</sup>Optical and Semiconductor Devices Electrical and Electronic Engineering, Imperial College, London SW7 2AZ, United Kingdom. <sup>5</sup>Precision and Microsystem Engineering Department of the 3mE Faculty, Delft University of Technology, Mekelweg 2, 2628 CD Delft, The Netherlands. <sup>6</sup>ESA-ESTEC, Keplerlaan 1, 2200 AG Noordwijk, The Netherlands.

**Introduction:** The generic term “Martian dust” refers to the fine-grained (micron-sized) fraction of solid material on the surface and in the atmosphere of Mars. The dust has a largely basaltic composition with the following minerals (sorted according to decreasing abundance): Framework silicates (plagioclase and/or zeolite) [1], pyroxene, olivine, (titano-)magnetite as well as some alteration phases including nanophase ferric oxide (npOx) [2,3] and (possibly) calcium sulfate [4]. The dust may have formed by a variety of processes: (a) Impact gardening, (b) Mechanical erosion and chemical weathering by liquid water, (c) volcanic eruptions, and (d) mechanical erosion by wind or thermal cycling. The (largely) basaltic mineralogy of Martian dust (as inferred from MER data, [2,4]) indicates that dry mechanical weathering of a basaltic precursor (process d) has been the dominant pathway for the formation of the dust [2]. Similar conclusions have been drawn from TES data during periods of high atmospheric opacity [1].

**Separability of mineral grains:** The Magnetic Properties Experiments (MPE) onboard the Mars Exploration Rovers (MER) have shown that some of the mineral components are separable according to their magnetization [2,4]. Figure 1 shows the accumulation of dust on the magnets onboard the Spirit rover (MER-A) on sols 184 and 425. Within a few sols prior to sol ~420, the wind had removed some of the bright (little/non magnetic) material from both of these magnets. The dark brown and (almost) black material that remained on the Capture (C) magnet turned out to be enriched in (titano-) magnetite as inferred from Mössbauer spectra. Figure 2 demonstrates the diversity and separability of Martian soil at the Phoenix landing site. The brownish and black grains in Figure 2a are 70-100  $\mu$ m in diameter. Figure 2b shows similar grains in a matrix of fine-grained (unresolved) dust. The relationship between the material acquired at the two

landing sites (Figure 1 for Spirit, Figure 2 for Phoenix) is unclear. However, we suggest that the dark fraction of the Phoenix soil is enriched in magnetite [5], similar to the dark fraction of Gusev dust.

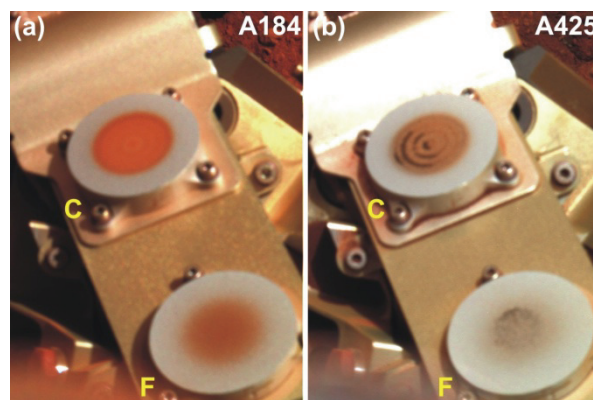


**Figure 1:** Separability of airborne dust as accumulated on the Spirit magnets by the action of wind (C: Capture magnet, F: Filter magnet). The gray top-plates of the magnets are 45 mm in diameter. (a) Sol A-184. (b) Sol A-425 (modified after [4]). The change in dust pattern occurred within a few sols just prior to sol ~420.

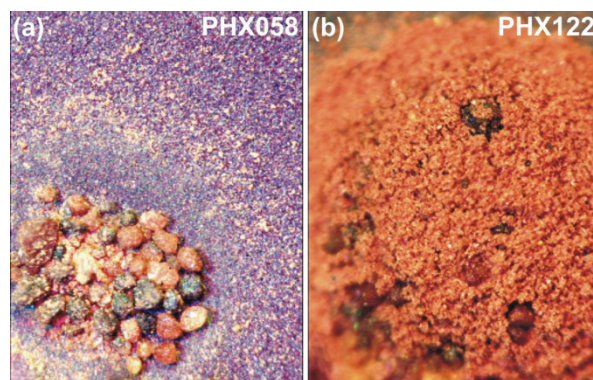


**Figure 2:** Separability of Martian soil at the Phoenix landing site (sols 58 and 122, respectively) as demonstrated by microscopic images. Each image is 1 mm wide.

**Vertical distribution of mineral grains in the atmosphere:** The separability of dust grains as discussed previously implies that the dust mineralogy may potentially vary as a function of altitude. Figure 3 shows reflectance spectra (calibrated to  $R^*$ ) of different dust units (#1: high-altitude dust, #2: near-surface airborne dust, #3: bright surface dust) and of dark sand dunes (#4, El Dorado in Gusev crater).

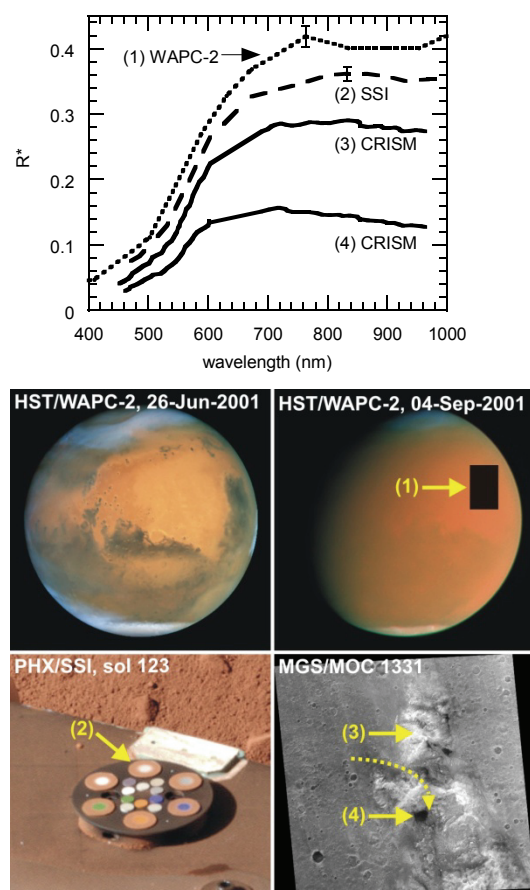


**Figure 3:** Spectral differences between surface units and airborne dust. The targets of the plotted reflectance spectra (top panel) are as follows (solid yellow arrows): (1) Mars bright region (black rectangle, located in Arabia) imaged by the Wide Angle Planetary Camera-2 (WAPC-2) onboard the Hubble Space Telescope (HST) on 26-Sep and 4-Sep-2001, respectively. Within this time frame a global dust storm had developed. (2) Near-surface airborne dust on the medium-grey magnet onboard the Phoenix lander [6]. (3) Bright surface dust at Clark Hill, Gusev crater, targeted by CRISM onboard Mars Reconnaissance Orbiter (MRO) [7]. (4) Same as (3), but for dark sand dunes (El Dorado, Gusev crater) [7]. The Gusev regions are specified in a MOC image (frame 1331, 2-Nov-2005, ~3 km wide). The dotted arrow in the MOC frame indicates the approximate itinerary of Spirit.

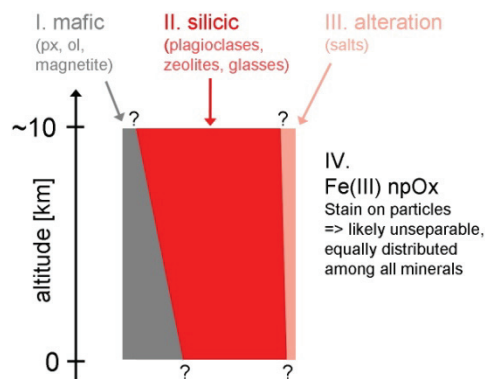


**Figure 4:** Potential vertical distribution of mineral grains in the Martian atmosphere

These spectra demonstrate the typical albedo range on the surface of Mars (excluding ice-covered regions). In particular the strong difference between the two airborne dust spectra (#1, #2), both in terms of absolute reflectance ( $R^*$ ) and spectral shape is interpreted as a difference in either mineralogy and/or grain size between both samples. The dominance of plagioclases in the upper altitudes (as inferred from TES spectra acquired during periods of high opacity, [1]) taken together with the significant variation in specific weight between different minerals (feldspars: 2.6~2.7, olivine: 3.3, magnetite: 5.2 g/cm<sup>3</sup>) suggest that some stratification according to mineral composition takes place in the atmosphere, at least during periods of steady dust fallout. A sketch on how that stratification might look like is shown in Figure 4.

**Conclusions:** Dust is a geological unit that mirrors the particular (late-stage) weathering environment on the surface of Mars. It is composed of a variety of (partially separable) mineral grains with strongly varying physical properties (size distribution, albedo, magnetization). The ferric npOx appears to be a stain on all dust particles and can therefore not be separated in pure form (Figure 4). Orbital observations (TES/MGS, HST/WAPC-2) and data from landed missions (Phoenix, MER) suggest that the dust composition varies within the atmospheric column according to effective specific weight and associated mineralogical composition, at least under particular atmospheric conditions, such as quiet fallout after a large dust storm. In particular these data suggest that ferric npOx stained framework silicates (high-albedo particles) dominate the entire atmosphere, while darker (low-albedo) mafic minerals prevail in the lower atmosphere. So far

atmospheric models have been treating dust as one single geological unit with given (average) physical and radiative properties. Allowing for some (likely time-dependent) vertical stratification of the dust mineralogy might improve simulations of Martian atmospheric dynamics.

**References:** [1] Hamilton V. E. et al. (2005) JGR, 110, E12006. [2] Goetz W. et al. (2005) Nature, 436, 62-65. [3] Morris R. V. et al. (2006) JGR, 111, E02S13. [4] Madsen M. B. et al. (2009) JGR, 114, E06S90. [5] Goetz W. et al. (2009) JGR, accepted for publication. [6] Leer K. et al. (2009) JGR, 113, E00A16. [7] Arvidson R. E. (2008), priv. comm.

## MARS CLIMATE SOUNDER LIMB RETRIEVALS OF DUST AND WATER ICE USING SCATTERING RADIATIVE TRANSFER: IMPLICATIONS FOR PARTICLE SIZE.

**SIZE.** Kleinböhl, A., Abdou, W. A., Schofield, J. T., Kass, D. M., McCleese, D. J., Jet Propulsion Laboratory, California Institute of Technology, Mail-Stop 169-237, 4800 Oak Grove Dr., Pasadena, CA, 91109 (armin.kleinboehl @ jpl.nasa.gov, wedad.abdou @ jpl.nasa.gov, john.t.schofield @ jpl.nasa.gov, david.kass @ jpl.nasa.gov, daniel.j.mccleese @ jpl.nasa.gov).

**Introduction:** The Mars Climate Sounder (MCS) [1] is a mid- and far-infrared channel radiometer on the Mars Reconnaissance Orbiter (MRO). It has been operating for more than 1.5 Mars years, observing the Martian atmosphere in limb- and on-planet geometry.

From the measured limb radiances, vertical profiles of atmospheric temperature, dust and water ice opacity are retrieved up to altitudes of about 80 km. The MCS retrieval algorithm [2] is based on a modified Chahine method [3] and retrieved profiles have been being submitted to the Planetary Data System (PDS).

Here we present updated dust profile retrievals from limb measurements that were performed assuming different dust particle sizes. We analyze radiance fits in the MCS A5 channel (centered at  $463\text{ cm}^{-1}$ ) and the MCS A4 channel (centered at  $843\text{ cm}^{-1}$ ). The extinction efficiency ratio between these channels exhibits a dependence on particle size. We use examples of the southern mid-latitude summer atmosphere to draw conclusions about the dust particle size distribution.

**Scattering Radiative Transfer:** The radiative transfer scheme for the MCS retrieval is based on a Curtis-Godson approximation. While the operational retrieval has used absorption-only radiative transfer so far, the radiative transfer scheme for this study has been expanded by adding a single-scattering parameterization.

When considering single scattering, the radiative transfer equation has two terms, one for absorption and one for scattering. The latter is a function of the single scattering albedo (SSA) and a scattering source function. Typically a scattering source function is computationally expensive to evaluate. We simplify this by assuming that the near nadir aerosol optical depth is small, the internal radiation field is dominated by the surface, and the internal radiation field is zero for zenith angles above the surface limb. These assumptions are reasonable for the martian

atmosphere when it is sufficiently transparent for the retrieval of limb measurements. Under these assumptions, the scattering source function can be described as the product of an integrated scattering phase function and the upwelling surface radiance.

The calculation of the integrated phase function can be accelerated using lookup tables that contain band-averaged phase functions for each channel and aerosol model. The aerosol models for the MCS radiative transfer are based on a modified gamma distribution for particle size. Band-averaged extinction efficiencies, SSAs, and phase functions are calculated using Mie-theory based on optical properties for dust by Wolff et al. [4] and for water ice by Warren [5]. If both dust and ice aerosol is present an effective single scattering albedo and phase function can be calculated.

Figure 1 shows the calculated extinction efficiencies due to dust for effective radii between  $0.75$  and  $6\text{ }\mu\text{m}$ , band-averaged for the different MCS infrared channels. For most cases extinction efficiency ratios

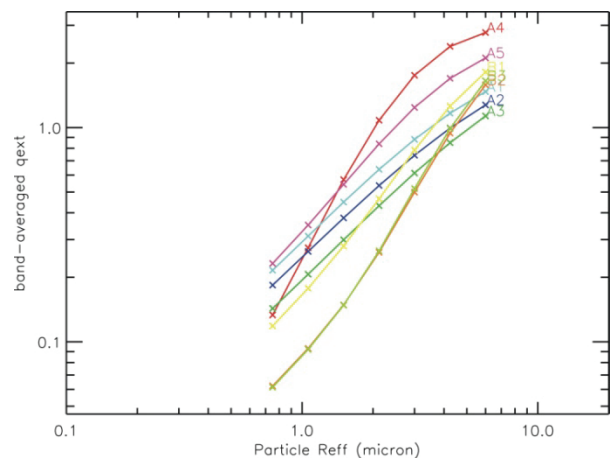


**Figure 1:** Band-averaged extinction efficiencies due to dust for the MCS infrared channels derived from Mie-calculations for particle size distributions with different effective radii.



between channels do not vary very much with particle size. However, one can see that the curves for the A4 and the A5 channels cross around  $1.5 \mu\text{m}$ , giving some leverage to deduce particle size.

**Results:** The left column of Figure 2 shows retrievals of dust and water ice opacity from a southern mid-latitude summer measurement. The individual plots show retrieval results with dust effective radii of  $0.75$ ,  $1.06$ ,  $1.5$ , and  $3 \mu\text{m}$ . The retrieved dust profile does not differ significantly between the different cases, each showing a maximum opacity around  $6 \cdot 10^{-3} \text{km}^{-1}$  close to the surface and a steep decrease of opacity with altitude around  $20 \text{ km}$ . The retrieved water ice profile does vary with the assumed dust particle size (the effective radius for water ice has been kept constant at  $1.4 \mu\text{m}$ ). In the case of a dust effective radius of  $1.5$  or  $1.06 \mu\text{m}$  a water ice layer is retrieved above the dust between  $20$  and  $25 \text{ km}$ , and little water ice is retrieved above and below. The errors are larger for the  $1.5 \mu\text{m}$  case. In the case of  $0.75 \mu\text{m}$  dust particles water ice is also retrieved at altitudes where significant dust is present. In contrast, in the case of  $3 \mu\text{m}$  dust particles even the water ice layer at  $20$ – $25 \text{ km}$  disappears. Note that the water ice error bars are also much larger than in the other cases.

The right column of Figure 2 explains this behavior. It shows the fits to the radiances measured in the A5 channel (where dust is retrieved) and the A4 channel (where water ice is retrieved). The radiances in the A5 channel are fitted very well in all cases. In the case of  $3 \mu\text{m}$  dust particles the fit to the A4 radiances is very poor, though. The reason for this is the dust, which gives rise to radiance in the A4 channel driven by a high A4-to-A5 extinction efficiency ratio when a  $3 \mu\text{m}$  dust particle size is assumed. The retrieval tries to fit the radiance in the A4 channel by reducing the water ice opacity but is not allowed to use negative opacities. Hence the fit stays poor and causes large error bars for the water ice opacity. Reducing the dust particle size gradually reduces the A4-to-A5 extinction efficiency ratio, which in turn improves the fit in the A4 channel. In the case of  $0.75 \mu\text{m}$  dust particles the extinction efficiency ratio is low enough that significant water ice opacity is required to fit the A4 radiances in the presence of dust. As this can be considered rather unlikely in the daytime mid-latitude atmosphere during perihelion season the assumption of a dust effective radius of  $\sim 1 \mu\text{m}$  or slightly below seems to be realistic.

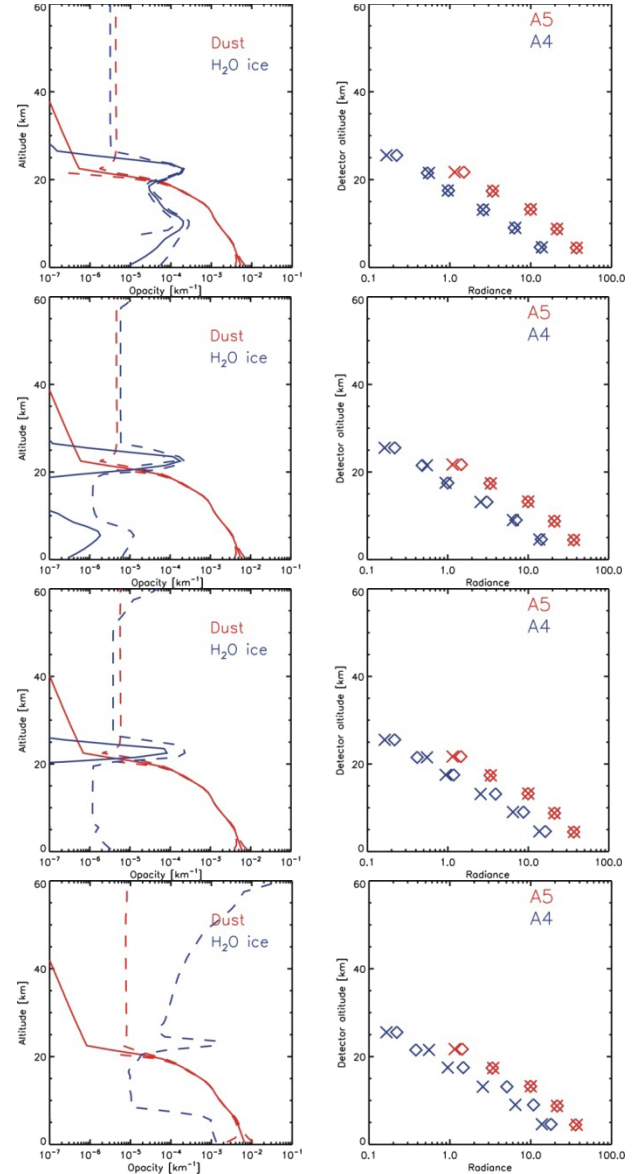


**Figure 2:** Left – Dust and water ice opacity profiles retrieved from a daytime measurement at  $52^\circ\text{S}$ ,  $58^\circ\text{W}$  at  $L_s = 336^\circ$  assuming different particle size distributions for dust. For the ice particle size distribution  $r_{\text{eff}} = 1.4 \mu\text{m}$  is assumed in each case. Dashed lines indicate error bars. Right – Radiance measurements in the A4 and A5 channels (crosses) and fits to the radiances after the retrieval (diamonds).

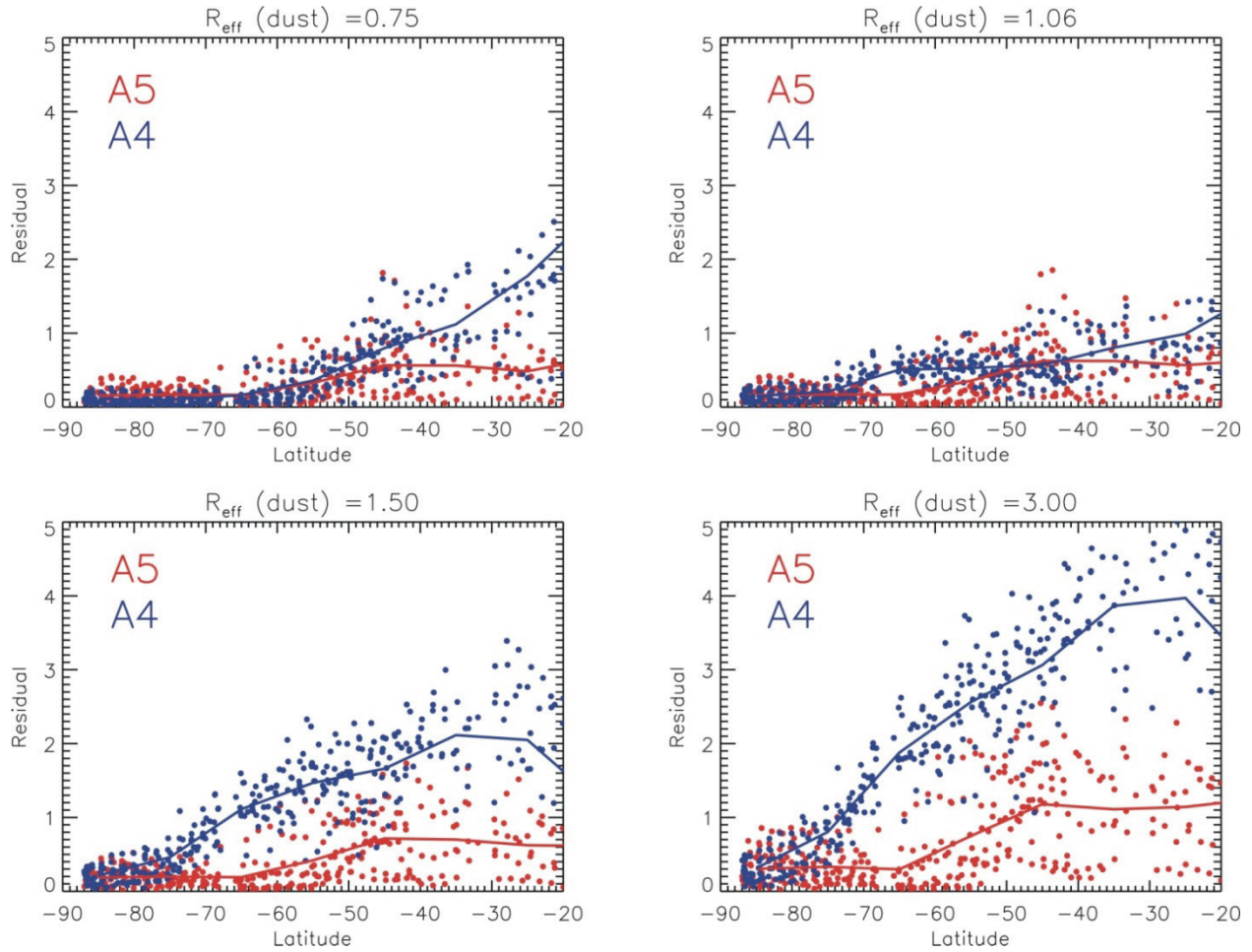


**Figure 3:** RMS radiance residuals for fits in the A5 channel (red) and the A4 channel (blue) for daytime measurements on October 25, 2007 ( $L_s=336^\circ$ ). Each dot corresponds to one individual measurement. The lines show averages over  $10^\circ$  latitude bins.

Figure 3 shows the radiance residuals for retrievals of a day of measurements at southern mid- and high latitudes at  $L_s=336^\circ$ . A radiance residual is calculated as the RMS over the differences between measured and calculated radiances in all detectors used for a retrieval. Residuals in the A5 channel are reasonably low for dust particles with effective radii of  $1.5\ \mu\text{m}$ .

**Conclusions:** We presented updated dust profile retrievals with a single-scattering radiative transfer scheme. We retrieved aerosol profiles assuming dust particle size distributions with different effective radii and analyzed the radiance fits. Concentrating on southern mid-latitude summer, we find that a dust effective radius between  $0.75$  and  $1\ \mu\text{m}$  gives the best results. At lower mid-latitudes an effective radius around  $1\ \mu\text{m}$  seem to be more realistic while at high

latitudes a particle size of  $0.75\ \mu\text{m}$  yields lower residuals. These effective radii for dust are somewhat smaller than results from nadir-viewing TES and MiniTES observations [4]. However, they do not seem to be inconsistent with initial results from limb-viewing TES measurements [6] and recent modeling efforts [7]. Further constraints on particles sizes might be obtained by analyzing the MCS broadband visible/near-IR channel in combination with the infrared channels.

**Acknowledgments:** We would like to thank the MRO spacecraft and MCS operations teams who make these measurements possible. Work at the Jet Propulsion Laboratory, California Institute of Technology, is performed under a contract with the National Aeronautics and Space Administration.



**References:** [1] McCleese, D. J., et al. (2007) *JGR*, 112, E05S06, doi:10.1029/2006JE002790. [2] Kleinböhl, A., et al. (2009) *JGR*, 114, doi:10.1029/2009JE003358. [3] M. T. Chahine (1972) *J. Atmos. Sci.*, 29, 741-747. [4] Wolff, M. J., et al. (2006) *JGR*, 111, E12S17, doi:10.1029/2006JE002786. [5] Warren, S. G. (1984) *Appl. Opt.*, 23, 1206-1225. [6] Wolff, M. J., et al., *this issue*. [7] Forget, F., *this issue*.

## THE VERTICAL DISTRIBUTION OF DUST IN MARS' ATMOSPHERE DURING NORTHERN SPRING AND SUMMER: THE PERSPECTIVE FROM THE MARS CLIMATE SOUNDER.

Heavens, N. G.<sup>1,\*</sup>, Richardson, M.I.<sup>2</sup>, Kass, D.M.<sup>3</sup>, Kleinböhl, A.<sup>3</sup>, McCleese, D.J., and the MCS Science Team.<sup>3</sup> \*Corresponding author ([heavens@gps.caltech.edu](mailto:heavens@gps.caltech.edu))<sup>1</sup>Division of the Geological and Planetary Sciences, California Institute of Technology, MC 150-21, Pasadena, CA, 91125; <sup>2</sup>Ashima Research, 300 S. Lake Ave, Pasadena, CA, 91106 ([mir@ashimagroup.net](mailto:mir@ashimagroup.net)); <sup>3</sup>Jet Propulsion Laboratory, California Institute of Technology, 4800 Oak Grove Dr., Pasadena, CA, 91109 ([dkass@jpl.nasa.gov](mailto:dkass@jpl.nasa.gov); [Armin.Kleinboehl@jpl.nasa.gov](mailto:Armin.Kleinboehl@jpl.nasa.gov); [daniel.j.mccleese@jpl.nasa.gov](mailto:daniel.j.mccleese@jpl.nasa.gov)).

**Introduction:** The distribution of dust with height in Mars' atmosphere is a critical unknown in the simulation of its general circulation and a source of insight into dust lifting, transport, and vertical mixing in the atmosphere. Consequently, observations of its optical properties and spatial and temporal variability have been a part of almost every major spacecraft mission sent to Mars. The information provided by these missions about the vertical distribution of atmospheric dust has been limited. Limb retrievals [1] from observations by the Mars Climate Sounder (MCS) on Mars Reconnaissance Orbiter (MRO) are now greatly expanding our knowledge of vertical dust variability.

This study focuses on the distribution of dust constructed from these retrievals during northern spring and summer and their implications for dust lifting and transport processes. This season attracts focus for three reasons: (1) most nightside retrievals meet current quality control standards [1]; (2) interannual variability between Mars Year (MY) 28 and MY 29 can be partially characterized; (3) MCS temperature observations near the south pole suggest that the atmospheric circulation in this season is more vigorous than simulated by most Mars general circulation models (GCMs), [2], which some have attributed in part to incorrect assumptions about the vertical distribution of dust [2,3].

**Dataset and Methods:** The limb retrieval procedure for MCS observations is described in detail in [1,4]. From the profiles of pressure, temperature, and dust opacity, the dust opacity can be scaled by the atmospheric density to produce the density-scaled opacity (DSO), a quantity that is a proxy for both the mass mixing ratio ( $q$ ) and the radiative heating due to dust in the case of pure absorption in optically thin conditions: that is:

$$DSO = \frac{3Q_{ext}}{4\rho_d r_{eff}} q \quad (1)$$

DSO is only an exact proxy if the extinction coefficient at the relevant wavelength ( $Q_{ext}$ ) and the effective radius ( $r_{eff}$ ) (and parameters related to shape and composition, such as  $\rho_d$ , the density of dust) are independent of space and time. However, neglecting the effects of any assumptions in the retrieval procedure, the uncertainty in  $q$  due to uncertainty in these parameters is no more than 15%. For the 463 cm<sup>-1</sup> channel observed by MCS, a DSO of 10<sup>-4</sup> m<sup>2</sup> kg<sup>-1</sup> is estimated to correspond to a mass mixing ratio of 1.12 ppm.

**Comparison with GCM Simulations:** For at least the last decade, modelers have attempted to represent both the lifting and transport of dust through the atmosphere with interactivity between dust, the radiation field, and/or surface dust reservoirs at a variety of scales. However, until now, it has been difficult to validate the results of these simulations. Figures 1a and 1b show two examples.

The inclusion of the mean meridional streamfunction in these figures is relevant to the dust distribution with which they are plotted. Once lifted from the surface (primarily in the tropics and northern hemisphere), these simulations suggest that dust is mixed through the atmosphere by the winds in such a way that the zonal mean dust distribution resembles the mean meridional circulation. In Figure 1a, the Mars Geophysical Fluid Dynamics Laboratory (GFDL) model primarily distributes dust within a strong cross-equatorial cell and less so within a weaker summer hemisphere cell. The highest values of dust mass mixing ratio are seen in the upwelling zones of these two cells, and their vertical extent in part seems to set the vertical extent of dust. The

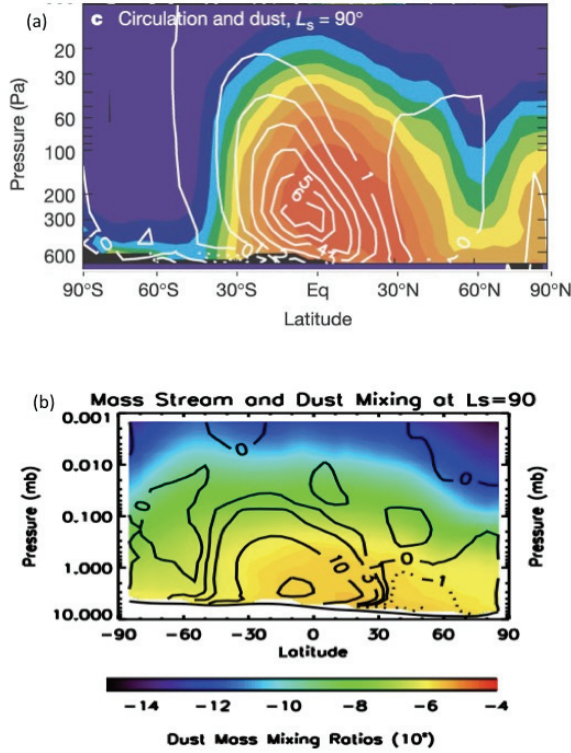


**Figure 1:** (a) Zonal mean “quantity linearly proportional to dust mass mixing ratio” (color contours) and mean meridional streamfunction ( $10^8 \text{ ms}^{-1}$ ) (contours) at northern summer solstice ( $L_s = 90^\circ$ ) [5]; (b) Zonal mean dust mass mixing ratio at the northern summer solstice (color contours; logarithmic scale) and mean meridional streamfunction (units unknown) (contours) [6].

downwelling zone of the cross-equatorial cell (and poleward of it) is nearly dust-free except at the surface, suggesting that the latitudinal extent of this cell is the boundary of advection of tropical dust into the winter hemisphere. The downwelling region of the weaker summer hemisphere cell is a local minimum in dust mass mixing ratio, where the vertical extent of dust is more limited. There is a dusty cell near the north pole, where the vertical extent of dust is greater than in the downwelling region of the summer hemisphere tropical cell but less than in the mutual upwelling region of the tropical cells.

The distribution in Figure 1b (generated by the Ames model) is slightly different (accounting for the logarithmic scale), but the basic relations of dust distribution and meridional cellular structure still hold.

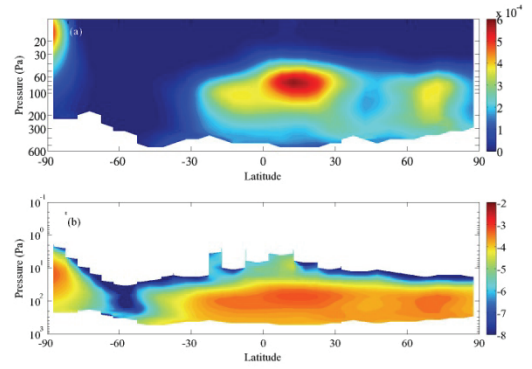


**Figure 2:** (a) Zonal mean DSO ( $\text{m}^2 \text{ kg}^{-1}$ ) for  $L_s = 85-95^\circ$ , MY 29, nightside retrievals (linear scale), directly comparable with 1(a); (b) Zonal mean DSO ( $\text{m}^2 \text{ kg}^{-1}$ ) for  $L_s = 85-95^\circ$ , MY 29, nightside retrievals (logarithmic scale), directly comparable with 1(b).

Figures 2a-b show the zonal mean DSO at the northern summer solstice from MCS retrievals. The axes and scaling have been chosen for as easy comparison with Figures 1a-b as possible.

The agreement of model and observations is generally good with respect to the latitudinal distribution of dust. There is an identifiable local minimum in the summer hemisphere; a near-surface maximum at  $30^\circ \text{ N}$ ; a maximum in dust near the north pole; a minimum of dust in the winter hemisphere, except near the south pole (where the retrieval procedure attributes aerosol to dust under conditions where  $\text{CO}_2$  ice could form, but  $\text{CO}_2$  ice is not presently retrieved). Indeed, a plausible mean meridional circulation emerges from the distribution of dust. In addition, the vertical extent of dust (within the detection limit of MCS) is similar. There are, however, two critical differences. First, the minimum in the winter hemisphere (at least at  $60^\circ \text{ S}$ ) is more extreme than the simulation of Figure 1b portrays by about three orders of magnitude. This region is exceptionally clear of dust. This has been observed and investigated using Thermal Emission Spectrometer data by [7], so we omit further discussion here. Second, there is a high altitude maximum in DSO over the tropics at  $\sim 60 \text{ Pa}$ . MCS limb retrievals do not reach the surface, so Figures 2 and 3 reflect a mass mixing ratio contrast of  $\sim 1.5-5$  between the lower end of the retrievals at  $\sim 8 \text{ km}$  and higher altitudes up to  $25-30 \text{ km}$ . They do not necessarily exclude the possibility of higher dust concentrations nearer the surface.

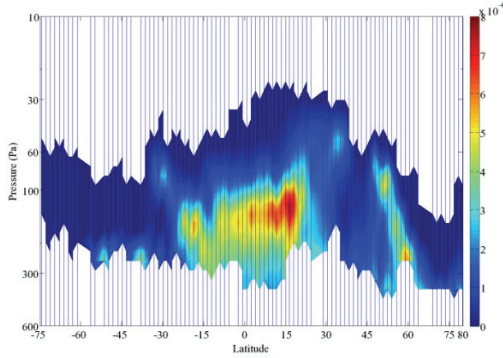


**Figure 3:** A cross-section of dust DSO ( $\text{m}^2 \text{kg}^{-1}$ ) made from retrievals from a single nightside pass at  $L_s=39.0522^\circ$ , MY 29 (1 March 2008). The longitude of the northern end of the cross-section is  $157^\circ \text{E}$  and  $112^\circ \text{E}$  on the southern end. The vertical lines mark the average latitude of the profile.

The seasonal and latitudinal variability in this feature indicates it is generally higher in magnitude and higher in altitude relative to the surface over the northern tropics and sub-tropics than in the southern tropics and sub-tropics. It is most apparent about northern summer solstice and is hard to identify after  $L_s=180^\circ$  in MY 28 and  $L_s=145^\circ$  in MY 29.

Since this high altitude tropical dust maximum is not represented by simulations that represent current understanding of dust lifting and transport processes, we suspect that some process that is not currently well-represented is responsible. Initial investigations of four possible processes are described below.

**Dust Storm Activity:** Since the work of [8], it has been suspected that dust storms can advect large amounts of dust above the boundary layer over areas where dust lifting is not active, producing high altitude maxima in dust mass mixing ratio. Observations in the visible suggest that the tropics are mostly free of local dust storm activity around northern summer solstice, though frequent dust storm activity near both polar cap edges is observed [9]. In addition, the disappearance of the high altitude tropical dust maximum in MY 29 coincides with “early season” tropical dust storm activity observed by MARCI and THEMIS [10, 11], making it unlikely that dust storm activity in the tropics produces the high altitude tropical dust maximum.

The possibility of a more remote source cannot be rejected immediately. Around 1 March 2008, visible imagery from MARCI showed widespread north polar cap edge dust storm activity [12]. Figure 3 shows a potential signature of this event: a deeply mixed plume of dust that may be advecting south at 20-30 km above the surface. This plume, however, is separate from the high altitude tropical dust maximum at lower latitudes. This particular event probably will be a good test case to assess the contribution of northern cap edge dust storm activity to the global dust distribution in this season.

**Orographic Activity (High Volcanoes):** Rafkin et al. [13] have proposed that dust lifting by anabatic-katabatic wind circulations may inject dust at high altitudes in the atmosphere. The example simulated in [13] is the spiral cloud observed around northern autumnal equinox over Arsia Mons, which may be restricted to that season for dynamical reasons. Such injection could produce a high altitude tropical dust maximum given the concentration of high volcanoes in the tropics and northern sub-tropics. MCS observations, however, show that areas around these volcanoes are much less dusty than elsewhere in the tropics. The area west of Elysium Mons is a possible exception, but the maximum in dust concentration is near Isidis-Syrtis Major. Fluctuations in dust there generally do not coincide with fluctuations around Elysium.

**Dusty “Pseudo-Moist” Convection:** Fuerstenau [14] has proposed that the solar heating of dust lifted near the surface in the thin martian atmosphere adds an important additional heating term to martian dry convection analogous to latent heat release in terrestrial moist convection and possibly comparable in magnitude. Such dusty parcels could break the boundary layer, injecting large amounts of dust at altitude and producing a high altitude tropical dust maximum. Dusty parcels could be initiated not only by primarily thermally forced convection such as dust devils and convective cell fronts but also by anabatic circulations along crater and valley edges [13].

This mechanism is attractive because the high altitude tropical dust maximum appears to originate from the northern edge of the tropics, an area that is most directly heated by the Sun at northern summer solstice and is often just outside the equatorial cloud belt. Large dust devils have been observed in this region and season by MOC [9].

We have adapted a terrestrial cumulus parameterization [15] to simulate this process. Figure 4 shows the temperature evolution of a simulated parcel in a dust devil at the Mars Pathfinder site. The Convective Available Potential Energy (CAPE) of this parcel is comparable to strong terrestrial thunderstorm activity. The warming of the parcel relative to the environment mainly takes place very near to the surface, primarily because entrainment is assumed to be inversely proportional to the square of velocity, so the parcel's dust concentration is strongly diluted by entrainment of environmental air. The heating effect from the more dilute dust loading above  $\sim 2500$  m is not strong enough to keep the parcel from cooling more strongly than the environment.

Figure 5 shows the results of a sensitivity study assuming two environmental temperature layers: a 4000 m thick layer near the surface with a lapse rate of  $-3 \text{ K km}^{-1}$  and a top layer with a lapse rate of  $-1.5 \text{ K km}^{-1}$ . At concentrations below 100 ppm, penetration of the upper layer is effectively impossible. Above this concentration, parcels of intermediate initial velocity can break into the upper layer. Entrainment limits parcel height at initially low velocities, while initially fast-moving parcels do not heat quickly enough to overcome adiabatic cooling.

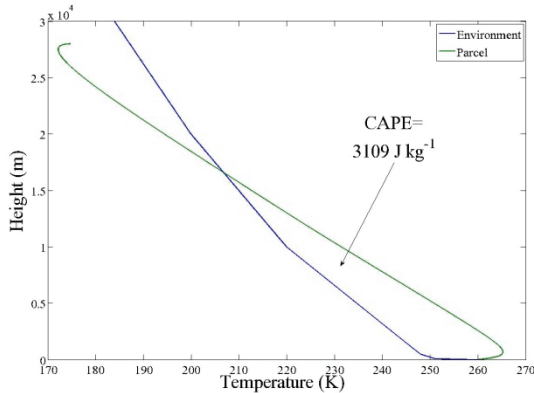


**Figure 4:** Results of simulation of dusty parcels at the Mars Pathfinder site showing parcel temperature vs. environmental temperature.

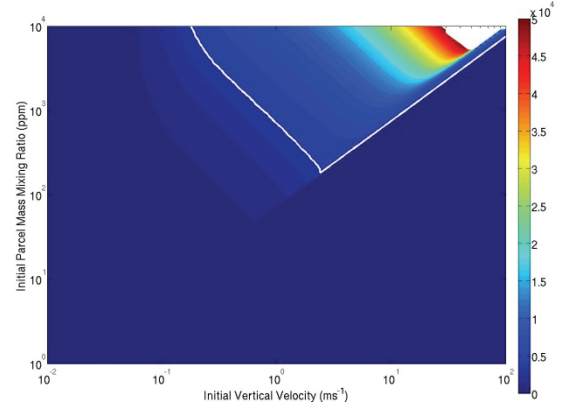


**Figure 5:** Sensitivity of level of neutral buoyancy (m) to initial parcel dust concentration (ppm) and initial parcel vertical velocity ( $\text{ms}^{-1}$ ). The white line indicates the 4000 m contour, the boundary of the lower or pseudo-boundary layer of the simulation. The white area indicates simulations in which the parcel leaves the simulation domain.

Dust devils (particularly those observed from orbit), however, do not cast shadows that suggest they reach the altitudes implied by these simulations [16]. Three effects may be important: (1) their helical circulations may enhance entrainment; (2) dusty parcels diluted by entrainment may not cast observable shadows; (3) attenuation of solar radiation in optically thick dust devil columns.

Exploration of this process in a large eddy simulation is contemplated in the future, not only to test its validity but also to develop a parameterization for modeling purposes.

**Scavenging by Water Ice Clouds:** Due to kinetic barriers to nucleation under even high levels of supersaturation, water ice clouds on Mars probably nucleate on dust particles. Thus, every ice particle potentially has a dusty center. Dust therefore can be removed from the atmosphere by condensing water ice on it, enhancing the aerosol's sedimentation velocity. Thus, below water ice clouds, there should be a population of dust particles whose ice coating has sublimated. Between two water ice cloud layers, the release of dust particles from above and the scavenging of dust particles from below could produce a strong maximum in the dust mass mixing ratio profile. There may be a strong tidal control on water

ice [17], which is very apparent at 30° S, ~30 km above the surface at the northern summer solstice, where the zonal average water ice opacities vary by nearly two orders of magnitude between dayside and nightside. We would expect a strong peak in dust on the nightside relative to the dayside if exposure of dust nuclei had a significant impact on concentration. No such feature is observed. One possible explanation is that the dust used as nuclei are on the very lower end of the size distribution and thereby contribute little additional cross-sectional area when their coatings sublime.

**Acknowledgments:** This work was supported by and performed in part at the Jet Propulsion Laboratory, California Institute of Technology under a contract with the National Aeronautics and Space Administration as part of the Mars Reconnaissance Orbiter project.

**References:** [1] A. Kleinböhl et al. (2009), *JGR*, doi:10.1029/2009JE003358. [2] D.J. McCleese et al. (2008), *Nature Geosci.*, *1*, 745-749. [3] D. Tyler and J.R. Barnes, this meeting. [4] A. Kleinböhl et al., this meeting. [5] M.I. Richardson and R.J. Wilson (2002), *Nature*, *416*, 298-301. [6] M.A. Kahre et al. (2006), *JGR*, *111*, E06008. [7] T.M. McConnochie et al., this meeting. [8] J.R. Murphy et al. (1995), *JGR*, *100*, 26357-26376. [9] B.A. Cantor et al. (2006), *JGR*, *111*, E12002. [10] M.C. Malin et al. (2008), MARCI Weather Report for 10 November 2008-16 November 2008, MSSS Captioned Image Release #59. [11] M.D. Smith (2009), *Icarus*, *202*, 444-452. [12] M.C. Malin et al. (2008), MARCI Weather Report for 25 February 2008-2 March 2008, MSSS Captioned Image Release #20. [13] S.C.R. Rafkin et al. (2002), *Nature*, *419*, 697-699. [14] S.D. Fuerstenau (2006), *GRL*, *33* (19), L19S03. [15] D. Gregory (2000), *QJRM*, *127* (571), 53-72. [16] J.A. Fisher et al. (2005), *110* (E3), E03004. [17] C. Lee et al. (2009), *JGR*, *114*, E03005.

---

## DUST VERTICAL DISTRIBUTION AND SIZE AS SIMULATED WITH THE LMD GENERAL CIRCULATION MODEL. Forget, F. Laboratoire de Météorologie Dynamique, Université Paris 6, BP 99, 75005 Paris, FRANCE ([forget@lmd.jussieu.fr](mailto:forget@lmd.jussieu.fr))

---

**Introduction:** Using the LMD General Circulation Model, I have performed a simple simulation with 26 tracers to represent the lifting, mixing, transport and gravitational sedimentation of dust particles with different sizes, assuming a typical martian year climate (Martian Year 24) with no global dust storm. The original motivation for this study was the prediction of the possible occurrence of relatively large particles (5, 10  $\mu\text{m}$  or more) above 30 km altitude which could affect the heat shield of a probe at entry (Exomars).

However the results of this study allows a better understanding of the 4D variations of the dust size distribution and of the vertical extension of the dust layer as observed from orbit. I must stress, however that I have neglected possible scavenging process resulting from the condensation of water ice on dust particles. Such processes are thought to play a key role in the vertical distribution of Martian airborne dust.

**The LMD General Circulation Model.** The LMD Mars atmosphere General Circulation Model (GCM) is described in [1]. To compute the radiative transfer and the heating of the atmosphere which controls the dynamic, the simulations employs a prescribed distribution of airborne dust following a “dust scenario” designed to mimic Mars as observed by Mars Global Surveyor from 1999 to june 2001 (Mars Year 24, or MY24), a typical martian year without a global dust storm. The dust opacity fields were derived from MGS TES observations using data assimilation technique [2]. The GCM has been extensively validated and shown to be well consistent with MGS radio occultation and TES observations [3].

Simulations were performed with a very coarse resolution of  $32 \times 24$  grid points horizontally, corresponding to  $7.5^\circ$  latitude by  $11.25^\circ$  longitude. In the vertical, the model uses the terrain-following  $\sigma$  coordinate system ( $\sigma$  is pressure divided by surface pressure) with 25 layers with the lowest layers at 5, 10, 20, 50, 100 m and up to  $\sim 80$  km.

**Modelling the dust cycle.** To estimate the dust spatial and size distribution, we performed 3D simulations in which the basic aspect of the dust cycle are parametrised:

- Representation of *dust lifting* by the general circulation or, alternatively, by local dust devils (see below).
- *Vertical turbulent mixing* of dust particles, especially in the planetary boundary layer. This mixing is performed by the GCM’s Mellor and Yamada 2.5 scheme assuming the same mixing coefficient than enthalpy (see [1]).
- *Vertical mixing by atmospheric convection.* The mixing of dust particles by convection is done in a similar way than for momentum in a convective adjustment scheme: when a section of atmosphere is shown to be convective, only a fraction of the dust is mixed, as described in [4].
- *Transport by the general circulation* using a “Van-Leer I” finite volume transport scheme [5].
- *Gravitational sedimentation.* The downward transfer of dust due to gravity is computed separately from the transport, but using a similar Van-Leer I scheme, taking into account the fact that the dust particles may fall through more than one model layer during one time step. The dust sedimentation velocity  $W_s$  is computed using the Stokes law corrected for low pressure by the Cunningham slip-flow correction [6]:
- *Size discretization.* We discretized the size distribution of airborne dust particles using 13 “sampling” size: radii of 0.025, 0.05, 0.1, 0.2, 0.5, 1., 1.5, 2., 5, 10., 15., 20., and 30  $\mu\text{m}$ . The discretization was chosen in order to keep the computation time acceptable and well represent the dust, taking into account that dust particles smaller than 0.02 micrometers are almost invisible (negligible extinction). Very large particle size, not abundant but relevant for our “shield ablation” study were however included. In practice, the GCM transports 26 tracers, since each size is represented by dust lifted by 1) dust devils and 2) dust storms (see below).



**Dust “Lifting”.** The lifting of dust results from two processes: 1) dust storms, and 2) dust devils. In practice, each particle size is represented by two distinct tracers, one for each lifting process. As a result, in our simulation the GCM transported a total of 26 tracers.

#### *Lifting by dust storms.*

The lifting of dust on Mars has been studied and simulated by several models [7-12]. These science studies have allowed major advances in our understanding of the dust cycle, but has also shown that accurately simulating the observed dust cycle using the interactive lifting of dust is not straightforward...Here, I have chosen to prescribe the amount of lifted dust as a function of space on time using the available dust climatology from Martian Year 24 (1999-2001)[13,14]. At every locations, everyday, dust particles (tracers 1 to 13) are lifted when the observed infrared dust optical depth  $\tau$  at 1071  $\text{cm}^{-1}$  is above 0.2. The flux of lifted dust (in  $\text{kg m}^{-2} \text{s}^{-1}$ ) is assumed to be proportional to  $\tau - 0.2$ . The ratio between the flux and  $(\tau - 0.2)$  is not computed during the GCM simulation, but during post-treatment (all the processes affecting the dust do not require to know the quantitative amount of dust, but only its relative value).

#### *Lifting by dust devils.*

During the clear seasons (Northern spring and early summer), a background of dust is assumed to be maintained in the Martian atmosphere by dust devils. Dust devils form due to convection in an atmosphere with a superadiabatic lapse rate. They preferentially occur over hot surface.

This process has been parameterized in the model based on the theoretical work of [15] (See also [9]) which was used to determine a “dust devil activity” from the depth of the convective boundary layer and the surface-atmosphere heat flux, both values which can be determined in the GCM. A “dust devil flux” is computed based on this activity. During the simulation, the dust lifted by this process is described by 13 additional tracers (tracers 14 to 26) and transported completely independently from the dust lifted by dust storms. This allows to fine tune the dust seasonal cycle and match the observations.

#### *Size distribution of the lifted dust.*

To represent the dust distribution of lifted dust aerosols, a lognormal distribution has been

shown to be well adapted, at least on Earth [16-17]. It is given by :

$$n(r) = \frac{1}{\sqrt{2\pi} \sigma_0 r} \exp\left(-\frac{[\ln(r/r_0)]^2}{2\sigma_0^2}\right)$$

with  $r_0$  and  $\sigma_0$ , the geometric mean radius and the geometric standard deviation. These values are related to the effective radius  $r_{\text{eff}}$  and variance  $v_{\text{eff}}$  (which are inputs easier to use for our studies since they are measured spectroscopically in the atmosphere) by  $r_0 = r_{\text{eff}} / (1 + v_{\text{eff}})^{5/2}$  and  $\sigma_0^2 = \ln(1 + v_{\text{eff}})$ . Each size of particles with radius  $r$  is lifted assuming a flux proportional to  $r^3 n(r)$ .

#### *Combining lifting by dust devils and dust storms.*

As explained above, during its full simulation of the Martian general circulation and dust cycle processes, the model lifts and transports 13 independant sizes of dust lifted by dust storms, and 13 more lifted by dust devils.

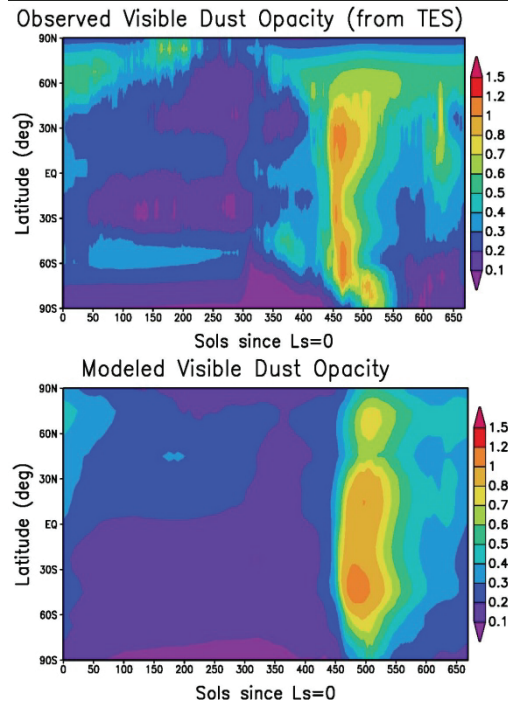


**Figure 1:** Seasonal cycle of the visible dust optical depth derived from TES IR measurements in 1999-2001 (top) and predicted by our multisize dust model (bottom) after the offline treatment. The agreement is far from perfect, but remains sufficient for our investigation on particle sizes.



For each of these 26 tracers, the output is proportional to a mixing ratio, although the coefficient of proportionality has to be determined relative to the others depending on the assumed size distribution of the lifted dust (see above), and assuming two scaling constant for 1) the dust storm dust ( $X_{\text{storm}}$ ) and 2) the dust devil dust ( $X_{\text{devil}}$ ). In practice, the dust mass mixing ratio  $mmr$  (kg/kg) of a given class size is computed as follow:

$$mmr = X r^3 n(r) q$$

with  $n(r)$  the shape of the lifted dust distribution (see above),  $q$  the “non-normalized” mixing ratio computed by the GCM and  $X$  one of the constant  $X_{\text{storm}}$  or  $X_{\text{devil}}$ .

$X_{\text{storm}}$  and  $X_{\text{devil}}$  are chosen so that the model output quantitatively mimic the minimum and maximum of the dust optical depth as observed by TES on Mars Global Surveyor. The optical depth of a given atmospheric column at a given time and location is assumed to be the sum of the optical depths of each layers, itself equal to the sum of the 26 optical depth of each dust tracers, given by :

$$\tau = \frac{3mmr \Delta p Q_{\text{ext}}}{4\rho r g}$$

with  $Q_{\text{ext}}$  the single scattering coefficient of the particle (the following values are taken for the 13 particle sizes: 0.005, 0.0186, 0.218, 1.55, 3.616, 2.42, 2.37, 2.29, 2.15, 2.1, 2.08, 2.06, 2.02),  $\rho$  the density of dust (2500 kg m<sup>-3</sup> is assumed in our model),  $r$  the (effective) radius (see table 2),  $\Delta p$  the thickness of the modeled atmospheric layer (Pa),  $g$  the acceleration of gravity.

To compute  $X_{\text{storm}}$  or  $X_{\text{devil}}$ , we assume that the yearly maximum and minimum global average of the dust optical depth must be equal in the model and the observations (2 unknown, 2 equations). Figure 1 shows the final seasonal dust cycle compared to the TES observations.

### Model results and validation.

Figures 2-5 illustrate key results of our study. Under the combined effect of transport, mixing and gravitational sedimentation, the effective radius  $r_{\text{eff}}$  of the dust particles is found to significantly decrease with altitude as expected by similar studies [18]. The effective variance  $v_{\text{eff}}$  remains close to the one assumed for the lifted dust. In fact, the model cannot predict the absolute value of  $r_{\text{eff}}$  or  $v_{\text{eff}}$  because it is

controlled by the assumed size distribution of the lifted dust which is unknown. Results are shown with a source tuned to yield  $r_{\text{eff}} \sim 1.8 \mu\text{m}$  in the lower atmosphere (as obtained by several studies [19,20]) or  $1.5 \mu\text{m}$  (as recommended by recent state of the art work by [21,22]). Interestingly it was found that, to first order, the dust effective radius primarily depend on pressure and that this dependency does not significantly vary with season. Thus it is possible to propose a typical profile of dust size distribution with pressure (Fig. 6).

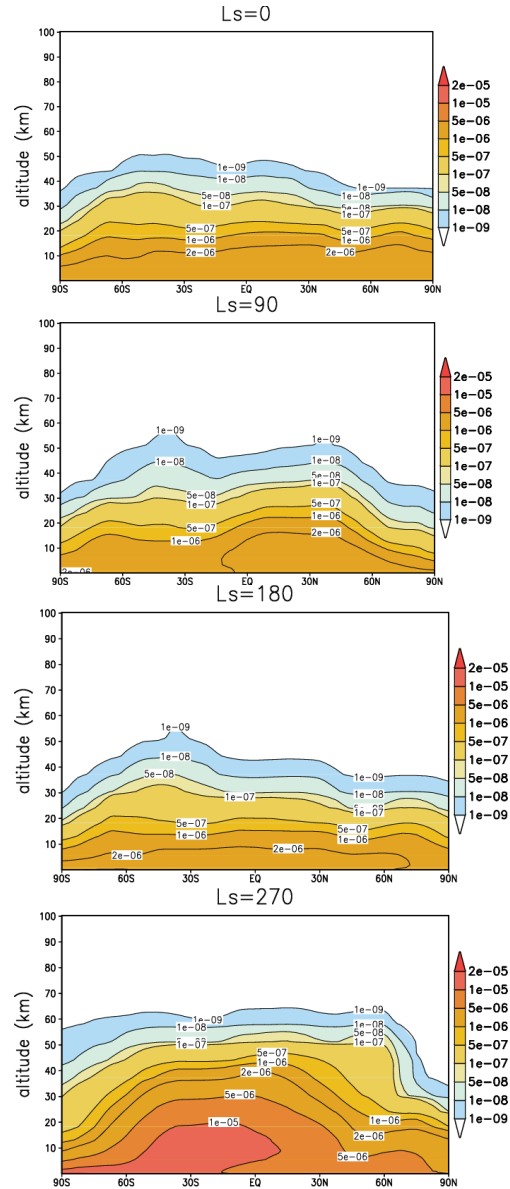


**Figure 2:** Zonal mean dust mixing ratio (kg/kg) for 4 martians seasons, as predicted by the 3D dust transport model. The altitude here is a pseudo-altitude ( $z = 10 \ln(p/p_s)$ ) with  $p$  pressure and  $p_s$  surface pressure.

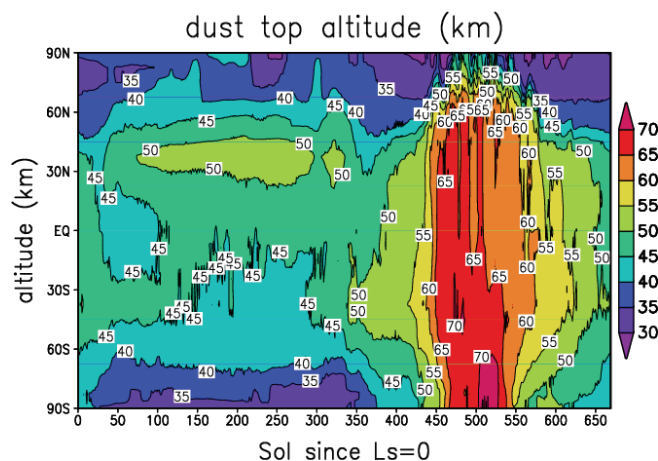


**Figure 3:** Seasonal variations of the zonal mean dust top altitude. The altitude is here the true altitude above the Mars geoid (areoid), which is accurately estimated by integrating the hydrostatic equation. The top of the dust is defined by a mass mixing ratio below  $10^{-8}$  kg/kg.

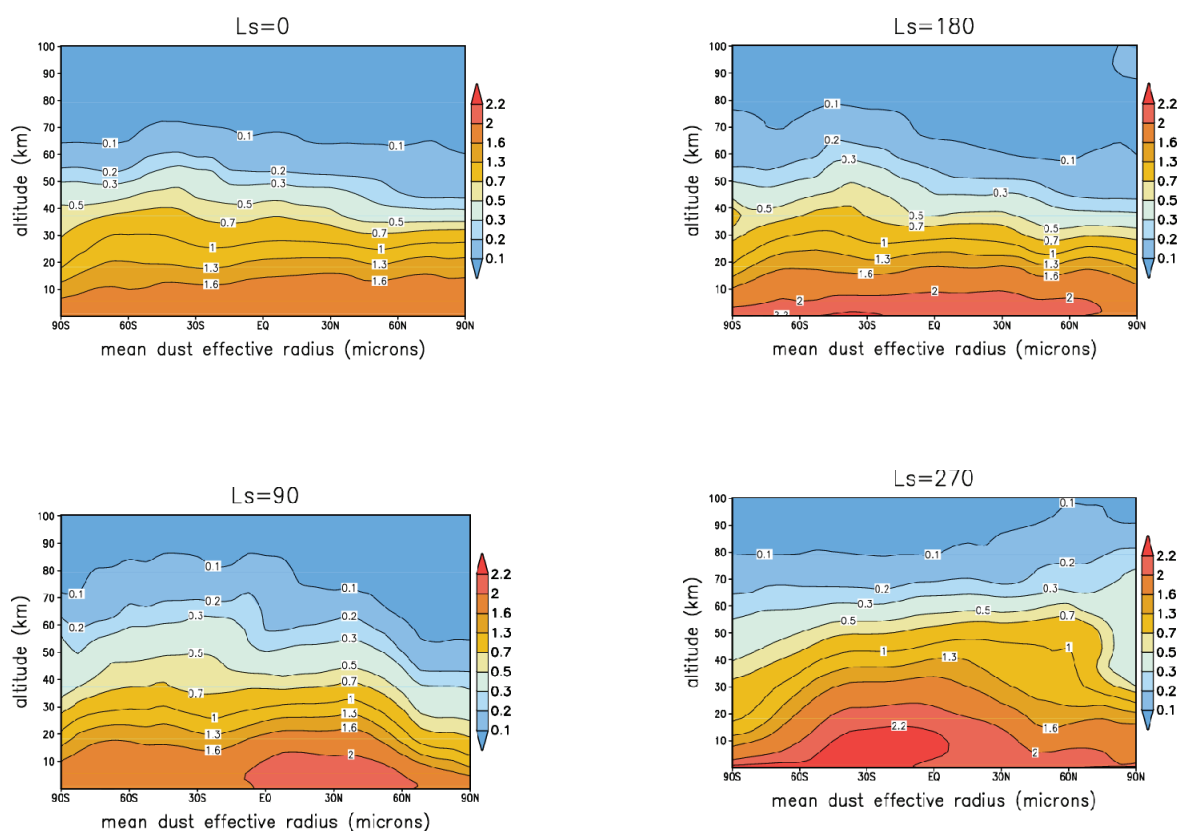


**Figure 4:** As in figure 2, but showing the mean dust effective radius.

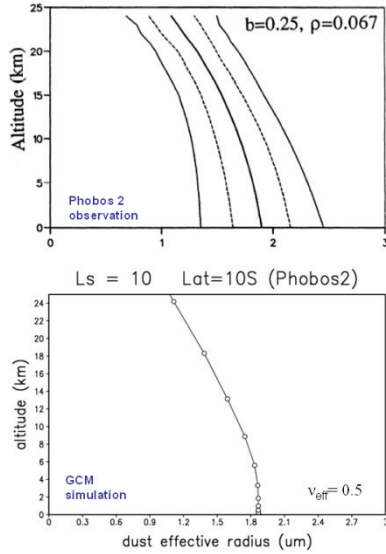


**Figure 5:** Comparison of the Phobos 2 dust particle size profile observations (Chassefiere et al. 1995) with model prediction at roughly the same locations and time.

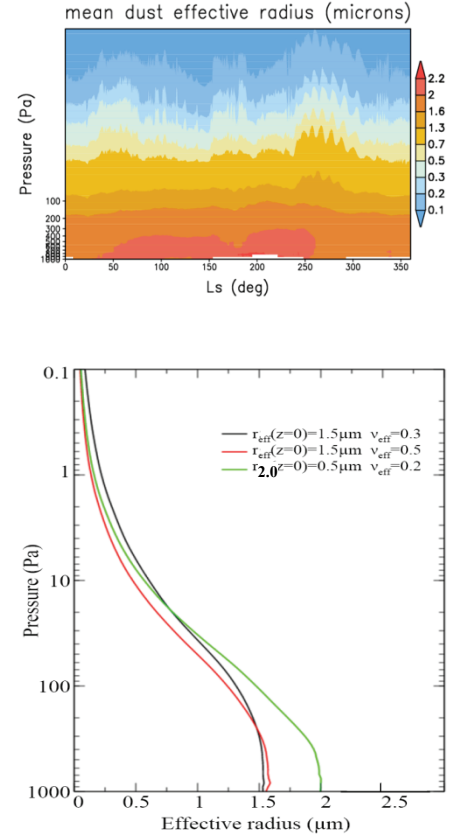


**Figure 6:** Seasonal variation of the mean dust effective radius for latitude below  $50^\circ$  as a function of pressure (**Top**). These variations are limited. Thus one can define an global annual mean (**Bottom**). The low atmosphere dust effective radius can be tuned to match the 1.5 or 2.0  $\mu\text{m}$  observed values. Above 1 pa it is primarily controlled by the assumed effective variance.

**References:** [1] Forget et al. JGR. 104, E10, p. 24,155-24,176, 1999 [2] Lewis et al. Icarus 192, Issue 2, p. 327-347, 1997 [3] Forget et al., 2008 [4] Hourdin et al. J. Atmos. Science 50, 3625-3640, 1993 [5] Hourdin and Armengaud Monthly Weather Review 127, issue 5, p. 822 (1999) [6] Rossow Icarus, 36 :1,50, 1978 [7] Murphy et al. JGR 100 :26357-26376, 1995 [8] Forget et al. 1998 [9] Newman et al. JGR (Planets), 107 :6-1, 2002 [10] Basu et al. JGR 109(E18) :11006 2004 [11] Basu et al. JGR 111(E10) :900 2004 [12] Kahre et al. JGR

111(E10) :6008. 2002 [13] Smith, Icarus, 167 :148-165 (2004) [14] Smith et al. 2001 [15] Renno et al. J. Atmos. Sci., 55 :3244-3252, 1998 [16] Alfaro et al. 1997 [17] Patterson and Gillette 1977 [18] Kahre Icarus, 195, Issue 2, p. 576-597, 2008 [19] Pollack et al. JGR 100, 5235-5250, 1995 [20] Clancy et al. JGR 100, 5251-5263, 1995. [21] Clancy Journal of Geophysical Research (Planets), 108, (E9), 2-1, 2003 [22] Wolff et al. JGR, 114, Issue E9, CiteID E00D04, 2009.

## DUST RADIATIVE EFFECT EXPERIMENTS USING THE LMD MARS GENERAL CIRCULATION MODEL.

Madeleine<sup>1</sup>, J.-B., Forget<sup>2</sup>, F., Millour<sup>3</sup>, E. and Wolff<sup>4</sup>, M. J. <sup>1,2,3</sup>Laboratoire de Météorologie Dynamique (LMD), CNRS/UPMC/IPSL, Université Paris 6, BP 99, 4 place Jussieu, 75252 Paris cedex 05, FRANCE (<sup>1</sup>[jbmlmd@lmd.jussieu.fr](mailto:jbmlmd@lmd.jussieu.fr), <sup>2</sup>[Francois.Forget@lmd.jussieu.fr](mailto:Francois.Forget@lmd.jussieu.fr), <sup>3</sup>[ehouarn.millour@lmd.jussieu.fr](mailto:ehouarn.millour@lmd.jussieu.fr)).  
<sup>4</sup>Space Science Institute, 18970 Cavendish Rd, Brookfield, WI 53045, USA ([mjwolff@spacescience.org](mailto:mjwolff@spacescience.org)).

**Introduction:** Correctly taking into account the radiative effect of dust in Global Climate Models (GCM) is vital to obtain realistic atmospheric temperature and dynamics. Until now, the radiative transfer of the LMD/GCM was using composite dust radiative properties built on the observations of Ockert-Bell et al., Toon et al. and Clancy et al. [1,2,3,4]. Since then, new data have allowed a full reconstruction of the dust refractive index, covering the entire solar and thermal infrared spectral range [5,6,7].

On this basis, we have provided the LMD/GCM with new dust radiative properties. For comparison, we ran three simulations, one using the “old” radiative properties and two using the updated properties of Wolff et al. These two simulations are based on different assumptions: spatially homogeneous scattering parameters on one hand, and size-dependent scattering parameters on the other. It is worth mentioning that clouds are not radiatively active in these experiments. After a short overview of the methods and data used to constrain the model, we will analyze the atmospheric thermal structures in the three cases, compare them to the UK/MGCM reanalysis [8,9], and discuss our ability to reconcile the LMD/GCM predictions with the available observations both in the visible and infrared ranges.

### Architecture of the model:

*1<sup>st</sup> simulation (“Ockert-Bell” scattering parameters):* The extinction coefficient, single scattering albedo and asymmetry parameter (i.e. scattering parameters) of the 1<sup>st</sup> simulation are built upon the analyses of [2] in the GCM solar channels (0.1-5 $\mu$ m), and upon IRIS/Mariner 9 observations [1] in the infrared channels (5-50  $\mu$ m). These latter properties have been generated using a sample of clay (montmorillonite 219b), and have been adapted for the GCM by removing the unrealistic absorptions at 20  $\mu$ m created by this mineral [4]. The black curve of Figure 1 represents, for instance, the resulting single scattering albedo. In this paper, we chose to focus on the Ockert-Bell dust properties, but it is worth

mentioning that measurements by [3] have been extensively used as well.

This dataset merges information from different instruments looking at different locations and times in order to cover the whole visible and infrared spectral range. It means that dust particle size distributions, which control the balance between dust absorption at solar wavelengths and emission in the infrared region, were different for the two domains. Consequently, a ratio of the extinction efficiency (and thus opacity) in the visible to the one in the infrared (later called the “solar over infrared ratio”) is used to correct for this bias and merge both datasets. Usually we use:

$$\tau_{0.67\mu m} / \tau_{9\mu m} = 2$$

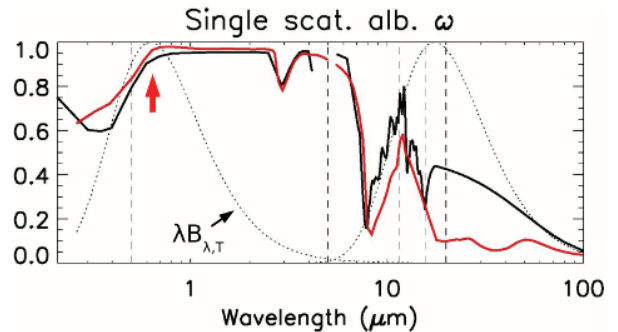


**Figure 1:** Dust single scattering albedo measured by [2] (black curve) and [6] (red curve). Dashed curves represent the blackbody emission spectra for temperatures of 5870K and 210K, respectively (area preserving representation). Vertical lines show the 6 channels of the GCM radiative transfer scheme.

*2<sup>nd</sup> simulation (“Wolff et al.” scattering parameters):* Over the last 10 years, many analyses of the dust scattering properties have been conducted at various wavelengths, using TES/MGS [10,5], Mini-TES/MER [11,6], OMEGA/MEx [12,13], CRISM/MRO [7] and MARCI/MRO [14]. In particular, the simultaneous observation of dust in the visible and infrared regions has been done using MGS

overflights of the Martian Exploration Rovers [6]. This allows the retrieval of the dust refractive index both in the visible and infrared regions, and avoids the use of an ad hoc solar over infrared ratio as mentioned above. To build the 2<sup>nd</sup> simulation, we have computed the dust scattering parameters using the T-Matrix code of M. Mishchenko [15] for a Gamma size distribution ( $r_{\text{eff}}=1.5\mu\text{m}$   $v_{\text{eff}}=0.3$ ) of finite cylinders ( $D/L=1$ ) [6]. The resulting single scattering albedo is given on Figure 1 (red curve). We can notice a small difference around  $0.7\mu\text{m}$  (red arrow) between the Ockert-Bell and Wolff et al. single scattering albedo. This is where most of the solar energy lies, and we can thus expect large differences in the predicted heating rates between the 1<sup>st</sup> and 2<sup>nd</sup> simulation.

*3<sup>rd</sup> simulation (size-dependent scattering parameters):* The dust refractive index can also be used to generate the dust scattering parameters for various dust particle sizes. After storing these scattering parameters in a look-up table, we can thus fully connect, in the GCM, the modeled size distributions to the radiative transfer scheme and let the scattering parameters evolve with the size of the particles. As a first step, we don't carry radiatively active dust explicitly in the model. Rather, we use the size distributions predicted by a separate dust transport experiment (see the paper of F. Forget in this issue). Seasonal variation in the predicted size distributions is shown to be relatively small, and thus, we use for our purpose a fit of the annual mean  $r_{\text{eff}}$  profile predicted in the dust transport experiment (see Figure 2) and a constant effective variance ( $v_{\text{eff}}=0.3$ ).

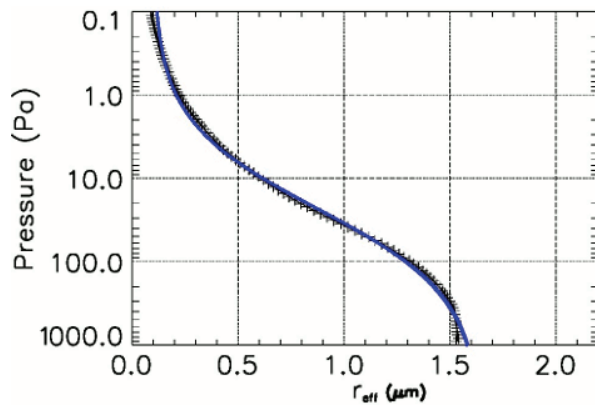


**Figure 2:** Fit of the dust annual mean effective radius profile predicted by the dust transport experiment (see the paper by F. Forget in this issue). This analytic function (blue curve) is used to describe the variation in the dust particle size along the vertical in our 3<sup>rd</sup> simulation, where dust is not carried explicitly by the model.

Scattering parameters are then computed in each grid-box by integrating on-line the parameters of the look-up table over a log-normal size distribution.

*Dust optical depth:* Once the scattering parameters are known, radiative transfer scheme needs the dust optical depth in each layer to finally compute the heating rates. As mentioned above, dust is not carried explicitly by the model in these experiments. Rather, the dust optical depth is deduced by using the space and time varying TES opacity, which corresponds to the total optical depth scaled to an equivalent 6.1 hPa pressure surface [16]. Therefore, the opacity along the vertical axis is computed by weighting the TES opacity with a Conrath function [17] (see [18] for further details):

$$q(z) = q_0 \exp \left( \nu \left[ 1 - \left( \frac{p_{\text{ref}}}{p(z)} \right)^{70/z_{\text{max}}} \right] \right)$$

TES opacity is an absorption opacity, and it also has to be converted to an extinction opacity, which is the opacity actually used by the GCM. We use for that the simple relation:

$$\tau_{\text{ext}} = \frac{\tau_{\text{abs}}}{1 - \omega}$$

Finally, in order to be as close as possible to the observations, the annual mean temperature at 1.06 hPa pressure level predicted by the GCM is compared to the UK/MGCM reanalysis temperature. The “input” dust opacity used to constrain the amount of dust in the atmosphere is then multiplied by a tuning factor to approach the observed temperatures. In other words, we slightly change the opacity of the atmosphere to fit the data. One of our goals is to reach a good tuning factor, i.e. to use an opacity that is close to what is really observed by TES, while at the same time predicting good temperatures.

#### Observational dataset:

Atmospheric thermal structure predicted by the LMD/GCM is compared to the reanalysis derived from TES temperature retrievals using the UK/MGCM [8,9]. Figure 3 shows the zonally and time averaged (over 10 days) temperature fields of the reanalysis. The warm perihelion season is clearly distinguished, as well as the comma-shaped temperature inversion in the mid-latitudes, which results from the adiabatic heating of the atmosphere in the descending branch of the Hadley cell.



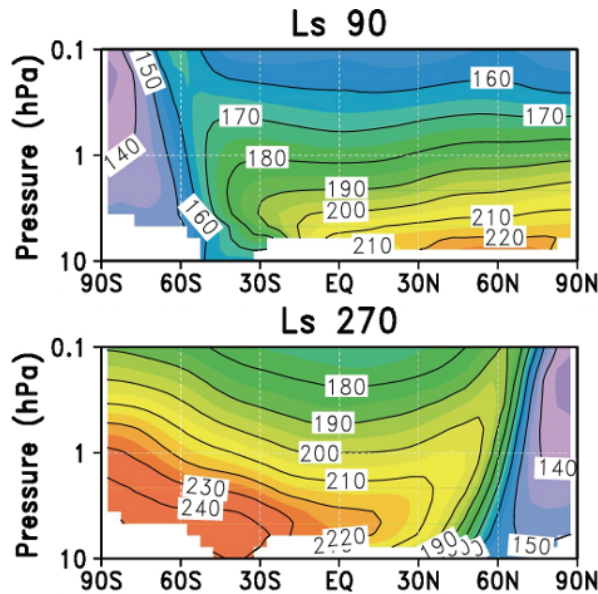


**Figure 3:** Zonally and time averaged (over 10 days) temperature fields from the UK/MGCM reanalysis [8,9] at two different seasons. This reanalysis is used as a guideline to evaluate the LMD/GCM.

#### Predicted thermal structures

*1<sup>st</sup> simulation:* Top panel of Figure 4 represents the temperature difference between the LMD/GCM (blue curve) and the UK/MGCM reanalysis (red curve) at 1.06 hPa pressure level. The two main differences occur around 30°N and in the north polar region. The first difference is possibly due a weaker intensity of the Hadley cell in the GCM than observed. The second difference results from the radiative cooling by water ice clouds that is not taken into account in these simulations. The agreement is thus encouraging, since radiatively active clouds will probably improve these results in the future.

The problem is that the tuning factor corresponds to an opacity equal to 42% of the actual TES opacity. This means that the TES opacity used to constrain the model's dust cycle (see section 2) has to be severely reduced to reach reasonable temperatures. This is a well-known problem due to dust being relatively dark in the Ockert-Bell dataset (see the single scattering albedo in Figure 1). Therefore, dust absorption at solar wavelengths is too large, and implies too much warming if dust opacity is not artificially reduced to lower values.

*2<sup>nd</sup> simulation:* Middle panel of Figure 4 now represents the same temperature difference when using the Wolff et al. radiative properties. Same difference is noticed in the north polar region, along

with a slight improvement in the northern branch of the Hadley cell. But the main improvement is the near disappearance of the tuning factor, which is now close to unity. Indeed, an excellent thermal structure is predicted using 94% of the observed dust opacity. The Wolff et al. dust properties thus allow us to predict good temperatures, while using at the same time realistic values of the dust opacity both in the visible and infrared ranges.

Figure 5 illustrates the zonally and time averaged (over 10 days) temperature difference between the UK/MGCM reanalysis (see Figure 3) and the 2<sup>nd</sup> GCM simulation, near aphelion (top panel) and perihelion (bottom panel). Radiative effect of water ice clouds (indicated by blue dashed lines and arrows) is prominent. For example, top panel shows a cold bias of the GCM near the equator and at 60°S which is comparable to the one discussed in [20] (see Figure 3c therein).

Similarly, warm biases in the mid-latitudes and polar regions are likely due to water ice clouds (see arrows in Figure 5). Significant differences are seen at the north pole for  $L_s=270^\circ$  (0.1 hPa level, bottom panel), but it is difficult to know whether the reanalysis or the GCM is right in these regions that are strongly dynamically controlled, and further analysis is necessary.

Apart from these differences, the overall agreement is really satisfying. The next step is to account for size-dependent scattering parameters.

*3<sup>rd</sup> simulation:* In this last simulation, scattering parameters are varying as a function of dust particle size. As seen in Figure 4 (bottom panel), the observed temperature at 1.06 hPa pressure level can be well reproduced again using a realistic dust opacity.

Figure 6 illustrates the zonal mean temperature difference between the UK/MGCM reanalysis and our simulation. When comparing Figure 6 to the bottom panel of Figure 5, we can see that most of the changes occur, as expected, at high altitude, where dust particles are smaller. The scattering parameters being now size-dependent, these particles have a smaller absorption at solar wavelengths, and the atmosphere is colder than in the 2<sup>nd</sup> simulation around the 0.1 hPa pressure level. Therefore, the equatorial and polar cold and warm biases are respectively more and less pronounced. Adding radiatively active water ice clouds is the next necessary step to further understand these biases.

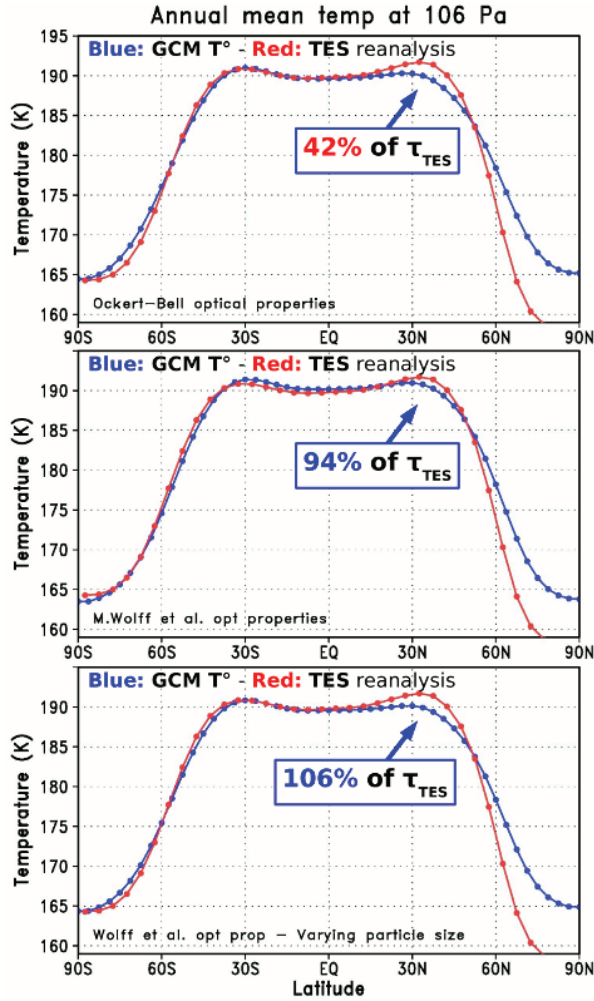


**Figure 4:** Zonally and time averaged (over one year) temperature at 1.06 hPa pressure level from TES reanalysis (red curve) and as predicted by the LMD/GCM (blue curve) for three different cases: a simulation using the Ockert-Bell radiative properties (top panel), another simulation using the Wolff et al. properties (middle panel) and a last simulation that uses size-dependent scattering parameters (bottom panel). The 1.06 hPa pressure level is chosen because of its proximity to the peak of the weighting function for the  $15\mu\text{m}$   $\text{CO}_2$  band [19].

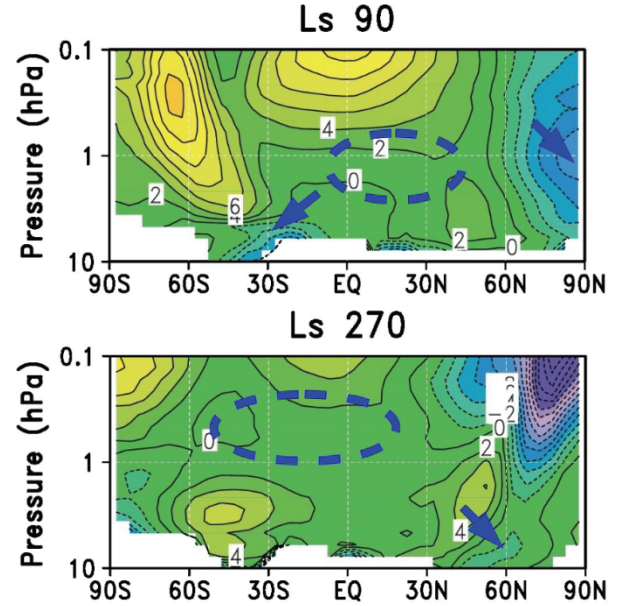


**Figure 5:**  $T_{TES} - T_{GCM}$ : Temperature difference between the UK/MGCM reanalysis and our 2<sup>nd</sup> simulation (Wolff et al. radiative properties and homogeneous scattering parameters). Contour interval is 2K. Blue dashed lines and arrows indicate the approximate location of water ice clouds.

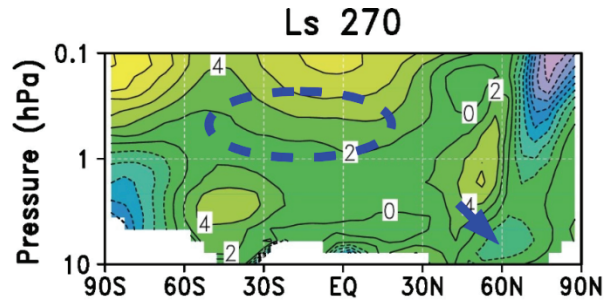


**Figure 6:** Same as Figure 5, but using 3D size-dependent scattering parameters.

## Conclusion

Dust radiative properties have been updated in the LMD/GCM using homogeneous and size-dependent scattering parameters, and main results can be summarized as follows:

- The use of the new Wolff et al. radiative properties results in a good thermal structure, while being at the same time consistent with the observed visible and infrared opacities. This was not the case for previous radiative properties and versions of the model;
- Taking into account the size-dependence of the dust scattering parameters has a significant impact on the GCM temperatures, especially at high altitude;
- Adding radiatively active clouds is the next necessary step to clarify the origin of the remaining differences between the LMD/GCM results and the UK/MGCM reanalysis.

**References:** [1] Toon, O. B. et al. (1977) *Icarus* 30, 663-696. [2] Ockert-Bell, M. E. et al. (1997) *JGR* 102, 9039-9050. [3] Clancy, R. T. et al. (1995) *JGR* 100, 5251-5263. [4] Forget, F. (1998) *GRL* 25, 1105-1108. [5] Wolff, M. J. and Clancy, R. T. (2003) *JGR (Planets)* 108, E9, 5097. [6] Wolff, M. J. et al. (2006) *JGR (Planets)* 111, E12S17. [7] Wolff, M. J. et al. (2009) *JGR (Planets)* 114, E00D04. [8] Lewis, S. R. et al. (2007) *Icarus* 192, 327-347. [9] Lewis, S. R. et al. (2008) *Third Int. Workshop on The Mars Atmosphere*, LPI Contribution n°1447, Abstract 9009. [10] Clancy, R. T. et al. (2003) *JGR (Planets)* 108, E9, 5098. [11] Smith, M. D. et al. (2006) *JGR (Planets)* 111, E12S13. [12] Vincendon, M. et al. (2007) *JGR (Planets)* 112, E08S13. [13] Määttänen, A. et al. (2009) *Icarus* 201, 504-516. [14] Wolff, M. J. et al. (2007) *7<sup>th</sup> Int. Conf. on Mars*, Abstract #3121. [15] Mishchenko, M. I. et al. (1996) *J. Quant. Spectrosc. Radiat. Transfer*, vol. 55, 535-575. [16] Smith M. D. et al. (2004) *Icarus* 167, 148-165. [17] Conrath, B. J. (1975) *Icarus* 24, 36-46. [18] Montmessin, F. et al. (2004) *JGR (Planets)* 109, 10004. [19] Conrath, B. J. et al. (2000) *JGR* 105, 9509-9520. [20] Wilson, R. J. et al. (2008) *GRL* 35, 7202.



# ***Poster Session***

## ***Day One***

*Tuesday, September 15, 2009*

*5:30 PM*



**DEVELOPMENT OF LIMB-SCATTERING RADIATIVE TRANSFER MODELS FOR MARS REMOTE SENSING AND DATA ASSIMILATION.** Eluszkiewicz, J., Flittner, D.E., Moncet, J.-L., and Wolff, M.J.

POSTER PRESENTER: Wolff, M., Space Science Institute, Boulder, CO

---

A current limitation in realizing the scientific potential of the growing dataset of limb measurements is the lack of publicly available (appropriate) radiative transfer models. Such models must be capable, in a computationally efficient manner suitable for retrieval and radiance assimilation work, of accurately representing both gaseous absorption and aerosol scattering in a spherical geometry. We report on work recently begun on developing rigorous radiative transfer models capable of simulating limb radiances in the presence of gaseous absorption and scattering. Our work has two overarching purposes. The first is to establish a set of rigorous benchmark calculations against which approximate methods to the limb absorption+ scattering problem can be validated. The second objective is to develop a fast parameterization capable of accurately and efficiently calculating limb radiances in the presence of gaseous absorption and scattering by aerosols.

## THE OBSERVATION OF ATMOSPHERIC DUST AND WATER VAPOUR CLOSE TO THE SURFACE OF MARS: THE MEDUSA EXPERIMENT. Esposito<sup>1</sup>, F., Colangeli<sup>1</sup>, L., Della Corte<sup>1,2</sup>, V., Palumbo<sup>2</sup>, P., Molfese<sup>1</sup>, C., Merrison<sup>3</sup>, J., Nørnberg<sup>3</sup>, P. Lopez Moreno<sup>4</sup>, J.J., Rodriguez-Gomez<sup>4</sup>, J.F., Ventura<sup>5</sup>, S., and The International MEDUSA Team.

<sup>1</sup> INAF – Osservatorio Astronomico di Capodimonte – Salita Moiariello 16, 80131 Napoli, Italy. <sup>2</sup> Dipartimento Scienze Applicate - Università di Napoli “Parthenope” – Centro Direzionale di Napoli Isola C4 - 80143 - Napoli, Italy. <sup>3</sup> Department of Physics and Astronomy - University of Aarhus - Ny Munkegade, Building 1520 - DK-8000 Aarhus C., Denmark. <sup>4</sup> Instituto de Astrofísica de Andalucía (CSIC) - c/ Camino Bajo de Huétor, 50 - PO Box 3004 - 18080 Granada, Spain. <sup>5</sup> Dipartimento di Ingegneria Aerospaziale - Università degli Studi di Napoli “Federico II”, Via Claudio, 21 – 80125 Napoli, Italy.

F. Esposito: [francesca.esposito@oacn.inaf.it](mailto:francesca.esposito@oacn.inaf.it); L. Colangeli: [colangeli@oacn.inaf.it](mailto:colangeli@oacn.inaf.it); V. della Corte: [v.dellacorte@gmail.com](mailto:v.dellacorte@gmail.com); P. Palumbo: [palumbo@na.astro.it](mailto:palumbo@na.astro.it); C. Molfese: [molfese@oacn.inaf.it](mailto:molfese@oacn.inaf.it); J. Merrison: [merrison@phys.au.dk](mailto:merrison@phys.au.dk); P. Nørnberg: [geopn@phys.au.dk](mailto:geopn@phys.au.dk); J.J. Lopez Moreno: [lopez@iaa.es](mailto:lopez@iaa.es); J.F. Rodriguez-Gomez: [julio@iaa.es](mailto:julio@iaa.es); S. Ventura: [sergio.ventura@na.astro.it](mailto:sergio.ventura@na.astro.it).

---

**Introduction:** Dust and water vapor are fundamental components of the Martian atmosphere. In view of tracing the past environmental conditions on Mars, that possibly favored the appearing of life forms, it is important to study the present climate and its evolution. Of major scientific interest are the abundance and physical, chemical and electrical properties of dust and the abundance of water vapor dispersed in the atmosphere and their exchange with the surface. Moreover, in view of the exploration of the planet with automated systems and in the future by manned missions, it is of primary importance to analyze the hazards linked to these environmental factors. The Martian Environmental Dust Systematic Analyzer (MEDUSA) experiment has been developed for the measurement of airborne dust and water vapor close to the surface of Mars and is suitable to be accommodated on Martian landers or rovers. MEDUSA implements a suite of sensors, based on optical and piezoelectric cumulative mass sensors, that aims to study, for the first time, in-situ and quantitatively, the physical properties of the airborne dust and water vapor. Measured quantities are the cumulative dust mass flux, the dust deposition rate, and its physical and electrification properties, the size distribution of sampled particles and the atmospheric water vapor abundance versus time.

MEDUSA has actually reached a Technical Readiness Level > 5 within the European ExoMars mission.

### Scientific Rationale:

#### *Dust on Mars*

Dust is permanently present in the atmosphere with variable abundance. Airborne dust contributes to determine the dynamic and thermodynamic evolution of the atmosphere [1], including large scale circulation processes, on diurnal, seasonal and annual time-scales. Dust-cycle, dust storms and dust devils [2] are typical phenomena involving atmospheric dust. Aeolian erosion, dust redistribution on surface and weathering are mechanisms coupling surface and atmosphere evolution and are driven by wind intensity and grain properties. The data accumulated so far (remote and in situ measurements) are rather poor and mainly qualitative.

Beside its scientific interest, the study of atmospheric Martian dust is relevant in the context of analysing hazard connected to the contamination/failure of payloads (e.g., solar panels, mechanisms, optical systems) and to the environmental risks for human exploration, due to dust deposition, impacts and electrification.

It results that to measure in situ the amount, mass/size distribution, deposition rate, dynamical properties and electrification of solid particles in the Martian atmosphere, as a function of time, is a fundamental step to shed light on the airborne dust evolution, in particular, and on climatic processes, more in general.

#### *Water vapour on Mars*

Water is a key component in relation to the presence of biologically relevant compounds. Atmospheric

water vapour is a primary indicator of seasonal climatic behaviour, linked to the exchange with surface natural reservoirs (polar caps, regolith) and to atmospheric transport mechanisms.

The information on abundance and distribution of water vapour available so far is mainly based on remote observations. Viking, Mars Global Surveyor, Mars Express and Mars Reconnaissance Orbiter missions collected information on atmospheric *water-cycle* [3], [4], [5], [6], [7], while the Mars Pathfinder [8], the Mars Exploration Rovers [9] and the Phoenix [10] have been, so far, the only missions to measure the atmospheric water vapour from the Mars surface. Despite the low abundance, relative humidity can overcome 100% close to the surface, giving rise to fogs and clouds. Due to the atmospheric pressure at the surface, comparable with the pressure of the water triple point (6.1 mbar), H<sub>2</sub>O is probably present exclusively in gaseous and solid states, at the surface level.

These elements suggest the importance of studying in situ water vapour content close to the surface and the its exchanges atmosphere - surface.

The goals of the MEDUSA experiment are to study in situ, directly and quantitatively the cumulative dust mass flux and dust deposition rate, the physical and electrification properties, the size distribution of sampled particles and the water vapour abundance versus time, a goal that has never been reached so far. The information that can be obtained by in situ measurements over different time spans (days, seasons, years) represents a key input in different areas of interest:

- in the context of search of life on Mars
  - to determine present climatic conditions at Mars surface
  - to search for water
  - to determine physical parameters impacting on life presence on Mars
  - to derive information about past history of Mars climate
  - to provide ground-truth for validation of data coming from orbiter observations
- in Mars operations
  - to evaluate hazardous conditions due to Martian environment
  - to place constraints on operative conditions at Mars
  - to support definition of future Mars exploration missions

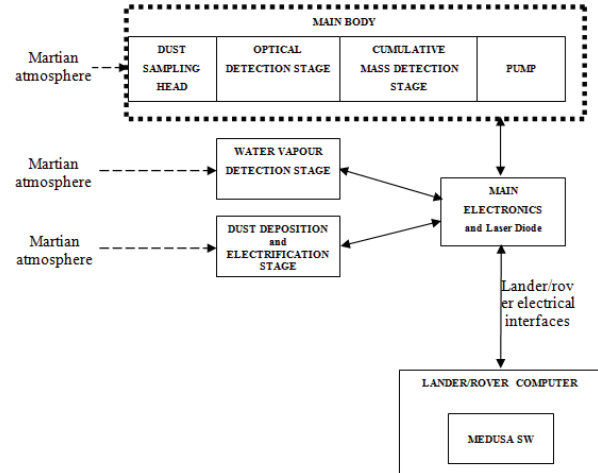


**Figure 1:** MEDUSA block diagram.

**Instrument architecture:** The MEDUSA experiment is based on the coupling of different techniques using optical detection and cumulative mass deposition. It consists in a dust collector, with separate stages for water vapour monitoring and for dust deposition and electrification measurement, as schematically shown in Figure 1. The experiment accommodates an Optical Stage (**OS**), embedded in the inlet nozzle and a collection stage for dust based on microbalance (**MBd**). A pump placed at the end of the acquisition chain guarantees gas and dust flux through the system. This configuration allows the best sensitivity coverage, ranging over more than 3 orders of magnitude in grain size. A separate microbalance, equipped with a Peltier device, for cooling and thermal stabilisation, is exposed to condense atmospheric water vapour (**MBwv**). Another separate stage includes 6 lasers and deposition chargeable surfaces for dust deposition and electrification measurements (**DDES** = Dust Deposition and Electrification Stage). Dust removal, electrical retardation and wind speed are also measured with DDES.

All the sensing subsystems forming MEDUSA have been or are being tested at MEDUSA Team's laboratories; some of them (**OS**, **MBd**) are identical to or directly derived from sensor already in use for space missions [11].

Each of the techniques used in MEDUSA returns directly important physical parameters of dust and water vapour in the Mars atmosphere as reported in Figure 2. Starting from the quantities directly measured by MEDUSA, important information is

derived about dust and water vapour environment in the sites explored by the future landers/rovers, as illustrated below.

• Atmospheric dust particle size distribution

MEDUSA is able to measure the size of atmospheric dust in the wide size range of interest (from 0.01 to 10  $\mu\text{m}$ ); complementary techniques covering different size ranges are coupled. MEDUSA is able to detect optically single particles  $\geq 0.3 \mu\text{m}$  in radius and to measure the cumulative mass of smaller grains.

• Number density of particles vs. size

This measurement is related to the previous result through the sampling operations. Once particle counting and/or mass measurements have been performed, dust number density can be derived, since the volume sampled by the system is known. From the operational point of view this requires a careful control of the atmospheric volume that is sampled. Due to the poor knowledge of the actual values for dust size distribution and number densities in Martian atmosphere, the instrument design allows a large versatility and considers sufficient margins to cope with a wide range of dust properties.

• Water vapour abundance in the atmosphere

This measurement is basically independent from the previous ones. The cumulative mass measurement of the water vapour condensed on the sensing device in a defined time interval and environment conditions (p, T) provides the water abundance monitoring.

Sensor	Primary Output	Derived Output
Dust Optical Detector	Scattered light in forward	Dust concentration
	Scattered light in backward	Grain size and shape
	Time of flight	Grain optical properties
Dust Collector based on microbalance	Dust mass in size range	Dust concentration
Water Vapour Detector based on microbalance	Collected water vapour	Humidity
Dust Deposition and Electrification Sensor based on 6 lasers + photodiodes + electrical field	Deposition of dust	Electrification of dust
	Wind speed	

**Figure 2:** Output of MEDUSA sensors and derived physical quantities.

• Dust Deposition, Removal, Suspension and Electrification

The dust deposition rate on the surface of the sensor is measured by detecting scattered light. Similarly, dust removal can also be quantified, thus giving the opportunity to study granular entrainment mechanisms. By applying electric fields to the dust accumulation surface the electrification level of the suspended dust grains can be determined. Using patterned laser beams suspended dust velocities (speed and angle) can be determined which quantifies the wind velocity (and the surface wind shear stress). From this measured wind speed and the suspended dust detection rate, the concentration of dust grains in the atmosphere can be obtained directly.

• Time evolution of the former quantities on long terms (seasons) and short term (days, hours) due to local events (e.g. winds, dust storms)

This implies mainly operation requirements. The system shall repeat the sampling and analysis of variable amounts of atmosphere. Different environment conditions could result in different dust number densities by orders of magnitude.

In addition, the experiment could be in principle capable to perform:

• Atmospheric dust sampling for other analytical measurements

Atmospheric dust could be sampled and delivered to other analytical experiments for characterization of chemical and physical dust properties, complementary to MEDUSA results.

**Performances and status:**

A breadboard of the MEDUSA instrument was built and tested under ESA and Italian Space Agency (ASI) contracts. This breadboard reached a Technical Readiness Level > 5 within the European ExoMars mission. Here we report some of the most interesting results.

*Microbalance for dust (MBd) measurement*

Micro-balances are sensor devices based on piezoelectric transducers, whose frequency is proportional to the mass deposited on the sensor. The measured physical quantity is the shift of the resonant frequency of a quartz oscillator [12].

Microbalances are available on the market as space qualified self-standing units. The sensor response has been evaluated vs. stability and temperature. Fixing room temperature, the stability in frequency has been verified to be within 0.05%. By varying the

temperature, it has been observed a variation in the resonance frequency. Anyway, this behavior is a reproducible hysteresis and the device has been calibrated. Moreover, the MBd has been calibrated versus the mass of deposited particles. The trend is linear with  $R^2 = 0.9952$ .

#### *Microbalance for water vapour (MBwv) measurement*

Micro-balances are also appropriate to measure quantitatively the mass of condensed volatiles (e.g., water vapour). The detection is achieved by cooling the crystal sensor below the frost point by a Peltier device and by monitoring the deposition curve. Frosting signal associated to a certain crystal temperature allows to obtain the value of the atmospheric vapour partial pressure and the relative humidity at the time of the measurement.

Tests on MBwv are based on the measurement of the vibration frequency of the MBwv for known concentrations of water vapour, by fixing the water vapour partial pressure at know values and by varying the sensor temperature. These tests have been performed under Martian water vapour partial pressure simulated conditions. The results are shown in Table 1: there is a good agreement between the measured and the expected frost temperature.

#### *Optical System (OS)*

Two different version of the OS breadboard have been developed: the first one (OS\_BB1) under an ESA contract and a second one (OS\_BB2) under a subsequent ASI contract.

OS\_BB1 showed some problems in the coupling of laser source and optics causing the presence of a large stray light and a reduction of laser source nominal power density; nevertheless the

Water vapour pressure	Temperature rate	Temperature measured	Nominal frost point
$2.6 \times 10^{-3}$ mbar	10 °C/min	-70.09 °C	-70 °C
	5 °C/min	-71.13 °C	
	1 °C/min	Not determined	
$5.5 \times 10^{-4}$ mbar	10 °C/min	-80.97 °C	-80 °C
	5 °C/min	-80.68 °C	
	1 °C/min	Not determined	
$1.4 \times 10^{-4}$ mbar	10 °C/min	-88.54 °C	-88 °C
	5 °C/min	-89.01 °C	
	1 °C/min	Not determined	

**Table 1:** Results of the water vapour condensation test for the MK20-2 QCM at three different vapour pressures and for different temperature rates.

performances test demonstrated that this sub-system was able to detect single particles with radii  $< 0.5 \mu\text{m}$ . This is very close to the OS nominal performances (detection limit:  $0.2 \mu\text{m}$ ). In the case the nominal power density is reached, this limit corresponds to the detection of  $0.2 \mu\text{m}$  particles.

All the problems related to laser source coupling with optics were solved during OS\_BB2 design by using a diode integrated with fibre optic; moreover this new configuration is able to work more efficiently in the Martian environmental conditions as the laser source can be located outside the instrument, in a safer and warmer position. With this new design the stray light has been highly reduced and the power density in the sampling volume has been maximized. Starting from the measured optical power in the sampling volume and the Mie's theory it can be shown that the minimum detectable particle radius is below  $0.2 \mu\text{m}$  in forward scattering (FW) and  $0.3 \mu\text{m}$  in backward (BW) scattering (Fig. 3).

Several experiments were performed injecting into the MEDUSA OS particles with different sizes. For each particles diameter the electrical response of the photodiodes was valued to verify the instrument performances. This work is in progress.

#### **Conclusions:**

The MEDUSA instrument has been designed for the measurement of airborne dust and water vapour close to the surface of Mars. A breadboard has been developed and successfully tested. MEDUSA has actually reached a Technical Readiness Level  $> 5$  within the European ExoMars mission and is well suited to be accommodated on future Martian landers or rovers..

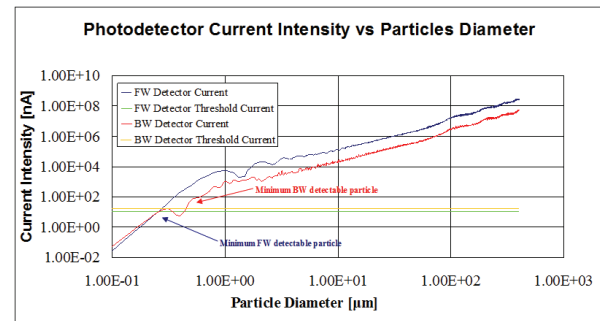


**Figure 3:** OS detector current intensity for forward and backward scattering. Detector dark current limit is shown for reference.

- References:** [1] Zurek, R. W. (1992), in *Mars*, Kieffer, H. H., Jakosky, B. M., Snyder, C. W., Matthews, M. S. eds., The University of Arizona Press, 799-817, 1992. [2] Metzger, S. M., Carr, J. R., Johnson, J. R., Parker, T. J. and Lemmon, M. T. (1999), *Geophys. Res. Letters*, **26**, 2781. [3] Jakosky, B. M. and Farmer, C. B. (1982), *J. Geophys. Res.*, **87**, 2999-3019. [4] Smith, M. D. (2002), *J. Geophys. Res.*, **107**, Issue E11, 25-1. [5] Fedorova, A., Korablev, O., Bertaux, J-L, Rodin, A., Kiselev, A. and Perrier, S. (2006), *J. Geophys. Res.*, **111**, Issue E9, CiteID E09S08. [6] Melchiorri, R., Encrenaz, T., Fouchet, T., Drossart, P., Lellouch, E., Gondet, B., Bibring, J.-P., Langevin, Y., Schmitt, B., Titov, D. and Ignatiev, N. (2007), *Planetary and Space Science*, **55**, 333-342. [7] Smith, M. D., Wolff, M. J., Clancy, R. T., and Murchie, S. L. (2009), *Journal of Geophysical Research* **114**, E9, CiteID E00D03. [8] Titov, D. V., Markiewicz, W. J., Thomas, N., Keller, H. U., Sablotny, R. M., Tomasko, M. G., Lemmon, M. T. and Smith, P. H. (1999), *J. Geophys. Res.*, **104**, 9019-9026. [9] Smith, M. D., Wolff, M. J., Lemmon, M. T., Spanovich, N., Banfield, D., Budney, C. J., Clancy, R. T., Ghosh, A., Landis, G. A., Smith, P., Whitney, B., Christensen, P. R. and Squyres, S. W. (2004), *Science*, **306**, 5702, 1750-1753. [10] Whiteway, J. A., Komguem, L., Dickinson, C., Cook, C., Illnicki, M., Seabrook, J., Popovici, V., Duck, T. J., Davy, R., Taylor, P. A., Pathak, J., Fisher, D., Carswell, A. I., Daly, M., Hipkin, V., Zent, A. P., Hecht, M. H., Wood, S. E., Tamppari, L. K., Renno, N., Moores, J. E., Lemmon, M. T., Daerden, F. and Smith, P. H. (2009), *Science*, **325**, 5936, 68-70. [11] Colangeli, L., Lopez-Moreno, J. J., Palumbo, P., Rodriguez, J., Cosi, M., Della Corte, V., Esposito, F., Fulle, M., Herranz, M., Jeronimo, J. M., Lopez-Jimenez, A., Mazzotta Epifani, E., Morales, R., Moreno, F., Palomba, E. and Rotundi, A. (2007), *Space Science Reviews*, **128**, Issue 1-4, 803-821. [12] Stockbridge C. D. (1966), in *Vacuum Microbalance Techniques*, K. Behrndt Ed., Plenum, New York, 5, 147.



---

**DUST PROPERTIES FROM A LOCAL DUST STORM OBSERVED BY OMEGA AND PFS ON MARS EXPRESS.** Määttänen<sup>1,2,3</sup>, A., Fouchet<sup>4,5</sup>, T., Forni<sup>6</sup>, O., Forget<sup>7,5</sup>, F., Savijärvi<sup>1</sup>, H., Gondet<sup>8</sup>, B., Melchiorri<sup>4,\*</sup>, R., Langevin<sup>8</sup>, Y. Formisano<sup>9</sup>, V. Giuranna<sup>9</sup>, M. and Bibring<sup>7</sup>, J.-P. <sup>1</sup>Department of Physics, University of Helsinki, P.O.Box 64, 00014 Helsinki, Finland. <sup>2</sup>Finnish Meteorological Institute, Space Research Unit, P.O.Box 503, 00101 Helsinki, Finland. <sup>3</sup>Presently at: LATMOS, CNRS/UVSQ/UPMC/IPSL, Réduit de Verrières, BP 3, Route des Gatines, 91371 Verrières-le-buisson Cedex, FRANCE (anni.maattanen@latmos.ipsl.fr). <sup>4</sup>Observatoire de Paris (thierry.fouchet@obspm.fr). <sup>5</sup>Université Pierre et Marie Curie. <sup>6</sup>Centre d'Etude Spatiale des Rayonnements (olivier.forni@cesr.fr). <sup>7</sup>Laboratoire de Météorologie Dynamique (francois.forget@lmd.jussieu.fr). <sup>8</sup>Institut d'Astrophysique Spatiale (firstname.lastname@ias.u-psud.fr). <sup>9</sup>Istituto di Fisica dello Spazio Interplanetario (firstname.lastname@ifsi.rm.cnr.it). <sup>\*</sup>Presently at: NASA/AMES, Moffett Field, CA, USA.

---

**Introduction:** Dust cycle is one of the major climatic cycles on Mars. Dust, present in the atmosphere in variable amounts, is lifted from the surface of the planet by the wind and advected by the atmospheric circulation. Dust has a strong effect on the atmospheric temperatures through the radiative budget and the heating rates. During a planet-encircling dust event the atmospheric temperatures can easily rise by 40 K. However, since the optical depth rises during such an event, less sunlight can penetrate through the atmosphere down to the surface, and thus the surface actually cools. These two opposing tendencies tend to stabilize the atmospheric temperature profile. Thus information on the optical properties of dust are important for modeling the radiative effects of dust in the Martian atmosphere.

We have analyzed a dust storm observation of MEx/OMEGA (Observatoire pour la minéralogie, l'eau, la glace et l'activité) to better constrain the optical properties of dust. We have also used temperature observations of the same dust storm by PFS (Planetary Fourier Spectrometer) and a one-dimensional atmospheric model to constrain the vertical profile of dust in the storm. The results have been published in Määttänen et al. 2009 [1].

**Methods:** OMEGA [2] is a spectro-imaging system aboard Mars Express, on orbit of Mars since December 2003. The instrument observes in the spectral range of 0.35-5.1  $\mu\text{m}$  with a spectral resolution of 0.01-0.02  $\mu\text{m}$  and the spatial resolution can be as good as 300m/pixel. PFS [3] observes in the range 250-8000  $\text{cm}^{-1}$  with a spectral resolution of 1.3  $\text{cm}^{-1}$  and a spatial resolution of 12 km at periaapsis. PFS can probe the atmospheric temperature from the surface up to 20 Pa.

We have studied two orbits only 3 sols apart, orbits 1201 and 1212, which fly over the same geographical zone but display very different atmospheric states. On orbit 1201 the surface can be seen well since the atmosphere is nearly clear of dust. Thus the orbit 1201 was used to retrieve the surface albedo, important for the dust storm analysis of the orbit 1212. The orbit 1212 shows a very dusty region near the equator, a clump of dust with a high optical depth. We used the data of these two orbits to retrieve the dust properties from the orbit 1212.

OMEGA has the ability to observe the variations in the atmospheric dust loading. The difficulty of observing dust in nadir viewing is how to separate the atmospheric dust from the signal of the surface. In the Martian  $\text{CO}_2$  atmosphere at some wavelengths the atmospheric  $\text{CO}_2$  absorbs all photons, and thus no surface reflection is seen. In these saturated  $\text{CO}_2$  absorption bands any reflection seen must come from atmospheric scatterers, like dust or clouds. However, the scatterers must be above a certain altitude (15-20 km), and assumptions on the dust distribution below this altitude must be made. We retrieved the surface albedo from orbit 1201 and used the surface pressure extracted from the Mars Climate Database [4], which compared well with the surface pressure values extracted from OMEGA observations of the orbit 1201 by Forget et al. 2008 [5] and Spiga et al., 2008 [6].

We base our retrieval on the very large dust optical depth in the dust storm region of the orbit 1212, which effectively decouples the dust reflectance from the surface albedo. Thus the dust optical thickness can be considered as quasi-infinite. This decoupling has been confirmed with an Independent Component Analysis (ICA, [7]), which is a method able to find the independent sources whose linear mixing

produces the observed signal. This analysis confirmed that the crucial assumption of the decoupling of the dust signal from the surface signal is valid.

Using the highest reflectance observed inside the dust storm, we fit the single-scattering albedo of dust. Using this analyzed single-scattering albedo, we retrieve the dust optical depth in whole of the dust storm. The retrievals are performed in the wavelength range 0.5-3.5  $\mu\text{m}$ .

**Results:** The single-scattering albedo retrieved shows that the dust is brighter than the commonly used Ockert-Bell dust properties [8]. In addition to this, we do not observe the absorption feature at 2.8  $\mu\text{m}$  seen by Fedorova et al (2002) [9]: most probably this is due to Fedorova et al (2002) observing the full disk of Mars (planet-average observations) during a period of low dust activity. With low optical thickness and dust most probably confined closer to the surface, the single-scattering albedo has been more difficult to analyze from the  $\text{CO}_2$  absorption band.

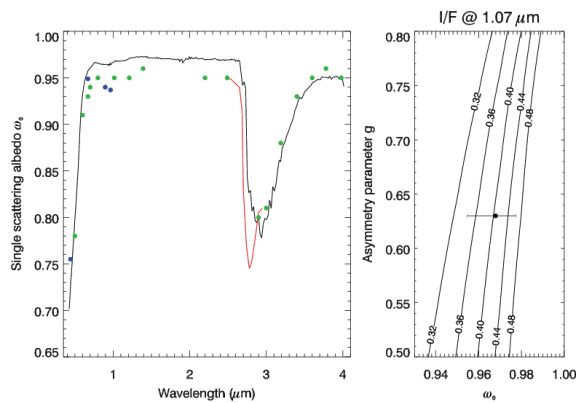


**Figure 1:** Left: the single-scattering albedo retrieved in this study (solid black line) and comparison with previous studies. Ockert-Bell et al. (1997) [8], green dots. Fedorova et al (2002) [9], solid red line. Tomasko et al. (1999) [10], blue dots. Right:  $I/F$  contours as a function of single-scattering albedo and asymmetry parameter for an infinite optical depth. The black dot shows the single-scattering albedo at 1.07  $\mu\text{m}$  retrieved in this study. The error bar shows the uncertainty due to the 15% calibration uncertainty of OMEGA.

The “quasi-infinite” maximum value of dust optical depth can be retrieved from the brightest spectrum inside the dust storm. This maximum value of optical thickness  $\tau$  is very high,  $\tau(1 \mu\text{m}) = 10$ . This value is very high, but it may be related to the facts that it is very local, it developed in less than 3 sols, and it seems very dynamic and even convective in nature. The storm encompasses an area of 180 km in north-south direction and 60 km in the east-west direction, although our view in this direction is limited by the width of the OMEGA image. The smallest details of the tops of the dust plumes that can be observed in the dust optical thickness maps are of the order of few kilometers.

The observations of PFS show the effect of the dust storm on the temperature field. The latitude-altitude cross-sections of the temperature field show how the thick dust cloud warms the middle atmosphere, but it shadows the surface and the lower atmosphere, cooling them down.

We modeled the effect of a dust storm and the dust vertical distribution on the atmospheric temperatures with a 1-D model of the Laboratoire de Météorologie Dynamique (Paris, France). We tested several dust vertical distributions in the model: well-mixed up to 55 km and profiles where the dust is confined lower in the atmosphere (with a cut-off at different altitudes). The modeling results were compared with the PFS temperature profile observations. The comparison showed that the dust should be confined to the lowest scale height of the atmosphere in the storm to match the observed temperature profile.

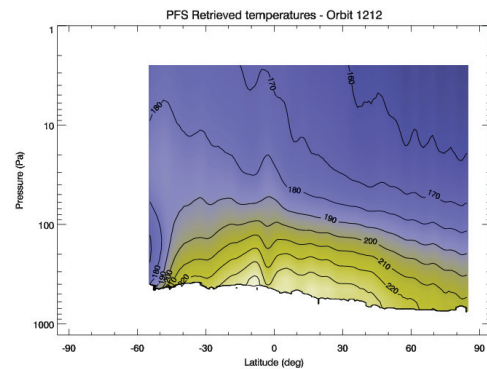


**Figure 2:** The latitude-pressure cross-section of temperature inverted from PFS observations on the dust storm orbit 1212. The dust storm is centered at around 3°S. The dust heats the upper atmosphere and cools the lower atmosphere.

However, OMEGA reflectance could not be fit with  $\tau=10$ , but a higher value of 20 would be required. Thus the question on the dust vertical distribution is still unresolved and more mutual observations are needed.

**References:** [1] A. Määttä et al. (2009), *Icarus* 201, 504-516. [2] J.-P. Bibring et al. (2004). ESA SP-1240: Mars Express: the scientific payload, p. 37-49, 2004. [3] V. Formisano et al. (2005) *Planet. Space*

*Sci.* 53, 963-974. [4] Lewis et al. (1999) *J. Geophys. Res.* 104, 24177-24194. [5] Forget et al. (2008) *J. Geophys. Res.* 112, E08S15. [6] Spiga et al. (2008) *J. Geophys. Res.* 112, E08S16. [7] Comon, P. (1992), In: Lacoume, J.L. (Ed.) Higher-order statistics. Elsevier, Amsterdam, pp. 29-38. [8] Ockert-Bell et al. (1997), *J. Geophys. Res.* 102, 9039-9050. [9] Fedorova et al. (2002), *Planet. Space Sci.* 50, 3-9. [10] Tomasko et al. (1999), *J. Geophys. Res.* 104, 8987-9007.

---

**ARES: AN IN SITU SENSOR TO CHARACTERIZE MARS ATMOSPHERIC ELECTRICITY.** <sup>1</sup>Montmessin, F., <sup>1</sup>Godefroy, M., <sup>1</sup>Hamelin, M., <sup>1</sup>Berthelier, J.J., <sup>1</sup>Yahi, S., <sup>2</sup>Aplin, K., <sup>1</sup>Simoes, F., Vieau, A.-J., and <sup>3</sup>Szago, K., <sup>1</sup>LATMOS, CNRS/UVSQ/IPSL, Paris, France, <sup>2</sup>Rutherford Appleton Laboratory, STFC, Didcot, United Kingdom, <sup>3</sup>KFKI, Budapest, Hungary ([franck.montmessin@latmos.ipsl.fr](mailto:franck.montmessin@latmos.ipsl.fr)).

---

**Introduction:** The Atmospheric Relaxation and Electric field Sensor (ARES) experiment is devoted to the investigation of atmospheric electric phenomena. It will measure the ionization state of the atmosphere, the electric fields that result from various charging mechanisms and investigate the planet global electrical circuit. Atmospheric electrical phenomena are an important issue in dust transport and surface and atmospheric chemistry. Electrification processes may also affect a landed vehicle and could be an important issue for their safe and reliable operation and, more generally, for future landed systems in the context of the human exploration of Mars.



ARES is a double probe electric field instruments with two cylindrical sensors that can be installed on the meteorological mast. It measures the magnitude of the vertical component of the electric field and the potential of the lander with respect to background from DC to 2 kHz up to  $\sim 250$  V/m which can be increased to  $\sim 20$  kV/m in dedicated modes of operation. The vertical electric component of electromagnetic waves and the AC fluctuations of the potential of the rover will be measured in the frequency range from 8 Hz to 4 kHz. This channel may also be used to detect the impacts of charged dust particles and infer their fluxes and charge distribution. Operated in the relaxation probe mode, the instrument will also provide a measurement of the atmospheric conductivity separately for positive and negative ions. Knowledge of the wind velocity, dust loading and specific weather phenomena (e.g. strong local vortices leading to dust devils) observed by the meteorological experiments will enable to investigate in depth the physics of charging mechanisms and the generation of electric fields. Double

probe electric field instruments have been flown on numerous balloon flights by members of our team, an initial version of ARES has been successfully validated on three balloon flights in 2004, 2005 and 2006. The mass of ARES is 120g and its average power consumption 200 mW.

**Instrument motivation:** A global atmospheric electrical circuit is likely to exist on Mars, between the surface and the ionosphere, with similarities and differences with the Earth's circuit. Atmospheric ionization should be similar to that of the Earth's stratosphere but impact charging through collisions between dust particles moved by the wind and the surface, or between dust particles themselves, is expected to be the dominant charging mechanism. Intense electric fields, possibly capable of producing electrical breakdown, are expected at the time of dust storms and in the vicinity of dust devils. Atmospheric electricity is also involved in several processes that have a noticeable impact on the surface and atmosphere. At times of dust storms, electrostatic forces on fine electrically charged dust grains may become larger than aerodynamic forces due to the wind. They are expected to play a significant role in the dynamics of suspended dust particles and their interaction with the surface, thus on the processes that contribute to the erosion and long term evolution of the surface. By energizing the free electrons, the atmospheric electric fields control their interaction with both the surface and the atmospheric gases. They have a thus a definite role in the chain of physical and chemical processes that govern the chemical state of surface materials and the production of oxidized constituents in the atmosphere with far reaching consequences on the sustainability of proper conditions for life.

The ELF and VLF electric fields measured by ARES will help in investigating electrical breakdown phenomena in the atmosphere and detect wave emissions from the distant ionized environment of Mars. By monitoring the charging of the lander, the ARES experiment will also provide engineering data of crucial importance to understand the electrical

charging of landed vehicles. In the extremely dry and tenuous Martian atmosphere landed vehicles can easily become electrified a situation that may jeopardize the safety and reliability of instruments or sub-systems operations in future Mars missions and, in particular, human flights.

**Instrument concept:** The very tight constraints imposed on the dimensions, mass and power of the instruments on Mars landers restrict the electric fields measurements to only one dimension, along the vertical direction. For obvious symmetry reasons, and as on Earth, the planetary large scale electric field of atmospheric origin is essentially vertical and this component is therefore of primary interest. The instrument makes use of the so called “double probe” technique to measure the vertical DC and AC electric fields. It relies on measuring the potential difference between two identical sensors that float at the local potential of the atmosphere. The high impedance of the sensors with respect to the external medium, due to the small conductivity of the atmosphere, makes it necessary to use high input impedance ( $> 10^{14} \Omega$ ), low leakage current ( $< 10^{-14} \text{ A}$ ) preamplifiers. Space qualified components with such performances are currently available. The electric conductivity is measured through the relaxation technique: the sensor potential is displaced from its normal level equal to the local floating potential and then let free to recover its equilibrium. The time constant  $\tau = \epsilon_0/\sigma$  readily provides the electric conductivity  $\sigma$  of the atmosphere. The double probe technique has been used on numerous balloon flights over more than 30 years and has provided a wealth of excellent and reliable data over a large range of altitudes, from a few kilometres to  $\sim 35 \text{ km}$ .

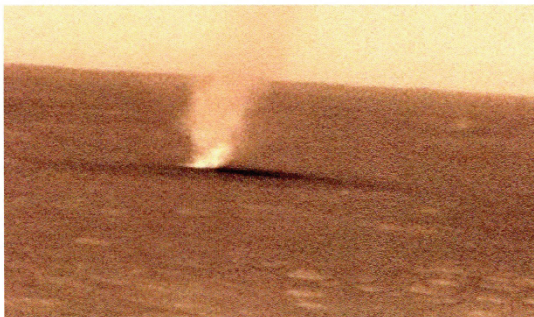


**Figure 1:** A dust devil seen on Mars by the Opportunity rover (credit: NASA).

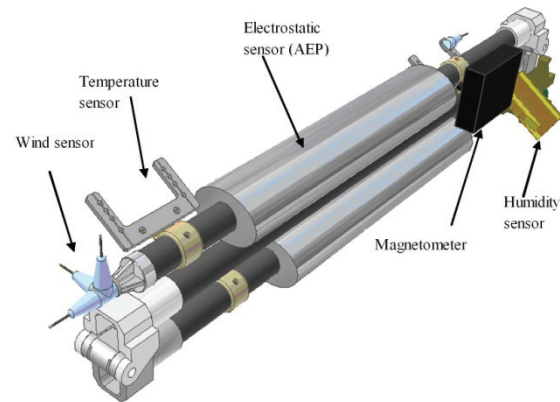


**Figure 2:** Mounting of ARES electrodes on a folded meteorological boom.

Electric fields from a few mV/m to several tens of V/m have been routinely measured as well as electric conductivities in the range  $10^{-13}$  to  $10^{-10} \text{ S/m}$  (see for example [1,2,3,4,5,6]).

**Measurement objectives:** The driving objectives of ARES measurements at Mars can be summarized into five main points.

*Characterizing the Mars global circuit.* On Mars, a global electric circuit is expected to exist due to the presence of the following elements:

- Dust devils and dust storms as generators
- A conductive ionosphere  $> 1 \text{ S/m}$  at 120 km altitude
- A slightly conductive atmosphere in quiet weather regions:  $10^{-11}$  to  $10^{-10} \text{ S/m}$  (ionization by UV, Cosmic rays, micro-meteorites)
- Ground conductivity ( $10^{-12}$  -  $10^{-7} \text{ S/m}$  - TBC) ARES will provide new insights into the properties of each of the circuit component.

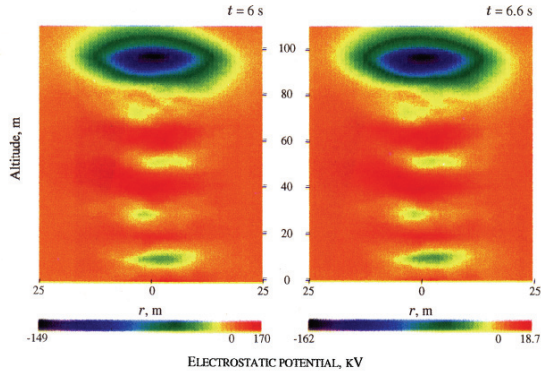


**Figure 3:** Figure extracted from [13] showing the simulated electric potential inside a Martian dust devil. Values close to breakdown can be noted.

Provides new insights into Mars dust cycle. Dust lifting and transport are driven by the following forces:

- Aerodynamic drag ( $F_D$ )
- Gravity
- Cohesion between particle
- ....and electric forces ( $F_E$ )

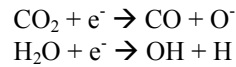
Simple computations indicate  $F_D \sim F_E$  []. Electric forces can concur with wind to enhance lifting, modulate wind influence on lifting, or can oppose/combine to wind motions.

The charging of dust particles and the associated electrostatic forces may play a key role in the dynamics of dust lifting and transport, and thus impact the entire Martian climate since the climate system is strongly controlled by the atmospheric dust cycle. Our current understanding of the mechanisms that control Martian global dust storms is poor. In particular, no models have succeeded to simulate the dust cycle and in particular its inter-annual variability. Most studies concluded that this is because of our poor understanding of the lifting (and near surface dust-dynamic processes) by the surface winds and dust devils [7,8,9].

However, there are more and more evidence that the charging of dust particles in the low atmosphere might be such that the electrical forces should play a

major role in lifting the dust and controlling its dynamics in the atmospheric surface layer. According to the traditional theories, the  $\sim 1$  micron-sized dust particles that constitute the bulk of the Martian aerosols cannot be easily lifted by the wind because of the strong cohesion forces that hold such small particles together on the surface. Larger particles are needed to dislodge the smaller particles... The strong upward electrical forces that could exist in dust devils (and dust storms) could explain how dust devils are so efficient to lift small particles directly [10]. This mechanism has been suggested to account for the near-perfect removal of the dust layer that had accumulated on the Mars Exploration Rover Spirit over 520 sols and was removed in just a few seconds by a dust-devil [N. Renno, private communication]. Through its effects on dust, atmospheric electricity could play a major role in Mars climate.

Provide new insights into Mars chemistry and habitability. Electrostatic fields energize free electrons and enhance the rate of chemical reactions:



According to models [11],  $\text{H}_2\text{O}_2$  production can be increased by a factor of 200.  $\text{H}_2\text{O}_2$  efficiently removes organic material, which constitutes a challenge for life development and maintenance at the surface of Mars. As such, electric fields might partly dictate Martian habitability conditions and may also participate to explaining the recently discovered spatial heterogeneity of Methane on Mars [12].

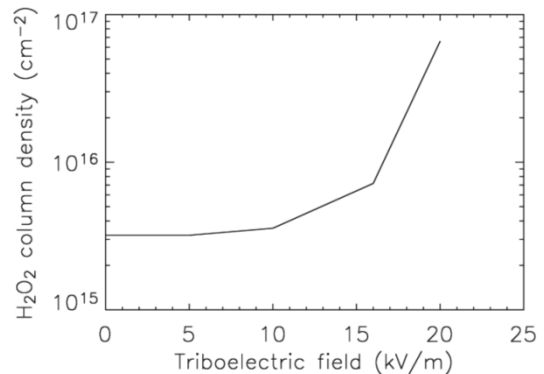


**Figure 4:** Figure extracted from [11] showing the expected rise of  $\text{H}_2\text{O}_2$  production under the conditions of increasing electric field.



*Characterize electromagnetic and cavity resonances.* Schumann resonances measurements give access to planetary scale electrical characteristics:

- Generators (lightning)
- Ionization state of atmosphere and ionosphere
- Surface conductivity

Several balloon test flights in Earth stratosphere have been performed in order to assess ARES performances in conditions close to those prevailing at Mars. The curves shown in the figure below indicate that Earth Schumann resonances can be readily detected, with prominent power spectrum peaks at 7, 14, 21, 28 Hz. Similar cavity phenomena should be observed at Mars with the expected occurrences of electrical breakdowns produced by the intense electrical fields of major dust storms.

*Evaluate electrostatic hazards.* Miscellaneous electrical phenomena related to hazards in future exploration can be assessed by monitoring Mars electric fields. These hazards can be listed non exhaustively as follows:

- HPL charging: On low conductivity ground as in Antarctica, grounding of vehicles and habitats is not obvious. In the case of Mars it is important to study the electrical potential of objects on the surface in various circumstances to take safety actions.

- Monitoring dust impacts: Dust impacts can damage hardware (solar cells) and they will induce electromagnetic noise that would disturb communications.
- Characterization of the EM background noise: It is necessary to study the ambient electromagnetic noise in various circumstances including dust storms to define reliable communication standards. Future subsurface exploration by electromagnetic methods such as ground penetrating radars requires a good knowledge of EM background and its daily, seasonal variations.

**References:** [1] Mozer, F.S. (1971) *Pure Appl. Geophys.*, 84, 32. [2] Berthelier, J.-J. et al. (1974) *SBARMO Bulletin*, 5, 4 [3]. Berthelier (2003) *EGS-AGU Meeting*, Nice, 7-11 April 2003. [4] Holzworth, R.H. and Bering, E.A. (1998) *AGU Monograph* 103. [5] Grad, R. et al. (1998) *Nature*, 607. [6] Berthelier, J.-J. et al. (2000) *Planet. Space Sci.*, 48, 1193-1200. [7] Newman, C. et al. (2002a) *J. Geophys. Res.*, 107, E10. [8] Newman, C. (2002b) *J. Geophys. Res.*, 107, E10. [9] Basu et al. (2004), *J. Geophys. Res.*, 109. [10] Kok and Renno, AGU, Fall Meeting 2005. [11] Atreya, S. (2006) *Astrobiology*. [12] Mumma, M. et al. (2009). [13] Melnik, O. and Parrot, M. (1998) *J. of Geophys. Res.*, 103, A12

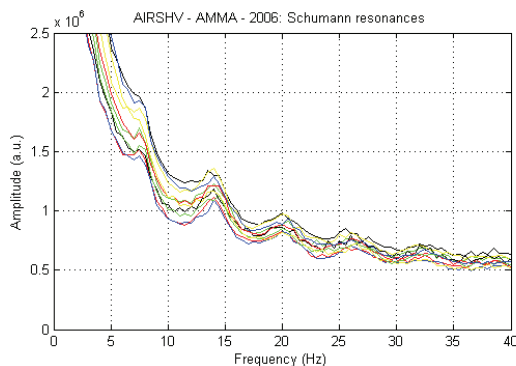


**Figure 5:** Power spectrum derived from ARES measurements during a balloon campaign in Earth stratosphere.



## VARIABLE OBLIQUITY AND LONGITUDE OF PERIHELION STUDIES WITH THE UKMGCM. Mulholland<sup>1</sup>, D. P., Read<sup>1</sup>, P. L. and Lewis<sup>2</sup>, S. R.

<sup>1</sup>Atmospheric, Oceanic & Planetary Physics, University of Oxford, Clarendon Laboratory, Parks Road, Oxford OX1 3PU, UK (mulholland@atm.ox.ac.uk, read@atm.ox.ac.uk)

<sup>2</sup>Department of Physics & Astronomy, The Open University, Walton Hall, Milton Keynes MK7 6AA, UK (s.r.lewis@open.ac.uk)

**Introduction:** The UK Mars General Circulation Model (UKMGCM) [1] is capable of simulating the either the dust cycle or water cycle, using parameterised lifting (by near-surface wind stress and by dust devils) and advection for the former [2], or with ice sublimation/condensation and subsurface diffusion for the latter [3]. Several experiments have been carried out using the model in its water-transporting form, applying various changes to Mars' orbital parameters intended to represent past climate scenarios. Atmospheric dust loading has been represented more precisely than in previous orbital-change studies (e.g. [4]).

**Obtaining appropriate dust opacities:** Changes in Martian obliquity or timing of perihelion are likely to induce changes in dust lifting patterns and produce global atmospheric opacities somewhat different to that observed today, affecting atmosphere and surface heating and thus altering the water cycle.

In order to represent this, results from a similar past-climate experiment performed using the dust-lifting UKMGCM [5] were used to derive annual visible dust opacity distributions as a function of latitude and season for each of the orbital scenarios studied (Fig. 1). These opacity fields (though involving considerable uncertainties) were then used in the water-transporting experiments as the prescribed field that the radiation code 'sees', as opposed to the present-day distribution typically used (which has a peak visible opacity of 0.5 in southern summer).

An increase in obliquity leads to greater lifting and more dust storms (particularly near perihelion), whereas a low obliquity climate sees reduced dust lifting and lower opacities. Predicted dust opacity for a 'reversed perihelion' climate (with perihelion occurring instead during northern summer) is not simply a mirror-image of the present-day distribution, for reasons thought to arise from Mars' topographic asymmetry.

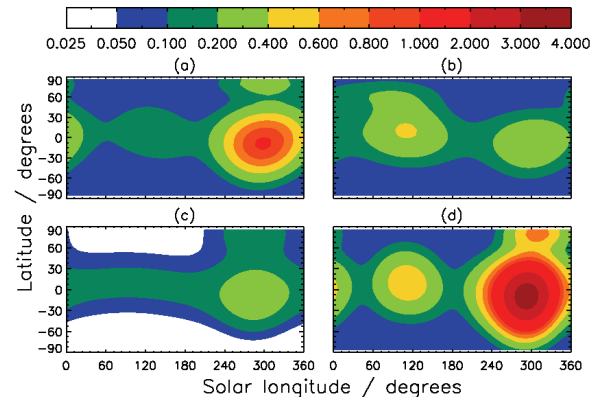


**Figure 1:** UKMGCM-derived visible opacities (referenced to a 610 Pa level) for (a) present-day, (b) perihelion switched to  $L_s = 71^\circ$ , (c)  $15^\circ$  obliquity, (d)  $35^\circ$  obliquity.

**Water cycle experiments:** Simulations were carried out using the water-transporting UKMGCM, run at a horizontal resolution of  $7.5^\circ$  by  $7.5^\circ$ , with 25 vertical levels extending to a height of  $\sim 100$  km. The modelled water cycle incorporates sublimation of surface ice, vapour advection in the atmosphere, a bulk ice cloud scheme, deposition of ice onto the surface and exchange of water between the atmosphere and subsurface regolith. The regolith extends to depths of a few metres, and allows water to exist either as vapour, adsorbate or ice. Cloud ice currently does not contribute to the atmospheric opacity.

**Reversed perihelion.** The switch to a dust loading appropriate for the reversed perihelion scenario benefits net annual north-south transport, as the more uniform opacity distribution allows the stronger perihelion circulation to dominate (by means of greater insolation) over the reverse transport at aphelion. Reduced atmospheric heating at aphelion limits cloud condensation height to 20 km or less, inhibiting cross-equatorial transport via the Clancy effect [6] (Fig. 2). The distinction between the two

summer seasons is, however, not as strong as it is in current orbital conditions, due to the lack of a significant perihelion peak in opacity in this case.

Southern polar cap accumulation is actually prevented with this particular opacity distribution due to the low ( $< 0.1$ ) visible opacity predicted over the south pole during summer, which causes surface temperatures to reach 230 K and prevents perennial ice deposits forming. A relatively dust-free south polar region should, however, imply higher albedo ice deposits (due to a lower dust/ice fraction), which stand a better chance of accumulating year-on-year. Alternatively the model may be underestimating dust amounts at the southern summer pole – only a small increase in opacity is required to allow the cap to accumulate year-on-year. It should also be noted that the UKMGCM does not predict a perennial south-polar  $\text{CO}_2$  cap under present-day conditions.

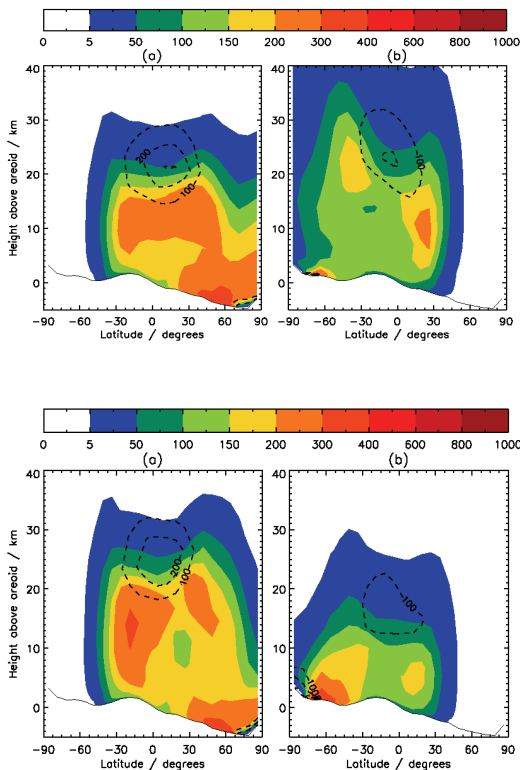


**Figure 2:** Top: Water vapour (coloured contours, in  $10^{-6}$  kg/kg) and ice cloud (dotted contours, same units) abundances at (a) perihelion and (b) aphelion, using a present-day dust loading. Bottom: The same using the opacity function derived for a reversed-perihelion climate.

*Increased obliquity.* The biggest increase in dust loading at  $35^\circ$  obliquity over the present-day occurs near perihelion, heating the atmosphere, strengthening the Hadley circulation and raising the saturation level (above 50 km in this simulation). Northward cross-equatorial transport is aided by this, resulting in an increase in vapour levels at northern mid-latitudes during the northern winter season (Fig. 3). A double-peaked southern hemisphere vapour maximum develops, with the second peak formed by regolith desorption due to higher south polar surface temperature allowed by this opacity function. Subsurface ice formation is promoted by the use of a larger dust loading due to the cooler daily mean surface temperatures that result. Perennial deposits are seen to form at the north pole, and in northern low-latitudes in regions of low thermal inertia.

*Low obliquity.* The low ( $15^\circ$ ) obliquity case was also considered, though atmospheric humidity proved harder to predict due to the strong dependence on initial regolith water content. Net south-north transport (favoured annually both by the topographic asymmetry and by the Clancy effect) is, however, inhibited (relatively) by the use of a climate-appropriate dust opacity, as the decreased atmospheric heating lowers cloud condensation levels by  $\sim 5$  km.

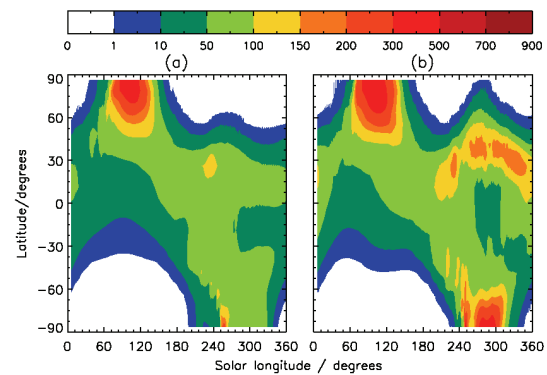


**Figure 3:** The vapour cycle at  $35^\circ$  obliquity (in  $\mu\text{m}$ ), using a present-day dust loading (a) and that predicted for these orbital parameters (b).

**Future improvements:** Several additions to the UKMGCM code, which will enable better representation of past (and present) climates, are planned. The first of these concern improving the accuracy of the water cycle through the inclusion of a radiative feedback scheme for water ice clouds, and a cloud microphysical scheme [7] to allow for particle size variation (currently ice particles are fixed at 2 $\mu$ m in radius). Modifications to the regolith scheme, such as allowing variation in soil thermal inertia where subsurface ice has formed, are also possible.

Simultaneous transport of dust and water will soon be possible, and some parameterisation of the interactions between the two cycles is a planned addition. These will take the form of an enhancement in cloud formation by the presence of dust particles (acting as condensation nuclei), and the subsequent change in radiative properties and accelerated removal from the atmosphere of the dust particles due to their encasement in ice. Such 'scavenging' interactions are thought to be an important missing component in the modelling of Mars' dust and water cycles.

**References:** [1] Forget, F. et al. (1999) *JGR*, E10, 24155-24176. [2] Newman C. E. et al. (2002) *JGR*, 107, 5123-+. [3] Böttger H. M. et al. (2005) *Icarus*, 177, 174-189. [4] Montmessin F. et al. (2007) *JGR* 112, 8-+. [5] Newman C. E. et al. (2005) *Icarus*, 174, 135-160. [6] Clancy R. T. et al. (1996) *Icarus*, 122, 36-62. [7] Montmessin, F. et al. (2002) *JGR*, 107, 5037-+.

**REGIONALITY OF DUST STORM EXPANSION.** Ogohara, K<sup>1</sup>. and T. Satomura<sup>1</sup>, <sup>1</sup>Earth and Planetary Sciences Division, Graduate School of Science, Kyoto University (Oiwake, Kitashirakawa, Sakyo, Kyoto, Japan. ogohara@kugi.kyoto-u.ac.jp).

**Introduction:** Many local dust storms occur in several regions on Mars. For example, local dust storms tend to occur in and around Noachis Planitia, the eastern Arcadia Planitia and Erysius Mons [1]. On the other hand, the number of regional dust storms is much less than that of local dust storms. [1] counted the number of local dust storms of various sizes. As a result, they found that the relation between the number and the size of local dust storms follows certain power law and concluded that dust storms develop by merging. However, according to their study, regions where many local dust storms occurred do not correspond to the locations where regional dust storms were observed. If merging was a dominant process of development of dust storms, regional dust storms should tend to occur around areas where many local dust storms occur. Therefore, this fact implies the existence of favorable and unfavorable regions for dust storms expansion on Mars. In this study, we show by GCM simulations where favorable regions for dust storm expansion are.

**Strategy:** We inject radiatively active dust into the atmosphere artificially from many dust sources located all over the planet and compare area of regions where dust injected from different dust sources is transported by modeled wind. This method is the most straightforward and useful. We can obtain global maps which show where favorable regions (FRs) on Mars are.

**Model:** Although our model is based on the spectral model used by [2], time integration scheme of dust mixing ratio has been modified. If dust mixing ratio was integrated by spectral method, circular errors is always generated in dust mixing ratio around a localized dust because of Gibbs phenomenon. In order to avoid this unrealistic dust transport,  $p_s q$  is integrated by finite difference scheme following,

$$\frac{\partial p_s q}{\partial t} = -\frac{1}{a(1-\mu^2)} \frac{\partial(p_s q U)}{\partial \lambda} - \frac{1}{a} \frac{\partial(p_s q V)}{\partial \mu}$$

$$\frac{\partial(p_s q \dot{\sigma})}{\partial \sigma} + S_{phys} + S_{source}$$

$q$  is obtained by dividing  $p_s q$  by  $p_s$ . 2<sup>nd</sup> order Van Leer scheme ([3]) is often used as an advection scheme for dust transport. However, we used 1D Cell-integrated Semi-Lagrangian scheme (hereafter 1D CISL) used by [4]. Grid configuration around the northern and southern poles is following [5,6].

In this study, season in the model is the northern fall (Ls=180 deg), the season when the global dust storm occurred in 2001. Resolution is T42L32 in the atmosphere and the number of layers in the ground is 21. A spin-up run is performed for one Mars year from Ls=180 deg. The one year spin-up run started from an isothermal (220 K) condition with constant surface pressure (7 hPa) and no wind over the entire planet.

CO<sub>2</sub> condensation and sublimation modify the surface wind around the edges of polar caps and possibly affect expansion of dust storms near polar caps. We derived the changing rate of the surface pressure due to CO<sub>2</sub> phase-change from CO<sub>2</sub> ice layer data on Mars Climate Database (<http://johnson.lmd.jussieu.fr:8080/las/servlets/dataset>). We introduced the surface pressure changing rate into the GCM as an external forcing on the surface pressure.

**Experiment description:** A global distribution of 576 dust sources is shown in Figure 1. Black dots indicate the locations of the centers of the dust sources. Dust is injected from sources whose centers are located on the black dots for 1 sol at the injection rate of  $2.0 \times 10^5 \text{ kg s}^{-1}$ . The thickness of a dust source equals to that of the mixing layer and the constant dust mixing ratio is added in the mixing layer inside the dust source ([7]). The horizontal structure of a dust source is given by,

$$S_{source} = p_s \left[ \frac{s_0}{2} \left\{ 1 + \cos\left(\frac{\pi r}{r_0}\right) \right\} \right]^{0.6} \quad (0 \leq r \leq r_0)$$

$p_s$ ,  $r$ ,  $r_0$  are the surface pressure, the large circle distance from the center of the source and the radius of the dust source, 667 km.  $s_0$  is a constant determined in the model so that injection rate of dust from a dust source is  $2.0 \times 10^5 \text{ kg s}^{-1}$ . A schematic

view of the structure of a dust source is shown in Figure 2.

**Results:** Figure 3 shows FRs in the northern fall equinox. Colored boxes indicate locations of dust sources shown in Figure 1. A box's color shows the maximum area of the region obscured by dust injected from the dust source for 1 or 2 sols after the end of dust injection. Note that it does not indicate the column mass of injected dust inside the colored box.

FRs founded in Figure 3 are 1) Acidalia Planitia, 2) Arabia Terra, 3) the east of Erysius Mons, 4) the eastern Tharsis and 5) Sirenum—Aonia region. In these regions, regional dust storms were observed between  $L_s=160$  and  $L_s=200$  as reported by [1].

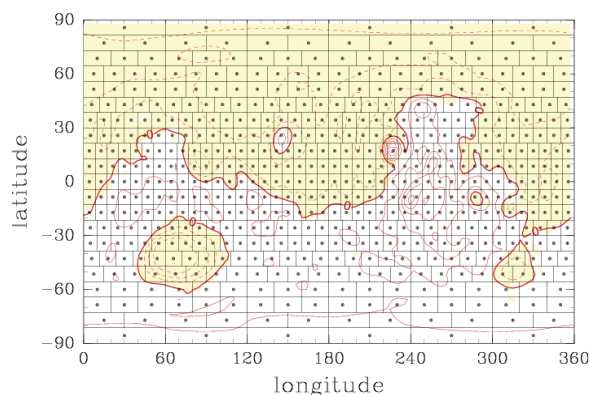


**Figure 1:** A global distribution of dust sources. The total number of the dust source is 576. Black dots indicate locations of the centers of the dust source. Red contours indicate topography and contour interval is 2000 m. Solid lines indicate positive altitudes and dashed negative altitudes.

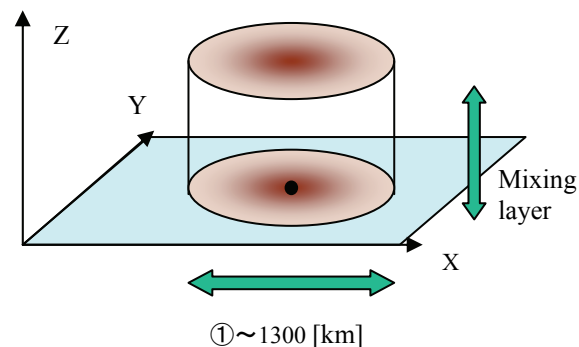


**Figure 2.** A schematic view of the structure of a dust source.

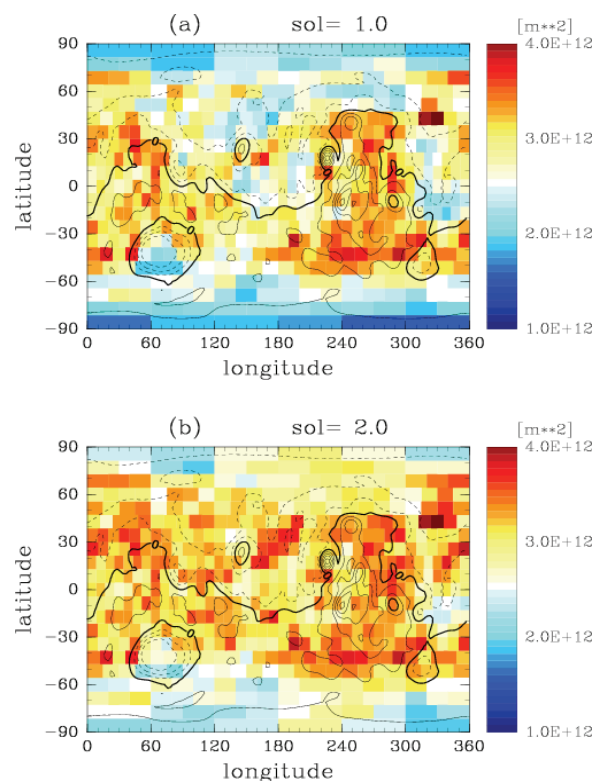


**Figure 3:** Global maps which shows locations of FRs in the northern fall. Colors shows the maximum area of the region obscured by dust injected from the dust source for 1 (a) or 2 (b) sols after the end of dust injection. Therefore, red regions correspond to FRs. Contours indicate topography and contour interval is 2000 m.

**Future works:** Our result is the first suggestion that expansion potential of dust storms varies considerably from one region to another. It leads to an understanding of mechanisms of dust storm expansion to reveal the reason why dust tends to spread extensively around FRs. We have to analyze the model output precisely and investigate expansion processes of injected dust around each FR.

**References:** [1] Cantor et al. (2001) *JGR*, 106, E10, 23,653–23,683. [2] Ogohara, K and T. Satomura (2008) *GRL*, 35, L13201, doi:10.1029/2008GL034546. [3] Van Leer, B. (1977) *J. Comp. Phys.*, 23, 276–299. [4] Nair, R. D. and B. Machenhauer (2002) *Mon. Wea. Rev.*, 130, 649–667. [5] Allen, D. J. (1991) *Mon. Wea. Rev.*, 119, 2,456–2,464. [6] Lin et al. (1994) *Mon. Wea. Rev.*, 122, 1,575–1,593. [7] Takemura et al. (2000) *JGR*, 105, D14, 17,853–17,873.

**VERTICAL PARTICLE SIZE VARIATIONS: THE TES DATASET.** Wolff, M. J., Clancy, R. T., Smith, M. D., and McConnochie, T.

**POSTER PRESENTER:** Wolff, M. J., Space Science Institute, Boulder, CO.

---

Dust aerosol heating rates and scattering properties are generally quite sensitive to the microphysical nature of the aerosols themselves. This fact strongly suggests that accurate dynamical models of the Martian atmosphere and limb-based remote sensing retrievals need to explicitly consider the variation of microphysical properties (such as particle-size) with altitude. Although some initial work has been done in this area, a set of systematic, planet-wide retrievals of particle size (as a function of altitude) across multiple seasons remains to be carried out. The TES spectral database is a natural dataset with which to begin: the IR wavelengths allow one to use simple particle shapes (i.e., a sphere or oblate disk), systematic sampling in both space and time is available, a fast, fully spherical code is available (which we have developed specifically for this purpose). We present initial results of our retrievals of vertical profiles of particle sizes. In addition, we also briefly present some validation calculations which compare our code with a 3D monte carlo algorithm as well as with the ubiquitous spherical-path-plane-parallel-source-function (SPPPSF) approach.





**Session Four**  
*Lifting Overviews and  
Laboratory Studies*

*Wednesday, September 16, 2009*

*8:30 AM – 10:00 AM*



**DUST ENTRAINMENT ON EARTH AND MARS.** Gillies<sup>1</sup>, J.A., Etyemezian, V.<sup>2</sup>, and Nikolich<sup>2</sup>, G, Division of Atmospheric Sciences, Desert Research Institute 2215 Raggio Parkway, Reno<sup>1</sup> and 775 E. Flamingo, Las Vegas<sup>2</sup>, NV USA (jackg@dri.edu, vic@dri.edu, george.nikolich@dri.edu).

Aeolian sediment entrainment and transport processes play an important role in the evolution of the Martian landscape. The most dramatic demonstration of aeolian activity on Mars is the planet-wide dust storm [1, 2, 3], although dust storms on the scale of  $10^2 \text{ km}^2$  to  $10^6 \text{ km}^2$  are more frequent. Data presented by Martin and Zurek [2] and more recently by Cantor et al. [4] indicate dust storms are a common occurrence on Mars, yet the mechanism that is responsible for dust entrainment and dust storm generation remains a poorly understood phenomenon [5]. Haberle et al. [6] have suggested that dust devils may also play a critical role in the dust-cycle of Mars. This short review paper is intended to provide a brief recounting of the particle entrainment literature with a focus on current understanding of the flow processes and surface characteristics that influence this critical component of the dust cycle.

Research to explain the physics of sediment transport by wind on Mars was presented in a series of landmark papers beginning with the work of Sagan and Pollack [7] and Hess [8]. Following on from this work, the laboratory simulations of Martian conditions in a specialized low pressure wind tunnel by Greeley et al. [9, 10], Iversen et al. [11] and Iversen and White [12] resulted in a more comprehensive understanding of the controls on particle entrainment by the fluid drag forces exerted by wind and retarding effects of inter-particle forces. This work produced threshold curves that relate the minimum wind shear velocity ( $u_*$ ,  $\text{m s}^{-1}$ ) needed to raise particles of different sizes from the Martian surface. Shear velocity is proportional to the shear stress ( $\tau_0$  [ $\text{N m}^{-2}$ ])= $\rho_a u_*^2$  [ $\text{m s}^{-1}$ ], where  $\rho_a$  is atmospheric density [ $\text{kg m}^{-3}$ ] imposed on the surface by the turbulent atmospheric boundary layer, which is critically influenced by the surface roughness. Gravity and inter-particle forces also influence the threshold of entrainment. The particle threshold curves for Mars derived by Greeley et al. [11] are based on wind shear stress exerted by boundary layer winds over relatively uniform and aerodynamically smooth surfaces. As demonstrated by Gillies et al. [13] shear stress partitioning effects, which occur in the presence of larger roughness elements will critically affect particle entrainment thresholds on Mars and complicate the threshold curves that have been published for smooth surfaces.

In addition to recognizing that roughness critically influences particle entrainment threshold, which can effectively be modeled for, recently Lu et al. [14] have probed more deeply into the fundamental control on particle threshold imposed by fluid flow properties and particle Reynolds number effects. According to Lu et al. [14], the long-standing basis of the theory of entrainment of sedimentary particles is that the dimensionless threshold shear velocity (Shields'  $A$ ) has a universal relationship with the particle Reynolds number.  $A$  is defined here as:

$$A = \rho_f u_{*t}^2 / ((\rho_p - \rho_f) g d) \quad (1)$$

and particle Reynolds number as:

$$\text{Re}_{*t} = u_{*t} d / \nu \quad (2)$$

where  $\rho_p$  is particle density,  $g$  is gravitational acceleration,  $d$  is particle diameter and  $\nu$  is kinematic viscosity. This has provided a powerful framework to understand particle thresholds. Experimental results from water and air, however, show that the theory fails to collapse available data into one universal function (Fig. 1).

Two major differences have been documented for air and water systems: 1) for large  $\text{Re}_{*t}$ , the values of  $A$  in water are, in general, a few times larger than those

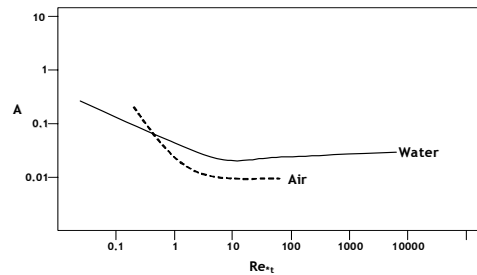


**Figure 1.** The relationship between the dimensionless threshold parameter  $A$  and particle Reynolds number for water and air.

observed in air, and 2) when  $Re_{*t}$  is  $<1$ ,  $A$  increases more rapidly in air than in water as  $Re_{*t}$  decreases. Lu et al. [14] have suggested these differences can be explained 1) by differences in the probability distribution of stream-wise velocity fluctuations for air and water, which follow from basic scaling laws in turbulent flow, and 2) by the different behaviors in inter-particle cohesion forces in air and water. Their new general expression for  $A$  has the formulation:

$$A = f_p F_1(Re_{*t}) F_2(Re_{*t}, Re_{*r}) G(d) \quad (1)$$

where  $f_p$  represents a particle packing function geometry,  $F_1(Re_{*t})$  represents the mean velocity profile effect,  $F_2(Re_{*t}, Re_{*r})$  the interaction between the mean velocity profile, turbulent fluctuations and particle removal probability, and inter-particle cohesion,  $G(d)$ . A critical component of this expression is the inclusion of the flow Reynolds number ( $Re_{*r}$ ) term, which Lu et al. [14] proposed for the first time. Therefore in their theory,  $A$  depends on the flow condition, which is a function of the fluid viscosity as well as the density ratio and particle size. This new formulation for  $A$  suggests that previously overlooked flow effects may be critical to evaluate the relationship between particle size and threshold conditions. To examine this phenomenon in this new framework will require paying attention to the flow regime (i.e., smooth, transitional or fully rough as defined by  $Re_{*r}$ ) as well as turbulence effects due to viscous properties of the atmosphere and boundary layer height ( $Re_{*r}$ ). Evaluating  $f_p$  and  $G(d)$  effects also remains a research challenge.

Much of the research on particle thresholds for Mars has focused on sand-sized particles with more limited research efforts on dust-sized particles. Contributions to dust entrainment knowledge for Martian conditions include Greeley et al. [15], Greeley [16], and Toigo et al. [17]. This work demonstrated that dust suspension from smooth surfaces may be difficult unless a critical amount of larger-scale roughness is present that essentially promotes erosion [18, 19]. A body of evidence is building however, that on Earth dust can be raised in the absence of saltation by purely fluid drag forces in opposition to earlier studies [20]. Direct entrainment of dust has been observed at wind speeds below the thresholds for sand-sized particle movement within wind tunnels [21, 22, 23] and in certain terrestrial locations such as the Columbia Plateau in Washington [24], which produces, on occasion, quite high concentrations of dust less than 10  $\mu m$  (aerodynamic) in diameter. This is an area of research that deserves more attention as observations from

Mars suggest that dust events are observed to be more frequent than aeolian transport events that involve the movement of sand.

Some research suggests that the ballistic impact model for dust emissions [25, 26], which requires that the threshold for sand-sized particles has been exceeded for dust emissions to occur, can be invoked on Mars. However, the critical assumption is that on Mars the sand-sized particles are low bulk density aggregates composed of  $<4 \mu m$  size dust grains [16, 27], which require much lower threshold shear stress for entrainment than higher density solid mineral grains. It is suggested that these dust aggregate particles break up following entrainment releasing micrometer-sized dust into the atmosphere.

Terrestrial studies will continue to be critical for advancing our knowledge of how particles become entrained by wind on Mars. Based on ideas presented in Lu et al. [14], however, terrestrial-based research to study particle threshold using devices such as wind tunnels [15, 27] or the PI-SWRL instrument developed by Etyemezian et al. [22] will need to consider having the ability to control atmospheric viscosity as well as density and pressure to evaluate threshold relationships under simulated Martian conditions.

Besides the flow environment, particle threshold is also influenced by surface characteristics such as the large and small scale roughness, and crusting. The effect of small scale roughness on entrainment has been observed to be complex, but generally increasing shear stress increases dust emissions regardless of roughness, but describing how small scale roughness itself affects the process is not well understood. The effect of large scale roughness on shear stress partitioning effects and by extension threshold and transport of aeolian sediments has been better characterized [13, 28, 29]. In general, on Mars higher regional shear stresses are required to initiate particle entrainment for surfaces that have the same physical roughness as defined by the roughness density term ( $\lambda$ ) compared with terrestrial surfaces mainly due to the low Martian atmospheric density. The role of crusting in constraining dust emissions is well-known, crusted soils are harder to erode than non-crusted or disturbed soil surfaces. Gordon and McKenna Neuman [30] have examined the absorption of momentum by saltating particles impacting loose and consolidated surfaces and found that loose beds absorb more momentum than crusted surfaces, and as a result have the potential for higher dust emissions. Research has still not identified which strength

parameter provides the means to characterize the relationship between binding energy, saltation energy, and dust emission.

Environmental conditions on Mars may also have a significant effect on particle entrainment thresholds, for example, its radiative environment, which may affect this system via charging of the dust-sized particles. In the absence of saltation, which creates charging by triboelectric processes, photoelectric charging [31, 32, 33, 34] may affect the susceptibility of particles to entrainment by the wind. In photoelectric charging, ultraviolet photons eject electrons from the surface of an isolated grain, giving it a positive charge [35]. Ground-based tests with Martian regolith simulant indicate that charging by photoemission is likely small compared to triboelectricity, but these results should be viewed with caution owing to the possible differences between the stimulant and the Martian regolith. On Mars there is a lack of a global electrical ground that would allow for the build up of localized potential differences in charge. Due to its low pressure, the atmosphere on Mars ionizes more easily, which dissipates electrical charges at a lower voltage. This “Paschen effect” [36] mitigates substantially large gradients in space charge compared to those that are possible on Earth. Nevertheless, electrical forces may be substantial and the effect that a lack of earth ground has on particle entrainment threshold has not been evaluated.

Many challenges remain to understanding dust entrainment processes on Earth and Mars. The way forward lies in a combined effort by theoreticians and empiricists with much to be gained from studies that use wind tunnels or similar devices. Experiments can be undertaken with available instrumentation to test the universal particle threshold model of Lu et al. [14], which can help to elucidate and define the magnitude of the secondary flow effects they describe. Evidence suggests in some cases thresholds can be affected by as much as 30% [37, 38] on Earth. How these effects modify particle thresholds on Mars remains to be determined. Additional research is also needed to evaluate the effects of particle cohesion and packing on entrainment processes. Based on new Mars Rover images [39] the creation of sand-sized dust particles of low bulk density that can be entrained at much lower shear stress than their solid mineral grain equivalents offers a complimentary explanation as to how dust can be cycled from the surface to the atmosphere of Mars. This could work in conjunction with direct fluid entrainment of dust-sized particles. The formation process of the low density dust aggregates on Mars is currently

unknown and the evaluation of the relative roles for direct fluid entrainment of dust and saltation-derived dust requires that a concerted research effort be focused on the dust lifting phase of the Mars dust cycle.

**References:** [1] Gierasch, P.J. (1974) *Review of Geophysics and Space Science* 12, 730-734. [2] Martin, L.J. and Zurek, R.W. (1993) *JGR* 98, 3221-3246. [3] Cantor, B.A., et al., (2001) *JGR* 106, 23,653-23,688. [4] Cantor, B.A. (2007) *Icarus* 186, 60-96. [5] Fenton, L.K., et al. (2007) *Nature* 446, doi:10.1038/nature05718. [6] Haberle, R.M., et al. (2006) *GRL* 33, L19S04, doi:10.1029/2006GL026188. [7] Sagan, C., and Pollack, J. (1969) *Nature* 233, 791-794. [8] Hess, S.L. (1973) *P&SS* 21, 549-1557. [9] Greeley, R., et al. (1976) *GRL* 3, 417-420. [10] Greeley, R., et al. (1980) *GRL* 7, 121-124. [11] Iversen, J.D., et al. (1976) *Icarus* 29, 381-393. [12] Iversen, J.D., and White, B.R. (1982) *Sedimentology* 29, 111-119. [13] Gillies, J.A., et al. (2009) *Geomorphology* 10.1016/j.geomorph.2009.02.016. [14] Lu, H., et al. (2005) *JGR-A* 110, doi:10.1029/2005JD006418. [15] Greeley, R., et al. (2000) *Planetary and Space Science* 48, 1349-1355. [16] Greeley, R. (2002) *Planetary and Space Science* 50, 151-155. [17] Toigo, A.D., et al. (2002) *JGR* 107, doi: 10.1029/2001JE001592. [18] Logie, M. (1981) *ESP&L* 6, 365-374. [19] Logie, M. (1982) *Catena Supplement 1*, 161-173. [20] Bagnold, R.A. (1941) *The Physics of Blown Sand and Desert Dunes*, Chapman and Hall, London. [21] Loosemore, G.A., and Hunt, J.R. (2000) *JGR* 105, 20,663-20,671. [22] Etyemezian, V., et al. (2007) *AE* 41, 3789-3796. [23] Macpherson, T., et al. (2008) *JGR-ES* 113, F02S06, doi:10.1029/2007JF000790. [24] Kjelgaard, J.F., et al. (2004) *ESP&L* 29, 221-236, doi: 10.1002/esp.1028. [25] Gomes, L., et al. (1990) *JGR* 95, 13,927-13,935. [26] Shao, Y. (2000) *Physics and Modelling of Wind Erosion*, Kluwer Academic Publishers, Dordrecht. [27] Merrison, J., et al. (2007) *Icarus* 191, 568-580. [28] Gillies, J.A., et al. (2006) *JGR-ES* 111, doi:10.1029/2005JF000434. [29] Gillies, J. A., et al. (2007) *B.-L. Meteorol.* 122, 367-396. [30] Gordon, M., and McKenna Neuman, C. (submitted) *JGR-ES*. [31] Sickafoose, A.A., et al. (2000) *JGR* 106, 8,343-8,356. [32] Sickafoose, A.A., et al. (2001), *PRL* 84, 6,034-6,037. [33] Krauss, C.E., et al. (2003) *New Journal of Physics* 5, 70. [34] Michael, M., et al. (2008) *JGR-P* 113 E7, E07010, doi:10.1029/2007JE003047. [35] Cross, J. A. (1987) *Electrostatics Principles, Problems and Applications*, Adam Hilger, Bristol. [36] Leach, R.N. (1991) NASA Conference Publication 10074, Tempe, AZ, pp. 53. [37] McKenna Neuman, C. (2003) *B.-L. Meteorol.* 108, 61-89. [38] McKenna Neuman, C. (2004) *Sedimentology* 51, 1-17. [39] Sullivan, R., et al. (2009) Mars Dust Cycle Workshop, 15-17 September, 2009, NASA Ames Research Center, Moffett Field, CA, pp. 21.

---

**DUST DEVILS IN THE LABORATORY: ESTIMATING ATMOSPHERIC DUST CONTRIBUTIONS.** Neakrase<sup>1,2</sup>, L.D.V., and Greeley<sup>1</sup>, R. <sup>1</sup>School of Earth and Space Exploration, Arizona State University, Box 871404, Tempe, AZ 85287-1404, <sup>2</sup>Department of Astronomy, New Mexico State University, P.O. Box 30001, MSC 4500, Las Cruces, NM 88003-8001. lneakras@nmsu.edu

---

**Introduction:** Atmospheric dust due to dust devils is one of the least understood processes within the martian dust cycle with respect to bulk amounts, diurnal and seasonal variability, and regional differences. Recent laboratory work involved sediment fluxes for lab-scaled dust devils using the *Arizona State University Vortex Generator* (ASUVG) [1,2,3]. Sediment flux measurements were conducted using dust ( $< 63 \mu\text{m}$ ) and ranges of sand ( $\sim 90$  to  $2000 \mu\text{m}$ ) with densities ( $1300$  to  $4800 \text{ kg m}^{-3}$ ) at Earth-ambient ( $\sim 1000 \text{ mbar}$ ) and Mars-analog ( $\sim 10 \text{ mbar}$ ) atmospheric conditions. At Mars-analog conditions, vortex strength denoted by the magnitude of the core pressure excursion ( $\Delta P$ ), is stronger than natural cases by a factor of  $\sim 2$  to  $8$  times due to mechanical efficiencies of the ASUVG at low pressure [2]. Resulting fluxes were scaled to natural strength dust devils for Mars by comparing the laboratory  $\Delta P$  to measured/inferred values from *Mars Pathfinder* (MPF) [4], and the *Viking* landers [5]. Flux was represented as a function of  $\Delta P$  that could be applied to natural distributions of dust devils on Mars to yield estimates of atmospheric dust contributions [2]. Dust flux estimates for Gusev Crater and Amazonis Planitia yield high values ( $\sim 1$  to  $43 \text{ kg km}^{-2} \text{ sol}^{-1}$ ), whereas regions like Chryse or Utopia Planitia are much lower ( $\sim 0.01$  to  $0.22 \text{ kg km}^{-2} \text{ sol}^{-1}$ ) depending on average sizes, duration of the activity, and surface roughness effects.

**Laboratory Sediment Fluxes:** The ASUVG is an apparatus that was constructed to simulate dust devils in the laboratory. The machine consists of a open cylinder that houses the fan and motor assembly that propagates a vortex down to the  $2.5 \text{ m}$  by  $2.5 \text{ m}$  test surface [6,1,2]. An array of pressure transducers were mounted beneath the test surface to measure pressure excursions at the surface, by which tangential velocities and core radii could be determined employing cyclostrophic balance and a Lamb-Oseen vortex curve fit. Sediment fluxes ( $Q$ ) were determined by measuring mass loss ( $\Delta m$ ) as a function of time ( $\Delta t$ ) through the associated cross-sectional area ( $A_c$ ) parallel to the test surface for the vortex. Flux could then be calculated as  $\Delta m / \Delta t / A_c$  for the range of sediments listed above. Both terrestrial ambient and Mars-analog conditions were used to

construct sediment flux curves for each environment. The resulting fluxes for bulk sediments (all sizes) were plotted against the ratio of lifting parameters ( $\Delta P / u_\theta$ ), where  $\Delta P$  is the maximum change in pressure in the core, and  $u_\theta$  is the maximum tangential velocity.

The resulting trends provide a parameterization of sediment flux from the laboratory, showing a clear dependence of sediment flux on the strength of the vortex [2]. The trends showed for Mars-analog conditions, the sediment flux ( $Q$ ) was proportional to the core pressure excursion ( $\Delta P$ )<sup>3</sup> in Fig.1 or the lifting parameter ( $\Delta P / u_\theta$ )<sup>4</sup> in Fig.2, which provides a means for estimating natural dust devil fluxes when scaled to natural strengths [2]. Mars-analog dust devil vortices were run at  $\Delta P \approx 1.5\text{-}5.0\%$  of ambient pressure due to the mechanical creation of the vortex at low atmospheric pressure. The laboratory fluxes can be assumed to be up to  $\sim 4$  times greater than their natural counterparts. Low-density walnut shells ( $\rho = 1500 \text{ kg m}^{-3}$ ) were used to account for the differences in gravity between Earth and Mars. Therefore, the mass loss in the sediment flux calculations should be rescaled by a factor of  $\sim 2$  to interpret lab results appropriately for silicate densities ( $\rho = 2500 - 3200 \text{ kg m}^{-3}$ ). Another factor controlling dust devil sediment flux could be surface roughness effects as presented in [3,7]. Small variations in roughness could possibly enhance sediment lifting potential by up to  $20\%$ .

**Approach:** Using the laboratory sediment flux trends presented in [2,3,7], sediment fluxes for natural distributions of dust devils on Mars can be estimated for populations where flux measurements have not been made. Dust devil dust atmospheric dust contributions were estimated by:

$$\Phi_d = \frac{NQ A_c \Delta t}{A_t} \quad (1)$$

where  $N$  is the number of dust devils per sol,  $Q$  is the average sediment flux,  $A_c$  is the lateral cross-sectional area of the vortex core,  $\Delta t$  is the duration of the dust devil, and  $A_t$  is the total area of the distribution. Dust

devil frequency information is available for Gusev crater (MER-A *Spirit*) [8], Ares Vallis (MPF) [4,9], Chryse Planitia (VL1) [10], Utopia Planitia (VL2) [5], and Amazonis Planitia [11,12]. By substituting the lab values for flux, an estimation of the mass removed from the surface and therefore injected into the atmosphere could be made for any distribution of martian dust devils.

**Results:** Estimations of dust devil dust fluxes for Mars were made for each of the sites listed above (Table 1). Gusev crater and Amazonis Planitia had the largest frequencies of dust devils compared to the other sites. Therefore these locales were estimated having larger amounts of dust injected into the atmosphere. The laboratory estimates show for the ~50 dust devils per square kilometer per sol at Gusev, dust fluxes were in the range of 3 to 29 kg km<sup>-2</sup> sol<sup>-1</sup>. For the 1.9 – 190 dust devils km<sup>-2</sup> sol<sup>-1</sup> at Amazonis accounting for possible smaller dust devils below the limit of resolution of the imager, the fluxes could be estimated at 3 to 43 kg km<sup>-2</sup> sol<sup>-1</sup>. These two regions can be assumed to contribute up to 2-3 orders of magnitude more material to the atmosphere compared to the Chryse/Ares Vallis and Utopia Planitia sites. Chryse Planitia studies estimated 1.5 dust devils sol<sup>-1</sup>, which yielded flux estimates of 0.009 – 0.072 kg km<sup>-2</sup> sol<sup>-1</sup> compared to Ares Vallis (South Chryse), where MPF studies estimated ~2.5 dust devils sol<sup>-1</sup> yielding 0.03 – 0.22 kg km<sup>-2</sup> sol<sup>-1</sup>. Utopia Planitia, the northernmost of the sites, was estimated having 0.6 dust devils sol<sup>-1</sup>, which yielded the lowest sediment fluxes of 0.003 – 0.036 kg km<sup>-2</sup> sol<sup>-1</sup>.

**Conclusions:** Recently published data from laboratory experiments of dust devil sediment flux using the Arizona State University Vortex Generator [2,3] have produced interesting trends for dust devil

sediment flux as a function of vortex strength as denoted by either the maximum core pressure decrease ( $\Delta P$ ) or a lifting ratio of key lifting terms ( $\Delta P/u_\theta$ ). In either case, the trends provide a sediment flux parameterization capable of predicting dust devil sediment fluxes on Mars for appropriately scaled dust devils when applied to natural distributions for different regions on Mars. Key factors that were considered for comparing the laboratory data to natural distributions included vortex strength ( $\Delta P$  as a percentage of ambient pressure), particle sizes and densities, and surface roughness. Mars-analog experiments focused on mainly 2 $\mu$ m silicate dust particles and larger lower-density walnut shell particles (surrogate particles simulating the lower gravity of Mars).

The ranges in the estimated sediment fluxes reflect specific key considerations. For the Mars-analog experiments, the sediment fluxes were artificially elevated because of mechanical inefficiencies of the vortex generator at low pressure resulting in higher strength vortices and thus higher fluxes. Although, walnut shells are ideal for simulating the lower gravity of Mars in most laboratory settings, it is necessary to consider that for mass flux experiments, the resulting fluxes need to be adjusted for silicate-type densities, which also increases the laboratory estimates. Results from the ASUVG roughness experiments [3] also suggest that surface roughness can play a large role controlling the amount of available material for dust devils to lift estimating as much as ~20% increase in sediment flux when roughnesses are low.

Comparing different regions should allow better parameterization of atmospheric dust contributions for modeling based on estimates of regional dust devil activity. This study showed that for regions where active dust devils have been observed, regional activity can be quite different, and hence the relative dust contributions to the atmosphere.

**Future Work:** Refinements of this estimation tool could include more laboratory experiments at Mars-analog atmospheric conditions, using more sediments and more variety in roughness arrays to obtain better trends used to extrapolate to natural distributions. Currently, this study was limited to places where observed distributions of active dust devils were made. Future efforts could also include estimates of dust devil activity based on dust devil track densities and potential refresh-rates of the tracks, which would

Location	Frequency (dd km <sup>-2</sup> )	Est. Flux (kg km <sup>-2</sup> )
Gusev Crater	50	3.7 - 28.4
Ares Vallis	2.5	0.03 – 0.22
Chryse Planitia	1.5	0.009 – 0.072
Utopia Planitia	0.6	0.003 – 0.036
Amazonis Planitia	19-190	3.4 – 42.6

**Table 1.** Estimations from ASUVG dust devil sediment flux experiments.



allow dust flux estimates to be extended to regions that currently have poor orbiter coverage during times of maximum dust devil activity or where active dust devils rarely have been imaged.

**References:** [1] Neakrase, L.D.V. et al. (2006) *GRL*, 33, L19S09. [2] Neakrase, L.D.V. and Greeley, R. *in press* (2009) *Icarus*. [3] Neakrase, L.D.V. and Greeley, R. (2007), *LPS XXXVIII*, Abstract #1402. [4] Murphy, J.R. and Nelli, S. (2002), *GRL*, 29(23),

2103. [5] Ringrose, T.J. et al. (2003), *Icarus*, 163, 78-87. [6] Greeley, R. et al. (2003), *JGR*, 108(E5), 5041. [7] Neakrase, L.D.V. (2009), *PhD Dissertation*, ASU. [8] Greeley, R. et al. (2006), *JGR*, 111, E12S09. [9] Metzger, S.M. et al. (1999), *GRL*, 36(18), 2781-2784. [10] Ryan, J.A. and Lucich, R.D. (1983), *JGR*, 88(C15), 11005-11011; [11] Fisher, J.A. et al., (2005), *JGR*, 110; [12] Stanzel, C. et al., (2008), *Icarus*, 107, 29-52.

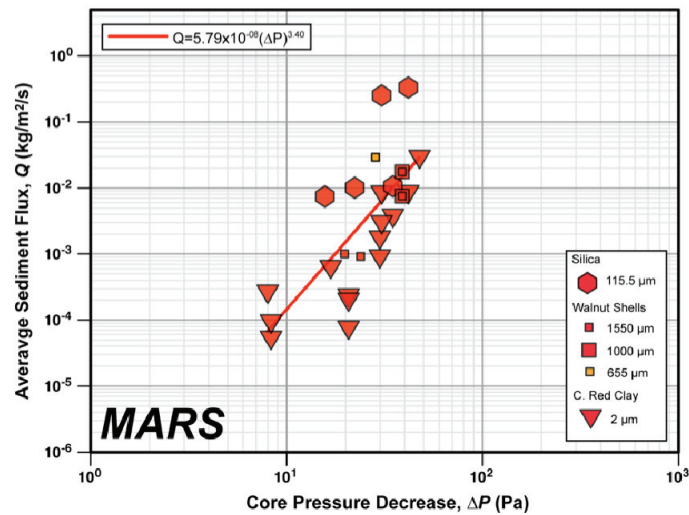


**Figure 1:** Plot of the Mars-analog data from the ASUVG showing the relationship of the sediment flux ( $Q$ ) and core pressure decrease ( $\Delta P$ ) [2].

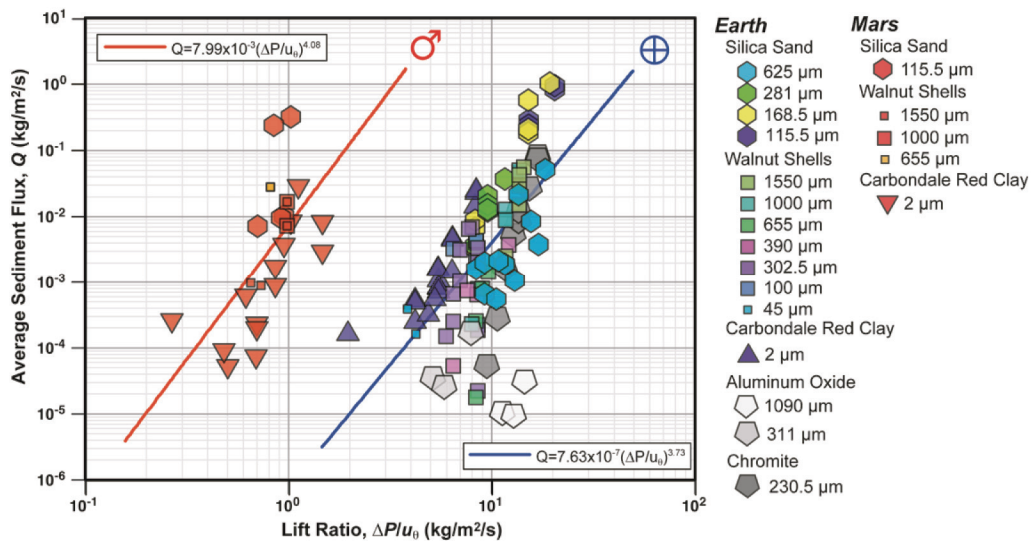


**Figure 2:** ASUVG data showing the relationships between sediment flux ( $Q$ ) and the lift ratio ( $\Delta P/u_0$ ) for Mars-analog (red) and Earth-ambient (blue) experiments [2].

## PARTICLE-SIZE DEPENDENT ELECTROSTATIC CHARGING OF MARTIAN REGOLITH SIMULANT.

Lacks, D.J.<sup>1</sup>, Forward, K.F.<sup>1</sup>, Sankaran, R.M.<sup>1</sup> Department of Chemical Engineering, Case Western Reserve University, Cleveland, OH 44106. (216)368-4238. daniel.lacks@case.edu.

**Introduction:** Mars dust can become electrostatically charged by triboelectric processes when the dust particles rub against each other or collide during dust events. This charging may be very important due to the large dust storms and dust devils that occur on Mars [1].

Electrostatic charging can have significant implications in regard to the Mars dust cycle. In particular, the electrostatic charge will affect the threshold for dust lifting, and thus alter the dust density in the atmosphere; the dust density in turn strongly affects the climate of Mars.

Electrostatic charging of dust also has implications in regard to Mars exploration. Electrostatic charge causes dust to adhere to equipment, which can affect the operation of the equipment. For example, dust adhering to solar panels will block the access of light to the panels, and thus render the panels inoperable.

The electrostatic charging is also believed to generate large electrostatic fields that significantly alter geochemical processes on the planet (e.g., H<sub>2</sub>O<sub>2</sub> content of the atmosphere).

However, the reason why negatively and positively charged particles separate spatially to create electrical fields is not clear. While it is generally hypothesized that this charge separation occurs because smaller particles charge negatively and larger particles charge positively, with gravity separating the particles by size, there has yet to be a direct demonstration of this particle-size dependence of electrostatic charge, or a compelling explanation for why this size dependence occurs.

**Experiments:** Experiments are carried out to study the triboelectric charging of Martian regolith simulant (JSC-1 Mars) under conditions that mimic Martian dust storms (most importantly, in a dust storm the particles charge by contact with only other particles). We have developed a methodology to investigate triboelectric charging where the particles have no contact with any surface besides those of other particles until after they are separated by charge polarity and collected [2,3]. First, we use a particle

mixing apparatus designed such that the moving particles contact only other particles, and not any other surfaces; as shown in Figure 1, this is accomplished with a fluidized-bed type of apparatus where the distribution plate has only a single hole at its center, thus fluidizing only the central portion of the bed. Second, we use a non-contact means of extracting particles of a desired polarity; we accomplish this extraction by suspending a charged plate over the bed (after flow is stopped), such that particles of the opposite polarity are extracted from the bed to the plate. The size distributions of the positive and negative particles extracted this way are then determined.

The results for experiments with the Mars regolith are shown in Figure 2. Our experiments show directly that under these conditions the smaller particles tend to charge negatively and larger particles tend to charge positively, which provides a mechanism for the spatial charge separation that creates electric fields in Martian dust events.

We have also carried out experiments with a more controlled sample consisting of soda lime glass with two particle sizes. In this case, it is certain that the differently sized particles are chemically identical

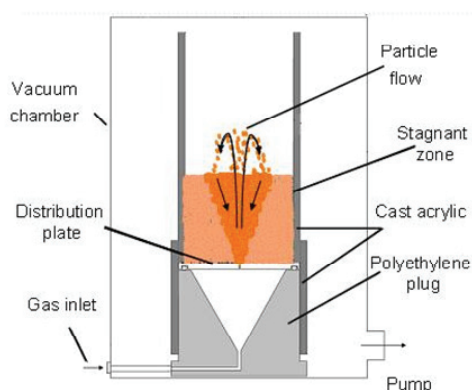


**Figure 1:** Schematic of particle mixing apparatus used in the experiments. The particles involved in the flow only contact other particles (which are either flowing or stagnant), but not the walls of the container.

(whereas for the Mars regolith stimulant there may be particles with different mineral constituents, which could affect electrostatic charging). The results for experiments with the soda lime glass are shown in Figure 3. Again, the results show that the smaller particles tend to charge negatively and larger particles tend to charge positively.

**Theory:** We believe that this particle-size dependence of triboelectric charging – i.e., that smaller particles tend to charge negatively and larger particles tend to charge positively – is universal (i.e., independent of material properties) in single component granular systems. We use statistical mechanics to show that this universality may follow from the simple idea that electrons in insulators are not at equilibrium, and surface contact allows electrons trapped in high energy states on one surface to relax to lower energy states on another surface [3,4,5].

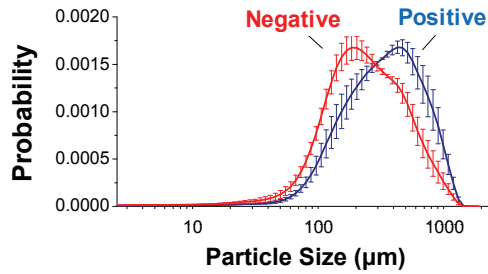


**Figure 2:** Experimental results for Mars regolith stimulant, showing the particle size distributions of the positive and negative particles.

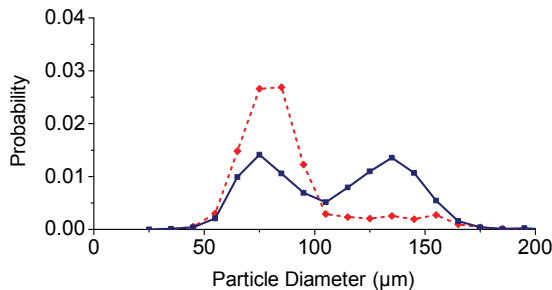


**Figure 3:** Experimental results for soda lime glass particles, showing the particle size distributions of the positive (blue solid line) and negative (red dashed line) particles.

Our ideas follows from the theory of Lowell and Truskott [7] for the triboelectric charging of identical bulk insulators due to asymmetric rubbing. In an insulator, electrons cannot always relax from high energy states to vacant low energy states that are spatially separated, and the electrons may remain trapped in these high energy states. However, contact with another surface can bring a vacant low energy state close to an electron trapped in a high energy state, and allow the electron to relax from this high energy state.

We show that this simple idea leads to the result that smaller particles tend to charge negatively and larger particles tend to charge positively. Initially all particles have the same surface density of trapped electrons, as shown schematically in Figure 4. In the first collision between these two particles, there will

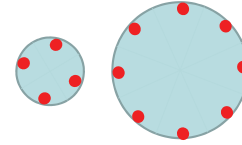


**Figure 4:** Schematic representation of the initial state of the system, in which all particles have the same surface density of trapped electrons.

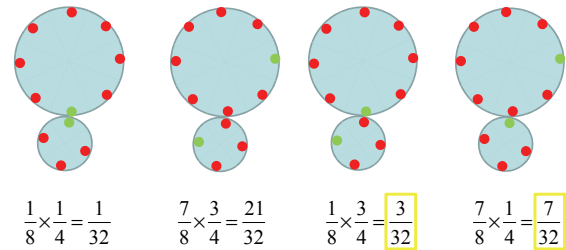


**Figure 5:** Schematic representation of the possible ways that the two particles shown in Figure 4 can undergo a second collisions (in the first collision, each particle transferred one trapped electron to a low energy state in the other particle). The trapped electrons are shown as red dots, and the low energy electrons are shown as green dots. Note that a red dot near the point of collision implies that this particle will lose an electron (and the other particle will gain this electron) – thus this analysis shows it is more likely that the small particle will gain an electron than the larger particle.

be a symmetric exchange of high energy trapped electrons on each particle to low energy states in other particle. The result of the first collision leads to nothing interesting – each particle has same number of electrons after the collision as before collision. However, as shown schematically in Figure 5, the second collision will likely lead to an asymmetric transfer of electrons, such that the smaller particle will more likely receive an electron from the other particle than to donate one to the other particle. These ideas have been examined elsewhere with rigorous analytical theories [4,5] and simulations [5,6], and qualitatively described more fully [2].

**References:** [1] Renno, N. O., and Kok, J. F. (2008) *Space Sci. Rev.*, 137, 419. [2] Forward, K. M. et al. (2009) *GRL*, 36, L13201. [3] Forward, K. M. et al. (2009) *PRL*, 102, 028001. [4] Lacks, D. J. et al. (2008) *PRL*, 100, 188305. [5] Lacks, D. J., and Levandovsky, A. (2007) *J. Electrostat.*, 65, 107. [6] Duff, N., and Lacks, D. J., (2008) *J. Electrostat.*, 66, 51. [7] Lowell, J., and Truskott, W. S. (1986) *J. Phys. D*, 19, 1281.



# ***Session Five***

## *Lifting and Dynamics Associated with Small-Scale Systems*

*Wednesday, September 16, 2009*

*10:30 AM – 3:00 PM*





---

**THE ELECTRODYNAMICS OF MARS DUST DISTURBANCES.** Barth<sup>1</sup>, E. L. Rafkin<sup>1</sup>, S.C.R., and Farrell<sup>2</sup>, W.M. <sup>1</sup>Southwest Research Institute, 1050 Walnut Street, Suite 300, Boulder, CO 80302 ([ebarth@boulder.swri.edu](mailto:ebarth@boulder.swri.edu), [rafkin@boulder.swri.edu](mailto:rafkin@boulder.swri.edu)), <sup>2</sup>NASA Goddard Spaceflight Center, Greenbelt, MD 20771 ([william.m.farrell@nasa.gov](mailto:william.m.farrell@nasa.gov)).

---

**Introduction:** Mars analog and laboratory studies and field campaigns on Earth provide the strongest evidence for the existence of active electrodynamic processes on Mars. Dust charging studies using Mars soil simulant [1], [2] suggest that the triboelectric charging of dust observed within terrestrial dust disturbances is very possible on Mars. In the field, a typical terrestrial dust devil has been found to generate macroscopic electric field perturbations in excess of 100 kV/m (Fig. 1; [3]). These strong electric fields are due to triboelectric charging of individual dust grains, most of which charging occurs in the saltation layer within the first few centimeters of the surface. Once charged, some of these grains are injected further into the air where they are transported upward by atmospheric currents. Differential transport and gravitational sedimentation size sorts the dust devil aerosols so that the lighter and predominantly negatively charged particles populate the higher portion of the disturbance while the heavier, positively charged particles fall to the ground or remain in the lower portion of the vortex.

Consideration of electrodynamic processes is significant for numerous reasons. First, electrodynamic processes are implicated in the local production of superoxides at concentrations orders of magnitude greater than expected through photochemistry, and are further implicated in the subsequent destruction of organics, including methane. Second, there are astrobiological implications of superoxide production ranging from the issue of sterilization to the use of electrochemically-produced oxides for metabolic energy. Third, there are potential hazards associated with an active electromagnetic environment, including lightning and communication disruption. And fourth, naturally occurring electromagnetic fields might be used to passively probe orders of magnitude deeper into the interior of Mars than is possible with conventional ground penetrating radars. However, to close all the above issues, basic and fundamental knowledge of the electrodynamic environment first needs to be established.

**Modeling:** We have modified the Mars Regional Atmospheric Modeling System (MRAMS) to include charge distribution as a function of dust particle size and composition. An analytic representation of the charge distribution is derived based on the individual particle charge values provided by the Macroscopic Triboelectric Simulation (MTS) code.

MRAMS is a nonhydrostatic model, which permits the simulation of atmospheric flows with large vertical accelerations, such as dust devils. MRAMS includes a number of microphysics routines which simulate the transport and microphysical interactions of dust, water ice, and CO<sub>2</sub> aerosols. The distribution of each of these species is represented by discrete mass bins (the number of which is user specified), and each of these bins is carried in the model as a scalar species that can be advected and diffused. Source and sink terms of the condensibles (and their interactions) are calculated within the microphysical routines. In the case of dust, sources are provided via a surface dust lifting scheme (see next subsection) or through sublimation of condensibles with dust cores, and the sink of dust is sedimentation to the surface. The dust lifting scheme includes multi-size dust transport capability. The dust surface source is parameterized [4] based on the work of [5]. Laminar wind and dust devil lifting are implicitly included in this single scheme. Dust devils occupy the tail end of the Weibull distribution in unstable ( $Ri < 0$ ) conditions.

MTS quantifies charging associated with swirling, mixing dust grains. Grains of pre-defined sizes and compositions are placed in a simulation box and allowed to move under the influence of winds and gravity. The model tracks the movement of grains in prevailing winds and charge exchange upon grain-grain collision. The composition of the grains is also a predefined variable and we impose a compositional mix to maximize the triboelectric surface potential difference between larger and smaller grains. Specifically, we apply the grain/grain contact electrification algorithm presented in [6].

The MTS simulation box is 1m x 1m x 2 m, which is a sub-gridscale box in the MRAMS model. Information describing each MTS dust particle (*i.e.*, charge, radius, and mass) are fed into the MRAMS dust lifting scheme for each MRAMS model grid-point. The MTS dust grains are binned into the appropriate microphysics radius bins. The charge data is then used to fit a log-normal function. The first and second moments of the charge distribution are sent as tracers to MRAMS so that as the dust grains move around in the MRAMS domain, the charge distribution can be reconstructed at any point. The coupled model enables a new research capability: the ability to simulate charging with a fully dynamic model in a manner that allows the wind field, dust distribution, and charging to be physically consistent. Thus, this is a major improvement to the dynamical studies of dust disturbances and the electrodynamic studies with prescribed wind fields.

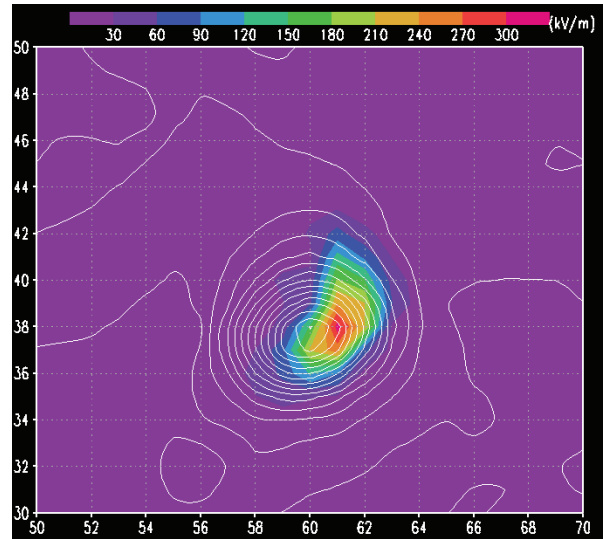
**Dust Devil Simulation Results:** MRAMS is run over a 15 km x 15 km domain up to a height of about 8 km. The MTS dust particles are classified as either metals or silicates based on their charge sign (negative or positive, respectively). The metals range from 0.5 – 2  $\mu\text{m}$  in radius, with most particles having a radius of 1  $\mu\text{m}$ ; the silicates are 2 – 100  $\mu\text{m}$  in radius, with the peak of the size distribution at  $\sim 4 \mu\text{m}$ . Because the silicates are much less dense than the metals, the smaller silicate particles fall at speeds comparable to the metal particles. A number of neutral particles are also present. The charge on individual particles ranges from about  $10^{-18}$  to  $10^{-15}$  C. The atmosphere is initialized using Viking temperature and wind field profiles at a local time of about 10am.

Figure 1 shows a snapshot of the electric field environment in the vicinity of a dust devil. Strong electric fields can be seen particularly in the layer near the surface. The profiles of the electric field at two locations within the region shown in Figure 1 are shown in Figure 2. The highest e-field values are found in the center of the dust devil.

The simulations also show strong electric fields developing in regions not associated with a dust devil, but along the edge of a convective cell where significant dust lifting is occurring (Fig. 3). These e-fields are of higher magnitude than those seen in the dust devil.

**Conclusions:** We have simulated the charge environment in Martian dust disturbances and have found that strong E-fields, at or exceeding breakdown

strength, were generated in dust devils. Disturbances other than dust devils also generate fields. This is a first look at the charge environment on Mars and so a number of processes are not yet included, such as ion drift processes (some neutralization would be expected in reality) and EM perturbations from current flow. Ultimately we will conduct additional simulations and then use output to drive electrochemical models.



**Figure 1:** Pressure contours showing the location of a dust devil overlaid on electric field contours. The area shown is 2km x 2km (the axes indicate x,y coordinates).

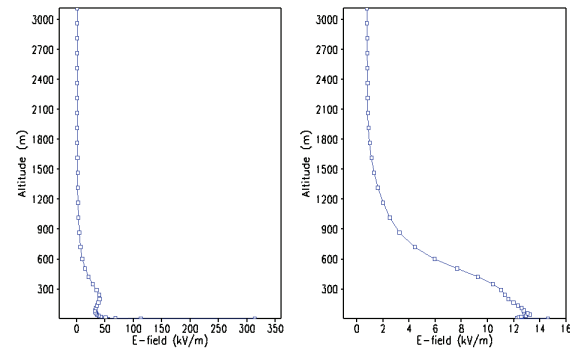


**Figure 2:** Profiles showing magnitude of the electric field generated by the charged particles in the dust devil shown in Figure 1. Left: Large E-fields generated near the center of the dust devil ( $x=61$ ,  $y=38$ ), Right: Smaller E-field near the edge of the dust devil ( $x=59$ ,  $y=42$ ). Away from the dust devil, E-fields are of order 100s of V/m up to 2.5 kV/m at the surface.

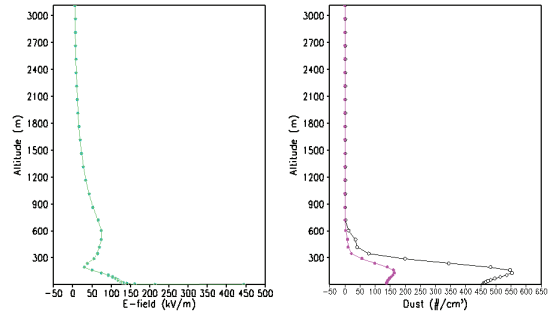


**Figure 3:** Magnitude of the electric field (left plot) and dust particle number density profiles (right plot) in a region of dust lifting with no associated dust devil. The number density curves show metals (black curve) and silicates (red curve).

**References:** [1] Krauss C. E. et al. (2003) *New J. Phys.*, 70.1-70.9. [2] Sternovsky Z. and Roberston S. (2002) *JGR*, 107, 5105. [3] Jackson T.L and Farrell W. M. (2006) *ITGRS*, 44, 2942-2949. [4] Michaels T. I. (2006) *GRL*, 33, L19S08. [5] Armstrong J. C. and Leovy C. B. (2005) *Icarus*, 176, 57-74. [6] Desch S. J. and Cuzzi J. N. (2000) *Icarus*, 143, 87-105.

## SOME OBSERVATIONS ON THE THERMODYNAMICS AND FLUID DYNAMICS OF DUST DEVILS ON MARS.

Fuerstenau, S.D., NovaWave Technologies, 900 Island Dr., Redwood City, CA 94065 sfuerstenau@novawavetech.com

Dust devils, a common atmospheric phenomenon in the desert regions of Earth, appear to be far more prevalent on Mars where they have been observed from orbit and from landers in many regions. Unlike their terrestrial counterparts, Martian dust devils can grow to enormous size reaching heights of up to 6 km with column widths extending to hundreds of meters. [1] Although the cause for this difference remains open to speculation by atmospheric scientists, a likely explanation is the strong positive feedback that occurs when sunlight warms suspended particles. Dust devils form when a rotating column of thermally unstable air rises from solar heated surface through cooler air above it. If the induced winds at the surface are fast enough, dust will be entrained in the column making it visible as a dust devil. As the column rises, it cools by adiabatic expansion until its temperature and density are that of the surrounding air. Sunlight will warm the suspended dust particles which quickly transfer the heat to the air in the column. By this means the temperature difference that gives rise to buoyancy is maintained to a greater height than would otherwise be the case in a dust free buoyant column. Lorenz attempted to observe this phenomenon in a desert whirlwind with a thermal imaging camera [2] and analysis by Kurgansky suggests solar heating of suspended dust can influence the dynamics of large dust devils on Earth [3]. The same effect will be *two orders of magnitude larger* on Mars owing to the low density, and hence low heat capacity, of that atmosphere. The action of positive feedback has long been known to drive the growth of large dust storms on Mars [4] but is generally regarded to operate on the time scale of days rather than minutes as do smaller scale dust devils.

### **Radiative Feedback Drives Martian Dust Devils**

The author has made estimates of the degree of warming from solar heating of suspended particles in a dust devil observed at the Pathfinder landing site which was estimated to contain a dust loading of  $7 \times 10^5$  kg/m<sup>3</sup>. In addition an alternative estimate was made by analyzing the shadow cast by a second dust laden column observed by the Mars Orbiter Camera on MGS [5]. By assuming the particles in the Pathfinder dust devil had an average diameter of three  $\mu$ m and an albedo of 89% (the particles absorb 11% of incident energy), one may calculate a warming rate of 0.05 °C

per second for the gas inside the dust devil plume. A method for estimating warming that requires no assumptions other than albedo is to analyze the depth of shadows cast by semi-transparent dust columns as observed from orbit. Blocked sunlight is measured directly with a known fraction resulting in warming. The shadow analysis leads to an estimated warming rate of 0.011 °C per second for the dust devil observed by MGS (MOC2-1231). The results are summarized in figure 1 which depicts the temperature vs. altitude of a thermally buoyant gas column on Mars, with and without suspended dust. The vertical velocity inside a typical dust devil is 10-20 m/s. A dust-free gas plume will cool at rate determined by the adiabatic lapse rate (B) with a buoyancy driven by the temperature difference between it and the ambient temperature (A). Solar warming due to dust - cases (C), (D), and (E) - maintains a large temperature difference. The case (E) is probably unrealistic since radiative cooling would keep the dust temperature from rising higher than the ground temperature, but it illustrates the magnitude of heating relative to cooling by adiabatic expansion. This result implies that radiative heating of dust-laden gas is a first order physical phenomenon that cannot be ignored in any realistic model of dust devils on Mars.

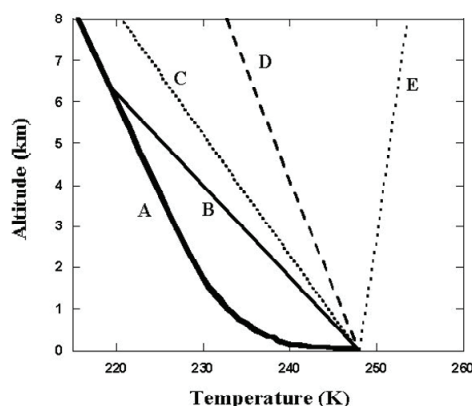


**Figure 1:** Temperature profiles: (A) measured above Opportunity rover at 13:30 local time [6], (B) dry adiabatic lapse rate for Mars 4.5 °C/km, (C) calculated for MOC2-1231 dust devil with estimated solar warming of 0.011 °C/s, and a gas parcel with  $7 \times 10^5$  kg/m<sup>3</sup> dust loading rising at 20 m/s (D) and 10 m/s (E).





## CHARACTERIZING THE SENSITIVITY OF DAYTIME TURBULENT ACTIVITY ON MARS WITH THE MRAMS LES.

Fenton<sup>1</sup>, L. K. and Michaels<sup>2</sup>, T. I. <sup>1</sup>Carl Sagan Center, NASA Ames Research Center, MS 245-3, Moffett Field, CA 94035-1000, lfenton@carlsagancenter.org, <sup>2</sup>Southwest Research Institute, tmichael@boulder.swri.edu.

**Introduction:** A significant goal of Mars science is to understand the present-day interaction between the atmospheric environment and the planet's surface that ultimately results in climatically- and geologically-important aeolian phenomena (*e.g.*, dust storms, dust devils, albedo changes, dune migration, and surface erosion). Although the potential impact of larger atmospheric flows on surface-atmosphere interactions has been studied at length with regional and global climate models (GCMs) [*e.g.*, 1-3], studies of simulations resolving the complex, highly three-dimensional dry convective circulations that produce dust-lifting events are still uncommon [*e.g.*, 4,5].

Figure 1 shows an example of the intricate pattern of turbulent activity typical of a convective boundary layer (in this case, at the Viking Lander 1 site near local noon, at  $L_s = 120^\circ$ , and with no mean wind). The figure shows a composite of three parameters: near-surface static stability in red, friction velocity in blue, and surface air pressure in green. Convective cells ~2-6 km across are outlined by narrow upwelling regions

of warm, buoyant air (in yellow). Within the cells, descending air produces broad regions of higher pressure (in green). After its descent, this air is heated by the hot surface and makes its way towards the cell boundaries via a network of near-surface conduits (the thin yellow features within the larger-scale cells). As the air nears the narrow updrafts comprising the cell boundaries, it accelerates, producing strong wind gusts (areas of high friction velocity, in blue/purple). Vertical vortices, which can become visible as dust devils if they manage to lift dust from the surface, typically occur at the intersections of cells (magenta spots).

Even mesoscale models cannot resolve the small-scale complex structures shown in Figure 1. In addition, the threshold friction velocities required to initiate sand saltation (and thus saltation-induced dust lifting) on Mars are roughly an order of magnitude larger than those on Earth [*e.g.*, 6]. As a result, the majority of winds on Mars may be too weak to produce saltation, making particle entrainment more difficult relative to Earth (although it clearly does occur [*e.g.*, 7]).

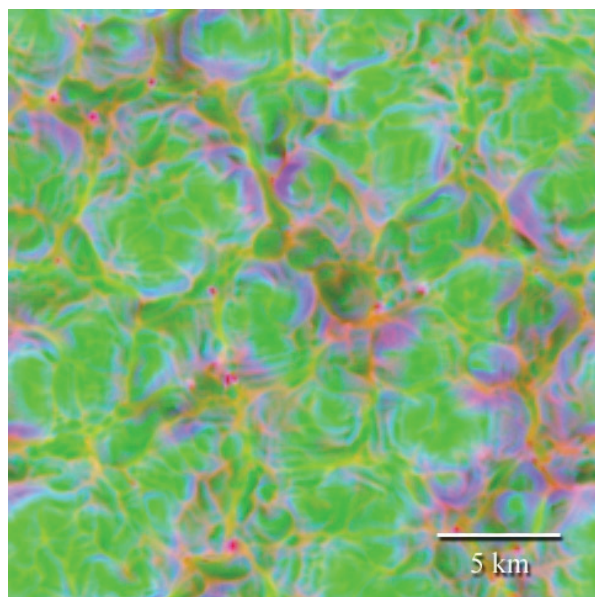


**Figure 1:** Example of complex convective structures near the surface in a convective boundary layer.

GCMs and regional climate models can be used to estimate aeolian sand and dust fluxes, but they require parameterizations that may not yet fully account for the realistic distribution of winds at smaller spatial scales. This is particularly true for the winds at the higher end of the wind magnitude distribution (*e.g.*, gusts and vortices), which are those winds most relevant to particle entrainment on Mars. The simplest method used to account for subgrid-scale winds involves reducing the estimated threshold friction velocity to a value that easily produces particle entrainment [*e.g.*, 1,2]. More sophisticated methods superimpose a Weibull distribution on the mean winds [*e.g.*, 5,8]. A Weibull distribution is often used to estimate power output in wind turbines on Earth because it often approximates the longer-term (*e.g.*, monthly or daily) distribution of wind speeds near the surface. However, the Weibull distribution is known to poorly fit wind measurements under many circumstances, particularly in locations with significant local topography and a high proportion of calm winds

[9]. The goal of this work is to explicitly simulate daytime turbulent wind distributions on Mars that may be applied as “perturbations” superimposed on regional-scale “mean” winds, better accounting for how these distributions vary according to local time, elevation, latitude, season, albedo, and thermal inertia.

We present preliminary results of large eddy simulations (LES) on Mars. In order to produce results that are directly comparable from one region or season of Mars to another, we have used idealized wind profiles as initial conditions to the simulations, rather than those derived from a coarser (but perhaps more locally realistic) regional climate model domain. We demonstrate that wind “gustiness” (*i.e.*, the stronger intermittent winds produced by daytime convective turbulence) is dependent on both the time variation of insolation and the initial wind profile.

**MRAMS Large Eddy Simulations (LES):** The Mars Regional Atmospheric Modeling System (MRAMS) is a non-hydrostatic, finite-difference, limited domain mesoscale model [10,11]. It can perform LES when the subgrid scale turbulence is modified to explicitly model eddies down to the domain resolution, based on the method of [12].

We have run several large eddy simulations at two locations on Mars: the approximate Viking Lander 1 (VL1) site (22.28°N, 312.05°E, elevation  $\approx$  -3640 m) and Phoenix Lander site (68.21°N, 234.26°E, elevation  $\approx$  -4130 m). Other than location and initial conditions inherited from mesoscale simulations, each LES was run with the same characteristics. The horizontal domain grid spacing was 100 m, spanning 24 km in each direction (240 x 240 grid points). The 99 vertical layers in the domain stretched in thickness from 4 m at the surface to 150 m near the top (at  $\sim$ 12 km). The dynamical time step was 1 s. Each simulation was run at  $L_s = 120^\circ$  (northern hemisphere summer), with a duration from approximately sunrise to sunset of a single day. In the VL1 runs the local mean solar time (LMST) ranged from 4.63h – 18.63h. In the Phoenix runs the LMST ranged from 3.45h – 21.45h, encompassing the hours during which arctic summer experiences the most direct insolation.

The LES were run under idealized conditions in order to most clearly distinguish the regional influences of insolation and elevation from more localized and situation-dependent conditions. For example, the LES setup did not include topography or variations in atmospheric dust content. In addition, H<sub>2</sub>O vapor/ice,

and CO<sub>2</sub> ice were not accounted for in the simulations. The LES used periodic boundary conditions to effectively simulate the atmosphere over a vast plain.

Typically, LES initial conditions are interpolated from lower resolution mesoscale simulations. Initial temperature and pressure profiles for the LES were specified in this way. However, realistic wind profiles can be complex and change during the day, so in order to isolate the effects on the boundary layer convection due to differing wind profiles, we used three idealized wind profiles chosen for their relative simplicity. The three initial wind profiles were defined as follows (see Fig. 2):

*Case 1:* No initial wind,  $u(z,t=0) = 0$ ,  $v(z,t=0) = 0$

*Case 2:* Uniform wind,  $u(z,t=0) = 5$  m/s,  $v(z,t=0) = 0$

*Case 3:* Wind speed shear,  $u(z,t=0) \approx 1.46z+2$ ,  $v(z,t=0) = 0$ , (such that  $u(z=0) \approx 2$  m/s and  $u(z=12$  km)  $\approx 20$  m/s).

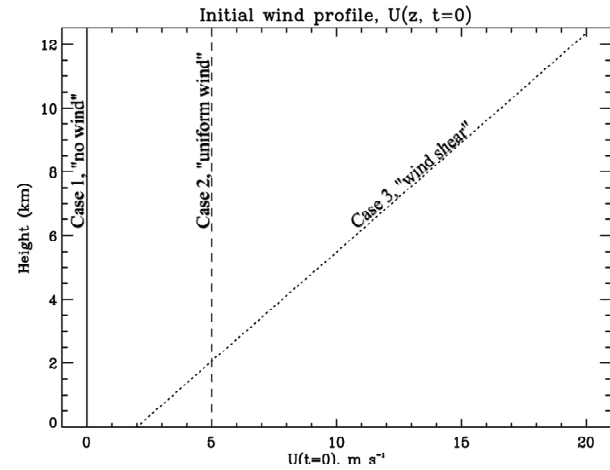


**Figure 2:** Idealized initial wind profiles.

**Results:** In order to determine how the developing convective boundary layer influences the potential for sand saltation and saltation-induced dust lifting, we have plotted the probability distribution of friction velocity ( $u_*$ ) modeled by the LES at the two different landing sites. For reference, using the empirically derived equations from [13], we estimate approximate threshold friction velocities for 100  $\mu$ m basalt sand to be  $\sim$ 1.8 m/s at the VL1 site and  $\sim$ 1.7 m/s at the Phoenix site at local noon (LMST) at  $L_s = 120^\circ$ .

*Case 1.* In the simplest of LES, there is no mean wind, so that all wind gusts (measured here at the surface as high values of friction velocity) are produced solely



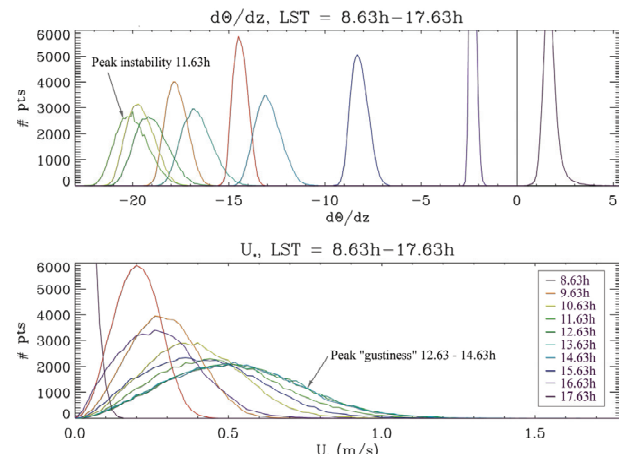
by the development of buoyantly-induced turbulence within the convective boundary layer. One measure of insolation-driven buoyancy is the vertical potential temperature gradient at the surface ( $d\theta/dz$ , the surface static (in)stability): values less than zero indicate static instability, where the solar forcing has heated the surface more than the near-surface atmosphere, triggering dry convective turbulence that tries to equalize the energetic disparity between the two.

Figure 3 shows the distribution of surface static instability and friction velocity at ten local times (8.63h – 17.63h LMST) across the VL1 domain. The surface air is statically unstable by midmorning, reaches a maximum level of static instability ( $\sim -20$  K/m) around local noon, and gradually grows less statically unstable as the afternoon progresses. By late afternoon (17.63h LMST), the sun is low in the sky and can no longer heat the surface enough to produce a negative vertical potential temperature gradient; at this point the convective boundary layer begins to collapse. Friction velocity distributions broaden throughout the morning and early afternoon, reflecting increased gustiness produced by buoyantly-driven turbulence within the boundary layer. The peak gustiness occurs in the early afternoon (12.63h – 14.63h LMST), shortly after the surface static instability has reached a maximum and the boundary layer has had time to react to this strong gradient with vigorous circulations. According to Mars lander observations, dust devil activity peaks in the early afternoon, consistent with our LES results [e.g., 14,15]. Although it is difficult to see in Figure 3, a few grid points in the LES domain do experience friction velocities that surpass the estimated saltation threshold during the hours of peak gustiness, demonstrating that convective turbulence with no imposed mean wind has the potential to produce particle entrainment on Mars.

Figure 4 shows similar plots of surface static stability and friction velocity at the Phoenix site, using the same axis ranges and similar local times as in Figure 3. As at the VL1 site, instability at the Phoenix site reaches a maximum around local noon, although at such northern latitudes insolation is not direct enough to produce as strong a vertical potential temperature gradient, reaching to only  $\sim -16$  K/m (at the VL1 site the sun peaks at  $\sim 89.4^\circ$  above the horizon; at the Phoenix site it peaks at  $\sim 43.4^\circ$  above the horizon). As the insolation decreases during the afternoon, the static instability decreases but much more slowly than at the VL1 site, since during the arctic summer the sun is above the horizon at all times. Thus the convective

boundary layer at the Phoenix site may not produce such vigorous turbulence as that at the VL1 site, but buoyantly-driven turbulence takes longer to subside in the evening. This result is reflected in the distribution of friction velocities in Figure 4, which never reach the same maxima as those at the VL1 site, but which take longer to weaken in the afternoon.

**Cases 2 and 3:** The idealized initial wind profiles (see Fig. 2) proved to have a significant impact on the distribution of friction velocity. Figure 5 shows resulting friction velocities from the three different wind profile cases at four local times (the solid lines



**Figure 3:** VL1 site, Case 1 domain distributions of surface instability and friction velocity in the morning and afternoon.

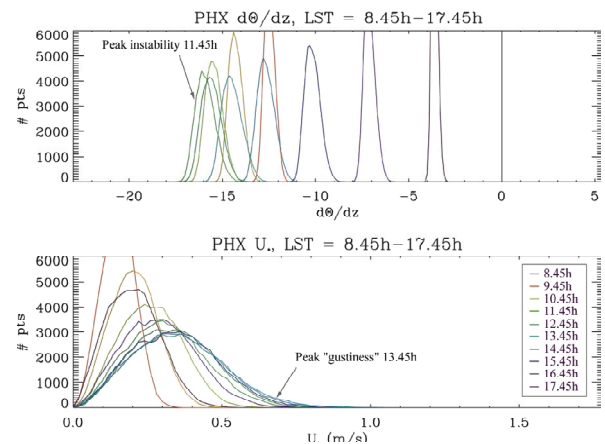


**Figure 4:** Phoenix site, Case 1 domain distributions of surface instability and friction velocity in the morning and afternoon.

denoting Case 1 output are also shown in Figure 3 and follow the same color scheme). At midmorning (8.63h LMST), the  $u_*$  distributions best reflect the influence of initial near-surface wind speeds (0 m/s for Case 1, 5 m/s for Case 2, and 2 m/s for Case 3). By late morning to early afternoon, the distributions have widened and nearly overlap one another, although the uniform wind and wind shear cases do exhibit slightly stronger wind gusts than those in the no wind case. In all cases, buoyantly-driven turbulence dominates over any wind-shear-driven turbulence caused by the initial wind structure. In the late afternoon (16.63h LMST), convective turbulence has weakened and the friction velocity distributions in the no wind and uniform wind cases are beginning to revert back to their initial distribution. The wind shear case, however, is still experiencing downward mixing of stronger winds (*i.e.*, higher momentum) from aloft, and thus its friction velocities are still stronger than those of the other wind profile cases.

The Phoenix site LES show a fairly similar pattern (see Fig. 6), with a few slight differences. As discussed above, convective activity at such high latitudes is not strong enough to widen friction velocity distributions as much as at the VL1 site, and this is reflected in all three initial wind profile cases. A secondary effect of this weaker activity is that it allows the initial wind structure at the Phoenix site to more prominently influence the turbulence – the difference between the no wind case and the other wind cases is slightly larger in the late morning (11.45h LMST) than at the VL1 site.

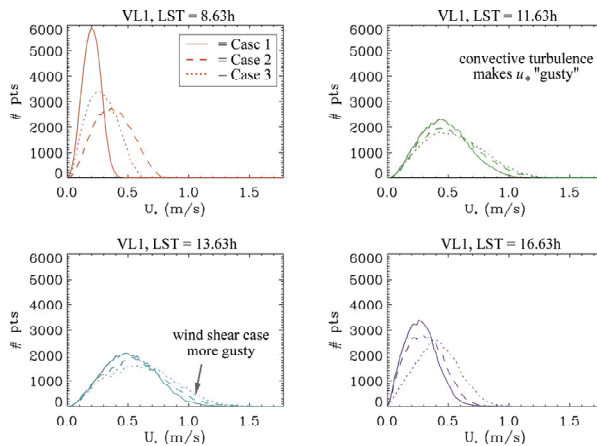


**Figure 5:** VL1 site friction velocities at 4 local times for each of the 3 initial wind profiles.

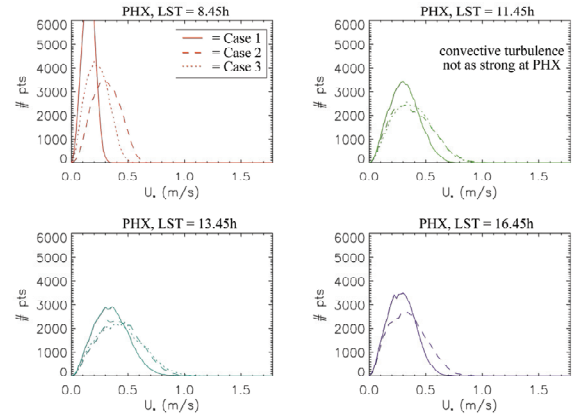


**Figure 6:** Phoenix site friction velocities at 4 local times for each of the 3 initial wind profiles. Case 3 16.45h output is not shown, as it was not available.

Thus the effects of insolation on producing vigorous convective turbulence (and therefore wind gustiness) are dependent on latitude as well as the initial wind structure. In reality, background winds will likely change continuously throughout the day (*e.g.*, as tidally- or topographically-driven winds shift and interact), so that the wind structure of the previous hours should be considered when superimposing LES friction velocity distributions on mesoscale winds.

**Conclusions:** Large eddy simulations, using idealized initial wind profiles at two lander locations, have demonstrated that daytime convective turbulence can significantly increase the likelihood of particle entrainment on Mars, and that the degree of this enhancement is dependent on (at least) several factors. Wind gustiness (*i.e.*, strong, intermittent friction velocities) generally increases with insolation, such that the strongest winds produced by convective turbulence would occur when the sun is highest in the sky, as dictated by local time and latitude (and presumably by season, although this has yet to be tested).

The distribution of friction velocities is also dependent on the initial wind profile, which influences wind gustiness throughout the day and varies in impact with insolation and local time. Such imposed “mean wind” structures generally elevate peak friction velocities, increasing the likelihood that particle entrainment will occur. When the sun is high in the sky, convective activity reaches its peak and, if vigorous enough, can nearly override the initial wind structure. Later in the day when convective activity subsides, the initial wind structure once again dominates the distribution of friction velocities. In the case where initial winds

included shear such that stronger winds blew aloft (which is likely typical of most wind profiles on Mars), convective turbulence throughout the day continued to mix down momentum from these stronger winds, leading to enhanced peak friction velocities that persist into later afternoon hours than would otherwise occur.

The general nature of these relationships is not surprising, since conceptually, the nature of turbulence is determined by the relative strengths of two competing production terms: buoyant processes (tied to surface insolation) and mechanical processes (tied to wind shear). We intend to continue our study of simulated wind distributions and their effect on particle entrainment. Large eddy simulations at other locations (with varying elevation, albedo, and thermal inertia) and seasons will help to establish how these factors influence wind gustiness. Ultimately our goal is to develop a parameterization of the high tail of friction velocities for researchers to use as “perturbation” winds that can be superimposed on “mean” winds from mesoscale models, leading to estimates of particle entrainment on Mars that are more realistic.

**References:** [1] Toigo A.D. et al. (2002) *JGR*, 107(E7), doi:10.1029/2001JE001592. [2] Haberle R.M. et al. (2003) *IC*, 161, 66-89. [3] Armstrong J.C. and Leovy C.B. (2005) *IC*, 176(1), 57-74. [4] Toigo A.D. et al. (2003) *JGR*, 108(E6), doi:10.1029/2002JE002002. [5] Michaels T.I. (2006) *GRL*, 33, doi:10.1029/2006GL026268. [6] Iversen J.D. and White B.R. (1982) *Sediment.*, 29, 111-119. [7] Sullivan R. et al. (2008) *JGR*, 113, E06S07, doi:10.1029/2008JE003101. [8] Newman et al. (2002) *JGR*, 107(E12), 5123, doi:10.1029/2002JE001910. [9] Tuller, S.E. and Brett A.C. (1984) *J. Climate and App. Met.*, 23, 124-134. [10] Rafkin S.C.R. et al. (2001) *IC*, 151, 228-256. [11] Michaels T.I. (2002) MSc thesis, San Jose St. Univ. [12] Deardorff J.W. (1980) *Bound.-Layer Meteorol.*, 18, 495-527. [13] Greeley and Iversen (1985) *Wind as a Geological Process*, Camb. Univ. Press. [14] Ellehøj et al. (2009) *LPS XL*, Abstract #1558. [15] Greeley, R. et al. (2006) *JGR*, 111, E12S09, doi:10.1029/2006JE002743.

**ATMOSPHERIC DUST AND MESOSCALE/MICROSCALE METEOROLOGY.** A. Spiga<sup>1</sup>, S.R. Lewis<sup>1</sup>, and F. Forget<sup>2</sup>. <sup>1</sup> Department of Physics and Astronomy, The Open University, Milton Keynes, United Kingdom ([a.spiga@open.ac.uk](mailto:a.spiga@open.ac.uk), [s.r.lewis@open.ac.uk](mailto:s.r.lewis@open.ac.uk)). <sup>2</sup> Laboratoire de Météorologie Dynamique, CNRS/IPSL, Paris, France ([forget@lmd.jussieu.fr](mailto:forget@lmd.jussieu.fr)).

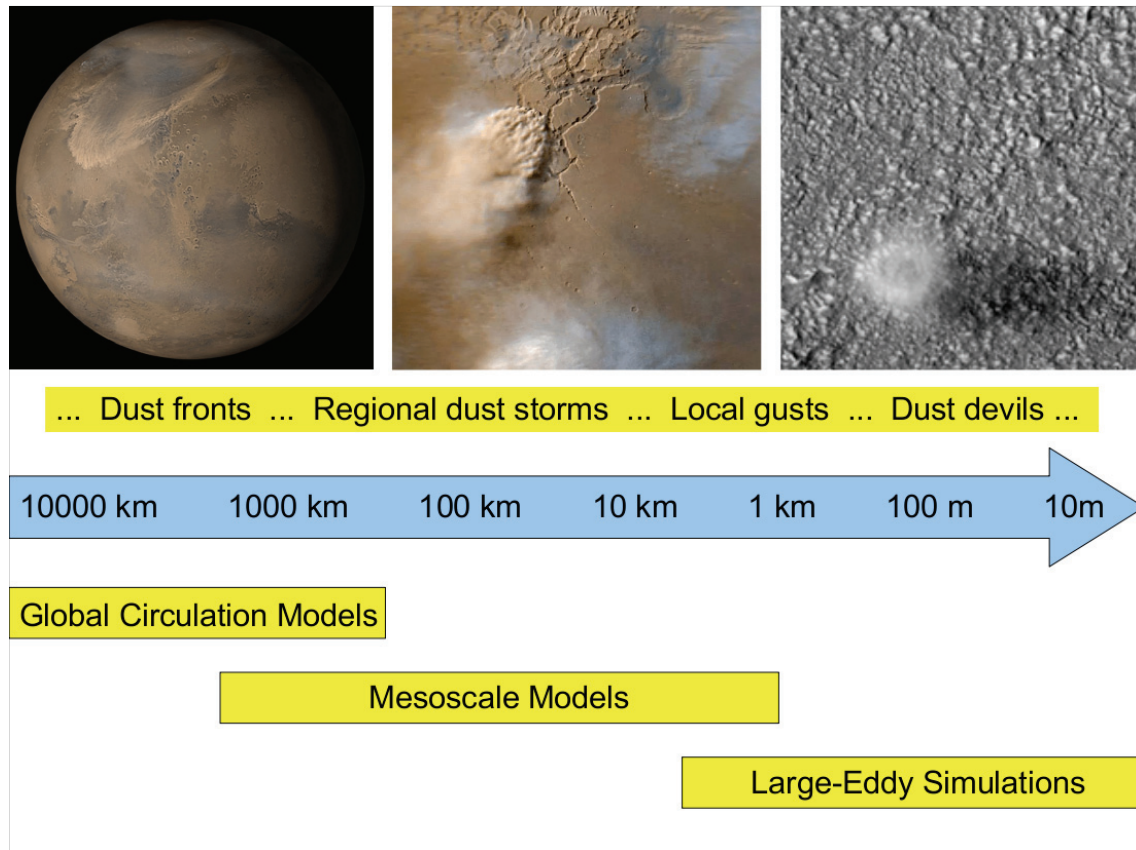


**Figure 1:** Dust lifting processes at various scales on Mars and related meteorological models suitable for their analysis. Note that the right limit of the GCM box keeps on being translated towards the right owing to advances in computational resources and modeling techniques. Note also that mesoscale modeling and Large-Eddy Simulations can be often carried out with the same non-hydrostatic dynamical core.

**Introduction:** On Mars, airborne dust is a crucial climate component influencing thermal structure and atmospheric dynamics at synoptic, meso- and micro-scales. The amount of dust in the atmosphere is controlled by lifting mechanisms and atmospheric transport at these various scales. Distinct numerical tools are needed to examine the lifting, transport and radiative coupled processes related to dust in the Martian atmosphere: general circulation models, mesoscale models, microscale models [Large-Eddy Simulations]. Figure 1 describes this diversity and emphasizes how the dust cycle on Mars involves horizontal scales spanning seven orders of magnitude.

The aim of our work is to examine the wind variability and its relationship to lifting within an area delimited by the usual GCM horizontal resolution (several hundreds of kilometers).

**Mesoscale variability:** We used high-resolution global circulation modeling by the UK spectral model [1] (40 km resolution) and mesoscale modeling in the Tharsis region by the LMD mesoscale model [2] (20 km resolution) forced by LMD GCM fields at its boundaries [3]. Mesoscale variability of friction velocity  $u^*$  appears controlled by topographical obstacles both in nighttime and daytime conditions.



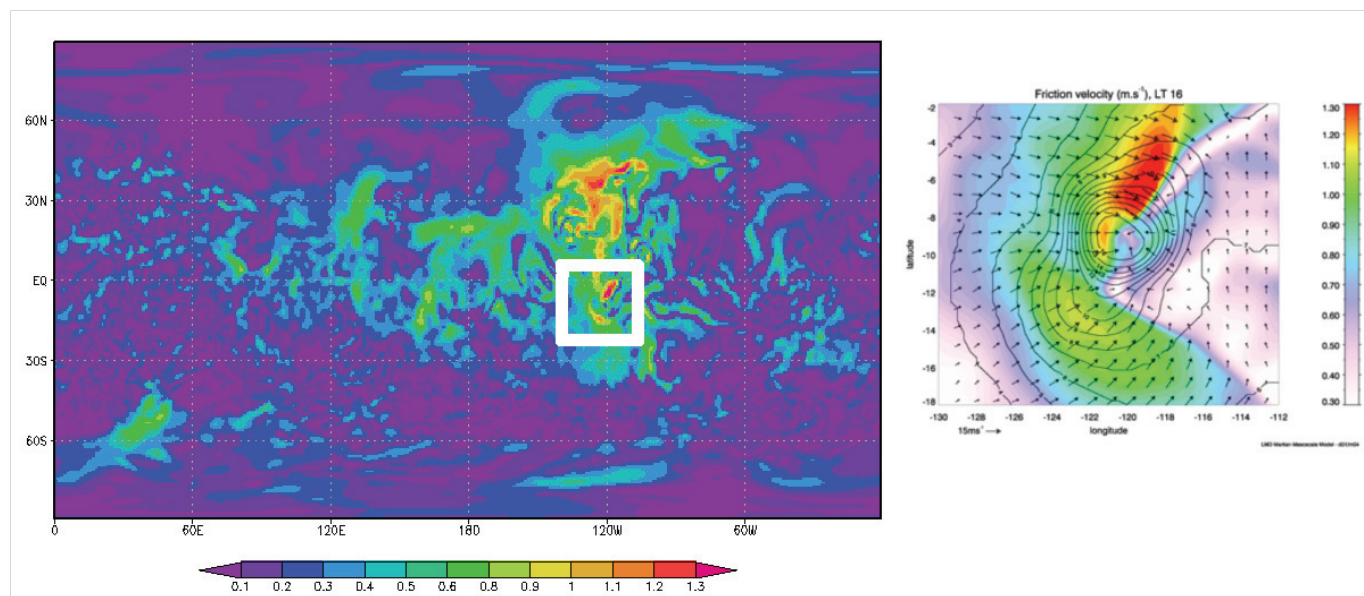


**Figure 2:** Friction horizontal velocities predicted in northern summer ( $L_s \sim 90^\circ$ ) at local time 16h in the Tharsis region. [left] High-resolution global circulation modeling by the UK spectral model (40 km resolution). [right] Mesoscale modeling in the Tharsis region by the LMD mesoscale model (20 km resolution) forced by LMD GCM fields at its boundaries.

Maximum values of  $u^*$  (1.3 – 1.4 m/s) relate to the influence of daytime anabatic and nighttime katabatic winds. During the day, higher values of  $u^*$  correspond to the maximum insolation in the summer hemisphere. Strongest lifting velocity occurs over Tharsis plateaus and Hellas rims. Note that the stress (density times friction velocity squared) is higher during the night owing to diurnal density cycle [4]. Except for lower nighttime friction velocities predicted in the high-resolution UK GCM than in the LMD mesoscale model, agreement between the two different strategies is satisfactory (Figure 2).

**Microscale variability:** In global circulation and mesoscale models, daytime convective mixing is parameterised, which yields an incomplete description of the local gustiness in the Martian atmosphere. A large part of this gustiness is related to turbulent motions in the boundary layer, which can be resolved by lowering resolution of mesoscale models to few tens of meters (with idealized settings) for so-called Large-Eddy Simulations (LES). Boundary layer growth, convective cells and dust devils are described in details by such simulations [5]. An encouraging agreement was found recently by comparing boundary layer depths predicted by LMD LES and measured by radio-occultation measurements on board Mars

Express [6]. Here we analyze the evolution of  $u^*$  in two 50m horizontal resolution LES over Amazonis plains and Tharsis plateaus (Figure 3). Maximum activity is predicted between 12h and 14h30. Even in Amazonis plains where mesoscale variability is low, the turbulent contribution is significant and reach 0.8 m/s in brief episodes of turbulent gustiness. Two distinct phenomena result in  $u^*$  being maximum (Figure 4): convective vortices (occurring at intersections of convective cells) and convective gusts (occurring mostly near walls of convective cells in areas of strong convergence). While intensity of convective gusts is similar in 50m and 100m simulations, convective vortices are poorly resolved in 100m simulations and their  $u^*$  signatures are not as strong as modeled in the 50m resolution case. Regional variations of boundary depth are expected, owing to the strong radiative control of the Martian lower atmosphere: in areas with similar surface temperatures, boundary layer depth is controlled by pressure [7]. This variability also applies for  $u^*$  which is related to the strength of convective mixing. Thus, on the Tharsis plateaus where the boundary layer is measured and modeled 2.5 km deeper than in the Amazonis plains, maximum values of  $u^*$  reach 1.2 m/s instead of 0.8 m/s.

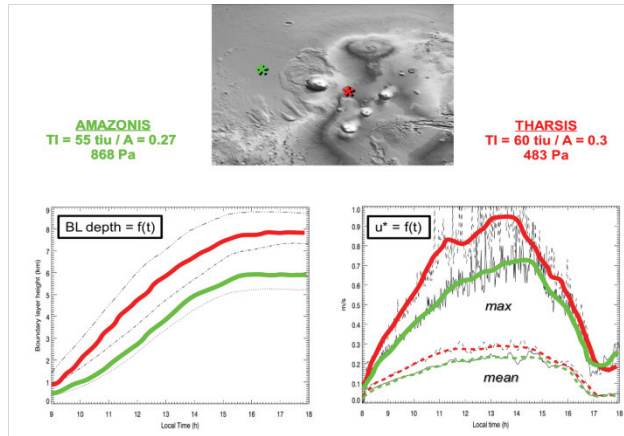


**Figure 3:** Evolution diagnosed from LMD LES of [left] boundary layer depth and [right] friction velocity  $u^*$  in two locations with similar soil properties but distinct altitudes (Amazonis plains in green and Tharsis mountains in red). Boundary layer depth at local time 17h00 is predicted in satisfying agreement with values derived from Mars Express radio-occultation experiments. Values of  $u^*$  in full (dashed) lines.

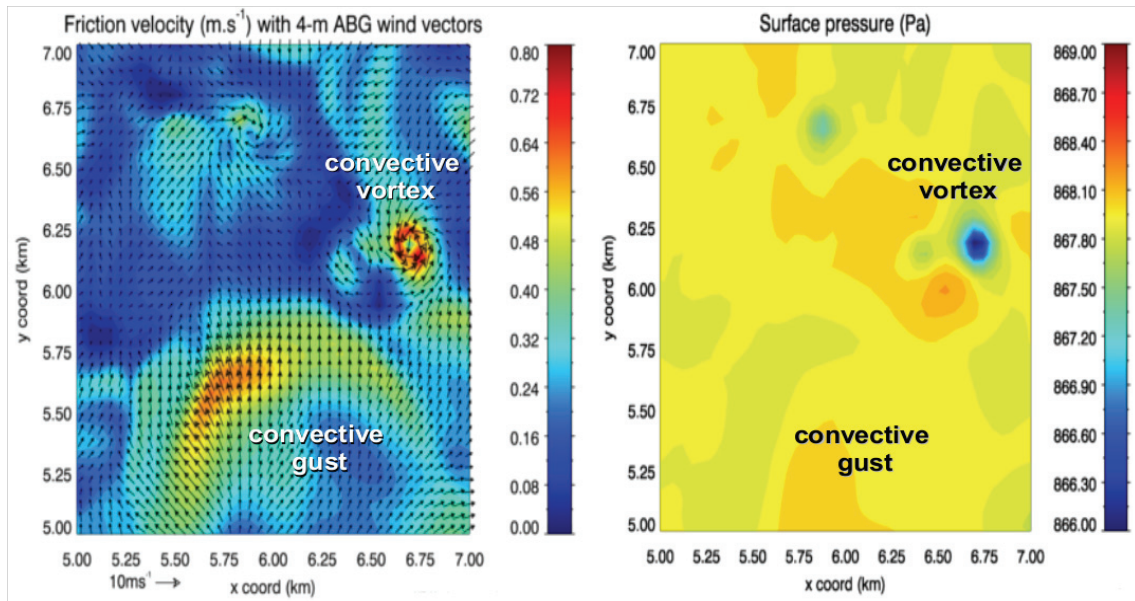


**Figure 4:** Horizontal map of [left] friction velocity (with wind vectors 4m above the surface superimposed) and [right] surface pressure around local time 13h30 in a chosen area of the simulation domain where maximum values for  $u^*$  are detected.

**Transporting dust:** High values of  $u^*$  is only one factor indicating possible dust lifting. The previous section suggests that Tharsis and Solis high-altitude regions are conducive to faster near-surface horizontal winds in convective vortices, which could facilitate dust lifting and dust devil formation. Maps of dust devils occurrence retrieved by MOC imagery [8] confirm that these low-pressure terrains are preferential areas for dust devil formation, but high-pressure terrains such as Amazonis or Hellas are also

key regions for dust devils formation. Next step was thus to include dust lifting and transport by the convective gusts and vortices resolved by the LES so as to get further insights into formation of dust devils – and not only convective vortices which are shown by LES to occur in any place on Mars. Preliminary work was carried out using parameterization based on saltation flux and sandblasting efficiency coefficient [9]. Note that the fixed threshold stress needed to be lowered to 0.01 Pa (instead of 0.025 Pa used in most

GCMs) for dust to be lifted by the resolved near-surface atmospheric winds [10]. The scheme was only tested in a preliminary 100m resolution LES over an Amazonis plain – thus dust was lifted by convective gusts but not by convective vortices. The 100m LES with transported dust enabled however to illustrate how vigorous the mixing in the Martian convective boundary layer is (Figure 5). Dust lifted from the surface by a turbulent wind gust around 13h is quickly advected by convective updrafts and reaches the top of the boundary layer (4 km) in 700s.

LES to examine dust lifting and transport by both convective gusts and dust devils. Even if the very short dynamical timescale for dust transport seems to preclude a significant radiative feedback in dust devils, the question remains open [11] and we will work on that topic with our “dusty” LES. The dust lifting parameterization scheme must be questioned too, so as to know to what extent other effects than saltation influence lifting of dust from the surface: electrostatics [12], direct lifting by winds without saltation [13], low pressure core effects in convective vortices [14]... In addition, sensitivity of boundary layer winds and dust lifting to surface properties (roughness length, thermal inertia) and background winds needs to be determined.

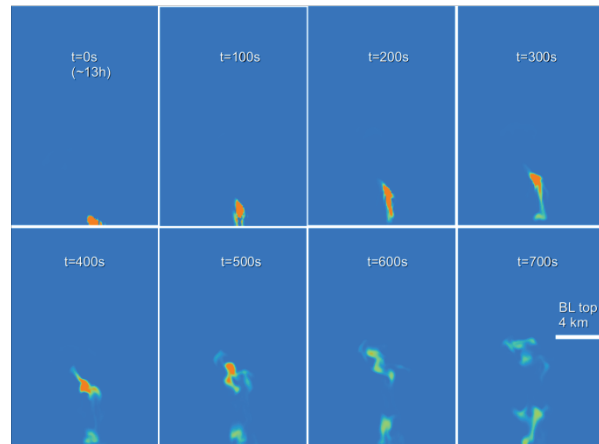


**Figure 5:** Evolution of dust mixing ratio predicted by a 100m LES on a longitude – altitude frame. An image is shown every 100s. At  $t=0$ , dust is lifted in the atmosphere by a convective gust. Local time is 13h. One order of magnitude separates orange to green and green to blue. This figure illustrates the low dynamical timescales for dust mixing in the Martian daytime boundary layer.

**Conclusions / Summary:** Meteorological scales between 100km and 10km can be studied by high-resolution GCM or mesoscale models and show a strong topographical control of the winds which leads to repetitive daytime and nighttime favorable conditions for dust lifting. Scales below 10 km and 1 km are dominated by turbulent gusts and dust devils which are two distinct boundary layer processes likely to lift dust from the surface. The Martian boundary layer features low mixing timescales and regional variability with, in specific conditions, boundary layer and  $u^*$  anti-correlated with pressure. Further studies will be carried out to parameterize lifting by these processes and dust radiative effects once transported in the atmosphere.

#### References:

- |      |                         |                |
|------|-------------------------|----------------|
| [1]  | Lewis and Read          | JGR 2003       |
| [2]  | Spiga and Forget        | JGR 2009       |
| [3]  | Forget et al.           | JGR 1999       |
| [4]  | Hollingsworth and Kahre | this issue     |
| [5]  | Michaels and Rafkin     | QRMS 2004      |
|      | Fenton and Michaels     | this issue     |
|      | Barth et al.            | this issue     |
| [6]  | Hinson et al.           | Icarus 2008    |
| [7]  | Spiga et al.            | submitted QJRM |
| [8]  | Cantor et al.           | JGR 2006       |
| [9]  | Marticonera et al.      | JGR 1995       |
| [10] | Michaels                | GRL 2006       |
| [11] | Heavens et al.          | this issue     |
|      | Fuerstenau              | this issue     |
| [12] | Kok and Renno           | PRL 2008       |
| [13] | Gillies et al.          | this issue     |
| [14] | Greeley et al.          | JGR 2003       |



## AEOLIAN REDISTRIBUTION OF DUST ON THE THARSIS VOLCANOS: SEASONAL AND EPISODIC VARIABILITY.

Lee<sup>1</sup>, S.W., Thomas<sup>2</sup>, P.C., and Cantor<sup>3</sup>, B.A. <sup>1</sup>Denver Museum of Nature & Science, 2001 Colorado Blvd., Denver, CO 80205, [Steve.Lee@dmns.org](mailto:Steve.Lee@dmns.org); <sup>2</sup>Department of Astronomy, Cornell University, Ithaca, NY 14853, [pthomas@astro.cornell.edu](mailto:pthomas@astro.cornell.edu); <sup>3</sup>Malin Space Science Systems, 9115 Brown Deer Rd., San Diego, CA 92121, [cantor@msss.com](mailto:cantor@msss.com)

**Introduction:** Beginning with the Viking Orbiter missions (with some hints as far back as the Mariner 7 flyby in 1969), aeolian activity on the Tharsis volcanoes has been observed in the form of dark “collars” on the flanks surrounding the summits. Early work [1, 2] indicated downslope winds could reach the threshold velocities necessary to entrain bright dust from a rough volcanic surface (even at ambient pressures of 0.5 mb or less!), yielding these dramatic variable albedo features. A great deal of topographic control over the wind direction was apparent. The Mars Reconnaissance Orbiter (MRO) Mars Color Imager (MARCI), Context Imager (CTX), and High Resolution Imaging Science Experiment (HiRISE) data are being used to extend the observations of dust transport in this region to the current era – with repeatable temporal and spatial coverage.

**MRO Observations:** At present, MRO has provided more than one martian year of observations of the surface and atmosphere, allowing the spatial and temporal behavior of aeolian activity in the Tharsis region to be examined in detail.

*MARCI mapping of the Tharsis Montes.* MARCI observations have been mosaicked into global albedo images with temporal resolution of about 3-4 weeks and spatial resolution of about 1-km per pixel at the equator. MRO observed a global dust-lifting event beginning in July 2007. Focusing on the Tharsis region (Figs. 1 and 2), the evolution of the “dark collars” on the Tharsis Montes following this global dust-lifting event can be followed both spatially and temporally.

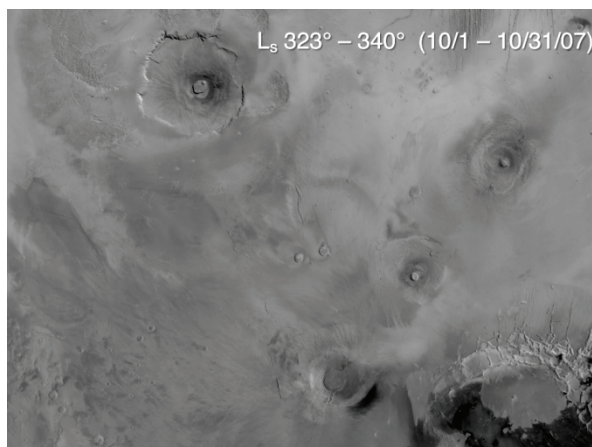


**Figure 1a:** MARCI albedo map (simple cylindrical projection, scale 64 pixels/degree [about 1 km/pixel at the equator], Lambert correction applied).

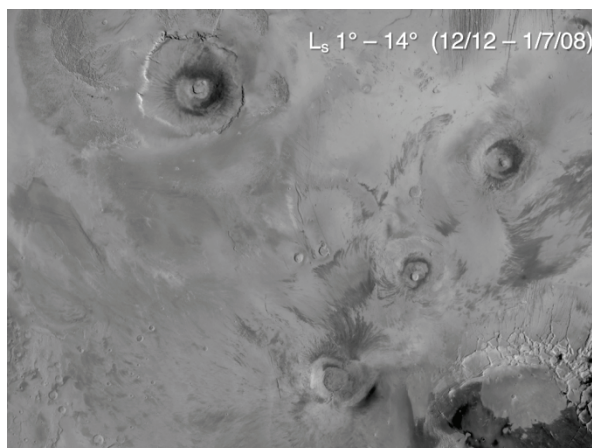


**Figure 1b:** (Mosaic details as for Fig. 1a).



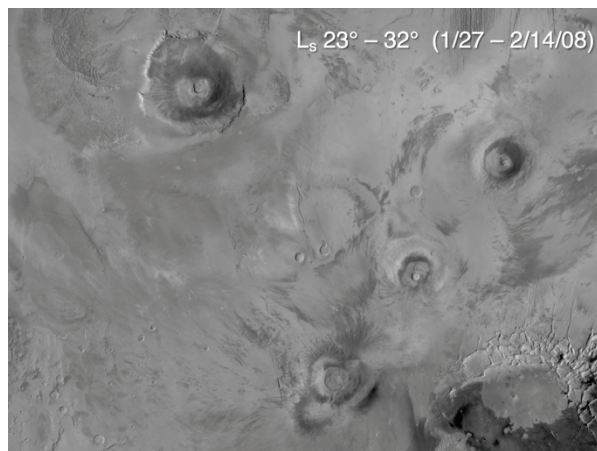


**Figure 1c:** (Mosaic details as for Fig. 1a).

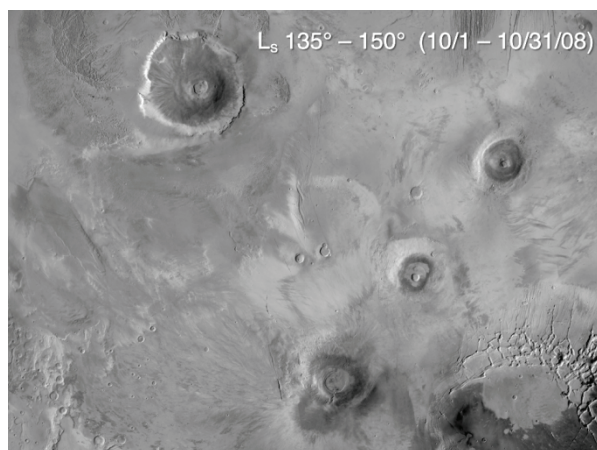


**Figure 1d:** (Mosaic details as for Fig. 1a).

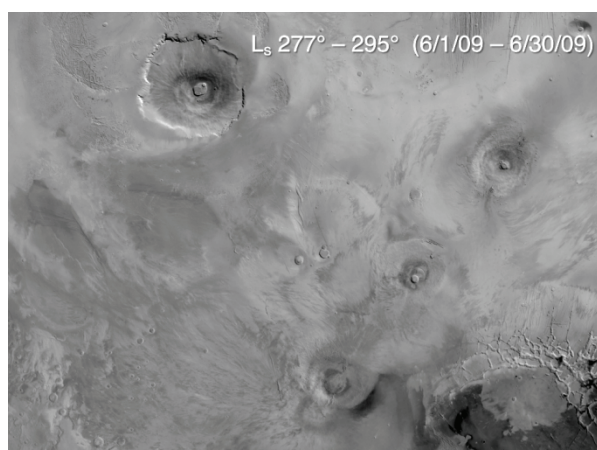


**Figure 1e:** Extensive dust-lifting occurred in several areas of Mars in February – March 2009, apparently “resetting” the contrast and configuration of the “dark collars” to a state similar to that following the 2007 global dust-lifting event (compare to Fig. 1a).

The MARCI observations are in agreement with those made two decades earlier by the Viking Orbiters, indicating topographic control of the wind patterns on and near the slopes of the Tharsis Montes. These observations support the idea that bright dust is deposited across the surface, even near the tops of the volcanoes, following global dust-lifting events; subsequent downslope winds exceed the threshold velocity necessary to entrain bright dust and sweep it from these surfaces. Aeolian activity is apparent even at the lowest atmospheric pressures existing on the planet’s surface. The observations are in accord with GCM results indicating net deflation of sediment in the Tharsis region under current conditions [3].

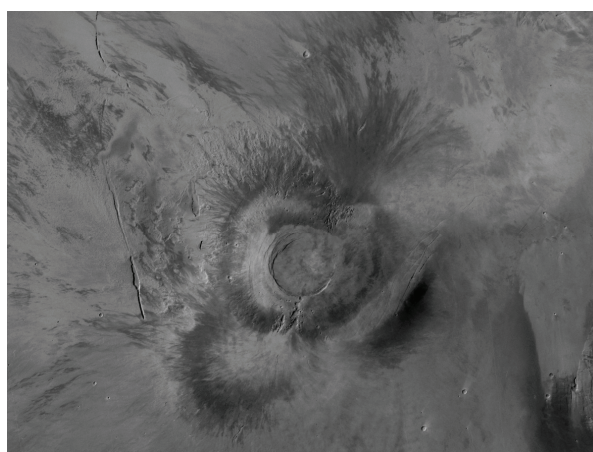


**Figure 2a:** Detail of the “dark collar” on Arsia Mons (from Figure 1c).

*CTX and HiRISE observations of the Tharsis Montes.* Observations with substantially greater spatial resolution are available from CTX (6 m/pixel) and HiRISE (25 cm/pixel), providing further insight into the processes leading to the dramatic variable albedo features observed by MARCI. The sedimentary history on the volcanoes, even at the tops, is shown by these high-resolution images to have been long, complicated, and continuing. Fig. 3 provides a key to a set of CTX and HiRISE images of portions of the “dark collar” on Pavonis Mons. Changes in the collar can be resolved into sawtooth and linear dark streaks, of multiple contrasts and probably multiple generations (Fig. 4). Some streaks are resolved as originating at topographic obstacles such as crater rims. CTX data also show that dark wind streak development high on Pavonis Mons currently occurs in multiple directions other than simply downslope (Fig. 5). Here, we see downslope streaks and other dark streaks with three distinct orientations.



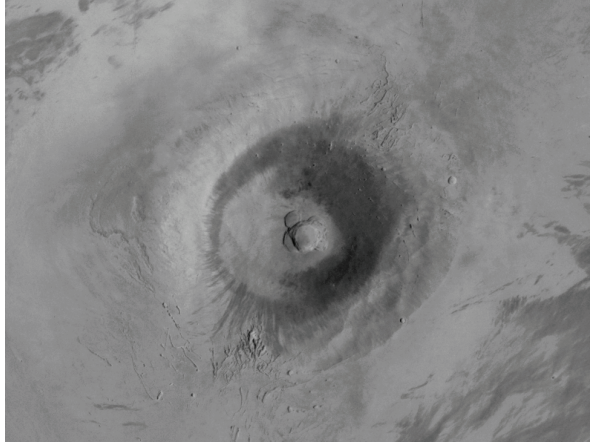


**Figure 2b:** Detail of the “dark collar” on Ascraeus Mons (from Figure 1c).

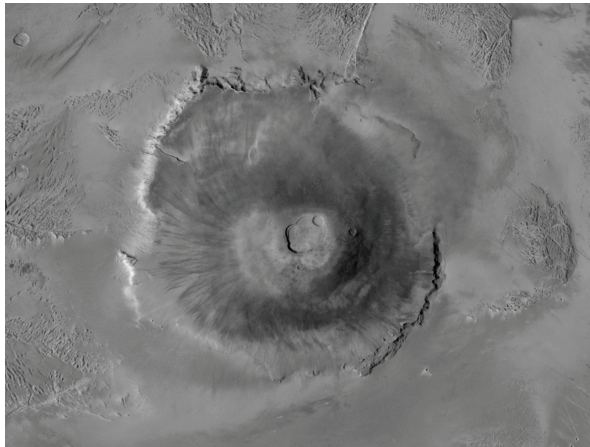


**Figure 2c:** Detail of the “dark collar” on Olympus Mons (from Figure 1c).

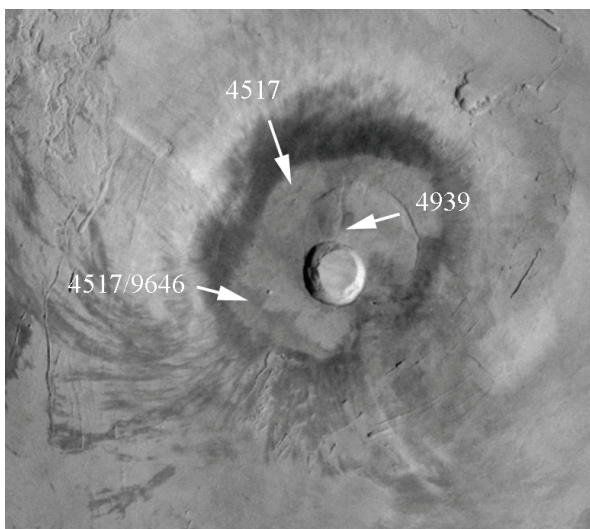


**Figure 3:** Detail of the “dark collar” on Pavonis Mons (from Figure 1c). The location of the CTX and HiRISE frames shown in Figs. 4 – 7 are indicated.

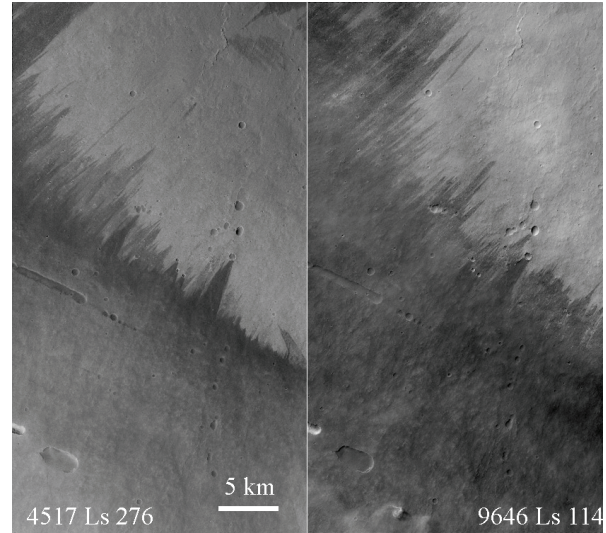


**Figure 4:** Co-registered CTX observations of variable boundary of the Pavonis Mons “dark collar”, taken about 13 months apart on MRO orbits 4517 (left) and 9646 (right). Refer to Fig. 3 for image location.

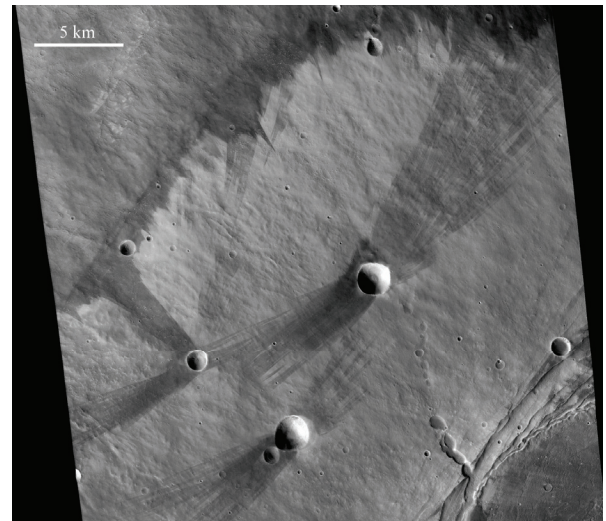


**Figure 5:** CTX image of the Pavonis Mons “dark collar” taken on MRO orbit 4517, indicating dust erosion by winds of multiple orientations. Refer to Fig. 3 for image location.



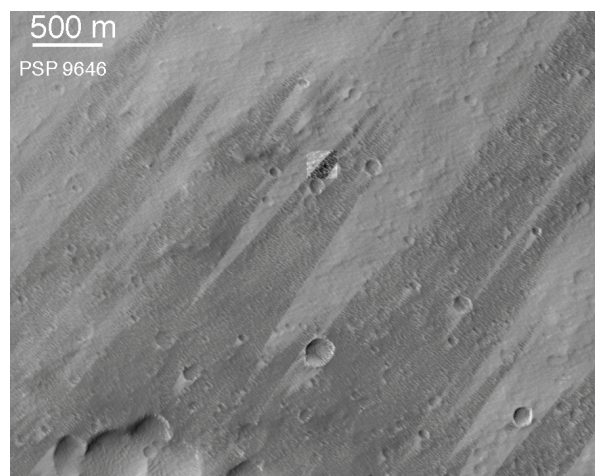


**Figure 6a:** HiRISE view of the Pavonis Mons “dark collar” boundary, taken on MRO orbit 9646. The highlighted box denotes the area covered by Fig. 6b. Refer to Fig. 3 for image location.

HiRISE views of the collar on Pavonis Mons show multiple generations and scales of bedforms. (Fig. 6). The dark streaks maintain sharp boundaries down to scales of a few m; at the highest scales the dark streaks are affected by underlying (transverse?) bedforms, seemingly occurring preferentially on one side of these forms. The underlying bedforms, ripples, or possibly dunes [4], are muted and appear slightly degraded, that is, possibly not active in recent years.

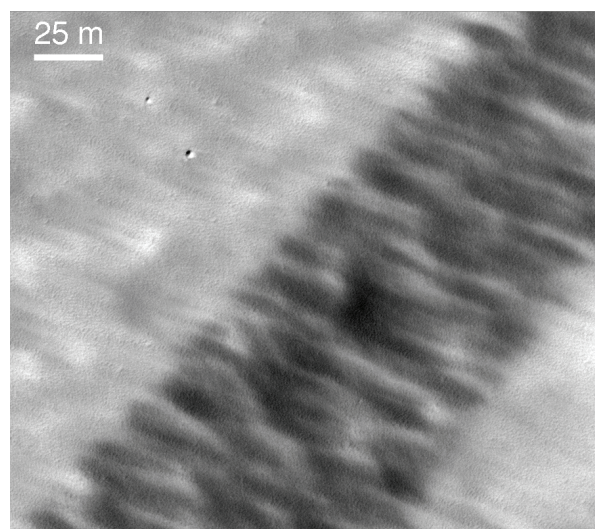


**Figure 6b:** Zoomed-in HiRISE view of the Pavonis Mons “dark collar” boundary. Refer to Fig. 6a for image location.

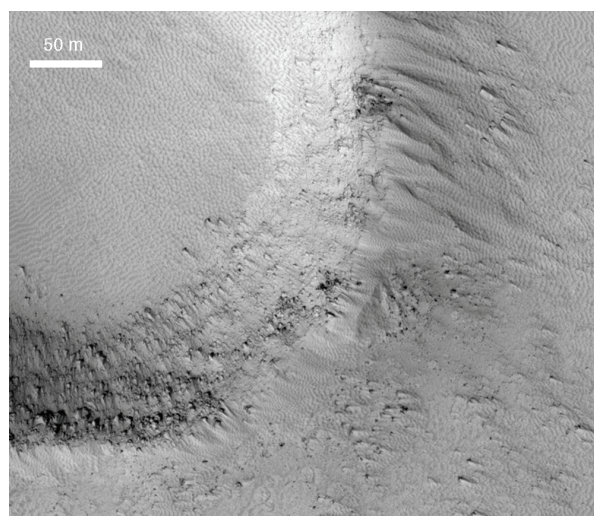


**Figure 7:** HiRISE image, obtained on MRO orbit 4939, of a crater near the summit of Pavonis Mons. Note the variety of yardangs near the crater rim, and the variety of small bedforms across the surface both interior and exterior to the crater. Refer to Fig. 3 for image location.

In another location on Pavonis Mons (Fig. 7), HiRISE data show yardangs or drifts and reticulated small bedforms (also mapped by [4]). These data show that the several meters of surface deposits high on Pavonis (and other Tharsis volcanoes) have been subject to multiple periods of deposition, transport by surface saltation (possibly of dust “aggregates” [4]), and erosion. Erosion may be the more dominant process in the recent period.

**Conclusions:** MARCI regional-scale mapping over much of a martian year, coupled with high spatial resolution CTX and HiRISE images, reveals a formation scenario for the “dark collars” on the Tharsis Montes considerably more complicated than “simple” downslope winds sweeping a veneer of bright dust from a darker substrate. At present, dust redistribution on the Tharsis Montes is primarily induced by downslope winds, but other wind directions are also evident - and obviously effective. Over the long-term, a complex sedimentary history, arising from multiple wind directions, is evident – at multiple spatial scales and over a range of ages.

**References:** [1] Lee S. W. et. al. (1982) JGR, 87, 10025-10041. [2] Magalhaes J. and Gierasch P. (1982) JGR, 87, 9975-9984. [3] Kahre M.A. et. al. (2006) JGR, 111, E06008. [4] Bridges N.T. et. al. (2009) Icarus, in press.

# ***Session Six***

## *Lifting and Dynamics Associated with Large-Scale Systems*

*Wednesday, September 16, 2009*

*3:30 PM – 5:00 PM*



## EXTRATROPICAL CYCLONES, FRONTAL WAVES AND MARS DUST: MODELING AND CONSIDERATIONS.

Hollingsworth<sup>1</sup>, J.L. and Kahre<sup>2</sup>, M.A. <sup>1</sup>Space Science and Astrobiology Division, Planetary Systems Branch, NASA Ames Research Center, Moffett Field, CA 94035 ([jeffh@humbabe.arc.nasa.gov](mailto:jeffh@humbabe.arc.nasa.gov)). <sup>2</sup>Bay Area Environmental Research Institute/NASA Ames Research Center, Moffett Field, CA 94035 ([kahrema@mintz.arc.nasa.gov](mailto:kahrema@mintz.arc.nasa.gov)).

**Introduction:** During autumn through spring, extratropical regions on Mars indicate profound equator-to-pole thermal contrasts. From data collected during the Viking era and from observations obtained from the Mars Global Surveyor (MGS) and recent Mars Reconnaissance Orbiter (MRO) missions, the imposition of this strong temperature contrast supports intense eastward-traveling weather systems (i.e., transient synoptic waves) [1,2,3,4,5] originating from the dynamical process of baroclinic instability. Having more “regular” lifecycles compared to those on Earth [6], such traveling disturbances and their poleward transports of heat and momentum, influence directly the global atmospheric energy budget. Further, transient baroclinic waves impact other atmospheric scalars (e.g., temperature, horizontal winds, dust mixing ratio, etc).

Mars exhibits distinctive “continentality.” Tharsis in the western hemisphere and Arabia Terra and Elysium in the eastern hemisphere, are the primary large-scale topographic features in northern midlatitudes. Tharsis and Argyre in the western hemisphere and Hellas in the eastern hemisphere are the primary topographic features in southern midlatitudes. These underlying orographic complexes cause latitudinal excursions of the seasonal mean westerly circum-navigating polar vortex but also modulate the intensity and preferred geographic regions of baroclinic weather systems [7].

Most numerical investigations of baroclinic instability in Mars’ atmosphere have adapted coarse horizontal resolution. With such resolutions, large-scale dynamical processes intrinsic to the development and decay of the traveling mid- and high-latitude transient baroclinic waves—the synoptic-scale cyclogenesis from which frontal structures can develop—are adequately resolved. Yet because the models have been coarse, energy associated with the synoptic scale cyclogenesis is limited in its cascade toward smaller and smaller spatial scales. This precludes resolving complex circulations such as shear and stretching deformations accompanying intense large-scale cyclonic and anticyclonic vortices, and scalar contractions and dilatations accompanying frontal waves on the sub-synoptic scale and less.

Our goal here is to ascertain the atmospheric environmental conditions under which near-surface and/or upper-level fronts (i.e., narrow zones of enhanced mass density, momentum and thermal contrasts within individual transient baroclinic waves) form within Mars’ baroclinic zone. We wish to investigate dynamical influences such frontal waves have on the lifting, organization and transport of atmospheric dust in the extratropics and its interaction with other circulation components (e.g., up-slope/down-slope flows, thermal tidal modes, quasi-stationary components, etc). Paramount is our desire to ascertain the atmospheric conditions conducive to frontogenetic (development) and frontolytic (decay) phases of individual frontal waves, and the roles such disturbances have on the transport of atmospheric dust, with the overarching goal of assessing the influences such systems have on the dust cycle of Mars.

**Climate Model:** In this investigation, we build upon previous mechanistic studies (i.e., high-resolution simple-physics global circulation models [8]) by applying a state-of-the-art, full-physics general circulation model (GCM) for Mars [9,10,11].

The NASA Ames Mars GCM is formulated using the ARIES/GEOS C-grid “dynamical core”, version 2 [15]. The vertical coordinate is a normalized pressure, terrain-hugging one. Improvements in the treatment of atmospheric transport of arbitrary scalars has been implemented using finite-volume techniques following the work of [16]. The particular version adapted for this investigation implements a radiatively-active dust cycle for a fixed particle size. Dust lifting is parameterized in terms of a surface-stress scheme [10,11]. Details on the physical parameterizations contained in the model are described in [9,10,11].

The model configuration we adapt has 24 unequally-spaced vertical layers with a model “top” pressure of  $5 \times 10^{-4}$  mbar. Vertical spacing between layers increases from O(10 m) at the surface to O(5 km) near the model top. We impose a  $2.0 \times 3.0$  longitude-latitude grid resolution in the horizontal.



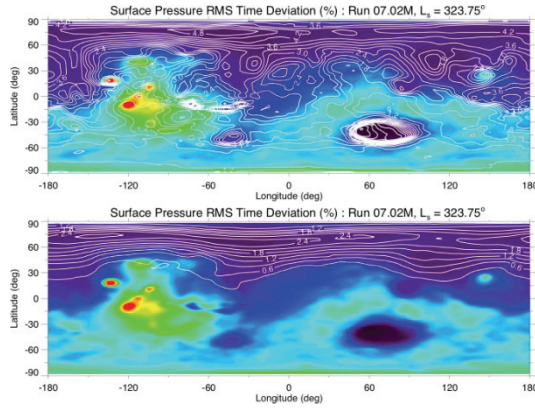


**Figure 1:** Surface pressure RMS time deviations for (a) unfiltered and (b) band-pass time filtered at  $L_s=323^\circ$ .

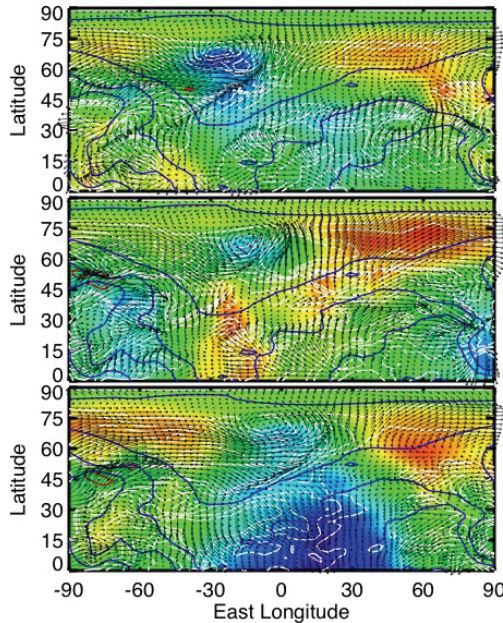


**Figure 2:** Surface pressure anomalies, low-level horizontal wind and surface stress time deviations separated by 6 hr intervals at  $L_s=315^\circ$ .

**Results:** From our multi-annual high-resolution simulation, we focus here on late northern winter ( $L_s=324^\circ$ ). We examine one extratropical synoptic weather event and its associated frontal wave, and the nature of dust lifting, organization and transport associated with this system. Forty sols of model output are analyzed to construct a “seasonal mean” state. Instantaneous time departures, both temporally unfiltered components (e.g., those associated with diurnally-varying modes) and band-pass filtered components (i.e., those associated with only synoptic-period modes), are examined. In this season, mean

zonal temperatures are far colder in the northern hemisphere (still at a near-winter state) with enhanced baroclinicity near the surface and aloft associated with the retreating seasonal  $\text{CO}_2$  polar ice cap. The mean thermal contrast supports a vigorous westerly polar vortex with wind speeds in excess of  $O(160 \text{ m s}^{-1})$  at altitude.

Figures 1–3 reveal that this season supports both intense diurnally-varying wave phenomena and synoptic-period transient weather systems. In Figure 1 are the root-mean-square (RMS) surface-pressure variations for both the unfiltered (i.e., diurnally-varying and thermal tidal modes included) and the synoptic period disturbances. Variability associated with the diurnally-varying components can be seen (Fig. 1 top) over the higher relief regions. A strong influence by such short-period modes on the day-to-day weather modes at middle and high latitudes is indicated (i.e., the northern hemisphere storm zone becomes enhanced and shifted in longitude). High- and low-pressure cores (Fig. 1 bottom) are confined to middle and high latitudes and travel eastward within the region of the seasonal polar cap. They generally peak in low-relief regions. Significant interactions occur at this season between the diurnally-varying modes and the synoptic-period weather, similar to predictions found in simpler global circulation modeling studies [6].

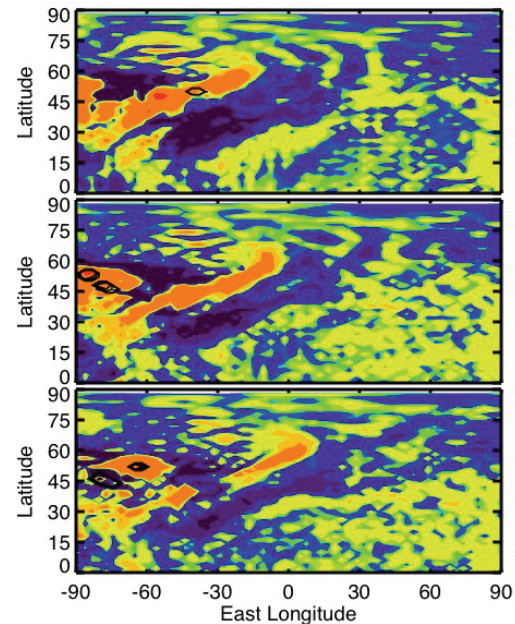


**Figure 3:** Dust mixing ratio time deviations separated by 6-hr intervals at  $L_s=315^\circ$ , corresponding to the kinematic fields depicted in Figure 2.

Connected to surface-pressure variability patterns are patterns of variability in surface stresses (not shown). Such patterns maximize in the western hemisphere (i.e., along the Tharsis volcanoes, Olympus Mons, Alba Mons) and are somewhat weaker in the eastern hemisphere (associated with the Arabia highlands and Elysium further to the east). Maximum surface stresses in the western hemisphere are a result of strong nocturnally dominant down-slope flows. These regions frequently exceed the stress dust-lifting threshold value of 22.5 mPa.

Figure 2 shows further evidence of intense synoptic-period transient weather systems (each panel in Figures 2–4 are separated by 6 hrs). The color-shaded field corresponds to surface pressure anomalies. A series of extratropical cyclones and anticyclones develop, intensify, decay and travel eastward. Surface pressure anomalies are associated with “troughs” and “ridges” that range between  $O(5\text{--}10\%)$  about a global reference value. The longitudinal scales of these transient waves are associated with zonal wavenumbers 1–3. These wavenumbers indicate a preferred “selection” for large-scale transient activity and cyclogenesis near the Rossby deformation scale. East-west (zonal) phase speeds of  $O(10\text{--}30\text{ m s}^{-1})$  are indicated. The weather systems are most intense in the lee of the Tharsis highlands. Within the western hemisphere, this region has been recognized to be an active storm zone [7,12,13,14].

The low-level horizontal wind indicates lines of convergence (i.e., frontal zones) in the low-relief regions of this hemisphere (Acidalia/Chryse). In the early stages, the frontal zone has a “wishbone”-like structure that coalesces by 12 hr into a single zone of convergence and then progresses eastward. In the high-relief regions to the west, surface stresses exceed the threshold value. These fields show classical signatures associated with frontogenetic processes: shear and stretching deformations, and flow contractions/dilatations that can alter atmospheric scalars (e.g., temperature, dust mixing ratio, etc). Peak low-level horizontal wind speed deviations in this region approach  $O(20\text{ m s}^{-1})$ . With a smaller planetary radius yet similar Rossby deformation scales, weather systems on Mars are more hemispherically effective at “stirring” and “mixing” the high-latitude cold air boundary into the subtropics.

In Figure 3 are low-level time deviations of atmospheric dust mixing ratio,  $q'$ . Maximum dust content occurs in the western hemisphere and within the frontal wave. The maximum dust-lifting rate (solid black contours) occurs primarily over the high-relief regions and does not occur along the frontal

convergence zone. Cross-frontal gradients in dust mixing ratio can be seen, with maxima occurring near the frontal boundary and minima both behind and ahead of the frontal wave. These patterns appear to indicate tracer (i.e., atmospheric dust) “focusing” and organization associated with frontal wave circulations.

Within 12 hr, the dust filament “breaks” apart in mid-section, with the northern part continuing northward and eastward with the parenting cyclone, and the southern part remaining near stationary over higher relief. Associated with strong horizontal flow convergence, dust is also organized and enhanced within the eastward flank of the core cyclonic system.

Clear cold-air and warm-air sectors associated with the transient surface pressure anomalies develop. Such frontal wave structures are low-level impressions of traveling, amplifying and decaying baroclinic waves. Large-scale orography plays a significant role in breaking the hemispheric symmetry of the martian northern cold polar front: it influences the meridional scale of individual baroclinic waves and the accompanying frontal waves.

**Circulation and Dynamical Considerations:** In terms of instantaneous fields of surface pressure, near-surface winds, temperature and dust mixing ratio, there is a relationship between spatial and temporal patterns of these scalars: they are all “entangled” within an individual frontal wave disturbance. This is necessary because of the requirements for dynamical balance within the fundamentally 3D-nature of the circulation associated with a developing large-scale cyclone/anticyclone pair, and the concomitant energy cascades toward smaller and smaller scales as visualized in sub-synoptic scale frontal impressions. Generally, there is no distinct single measure of the location/identification of a “front” since it necessarily depends on the particular thermal, dynamical or tracer quantity of interest. Spatial/temporal differences in such fields delimit different morphologies within a given sub-synoptic scale system, and for balance constraints, temporal and spatial offsets are requisite for the transport of heat, momentum and individual tracer species within a developing/decaying frontal wave.

We have explored temporal and spatial evolution of higher-order diagnostic quantities such as time deviations in relative vorticity. Examinations of instantaneous fields of relative vorticity clearly capture locations of the parenting cyclone and the associated frontal convergence zone which acts to organize (via horizontal transport) atmospheric dust within a given frontal wave. Relative vorticity can identify regions where frontal waves become “fractured” in the



horizontal which then can lead to a subtropical dust remnant that is free to be transported further southward within the low-relief corridors, depending on the timing and phase of the thermal tidal circulation. Such large dust-activity events have been observed to be advected well into the southern hemisphere [13,14] and have been denoted “flushing” storms.

The circulation within an cyclone/anticyclone disturbance and its accompanying frontal wave is richly 3D due to requirements of thermal and dynamical balance within an individual weather system [17,18]. Associated with the convergent/divergent and stretching/deforming quasi-horizontal circulations in a frontal system is a secondary, cross-frontal (ageostrophic) circulation [17,18] which results in ascending (descending) motion ahead (behind) the frontal zone. The occurrence of this secondary circulation can be assessed in terms of the so-called  $\mathbf{Q}$  vector where  $\mathbf{Q} = (Q^{(x)}, Q^{(y)}, 0)$  is a horizontal vector whose components are comprised of the products of horizontal shears in the horizontal wind and directional derivatives in potential temperature [19]. Further,  $\mathbf{Q}$  is a good dynamical indicator of frontogenetic/frontolytic processes within a front, and the cross-frontal (secondary) circulation can be shown to be proportional to its divergence.

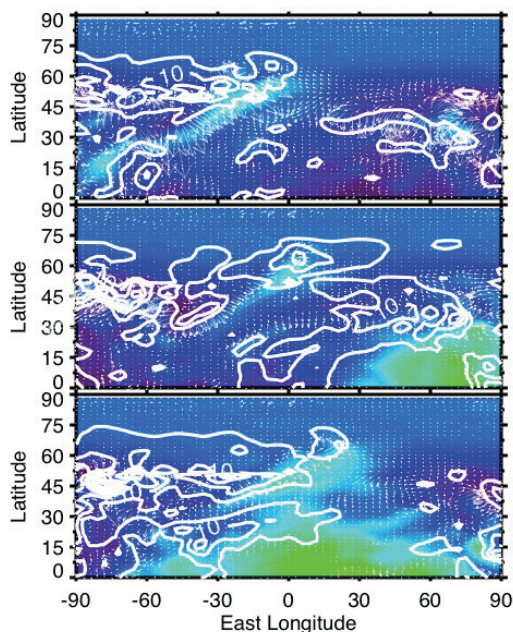


**Figure 4:** Near-surface temperature anomalies, surface stress magnitudes and the  $\mathbf{Q}$  vector separated by 6-hr intervals at  $L_s=315^\circ$ , corresponding to the kinematic fields depicted in Figure 2.

Figure 4 shows longitude-latitude sections of the instantaneous thermal anomaly (color shading), together with surface stress magnitudes and  $\mathbf{Q}$  for the same time steps as in Figures 2 and 3. Instantaneous surface stress maximize *behind* the convergence zone of the front and they are enhanced on the eastward side of the parenting cyclone. Rarely do the stresses accompanying the front exceed the threshold lifting stress. They are significantly weaker than those found upstream in the high-relief regions associated with the nocturnal down-slope flows. The thermal anomaly associated with the sub-synoptic weather system has a filament-like structure in the extratropics, similar to the dust mixing ratio seen in Figure 3. Warm anomalies are accompanied by clear ascending motion, evidenced by the convergence of  $\mathbf{Q}$  just ahead of the front.

**Summary and Conclusions:** The imposition of Mars’ strong baroclinicity supports intense and vigorous eastward traveling weather systems (i.e., transient synoptic-period waves), particularly in northern late winter/early spring that on large scales have accompanying sub-synoptic scale ramifications on the atmospheric environment through cyclonic/anticyclonic winds, deformations and contractions/dilatations in temperatures, and sharp perturbations amongst atmospheric tracers (e.g., dust).

High-resolution GCM simulations with the NASA Ames Mars general circulation model with a consistent, interactive dust cycle suggest that in the northern hemisphere, dust is lifted primarily by nocturnal down-slope flows over the Tharsis volcanoes and Alba Mons of the western hemisphere. Maximum surface stresses typically occur in these regions and just on the leeward side of Alba Mons (e.g.,  $-80^\circ\text{E}$ ). Temporal variability is highest in these regions as well, and instantaneous surface stresses often exceed the threshold stress value required for stress-related dust lifting (22.5 mPa). Dust that is lifted into the atmosphere can become *organized* and *carried downstream* associated with synoptic weather systems and frontal-related circulations.

Observations appear to indicate that dust lifting may very well be occurring along frontal convergence zones themselves. Thus far, our GCM simulations indicate that stress-related dust lifting occurs primarily upstream, and that dust can become “focused” within the frontal systems via intense circulations, and deformations and dilatations. This bring to light that stress-related dust lifting parameterizations to date are perhaps insufficient and may be lacking key physical processes required to raise dust within highly gusty and/or turbulent environments likely to be occurring

within Mars' frontal disturbances. It may be the case that keying dust-lifting off of a higher-order, sub-synoptic scale circulation quantity can better capture dust raising in frontal systems. Further work is required to assess the thermal tidal "gate" and the interactions of the low-topographic relief "duct" to understand the modulations of interhemispheric dust transport initiated via extratropical cyclones and frontal waves.

**References:** [1] Barnes J.R. (1980) *JAS*, 37; Barnes J.R. (1981) *JAS*, 38. [2] Barnes J.R. (2003) *MAMO2003*; Banfield D. et al. (2004) *ICA*, 170. [3] Hinson D.P. and Wilson, R.J. (2002) *GRL*, 29. [4] Hinson D.P. (2006) *JGR*, 111. [5] Hinson D.P. and H.

Wang (2009) *ICA*. [6] Collins M. et al. (1996) *ICA*, 120. [7] Hollingsworth J.L. et al. (1996) *NAT*, 380; Hollingsworth J.L. et al. (1997) *ASR*, 19. [8] Hollingsworth J.L. (2003) *MAMO2003*. [9] Haberle R.M. et al. (1999) *JGR*, 104. [10] Kahre M.A. et al. (2006) *JGR*, 111. [11] Kahre M.A. et al. (2008) *ICA*, 195. [12] James P.B. and Cantor B.A. (2001) *ICA*, 154. [13] Wang H. et al. (2003) *GRL*, 30. [14] Wang H. et al. (2005) *JGR*, 110. Suarez M.J. and Takacs L.L. (1995) NASA Tech. Memo. 104606. [16] Hourdin, F. and Armengaud, A. (1995) *MWR*, 127. [17] Hoskins, B.J. and Pedder, M.A. (1980) *QJRM*, 106. [18] Sanders, F. and Hoskins, B.J. (1990) *WXP*, 5. [19] Kurz, M. (1992) *MAP*, 48.

## THE ROLE OF SPATIALLY VARIABLE SURFACE DUST IN GCM SIMULATIONS OF THE MARTIAN DUST CYCLE.

R. J. Wilson<sup>1</sup> and M. A. Kahre<sup>2</sup>. <sup>1</sup>NOAA/Geophysical Fluid Dynamics Laboratory, Princeton, NJ 08542 (John.Wilson@noaa.gov), <sup>2</sup>Space Science Division, NASA/Ames Research Center, Moffett Field CA, 94035.

**Introduction:** An outstanding problem for simulating the present Mars climate is representing the spatial and temporal variability of aerosols and the feedbacks that connect dust raising and transport with the evolving atmospheric circulation. Various modeling groups have simulated aspects of the dust cycle with Mars global climate models (MGCMs) with limited success [1,2,3,4,5,6]. A particular challenge has been the inability of MGCMs to realistically simulate interannual variability, most notably in the occurrence of major dust storms. The threshold for dust lifting by resolved surface stresses plays a central role in the current parameterizations of dust lifting used in these simulations. To date, MGCM studies have employed a globally uniform stress threshold ( $\sigma_t$ ) as one of the tuning parameters. This assumption can be problematic for simulating large dust storms because there are very strong spatial (and seasonal) variations in resolved surface stress that are associated with specific topographic features. As a result, a few regions tend to unrealistically dominate the simulated dust storm climatology. *Pankine and Ingersoll* [7,8] developed a simple atmospheric model to show that surface/atmosphere dust interactions could plausibly yield an evolving, self-organized  $\sigma_t$  that supports aperiodic global dust storm activity. We have begun exploring this possibility in a more realistic context by implementing a finite surface dust reservoir in the GFDL MGCM and allowing  $\sigma_t$  to vary as a function of the evolving surface dust depth.

**Previous dust cycle modeling results:** To date, all MGCM simulations of dust lifting for Mars have employed parameterizations based on convective activity (so-called “dust devil lifting”) and explicitly resolved surface stress. It is generally accepted that surface stresses account for much of the dust lifting associated with storm events. Stress-related dust lifting parameterizations are characterized by two tunable parameters:  $\sigma_t$  (equivalently  $U_t$ , the threshold drag velocity) and  $\alpha$ , the so-called “efficiency factor” [1,4,5]. A stable, seasonally-varying dust cycle can be achieved for a range of choices of the tuning parameters, with a global mean opacity that is more or less strongly peaked around  $L_s=270^\circ$ , reflecting the

relative weighting of dust devil and surface stress sources. Wind stress lifting accounts for the peak in dust lifting during the SH spring/summer season, while dust devil lifting is required to provide the background dust opacity present in other seasons when stress levels are generally weak. Such simulations are only in rough agreement with the observations, which generally show pre- and post-solstice peaks in opacity [9,10,11]. Moreover, significant interannual variability (major dust storms some years, and quiescent storm seasons in others) has been elusive.

*Pankine and Ingersoll* [7,8] considered the issue of interannual variability of global dust storms in the context of a highly simplified model that represented the Hadley cell. The circulation intensity was set to depend on dustiness, which was coupled to the implied surface wind. For fixed values of the model parameters, [7] showed that stochastic forcing, representing the influence of transient weather systems, was required to yield aperiodic dust storm behavior, but only for a very narrow range of values of  $\sigma_t$ . The stochastic forcing enables transitions between a climate state with no major dust storms to a state of a dust storm every SH solstice season. This behavior is the basis for the interannual variability present in the MGCM simulations described in [6]. These simulations required specifying  $\alpha$  and  $\sigma_t$  within very narrow margins. The relatively high value of  $\sigma_t$  severely limited the regions from which lifting could be initiated so that the resulting dust cycle showed insufficient spatial variability. As in [7] and other studies, the dust lifting was broadly peaked about the SH solstice season.

*Pankine and Ingersoll* [7] proposed that a feedback between  $\sigma_t$  and the atmospheric dust activity could provide a means of “self-tuning”, whereby  $\sigma_t$  to evolve to hover about a critical value allowing intermittent major storms. It was suggested that as source regions become depleted of dust, the remaining dust would become increasingly sheltered by nonerodible surface features, thus effectively increasing  $\sigma_t$  above a nominal value. The presence of a restoring process (circulation) that provides for the resupply of dust particles could yield a system with a lifting threshold that hovers

about a critical value, enabling aperiodic dust storm behavior. *Pankine and Ingersoll* [4] introduced two variables,  $\Delta U_t$  and  $\dot{U}_t$  to represent the rapid increase in threshold friction velocity associated with dust injection following a global dust storm and the resupply of dust on a much longer timescale by small-scale processes (dust devils were proposed). The resulting model system yielded interannually variable dust storm behavior when the time scale defined by  $\Delta U_t / \dot{U}_t$  was longer than an annual cycle. The intensity of the stochastic forcing (“weather noise”) influenced the interannual variability, yielding longer or shorter intervals (in a statistical sense) between storm years.

*Kahre et al.* [5] carried out MGCM simulations with a finite surface dust reservoir to investigate the possibility that the local depletion of surface dust could provide the basis for a shifting pattern of source regions as dust is redistributed. They found that dust could not be adequately resupplied to source regions to counter the stripping of dust during high stress periods. The result was that there was insufficient dust in any of the regions with high enough stresses to allow appreciable dust lifting. The implementation and initial testing of the self-tuning concept in the GFDL MGCM is described in the following sections.

**GFDL Mars general circulation model:** The current GFDL Mars GCM is based on a finite volume atmospheric dynamical core that has been implemented on a cubed-sphere grid. The modeling described here uses resolutions of  $4^\circ \times 4^\circ$  and  $2^\circ \times 2^\circ$ . The MGCM includes surface and subsurface physics, which allow the calculation of realistic surface temperatures; a budget for gaseous and condensed  $\text{CO}_2$  which yields a realistic annual cycle of global atmospheric mass; and a turbulent boundary layer parameterization. Spatially-variable input fields include topography, surface albedo, thermal inertia, emissivity and surface roughness. The advection scheme can transport an arbitrary number of tracer constituents that are used to represent the particle size distributions of dust aerosol, water vapor, and cloud ice. The model maintains mass-conserving inventories of dust mass (surface dust and aerosol, by particle size), which are used for accounting where dust has been lifted and deposited on the surface. The NASA/Ames radiation code [12] is used to account for solar and infrared radiative heating by gaseous  $\text{CO}_2$  and atmospheric aerosols. Aerosol heating rates are calculated using the optical properties of the evolving aerosol size distribution. The simulations described here were restricted to a single particle size ( $1 \mu\text{m}$ ) to avoid the complications associated with tuning the lifting for a range of particle sizes.

The MGCM is run with fairly typical representations of convective and wind stress lifting [5]. We have specified  $\sigma_t$  as a function of the surface dust depth, varying about a nominal value of  $0.028 \text{ N/m}^2$ . We have also included a provision for dust replenishment in regions where the accumulated surface dust has fallen below the initial, globally-uniform value. This replenishment is in addition to dust accumulation associated with transport and sedimentation and is intended to compensate for the gradual export of dust to the polar regions. Since lifting is not allowed from surfaces that are covered by  $\text{CO}_2$  ice, these growing high latitude deposits tend to be effectively isolated from the simulated dust cycle. The weak replenishment tendency enables a “stable” dust cycle over long runs. We have elected to arbitrarily eliminate dust lifting in a grid box whenever the local column depth exceeds a specified ceiling. A value of  $\tau_{\text{max}} = 5$  was used in the runs described below. This eliminates the possibility of run-away dust events and provides an extreme form of a lifting shutdown mechanism, a negative feedback mechanism that is otherwise missing in current stress lifting formulations.

**Dust cycle simulation results:** We have carried out simulations that were initialized with a spatially-uniform finite surface dust reservoir and the threshold stress specified as a function of the surface dust depth. Figure 1 shows the globally integrated dust opacity from one such run, illustrating interannual variability over a 150 year simulation. The record is characterized by periods of dust storm activity, with storms occurring at one and two year intervals, interspersed with long stretches of quiescent activity. In the run shown, dust was replenished at a rate of  $0.2 \mu\text{m}/\text{year}$

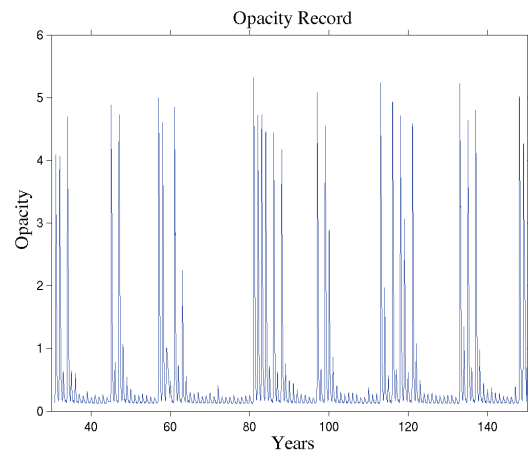


**Figure 1:** Time series of globally averaged dust opacity in a simulation ( $4^\circ \times 4^\circ$  resolution) with an evolving surface stress threshold based on surface dust depth.

whenever the local surface dust fell below the initial value. This rate is sufficient to maintain a relatively constant integrated dust mass equatorward of  $75^\circ$ . The majority of the net change in global dust mass occurs northward of  $75^\circ$ , and results from deposition of dust onto the winter ice cap during major dust storm seasons. The simulations typically lack significant dust lifting along the retreating edge of the north polar cap during the NH spring season and consequently the north pole acts as a net sink for dust.

The corresponding composite seasonal dust cycle (Figure 2) indicates that the major dust storms are initiated soon after  $L_s = 240^\circ$  and result in a broad global opacity maxima centered about the NH winter solstice season. This result is rather similar to that obtained by [6]. In both studies, storm expansion is due to the strong positive feedback between aerosol and the intensified circulation, particularly thermal tides winds and the SH subtropical jet.

The model surface dust evolves towards a statistically stable distribution (apart from the polar regions) that reflects the seasonally-integrated effects of stress dust lifting (Figure 3). While the details of the depletion pattern depend on the model resolution, the basic pattern is quite robust. The significance of the evolved pattern is that the threshold for dust lifting has developed spatial structure. Dust is relatively depleted in the vicinity of Hellas, Alba Patera, and the Tharsis volcanoes, and  $\sigma_t$  is significantly greater than the assumed nominal value. Thus the impact of these high stress regions is reduced, allowing greater spatial variability in the source regions than in previous simulations with an infinite dust reservoir [5,6].

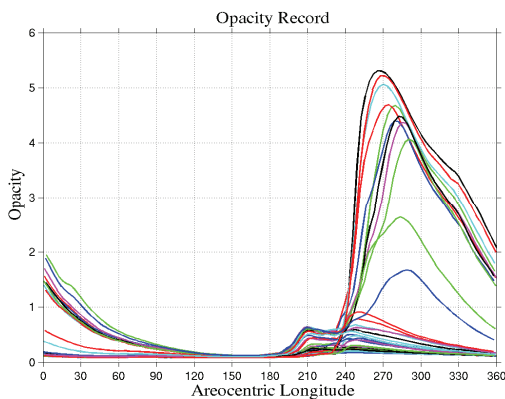


**Figure 2:** Composite seasonal variation in global opacity corresponding to the simulation shown in Figure 1.

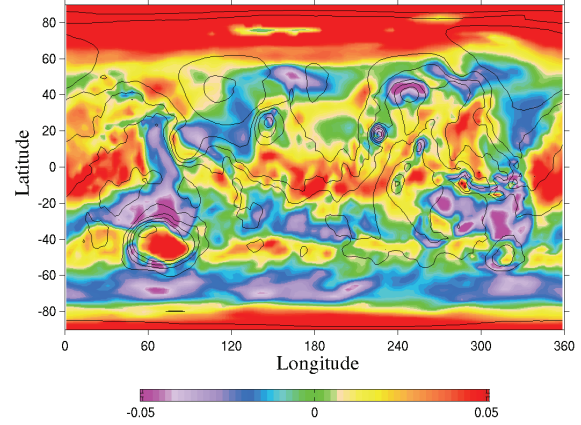


**Figure 3:** Spatial distribution of the change in surface dust mass ( $\text{kg/m}^2$ ) from an initially uniform field. The model resolution is  $2^\circ \times 2^\circ$  and the integration has run 36 years. The mean surface pressure field is contoured. Surfaces with depleted dust have an increased stress lifting threshold,  $\sigma_t$ , reflecting the assumed increased difficulty in lifting the remaining dust.

Other depleted regions correspond to the latitudes dominated by the SH summer tropical jet and the high stress region that develops along the retreating south polar cap, peaking at  $L_s \sim 240^\circ$ .

Figure 4 shows the time series of dust accumulation, overhead column opacity, dust lifting contribution and local surface stress at a location north of Hellas. The time record of dust at individual sites reveals very rapid drops in surface dust (with associated sharp increases in threshold stress,  $\sigma_t$ ) at locations that contribute significantly to atmospheric opacity, in close analogy to the discrete  $\Delta U_t$  formulation used in [8]. The close coupling between the increased dust opacity and the surface stress is the basis for the positive feedback responsible for major storm growth.

Following a simulated major dust storm, dust is redistributed globally, setting the stage for future storm activity. This replenishment was explicitly imposed as  $\dot{U}_t$  in [8]. By contrast, the simulated redistribution occurs over a range of time scales, with the most rapid replenishment occurring during the storm decay periods when sedimentation is maximal. As in [3], the parameterized dust devil lifting is insufficient for resupplying the surface dust reservoirs. Instead, it appears that the imposed replenishment ( $0.2 \mu\text{m}$  per year in this simulation) plays a significant role in resupplying source regions in years without major dust storms. Changing this replenishment contribution appears to influence the periods between the intervals (bursts) of significant storm activity in the simulations described here.



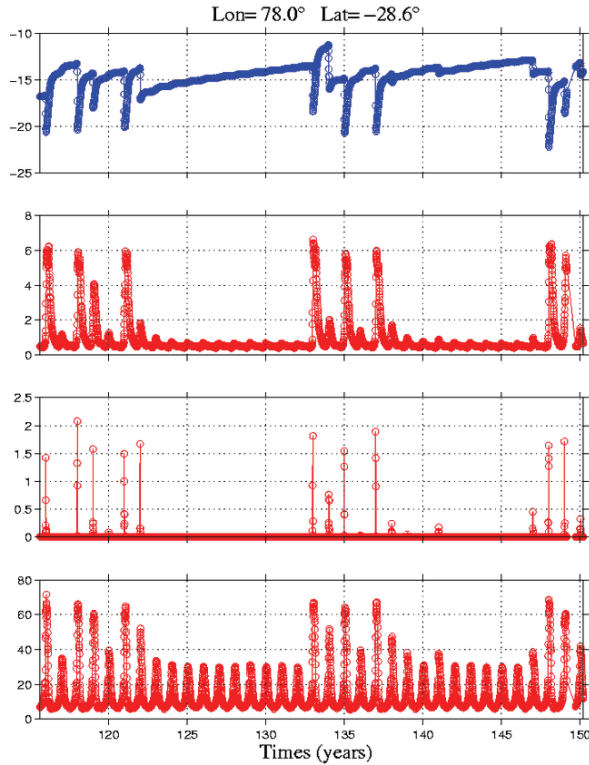


**Figure 4:** The time evolution of (a) dust accumulation (mm), (b) column opacity (c) dust stress lifting ( $10^8 \text{ kg/m}^2/\text{s}$ ) (d) diurnally-averaged surface stress ( $10^{-3} \text{ N/m}^2$ ). Dust lifting by saltation requires a stress of roughly  $0.03\text{-}0.04 \text{ N/m}^2$ . The location is on the north rim of the Hellas basin and 5-sol averages are shown.

The simulated storm record (Figure 1) is likely a consequence of the effective time scale in the MGCM simulations (the distributed analog of  $\Delta U_t / \bar{U}_t$  in [8]) having a bimodal distribution that varies markedly from being less than an annual cycle to much greater than an annual cycle. This time scale was a specified constant in the simple model of [8], allowing a clean separation between depletion and replenishment. Insufficient spatial variability in the simulated storms results in a widespread distribution of dust, rather than on a more regional scale. Dust deposition with a broader range of time scales could be achieved by greater variability in the spatial extent of simulated storms, since any given location could be occasionally replenished by nearby lifting activity.

**Summary and Future Work:** The onset of major storm activity in the current simulations shows more realism than in the simulations with an infinite dust reservoir described in [6]. Storms are typically initiated in the SH following a sequence of flushing storm

events originating in the northern hemisphere. This activity leads to a triggering of dust lifting along the high-stress region that migrates southward with the retreating south polar  $\text{CO}_2$  ice cap. The Chryse and Isidis channels make significant contribution to flushing storm activity. There is now greater variability in localized lifting along the edge of the retreating south polar cap. The new simulations still have the unrealistic aspect of persistent dust lifting through the SH summer solstice season in years when major dust activity is triggered. The dominating positive feedback in the SH subtropical jet is prominent in all published dust cycle simulations, and results in a persistent simulated dust opacity peak around solstice ( $L_s = 270$ ). Note that the storms simulated by [7,8] are global scale solstitial dust storms, as the only circulation element that is resolved in the simple model is the Hadley circulation.

The lack of regional scale dust storms, with moderate opacity levels, is a major shortcoming in our modeling to date. We speculate a more realistic range of storm activity should yield greater variability in surface dust deposition and reduce dependence on the arbitrary weak replenishment employed in the simulations.

A consequence of the spatially-variable  $\sigma_t$  is that a relatively greater fraction of the planetary surface is primed for explosive dust lifting compared with the case with fixed and uniform  $\sigma_t$ , since lifting in the highest stress regions has been de-emphasized. Thus there is a decreased tendency for strong, localized dust lifting events in the SH to remain confined as regional storms. There may be other mechanisms which may inhibit this potential for global instability, which results in the all-or-nothing behavior seen in the current simulations.

In terrestrial modeling, preferred lifting regions have been identified on the basis of topographic, geomorphologic and hydrologic criteria. It is likely that similar considerations will need to be applied to martian climate modeling. Spacecraft data show that albedo is a climatologically active variable rather than a static boundary condition [13]. We expect that changes in surface fields play an important role in the interannual variability in dust storm occurrence and intensity by introducing a long term memory into the system and thus contribute to climate variability. We are exploring the consequences of allowing the current spatially uniform function relating  $\sigma_t$  to predicted surface dust to be modulated by other surface characteristics. The dust lifting efficiency  $\alpha$  may also be best modeled as spatially variable.

- References:** [1] Newman, C.E. et al. (2002), *J. Geophys. Res.*, 107(E12), 5123. [2] Newman, C.E. et al. (2002), *J. Geophys. Res.*, 107(E12), 5124. [3] Kahre, M.A. et al. (2005), *Geophys. Res. Lett.*, 32, L20204. [4] Kahre, M.A. et al. (2006), *J. Geophys. Res.*, 111, E06008. [5] Basu, S. et al. (2004), *J. Geophys. Res.*, 109, E11906. [6] Basu, S. et al. (2006), *J. Geophys. Res.*, 111. [7] Pankine, A.A., and A.P. Ingersoll (2002), *Icarus* 155, 299-323. [8] Pankine, A.A., and A.P. Ingersoll (2004), *Icarus* 170, 514-518. [9] Smith M. D. (2004) *Icarus*, 167, 148-165. [10] Wang, H. et al. (2006), *J. Geophys. Res.*, 110, E07005. [11] Wilson, R.J. et al. (2006) Proceedings Second International workshop on Mars atmosphere modeling and observations, Granada, Spain. [12] Kahre, M.A. et al. (2008), *Icarus*, 195(2), 576-597. [13] Szwast, M. et al. (2006), *J. Geophys. Res.*, 111(E11), E11008.

---

## IN SEARCH OF MORE REALISTIC MODEL PARAMETERIZATIONS OF AEOLIAN PROCESSES ON MARS. Michaels<sup>1</sup>, T. I. <sup>1</sup>Southwest Research Institute, 1050 Walnut St Suite 300, Boulder, CO 80302, USA, tmichael@boulder.swri.edu.

---

**Introduction:** The external face of a world with a significant atmosphere (*i.e.*, with a surface air pressure greater than  $\sim 0.1$  Pa) undergoes continuous alteration via a vast number of direct and indirect processes. A wide spectrum of temporal and spatial scales are involved, from that of atomic processes to geologic time and the spatial dimensions of the body. Furthermore, complex inter-scale and inter-process feedback is common. A relatively small, but important, subset of the above-mentioned processes is the transport (involving wind) of solid particles to/from/across the surface. Manifestations of this type of process on Mars include dunes, ergs (sand seas), particulate ripples of all shapes and sizes, dust devils and their tracks, local, regional, and world-encircling dust events, wind streaks (dark and bright), ventifacts, the burial and exhumation of substrate features (*e.g.*, craters), albedo and emissivity changes, and the nearly ubiquitous atmospheric dust loading. Perhaps most importantly, these aeolian solid particle transport processes play a dominant role in Mars' dust cycle.

**The Physical Root of the Problem:** Processes that directly result in the aeolian entrainment of dust on Mars (and elsewhere in our stellar system) occur at sub-meter scales. In no particular order, they are: (a) thermophoresis (*e.g.*, [1]), (b) the saltation of sand-sized particles (monolithic and/or agglomerate), (c) electrostatic interaction, (d) levitation by gas emanating from the substrate (*e.g.*, during the sublimation of “dirty” ice, and as a result of a rapid pressure drop within dust devils), and (e) direct turbulent atmospheric interaction. The above details are part of an aeolian process, and therefore their effectiveness (and for some, even their existence) depends significantly on the nature of the winds that are present. Furthermore, the characteristics of the surface and subsurface (*e.g.*, spatially-varying composition, roughness elements, cohesion, volatile inventory/state) at sub-meter scales are important to all of these mechanisms, as are the characteristics of the target particle population(s) involved in the aeolian process (*e.g.*, composition, size distribution, shape).

**Some Practical Considerations:** Discretized numerical models are used to estimate, at the macroscale (*i.e.*, using a model grid spacing of  $\sim 1$  m

to 100 km), the three-dimensional thermodynamic state of an atmosphere. Currently (and for the foreseeable future) such models do not have quantum mechanical spatial and temporal resolution – therefore they *must* employ parameterizations of subgrid-scale physical phenomena. Fortunately, the ability to construct and utilize such parameterizations continuously improves in parallel with additional knowledge of these subgrid-scale processes (and their relative significance) and with advances in computational techniques and capabilities. However, all too often, parameterizations within a complex numerical model are not improved or replaced when such an operation becomes feasible.

What is a parameterization? In this context, a parameterization is an *approximate* representation of a physical phenomenon that otherwise cannot be properly treated (due to limited spatial or temporal resolution, for example). A parameterization generally contains (both explicitly and implicitly): *i*) Assumptions and approximations, which may be good, poor, and/or non-physical, and *ii*) Scaling factors (“knobs”), which are often used to crudely take the place of highly unknown quantities. Thus, no parameterization is perfect, and it will age with time (often not gracefully) as computational techniques and capabilities improve, and/or as more knowledge is gained about the parameterized physical phenomenon. Parameterizations can also hide myriad sources of error, particularly when poor documentation of such caveats are combined with the passage of time.

**The Multi-Scale Nature of Winds:** The characterization of the realistic spatial and temporal nature of the winds involved in aeolian processes on Mars is perhaps one of the highest priority (and one of the most tractable) activities that can be undertaken at present. For example, it is tempting to use a parameterization of the very small-scale aeolian entrainment process(es) with *any* model-predicted winds. In reality, however, there exists a spectrum of superposed atmospheric winds (created and/or modified by various atmospheric phenomena) spanning a huge range of scales. The components of this wind spectrum might be grouped into three broad categories: “purely” dynamical winds, topographically-induced (via thermal and/or obstacle effects) winds,



and winds that are part of turbulence (e.g., that in the daytime boundary layer). All three of these groups often contain wind speeds relevant to aeolian processes (i.e., none of these groups can be wholly neglected).

At 1km – 100km resolution, the “purely” dynamical wind type is evident nearly everywhere, and is dominant over the relatively flat northern plains of Mars and where/when lower surface insolation conditions occur. However, the topographically-induced wind type is generally dominant in regions of complex topography (i.e., much of Mars), at least where/when relatively high surface insolation occurs (i.e., most places at most times; see Figure 1). At resolutions between about 1 km and 100 m, daytime convective (turbulent) cellular structure is dominant, superposed on the larger-scale winds. Near the surface at < 100m resolution, the strongest winds often manifest as turbulent gust fronts (see Figure 2) and vertical vortices (such as dust devils). It is these small-scale winds which most directly impact the atmosphere's interaction with surface particles.

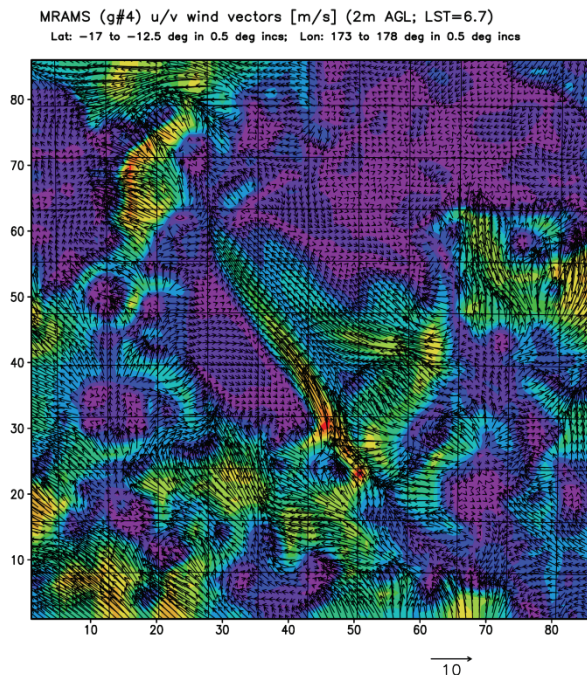


**Figure 1:** Example of near-surface nighttime winds (magnitude shaded; red is ~15 m/s) at Gusev Crater, modeled by MRAMS (a regional climate model) using a grid spacing of ~3.5 km. Note the jet emanating from the mouth of Ma'adim Vallis (just below the center of the plot).

It is of great importance to understand that the nature of winds often changes dramatically with time. All three of the previously listed wind categories frequently have large diurnal and seasonal variations. In particular, nighttime is not the same as the daytime with regard to the wind environment. During the day, boundary layer convection is nearly ubiquitous, with the attendant convective gusts and vortices (e.g., dust devils), and air tends to flow over smaller obstacles (versus around them). At night, the atmosphere in most places rapidly stabilizes, damping out buoyantly-dominated convection, and causing the night air to flow primarily around smaller obstacles (the atmospheric static stability significantly inhibits vertical motion). However, mechanically-driven turbulence can still exist at night, but requires more energy (versus buoyant turbulence) to overcome the atmospheric static stability.

**Towards Better Representations of Winds:** A model's spatial resolution limits its ability to capture the full spectrum of winds. Most Mars global climate models have an effective grid spacing of 200 km or more, so that they cannot properly resolve any circulations with a horizontal scale smaller than ~600 km. Thus in Mars' many regions of complex topography, such models are oblivious of the strong multi-directional winds that are induced by the topography, and they cannot hope to resolve the

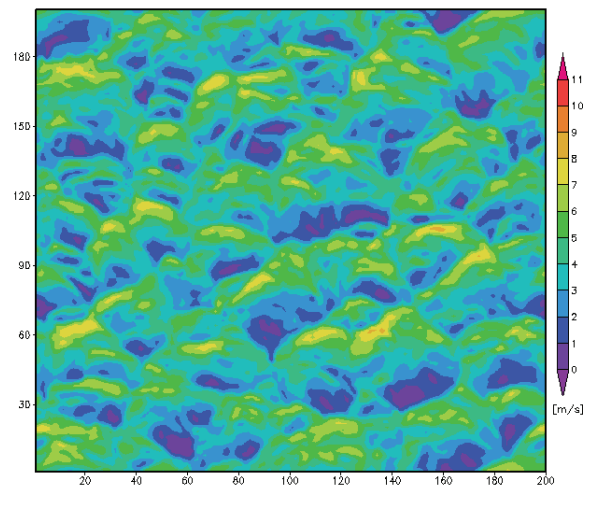


**Figure 2:** Example plot of near-surface ( $z=2m$ ) horizontal wind speed from a large-eddy simulation (LES; grid spacing of 100m) of afternoon boundary layer convection on Mars. The mean wind is blowing from the bottom towards the top of the plot, helping align and strengthen the turbulent gust fronts (warm-colored arcuate features).

turbulent gusts and vortices that are ubiquitous within the daytime boundary layer on the planet. Even a regional climate model using a grid spacing of 5 km cannot properly resolve these boundary layer phenomena, although it will explicitly resolve the vast majority of topographically-induced winds. Given these limitations, how can Mars global and regional climate models better represent the true nature of winds that drive aeolian processes (including dust lifting and transport)?

*Topographically-induced winds.* A Mars regional climate model using a grid spacing of < 20 km in the region of interest should resolve a majority of the most significant such winds, and importantly, such an operating procedure is computationally practical. Achieving such a spatial resolution with current global climate models, however, is generally either poorly tractable or results in the significant simplification of important physical process parameterizations such as radiative transfer and aerosol microphysics. Another potential way forward would be to outfit lower-resolution global climate models (*e.g.*, 120 km grid spacing) with a parameterization of subgrid-scale topographically-induced flows, preserving the use of more-realistic physical process calculations. Such a parameterization would likely be a function of the solar insolation (since these are largely thermally-driven flows) and some statistic of the subgrid-scale topography.

*Turbulent winds.* It is not currently practical to run a Mars global or regional climate model with the grid spacing necessary (< 100 m) to satisfactorily resolve the majority of significant turbulent wind gusts and vortices. Another more practical approach might be to use semi-idealized (*i.e.*, no topography, archetypal initial wind profiles) large eddy simulations (LES; grid spacing of 100 m or less) to characterize the dependence of the turbulent gusts and vortices (their strength and number) with regard to several plausible parameters (*e.g.*, the mean wind profile, insolation). In fact, such an investigation (of which the author is a participant) is currently underway [2]. This information could then be used to create a physically-grounded parameterization for utilization by a regional climate model (or a global climate model that employs a topographically-induced wind parameterization). Such a parameterization might take the form of a semi-empirical equation or lookup table.

**References:** [1] Wurm G., et al. (2008) *GRL*, 35, L10201, doi:10.1029/2008GL033799. [2] Fenton L. K. and Michaels T. I. (2009) *Mars Dust Cycle Workshop*, in this publication.



# ***Poster Session***

## ***Day Two***

*Wednesday, September 16, 2009*

*5:30 PM*



**CHARACTERISTICS OF BAROCLINIC EDDIES AND THEIR INFLUENCE ON THE TIMING AND LOCATION OF REGIONAL DUST STORMS.** Hinson, D.P., and Wang, H.

**POSTER PRESENTER:** Hinson, D.P., SETI Institute, Mountain View, CA

---

We have investigated the near-surface meteorology in the northern hemisphere of Mars through detailed analysis of data obtained with Mars Global Surveyor in January-August 2005. The season in the northern hemisphere ranged from midsummer through winter solstice of Mars Year (MY) 27. We surveyed composite images from the Mars Orbiter Camera and assembled a catalog of regional dust storms. As in previous martian years, significant “flushing” dust storms occurred in autumn of MY 27 in each of the major topographic basins of the northern hemisphere, most frequently in Acidalia Planitia. We also used atmospheric profiles retrieved from radio occultation experiments to characterize eddy activity near the surface at high northern latitudes. There are strong correlations between the two sets of observations, which allowed us to identify several factors that influence the timing and location of the regional dust storms: (1) transitions among baroclinic wave modes, which strongly modulate the intensity of meridional winds near the surface, (2) storm zones, which impose strong zonal variations on the amplitude of some baroclinic eddies, and (3) stationary waves, which further modulate the wind field near the surface. The surface stress is also influenced by systematic variations in the vertical structure of the boundary layer, which is resolved by these atmospheric profiles. The flushing dust storms ceased abruptly in mid-autumn, possibly due to some combination of source depletion, CO<sub>2</sub> condensation, a shift in the period of the baroclinic eddies, and changes in the wind field near the surface resulting from dust-storm amplification of the semidiurnal tide.

## **SIMULATING DUST CYCLES AND STORMS IN MARS WRF WITH LIMITED SURFACE DUST.**

Newman<sup>1,2</sup>, C. E., Richardson<sup>1,2</sup>, M.I., and Toigo<sup>3</sup>, A.D. <sup>1</sup>California Institute of Technology, MC 150-21, GPS, Caltech, 1200 E. California Blvd., Pasadena, CA 91125, USA, <sup>2</sup>Ashima Research, 600 S. Lake Ave., Suite 3030, Pasadena, CA 91106, USA, [claire@gps.caltech.edu](mailto:claire@gps.caltech.edu), [mir@gps.caltech.edu](mailto:mir@gps.caltech.edu), <sup>3</sup>Cornell University, 326 Space Sciences Building, Cornell, Ithaca, NY 14853, USA, [toigo@astro.cornell.edu](mailto:toigo@astro.cornell.edu).

---

**Introduction:** The amount and distribution of atmospheric dust has a huge impact on radiative transfer through the thin Martian atmosphere. The largest dust storms occur during the southern spring and summer seasons, with a wide range of starting times, starting locations and growth mechanisms [1]. Some remain quite localized in one hemisphere, others expand as they travel from north to south (so-called ‘flushing storms’, [2]), others develop via several individual lifting events that combine to cover an entire hemisphere (planet-encircling) or even the entire globe (global) [3]. Though statistics remain limited, planet-encircling or global storms appear to occur roughly one year out of three.

**The problem and a possible solution:** To date, simulations of Martian dust storms in Mars general circulation models (GCMs) produce only a small range of storm types (in terms of start times, locations, etc.) and underestimate the extent of interannual variability [4,5,6]. In addition, simulated decay rates are often too slow in comparison with many observed global storms. However most of these simulations assumed an infinite supply of surface dust, with no regions ever running out. This is a highly unrealistic assumption: from observations we know that some areas - including many where major storms are seen to begin - lose most of their dust cover in some years [7], which clearly will have a huge impact on the storms produced.

In other words, the key problem is that most models treat regions of peak long term wind stress as the biggest dust source regions, but ignore the fact that such high wind stresses mean dust is removed from them far too easily to allow them to be long term sources of dust.

**Hypothesis.** In this paper we hypothesize that there are regions on Mars that are equally sources *and* sinks of dust when averaged over a few Mars years. If correct, this would mean that a stable situation can be reached in which *most* initial source regions have been (more or less) permanently depleted, but a *few* are still being resupplied over a multi-year cycle, allowing realistic storm peaks to continue to appear.

**Goal.** Our goal is to find these resuppliable source regions by allowing the model itself to eliminate all of the non-resupplied areas (those that only *appear* to be the primary source regions for dust storms because they have the highest wind stresses). If the model were a perfect representation of Mars, and if we could convert *e.g.* thermal inertia and albedo maps exactly to the amount of dust cover on the surface, we could use observations to determine the resuppliable regions and thus to set the initial surface dust distribution for our simulations. However producing such maps is highly uncertain, particularly if particle size distributions are considered. More importantly, no GCM is perfect, so a surface dust map based on observations would be unlikely to correlate well with what the GCM would predict based on its own lifting and deposition schemes. We must therefore allow the GCM to *predict* the surface dust distribution in an internally consistent manner, as detailed in the ‘method’ section below.

**Assessing simulated storms:** There are several ways to assess how well a simulation captures the observed dust cycle and storm events by comparing to observations. Dust storm evolution and coverage can best be visualized using time-series maps of observed infra-red or visible dust opacity [8, 9, 10, 11].

However, even though these maps do not represent the vertical dust distribution, they still result in a huge amount of information when multiple storm events and multiple decades of observations are included. One way of organizing this information is to zonally average opacities to produce season vs. latitude contour plots [10, 12] or to globally average to show multiple years of opacity as a function of season on a single plot [13].

Equivalently, because of dust’s huge influence on atmospheric temperatures, the atmospheric temperature in the middle atmosphere can be used as a proxy for atmospheric dust loading. The Viking Orbiter’s Infrared Thermal Mapper (IRTM) instrument had a 15 $\mu$ m channel chosen such that its brightness [‘T-15’ temperatures] were representative of a broad region from ~10-40km centered at ~25km. In this paper we convolve model output with the IRTM response function to give T-15 temperatures for each simulation,



and use globally-averaged T-15 plots from simulated dust cycles to gauge the realism of our dust storms and cycles, in comparison with typical observed T-15 plots [14].

Figure 1 shows a cartoon representation of 4 years of observations adapted from [14], and demonstrates the sort of variability we are aiming for.

**The model:** We used the MarsWRF [15] general circulation model (GCM) with a suite of dust lifting and sedimentation parameterizations (described below). Dust is also advected by atmospheric winds and mixed by the model's vertical and horizontal diffusion schemes and is treated as a radiatively active tracer. To explore the impact of surface dust running out and/or being replenished over time, the amount of surface dust is tracked, with no lifting allowed if a grid point is fully depleted at any given time.

*Dust parameterizations.* In these experiments, two particle sizes were used (with diameters=1.25 and 2.5 $\mu\text{m}$ ) with sedimentation calculated separately for each using a 1-D advection scheme that remains stable even when particles fall through more than one grid space in a given timestep [16]. The wind stress parameterization lifts dust when surface stress,  $\tau_t$ , exceeds a threshold, using the formula of [17] to calculate the sand flux during saltation. Tunable parameters are (1)  $\tau_t$  and (2)  $\alpha_N$ , the ratio of vertical dust to horizontal sand flux. The dust devil parameterization sets the dust flux proportional to the 'dust devil activity' defined in [18]. The proportionality constant,  $\alpha_D$ , is the only tunable parameter. As in [5],  $\alpha_D$  is tuned to match the background T-15 curve (shown as a dotted line in Figures 2, 5, 8 and 9) then  $\alpha_N$  is tuned for each  $\tau_t$ .

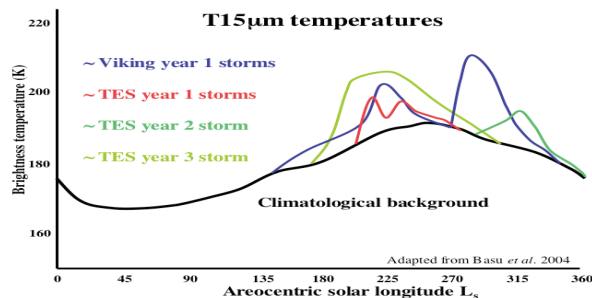
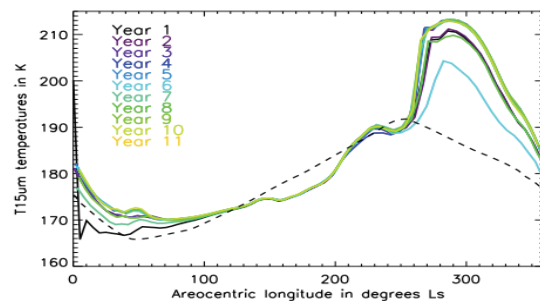


**Figure 1:** Globally-averaged T-15 Temperatures for four Mars years with moderate to major dust storms, adapted from [14].

**Method of producing internally consistent surface dust distributions:** As discussed above, we need to use MarsWRF itself to find a hypothesized surface dust distribution that is quasi-stable over time and gives rise to realistic dust storms and cycles. The method is as follows: Step (1) A simulation is initialized with uniform surface dust and using a relatively low value of  $\tau_t$ , with  $\alpha_N$  set high enough to produce stormlike peak T-15 values during southern spring and summer. Because of the low threshold chosen, these storms are rather unrealistic (very broad, smooth peaks) and there is too much dust lifting in northern summer. This simulation runs until the primary source regions are depleted and the storm peaks disappear. Step (2) The simulation is restarted from this point (*i.e.*, using the current surface dust distribution) but now with  $\alpha_N$  increased enough to produce large peaks once again. The simulation is continued until the new main source regions are depleted as well, and storms again disappear. Step (2) is then repeated until the only source regions left gain as much over several years as they lose during major storms, and global storms continue to occur *without further increases in  $\alpha_N$  required*.

Note that beginning with this final (large)  $\alpha_N$  value would instantly crash the model if using radiatively active dust, however if dust is treated as a passive tracer then several feedbacks are ignored and the patterns of lifting (hence depletion) are significantly altered. Thus a gradual 'homing in' approach (as described above) is required.

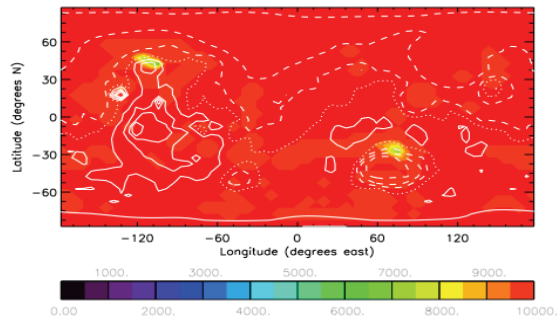
**Results:** As an example of the problem we are attempting to solve, Figure 2 shows global mean T-15 for >10 years of a simulation in which the initial surface dust cover was set sufficiently high that no regions were fully depleted over this time period.



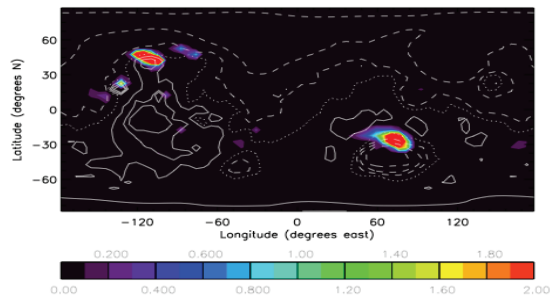
**Figure 2:** Globally-averaged T-15 temperatures for a MarsWRF active dust simulation with effectively unlimited surface dust and  $\tau_t = 0.034 \text{ Nm}^{-2}$ .

In this simulation the  $\alpha_N$  value used produces large regional to global storms every year, but there are no storm-free years and although there is some variability in peak opacity (particularly in year 6) there is almost no interannual variability in the storm's evolution or decay phase. Surface dust cover by the end of the simulation is shown in Figure 3, with dust lifting over the final year in Figure 4, revealing strong lifting and net removal of dust over northern Hellas and Alba Patera, though no regions are close to running out.

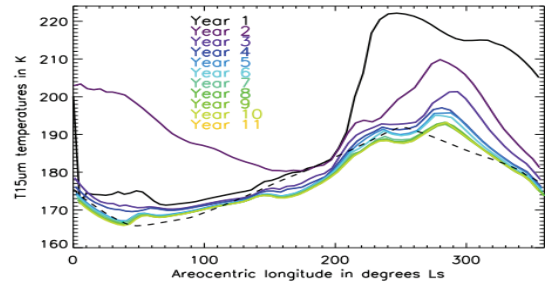
*Running with limited surface dust.* Figure 5 shows T<sub>15</sub> for the Step (1) simulation (see ‘methods’ section above), using an initially uniform surface dust cover of 100 (in arbitrary units) and with a relatively low wind stress threshold ( $\tau_i = 0.026 \text{ Nm}^{-2}$ ). The setup for this simulation is otherwise identical to that shown in Figure 2. The peak opacity gradually lowers over years 1 to 8 as the main source regions are depleted, and from year 3 onwards no major storms are produced.



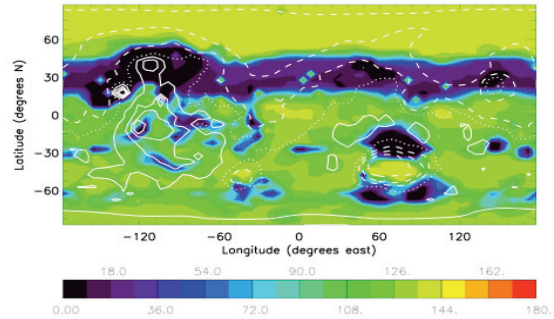
**Figure 3:** Surface dust cover after 10 years for the same simulation shown in Figure 2. Initial surface dust cover was uniform at 10,000 (in arbitrary units).



**Figure 4:** Wind stress lifting (in arbitrary units) averaged over the final year of the simulation shown in Figure 2.



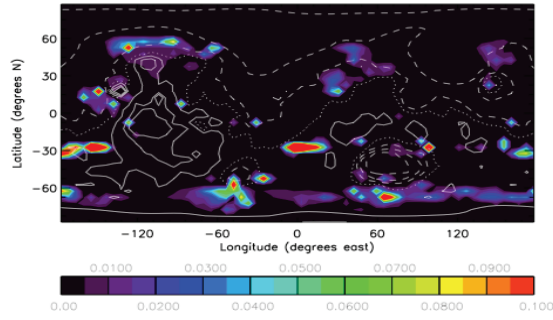
**Figure 5:** As in Figure 2 but for a simulation with a lower initial dust cover and a lower threshold of  $\tau_i = 0.026 \text{ Nm}^{-2}$ .



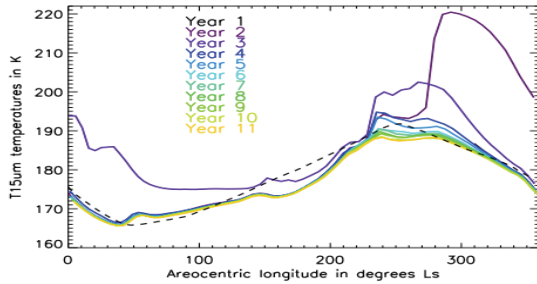
**Figure 6:** As in Figure 3 but for the simulation shown in Figure 5.

Figure 6 shows the surface dust distribution at the end of the Step (1) simulation. By this time a broad swath of northern latitudes (including Alba Patera and Olympus Mons) and large regions surrounding the Hellas basin have been fully depleted of dust.

Figure 7 shows the lifting averaged over the final year of the Step (1) simulation, and demonstrates how different the pattern of lifting has become now that the primary source regions (seen in Figure 4) around Alba Patera and Hellas have practically disappeared. Lifting peaks in a few regions at 30 degrees south, and along the edges of the south polar cap (not marked), particularly to the south of the Hellas and Argyre basins in the vicinity of strong slope flows. However it is important to note that this lifting does not produce global storms (as by the final year of the simulation they have long since ceased to occur).



**Figure 7:** As in Figure 4 but for the simulation shown in Figure 5.



**Figure 8:** As in Figure 2, but continuing on from the end of the simulation shown in Figure 5 with  $\alpha_N$  doubled.

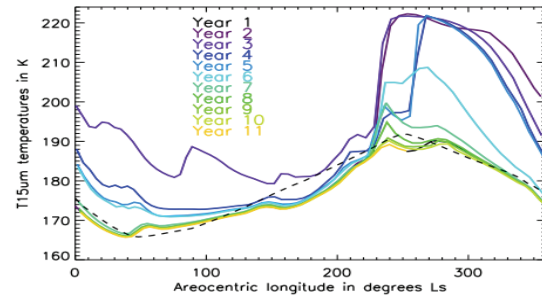
We then proceeded to Step (2) of the method by continuing with a second simulation *started from the final atmospheric and surface* (Figure 6) *dust distributions of the previous simulation, but with  $\alpha_N$  doubled*. Figure 8 shows T-15 for the next 10 years. Doubling  $\alpha_N$  produces an initial increase in lifting from the remaining source regions that is sufficient to produce a large global storm in the first year. However in subsequent years no further global storms are produced, and soon no large storms occur at all, as the remaining source regions are themselves further depleted.

The surface dust distribution by the end of this simulation is very similar to that shown in Figure 6, though with slightly more depletion of surface dust at southern mid to high latitudes. The pattern of lifting in the final, storm-free year is also quite similar to that shown in Figure 7, though with less mid-latitude and more high-latitude lifting in the southern hemisphere.

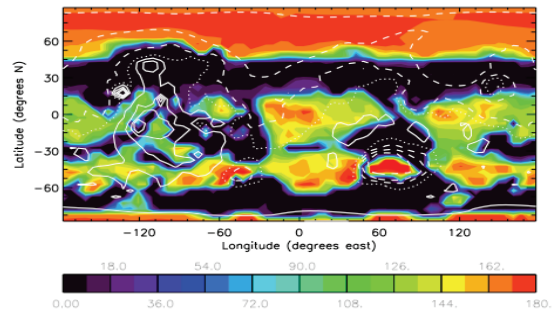
A third simulation is then continued from the final atmospheric and surface dust distributions of the second, but now with  $\alpha_N$  tripled to make it six times larger than it was originally. Figure 9 shows T-15 temperatures for 10 years, and – although clearly some source regions are still depleting, and we have yet to reach the hypothesized ‘stable state’ – the large dust storms continue to occur for the first four or five years, suggesting that we may be closing in.

Figure 10 shows the surface dust distribution by the end of this simulation, and reveals a build-up of dust at high latitudes in both hemispheres, net accumulation in central Hellas and Argyre, and net depletion over roughly half the planet.

Lifting average over the final year of this simulation is shown in Figure 11, and looks similar to that in Figure 7, with strong localized peaks around the northern cap edge and topography and along the southern cap edge, though with less lifting at mid-latitudes and more at high latitudes in the southern hemisphere.



**Figure 9:** As in Figure 2, but continuing from the end of the simulation shown in Figure 8 with  $\alpha_N$  tripled (making it six times larger than that used originally to produce Figure 5).



**Figure 10:** As in Figure 3 but for the simulation shown in Figure 9.

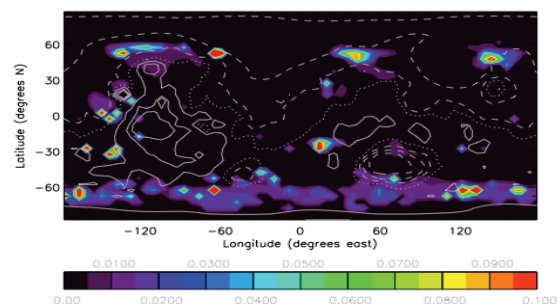


**Figure 11:** As in Figure 4 but for the simulation shown in Figure 9.

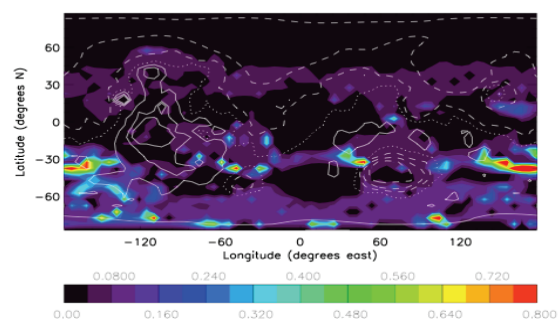


**Figure 12:** As in Figure 11 but for the third year of this simulation when global storms are still being generated.

Of more interest is Figure 12, showing lifting averaged over the third year of this simulation when global dust storms are still being generated. This highlights the difference between primary storm source regions when dust cover is not an issue (Figure 3) and when regions that are not resupplied on multi-year timescales are allowed to deplete. Notable differences are the lack of lifting peaks over northern topography (compared to strong lifting over Alba Patera in Figure 3), increased lifting at high southern latitudes, and southern mid-latitude lifting in regions other than northern Hellas.

**Conclusions:** More work is needed to prove or disprove the hypothesis that a stable situation exists with intermittently repeating global dust storms and regions that are replenished and depleted on several year timescales. However these preliminary results show promise, and in particular support the idea that the oft-predicted, vast primary source regions associated with northern topography likely disappear when regions of high wind stress are allowed to realistically deplete. This also has implications for the ‘runaway positive feedbacks’ seen in many Mars GCMs with active dust, as they are often associated with unrealistically large amounts of northern hemisphere lifting.

**References:** [1] Zurek R. W. and Martin L. J. (1993) *JGR*, 98, E2, 3247-3259. [2] Wang H. et al. (2003) *GRL*, 30, 9, doi: 10.1029/2002GL016828. [3] Strausberg M. J. et al. (1995) *JGR*, 110, doi: 10.1029 / 2004JE002361. [4] Newman C. E. et al. (2002) *JGR*, 107, E12, doi: 10.1029 / 2002JE001920. [5] Basu S. et al. (2006) *JGR*, 111, E9, doi: 10.1029/2005JE002660. [6] Kahre M. A. et al. (2006) *JGR*, 111, E6, doi: 10.1029 / 2005JE002588. [7] Szwast M. A. et al. (2006) *JGR*, 111, E11, doi: 10.1029 / 2005JE002485. [8] [http://tes.la.asu.edu/webdata/dust\\_mov/](http://tes.la.asu.edu/webdata/dust_mov/). [9] Wang H. (2007) *Icarus*, 189, 2, 325-343. [10] Smith M. D. et al. (2001) *JGR*, 106, E10, 23929-23945. [11] Cantor B. (2007) *Icarus*, 186, 1, 60-96. [12] Horne D. and Smith M. D. (2009) *Icarus*, 200, 1, 118-128. [13] Smith M. D. (2004) *Icarus*, 167, 1, 148-165. [14] Basu S. et al. (2004) *JGR*, 109, 11, doi: 10.1029/2004JE002243. [15] Richardson M. I. et al. (2007) *JGR*, 112, E9, doi: 10.1029 / 2006JE002825. [16] Francois Forget, personal communication, 1998. [17] White B. R. (1979) *JGR*, 84, 4643-4651. [18] Renno N. I. (1998) *JAS*, 55, 3244-3252.

---

## AN INVERSE APPROACH TO MODELING THE DUST CYCLE WITH TWO MARS GENERAL CIRCULATION MODELS.

Kahre, M.A.<sup>1</sup>, Wilson, R.J.<sup>2</sup>, Haberle, R.M.<sup>3</sup> Hollingsworth, J.L.<sup>3</sup> Bay Area Environmental Research Institute, <sup>2</sup>NOAA Geophysical Fluid Dynamics Laboratory, <sup>3</sup>NASA Ames Research Center, (NASA Ames Research Center, 245-3, Moffett Field, CA, 94035, 650-604-3863, melinda.a.kahre@nasa.gov).

---

**Introduction:** The dust “cycle” consists of dust emission (“lifting”) from the surface, atmospheric transport, and removal processes such as gravitational sedimentation and scavenging by H<sub>2</sub>O and CO<sub>2</sub> clouds. Recent GCM dust cycle simulations have typically included parameterizations for two dust lifting mechanisms: wind stress and dust devil dust lifting. While the combined effect of these lifting schemes enables the reproduction of some features of the observed dust cycle well [1, 2, 3], there are marked differences between the simulated and observed dust cycle. For this investigation, we tackle dust cycle modeling using dust assimilation methods. We utilize two Mars GCMs (the NASA Ames MGCM and the GFDL MGCM) that include independently developed schemes to inject dust from the surface when necessary to track spatially and temporally evolving TES-observed dust opacity fields. When dust enters the atmosphere, it is transported and undergoes gravitational sedimentation. This dust treatment is distinct from other modeling studies, including the UK data assimilation [4], which specify the vertical distribution of dust. The goals of this work are: to infer dust sources and sinks (which will help us understand how the Martian surface is evolving currently); to increase our understanding of the how the vertical distribution of dust changes in time and space; and to put constraints on the development of more physically appropriate dust lifting parameterizations.

**General Methodology:** The spatial and temporal evolution of atmospheric dust results from a combination of dust lifting, transport, and removal processes. If we assume that the GCMs treat transport and removal processes (i.e., sedimentation) correctly, allowing the model to lift dust when necessary to match observed dust opacity fields should give us information about where dust must be lifted from the surface in reality. This general methodology was used to independently develop and implement dust lifting schemes in two separate GCMs. The key outcome of these modeling efforts is a robust agreement in the major dust source regions. The details of these schemes and models are described below.

**Model Details:** Two GCMs were used for this study, the GFDL model and the NASA Ames model. The NASA Ames Mars GCM is a finite-difference numerical model that runs on an Arakawa C-grid with a nominal horizontal resolution of 5° in latitude by 6° in longitude. The Ames dynamical core conserve energy and mean-square enstrophy, and it is fourth-order accurate in terms of vorticity advection by the non-rotational component of the flow. The GFDL Mars GCM is based on a finite volume (FV) atmospheric dynamical core implemented on a cubed-sphere horizontal grid. The GFDL dynamical core employs conservative flux-form semi-Lagrangian horizontal discretization with monotonic constraints; it runs on a cubed-sphere grid, which provides relatively uniform spatial coverage and avoids the computational issues associated with the convergence of meridians of longitude. The modeling described here uses a resolution of 4° x 4°.

Both GCMs employ a correlated-k two-stream radiative transfer model. The optical properties of dust at visible wavelengths are based on the results of [5]. In the IR, the Ames model utilizes the dust properties of [6], and the GFDL uses those of [7]. Dust tracers can be radiatively active or passive. Mie calculations are used to create a look-up table of dust optical properties for a temporally and spatially evolving particle size distribution. For the simulations present here, the tracers are treated as radiatively active in the GFDL model and radiatively inert in the Ames model.

The advection schemes utilized by the models are similar in that they are both finite-volume schemes. In the Ames model, the Van Leer tracer transport scheme with slope limitations has been implemented. Both the GFDL and Ames advection schemes allow for advection across more than one grid-box in one dynamical time step in the zonal direction.

Lifted dust is represented in the Ames model with a lognormal size distribution with an effective particle radius of 2.5 microns and an effective variance of 0.5. Carried in the model as two moments (mass and number), the particle size distribution evolves in both



time and space. GFDL model simulations use 5 dust tracers (0.2, 0.5, 1.2, 2.5 and 5  $\mu\text{m}$ ). The input size distribution is adjusted to best satisfy the comparison between simulated and observed temperatures.

The vertical distribution of dust has a particularly notable effect on polar temperatures. In both models, the Stokes-Cunningham relationship is applied to calculate the sedimentation velocity for tracers based on their size, and an implicit numerical scheme is used to update the vertical profiles of dust based on sedimentation and mixing fluxes. In the Ames model the local mass- and number-weighted mean dust particle radius are used to calculate fall velocities, while in the GFDL model each particle size is carried explicitly. Both methods enable vertical stratification of effective dust particle size.

**MGS/TES Data:** The key data set used for all simulations is the MGS/TES-derived column dust opacities from TES mapping year 1 (MY24/25) [8]. Observations were only derived when sufficient surface/air temperature contrast was present (in practice,  $T_{\text{sfc}} > 215 \text{ K}$ ) so that opacities are not present in the vicinity of and over the polar ice caps. The TES data used by the Ames model are binned at the horizontal resolution of the model ( $5^\circ$  by  $6^\circ$ ) and 10-sol temporal averages are applied. The input data set used by the GFDL model are initially binned at a horizontal resolution of  $3^\circ$  by  $7.5^\circ$  by  $5^\circ$  degree resolution in latitude, longitude and  $L_s$  (~10-sol temporal average); these data are subsequently rebinned at the desired model resolution and grid (cubed-sphere) structure. In a simulation, the opacity of a column at any given  $L_s$  is an interpolation in time between the appropriate 10-sol (or  $5^\circ$  of  $L_s$ ) averaged maps.

Gaps in the TES observations (i.e. when  $T_{\text{sfc}} < 215 \text{ K}$ ) have been treated differently for the two models. In the GFDL simulations, gaps in the TES observational record are not filled in or extrapolated. In the Ames model, schemes are implemented to fill in both interior (i.e., surrounded on all sides by data) and exterior (i.e., polar regions) gaps. Interior gaps are filled in by interpolating data from the surrounding longitudes. Exterior gaps are filled in by fitting a curve as a function of  $L_s$  to the data surrounding the temporal gap and mirroring that curve to fill in the data gap. This scheme will soon be revisited because it appears to produce too much dust in the polar night compared to TES limb observations.

**Dust Injection Schemes:** The dust injection schemes were designed to nudge the models toward carrying an atmospheric dust tracer spatial and temporal distribution that closely tracks the observed dust column opacity during Mars Year (MY) 24/25. To do this, a comparison is made on each column at each physical time step between the transported column dust opacity and the observed column dust opacity. In the Ames model, when the transported dust opacity is low relative to the observed dust opacity, a prescribed amount of dust (equal to 0.1 optical depths / sol) is added to the lowest model layer; if the transported dust opacity is high relative to the observed dust opacity, nothing is added or subtracted from the tracer field.

There are two modes for carrying out simulations with the GFDL model: adding dust to the boundary layer if the tracer-calculated column opacity is low and doing nothing if the tracer calculated column opacity is high; and adding or subtracting dust from the boundary layer to force the dust tracer opacity to precisely match the TES-observed column opacity. The GFDL model results presented here utilize the former method.

**Results:** Surface sources and sinks for dust are predicted by these models on timescales ranging from days to a full annual cycle. In order to have confidence in the predicted source and sink regions, we must first understand how well our dust lifting scheme works. To do this, we compare the zonally averaged transported dust opacity to the zonally averaged TES-observed dust opacity (Figure 1). The seasonal variation of dust opacity in the two simulations closely reflects the observed dust opacity. The simulated and observed atmospheric dust is at a maximum during northern fall and winter and at a minimum during northern spring and summer.

Although there is good general agreement between the transported and observed dust opacity, there are regions and seasons that are not in agreement. Specifically, the observed opacity maximum at high southern latitudes during northern fall is not captured by the Ames model. This discrepancy arises from the extrapolation routine used for filling in missing dust opacity data, and (as mentioned above) is suspect. Other minor disagreements between the TES-observed and tracer opacities suggest that minor adjustments to the dust lifting/removal scheme and/or dust particle size distributions are appropriate for ongoing and future simulations (see discussion below).

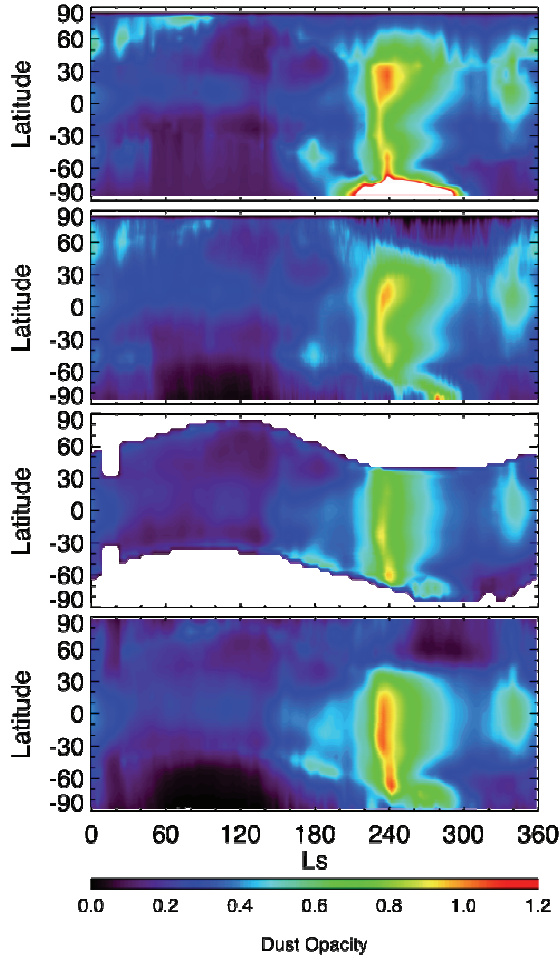


**Figure 1:** Top panel: TES-observed opacities utilized in the Ames model; Second panel: Tracer-calculated opacities from the Ames model. Third panel: TES-observed opacities utilized in the GFDL model; Bottom panel: Tracer-calculated opacities from the GFDL model.

**Seasonal Dust Sources and Sinks:** Understanding the evolution of dust sources and sinks on seasonal timescales gives insight into the processes that play a role in dust lifting events on Mars. Both models predict that active dust source regions occur predominately at high northern and southern latitudes in the vicinity of the edge of the seasonal  $\text{CO}_2$  ice caps (Figure 2). Further, both models predict similar zonally averaged patterns of net dust injection/removal rates.

Differences in these predicted rates produced by the separate models can be traced to differences in the inputted TES opacity maps used to drive the simulation. For example, increased dust injection rates in the Ames model along the north retreating seasonal  $\text{CO}_2$  ice cap is due to the extrapolation of the TES-

observed opacities over surface with  $T_{\text{sfc}} < 215$  K. The robust result of both models that the dust injection rates peak along the seasonal  $\text{CO}_2$  cap edges strongly suggest that cap edge dust lifting plays a critical role in producing the observed pattern of airborne dust.

**Annual Dust Sources and Sinks:** Examining the annually integrated dust source and sink regions enables insight into the evolution of the Martian surface over time under the current climate regime. In general, there is very good qualitative and quantitative agreement of the annual net dust source and sink pattern between the two models. Simulated annual sink regions for dust in both models include the equatorial regions and the polar regions (Figure 3). Simulated annual source regions for dust in both models include the middle northern and southern latitudes and the volcanoes in the northern hemisphere.

There are localized differences in the net dust source/sink patterns between the models. The Ames model predicts a sink for dust in the center of the Hellas basin, while the GFDL model predicts that Hellas is a source for dust. The reason for this discrepancy has not yet been fully understood, but highlights the need to develop common TES-derived dust opacity fields to drive the models.

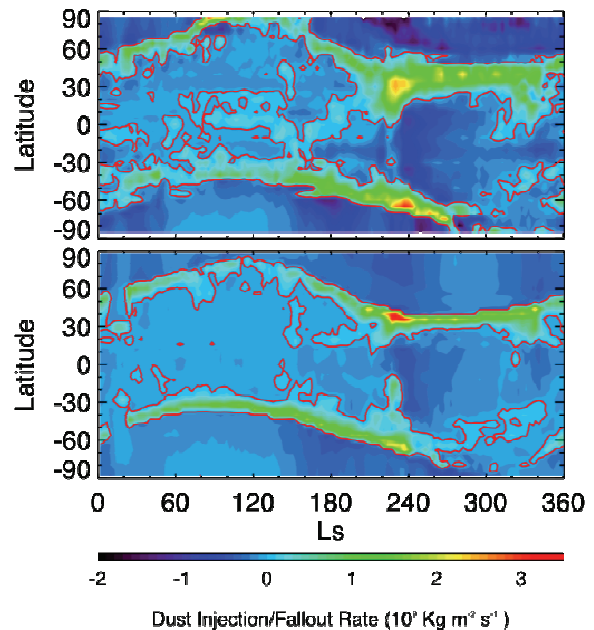


**Figure 2:** Zonal mean net dust lifting/deposition rates from the Ames (top) and GFDL (bottom) models. Solid red contours indicate no net gain or loss. Both models robustly predict maximum dust lifting rates along the north and south seasonal  $\text{CO}_2$  ice caps.



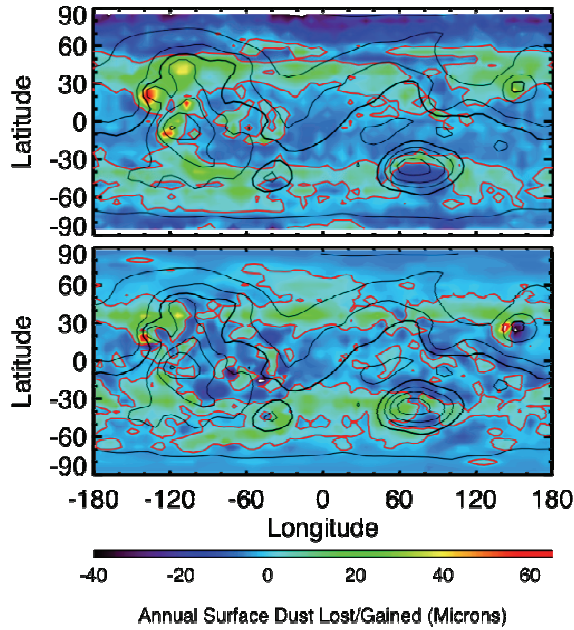


**Figure 3:** Annually surface gain and loss from the Ames (top) and GFDL (bottom) models. Solid red contours indicate no net gain or loss. Solid black contours show topography.

**Discussion and Ongoing Work:** This method for modeling the Martian dust cycle can be used to investigate many aspects of the current climate system and dust cycle. Additionally, there is work still to be done to improve the implementation of this dust scheme and the simulation of Mars' current climate. Our goal is to simulate all aspects of the climate as carefully as possible, which includes matching observations of atmospheric and surface temperatures and atmospheric dust opacity and particle sizes. In the following sections, we highlight preliminary implications for the dust cycle and the evolution of the Martian surface, and we discuss future plans for model improvements.

**Dust Cycle Implications:** An open question about the Mars dust cycle is where and how dust leaves the surface and enters the atmosphere. Previous interactive dust cycle modeling investigations have included parameterizations for threshold wind stress and dust devil lifting [1, 2, 3]. While those simulations reproduce aspects of the dust cycle well, it is clear when comparing them to these TES-dust simulations that they under-represent cap edge dust lifting. Additionally, our current modeling results suggest that the contribution to the global dust cycle from dust

devils may be small because predicted dust lifting at low latitudes is relatively small.

**Evolution of the Martian Surface:** A second key open question about the Mars dust cycle is where the net surface sources and sinks for dust are located. The two GCMs used for this study agree on the general pattern of annual surface dust sources and sinks. According to these simulations, major sources for dust include longitudinally extensive bands in the middle northern and southern latitudes. These regions correspond well to the spatial patterns of MGS/MOC observed dust lifting events [9]. The model suggests that the dust lifted in these events escapes these regions and accumulates at low latitudes and in the polar regions.

**Method Challenge:** Although the TES-dust scheme method presented here should enable the accurate prediction of "real" dust lifting events in principle, there are uncertainties involved in both the data and the models that are worth discussion. Although the data are critically important for this project, they have limitations. The sun-synchronous nature of the Mars Global Surveyor orbit enables only limited time of day coverage (i.e., approximately 2 pm). As a result, we are unable to capture details of the diurnal cycle embedded in the dust cycle. The nadir viewing orientation of data acquisition that was used to collect this data set does not allow for information regarding the vertical distribution of dust. Although TES limb observations can provide some constraints on the vertical distribution, the limb data have only coarse vertical resolution and less than desirable spatial and temporal coverage.

Uncertainties also exist in the models themselves. The assumption is made that the general circulation predicted by the models is correct and the tracer transport schemes are accurate. Although in general these are likely good assumptions, the models are certainly not perfect. Additionally, the transport of dust opacity throughout the model atmosphere depends on the assumed dust particle size distribution, which can be represented by individual particle sizes (GFDL) or by the moments of the distribution (Ames). Due to the 10-sol averaging performed to construct the TES dust opacity maps, the models cannot well-capture short-lived, spatially confined dust lifting events. Our goal here has been to capture the seasonal and annual variations of the dust cycle.

*Improving TES opacity maps:* The shortcomings of the TES-observed opacity fields argues for the construction of new maps that combine multiple data sets and logic based judgement in order to as realistically as possible fill in both spatial and temporal gaps in the data. Constructing a dust map in the winter polar regions where the nadir TES data are absent is a place to focus on. One possible method for this is to impose an exponential decay in the column dust opacity as a function of latitude toward the pole starting at the edge of the seasonal CO<sub>2</sub> ice cap (as identified by the locations where TES surface temperature data suggest the presence of CO<sub>2</sub> ice). MGS/MOC image data can be utilized as a guide for filling in interior data gaps or replacement of suspect data. This method for creating improved dust opacity maps has been employed to simulate the 2001 global dust storm with the GFDL model [10].

**References:** [1] Newman et al., (2002) *JGR*, 107,(E12). [2] Basu et al., (2004) *JGR*, 109, (E11). [3] Kahre et al., (2006) *JGR*, 111, (E6). [4] Montabone (2006) *Icarus*, 185,p 113-132. [5] Ockert-Bell et al., (1997) *JGR*, 102,9039-9050. [6] Forget et al., (1998) *GRL*, 25, (7). [7] Wolff and Clancy, (2003) *JGR*, 108, p 5097. [8] Smith et al., (2004) *Icarus*, 167,p 148–165. [9] Cantor et al. (2001), *JGR*, 106, (E6). [10] Wilson et al., (2008) *Mars Atmosphere: Modeling and Observations*. Abstract # 9023.

## POWER LAW DISTRIBUTION OF DUST DEVILS ON MARS AND EARTH. R. D. Lorenz<sup>1</sup>. <sup>1</sup>JHU Applied Physics Laboratory, 11100 Johns Hopkins Road, Laurel, MD 20723 ralph.lorenz@jhuapl.edu

**Introduction:** Published visual surveys of terrestrial and Martian dust devils differ by almost four and three orders of magnitude respectively in reported frequency per unit area. These surveys can be shown [1] to be mutually consistent for a dust devil population having a power law frequency distribution, with number proportional to the inverse square of diameter, if it is assumed surveys have an angular size detection threshold such that wider-area surveys have a proportionately larger diameter threshold. Examination of the dust devil population observed on Mars by the Spirit rover shows that indeed a -2 power law fits the data better than a previously-advocated exponential distribution. Additionally, I show here that in-situ measurements of pressure-drops [2] recorded by Mars Pathfinder follow a similar power law.

**Dust Devil Populations:** Obtaining a visual census of dust devil populations on Earth is time-consuming, tedious and hot, and only a handful of surveys have been published [see summaries in 1,3]. While the surveys all agree on the diurnal variation of activity, the overall reported populations in terms of dust devils per unit area per unit time are vastly different. This is a puzzle: while there is clearly spatial variation in dust devil frequency owing to dust availability and terrain features that may provide vorticity, the surveys are by definition performed in areas known to have frequent dust devils and the dust devil populations are likely reflecting roughly the same convective heat flux corresponding to summer clear-sky conditions. Thus it seems hard to explain the  $\sim 4$  orders of magnitude difference in dust devil frequency of these terrestrial surveys. In recent years, quantitative surveys on Mars have been made possible by the image data returned from landers and rovers : in particular, some higher-quality statistics have been generated by analysis of Spirit imagery at Gusev crater on Mars [4] – it can be shown [1] – see figure 1 – that these data follow a power law.

**Reconciling Discrepant Surveys:** The power law provides a framework to reconcile the discrepant visual surveys, which suggest dust devil densities from as few as 0.05 devils per km<sup>2</sup> per day to over 500.

Specifically, the surveys have widely different observation areas, and the effective size threshold for counting will be higher for wider-area surveys, since small, distant devils are invisible. Per the power law size distribution, such devils are abundant, and so wide-area surveys will tend to develop lower densities [1,3] – this is exactly the trend that is seen (figure 2). Indeed, with a fixed solid angle threshold, the observed density for a -2 power law intrinsic population should vary as the reciprocal of area.

**Terrestrial Size Distribution:** In fact, the Mars data [4] is presently better than the size statistics available on Earth. It should be straightforward to remedy this situation by setting up timelapse cameras in the field and analyzing the image sequence post-hoc in the same manner as was done for the Spirit data at Mars, or even by using automated change detection methods. Efforts are presently underway in this direction and preliminary experiments with timelapse cameras indicate favourable results [5].

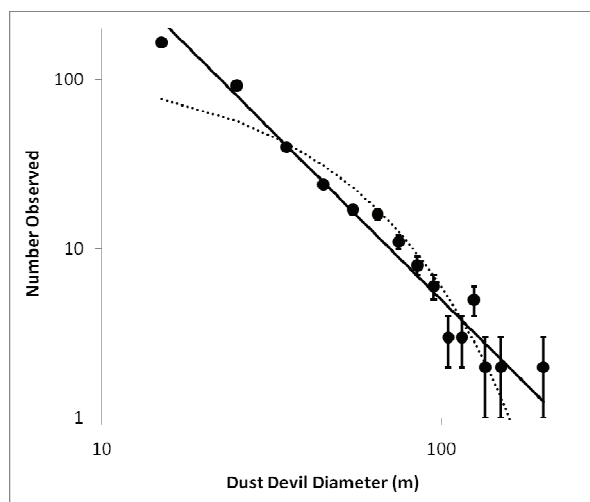


**Figure 1:** Measured diameter of dust devils at Gusev from [4] with root-N error bars. Solid line is a -2 differential power law fit. Dotted line is an exponential, which does not fit very well.

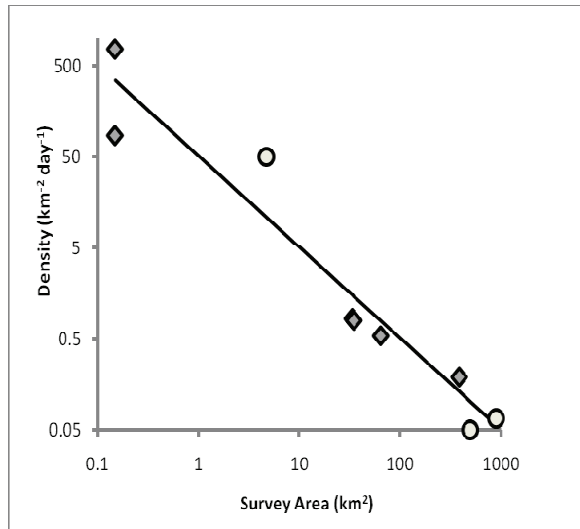


**Figure 2:** Dust devil frequency as a function of survey area in published visual census data. Diamonds are Earth surveys, circles are Mars. The solid line is a notional fit of  $Density = 50/Area$ .

**In-Situ Measurements:** There are relatively few in-situ data available, but a brief inspection of the pressure drops recorded by Mars Pathfinder [2] shows that these too follow a power law – see figure 3. However, this should not be directly compared with the diameter distribution, since first this is a cumulative distribution not a differential one and second, that the peak pressure drop depends both on the intrinsic peak drop at the vortex core, and on the miss distance which is not known for a single station.

**Future Work:** It will be interesting to explore the relationship of observed diameters and pressure drop and windspeed as a function of distance from the center of the vortex. With a single station these features cannot be disentangled, since the miss distance is not known. However, the statistics of these properties may be addressed with Monte-Carlo modeling.

Better in-situ data at Earth is an outstanding need, and will be sought next year with a set of some 80 small meteorological stations. These use USB memory sticks to allow recording of data at high rates ( $\sim 1/s$ ) over long periods. Emplaced as an array, probably  $4 \times 20$  or similar, these stations should be able to acquire robust statistics of many dust devils and enable correlations of dust loading with pressure drop etc. Furthermore, the

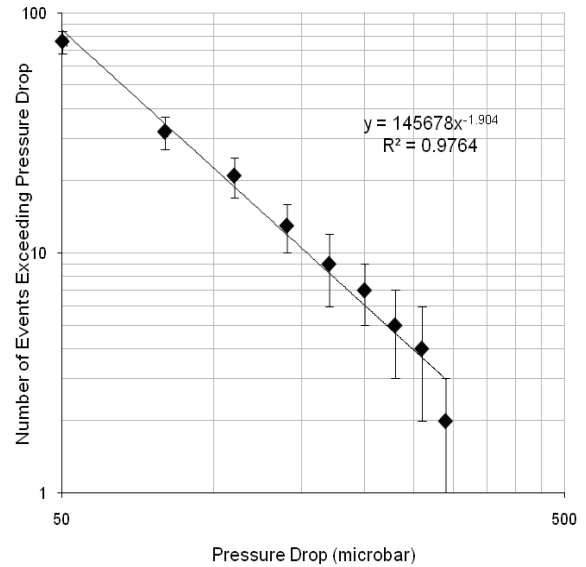


**Figure 3:** Cumulative frequency of pressure drops recorded by Mars Pathfinder [2] attributed to convective vortices and dust devils.

2-dimensional structure of the devil can be investigated (e.g. ‘spiral arms’ of wind are predicted, rather than a radially-symmetric inflow). It is hoped that these in-situ data can be obtained with contemporaneous image data from timelapse cameras.

**References:** [1] Lorenz, R. D. (2009) *Power Law of Dust Devil Diameters on Mars and Earth*, *Icarus*, 203, 683-684 [2] Murphy, J. P. and S. Nelli (2002), *Mars Pathfinder convective vortices: Frequency of occurrence*, *Geophysical Research Letters*, Volume 29, Issue 23, pp. 18-1, CiteID 2103 [3] Balme, M. and R. Greeley (2006) *Dust Devils on Earth and Mars*, *Reviews of Geophysics*, 44, RG3003 [4] Greeley, R. P. et al., (2006). *Active dust devils in Gusev crater, Mars: Observations from the Mars Exploration Rover Spirit*, *Journal of Geophysical Research*, 111, E12S09 [5] R. D. Lorenz and B. Jackson and J. W. Barnes (2009) *Inexpensive Timelapse Digital Cameras for Studying Transient Meteorological Phenomena : Dust Devils and Playa Flooding*, *Journal of Atmospheric and Oceanic Technology*, in press.

**Acknowledgement:** This work was supported via the NASA Applied Information Systems Research program.

**INVESTIGATING DUST STORM FEEDBACK PROCESSES UNDER REALISTIC CONDITIONS.** Rafkin, S.C.R. Department of Space Studies, Southwest Research Institute, 1050 Walnut Street, Suite 300, Boulder, Colorado, USA, 80302, rafkin@boulder.swri.edu, ebarth@boulder.swri.edu.

**Introduction:** In previous studies, a positive radiative dynamic feedback process has been shown to operate under specific conditions within idealized local dust disturbances on Mars [1]. Here, we extend these studies to more realistic conditions by analyzing mesoscale simulations of local and regional dust storms using a radiatively active dust cycle.

Briefly, the positive feedback mechanism works as follows (Fig. 1): 1) wind lifts dust from the surface into the atmosphere; 2) the increased atmospheric dust load results in increased radiative heating of the atmosphere during the day, or less radiative cooling during the night, thereby producing a relatively warm region on

the scale of the lifted dust; 3) Surface pressure is hydrostatically lowered in the warm region, which leads to an amplification of the low-level pressure gradient force; 4) The increased pressure gradient results in stronger winds, which lift more dust, and thus completes the positive feedback loop.

The question as to whether this feedback mechanism can operate under realistic conditions, as opposed to the idealized conditions imposed in the earlier study, remains open. The following questions are also unanswered: How does dust modulate the local and regional scale circulations? What are the conditions inside a dust storm near regions of active lifting? Does a radiative-dynamic feedback process operate under more realistic conditions? What influence do topography, background thermal state, and winds have on any feedback? How do dust lifting physics and parameters affect the feedback?

**Methodology:** Ongoing MRAMS simulations to assess the atmospheric environment at potential MSL landing sites are leveraged for this study. Here, results from three Mawrth Valles landing site (~22.3N, 16.5W) simulations are presented and discussed (Fig. 2). All simulations are configured identically with four grids, beginning with a nearly hemispheric grid at 240 km horizontal grid spacing and decreasing by a factor of three on each successive grid down to 8.9 km on the fourth grid. All three simulations use the same dust lifting scheme based on that from Michaels (2006) [2]. The dust surface source is parameterized based on the work of Armstrong & Leovy (2005) [3], where the mass flux,  $F_d$ , of entrainable particles is

$$F_d = C_N (\rho_a \rho_d)^{0.5} u_*^3 \left(1 - \frac{u_t}{u_*}\right) \left(1 + \frac{u_t^2}{u_*^2}\right), \quad (1)$$

and subgrid-scale variation of the friction velocity is included by weighting the mass flux above by a Weibull probability distribution function  $W$ :

$$F_d^*(u_*) = W(u_*, \gamma) F_d, \quad (2)$$

where  $u_*$  is surface friction velocity;  $\rho_a$  is surface air density;  $\rho_d$  is particle density;  $u_t$  is minimum value of threshold friction velocity over all particle sizes;  $C_N$  is

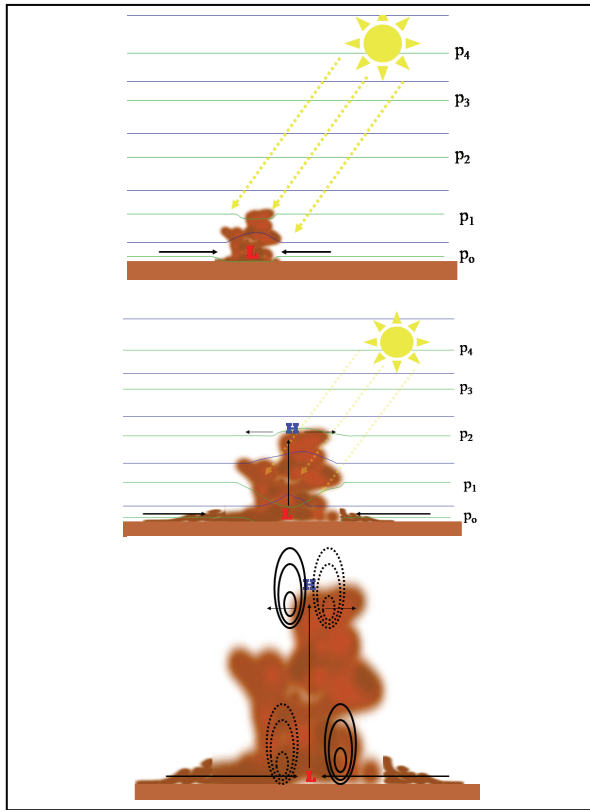


**Figure 1:** Schematic of the proposed positive feedback mechanism. An initial dust disturbance differentially warms and results in hydrostatically lowered pressure and low level convergence (top). The converging winds lift and concentrate more dust, further lowering the pressure (middle). The system matures and begins to rotate due to coriolis accelerations. (bottom).



a numerically estimated normalization factor;  $g$  is width of the PDF, determined as a function of the Richardson Number. Laminar wind and dust devil lifting are implicitly included in this single scheme. Dust devils occupy the tail end of the Weibull distribution in unstable ( $Ri < 0$ ) conditions.

There are two types of dust species in the model. Lifted dust is carried in the model via eight discretized mass bins. Dust in each bin is free to advect, diffuse, and sediment. In all simulations, the dust is radiatively active. In addition to lifted dust, there exists a radiatively active background dust distribution that varies in space and time based on that retrieved from MGS TES. Therefore, the lifted dust should be viewed as positive perturbations to this background dust field.

**Simulations:** The dust efficiency factor in the lifting parameterization is varied to provide a range of conditions between slightly perturbed dustiness ( $\sim 0.1$  opacity) to severely dusty ( $> 4.0$  opacity). In addition, one simulation uses a high efficiency factor on the fourth nested grid (an area approximately the size of that shown in Figure 2) and low efficiencies elsewhere. This mimics the production of regional dust storms.

To the extent that dust is a passive tracer, all the simulations should evolve in a similar manner. As will be shown, this is not the case, indicating that dust does alter the circulation not just on the global scale (as is previously known [4]), but also on the local and regional scale.

#### Local Impacts of Global Dust Changes

By setting the dust efficiency factor to a large value ( $9.e-7$ ) on all grids, the entire model domain becomes increasingly dusty with time. This mimics the growth

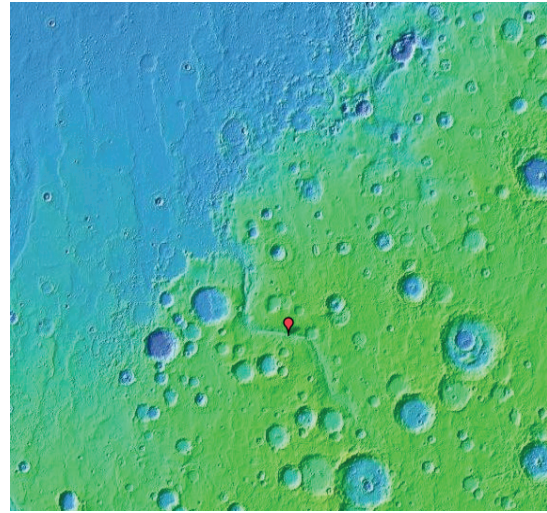


**Figure 2:** Topography in the region of Mawrth Valles (GoogleMars). The proposed MSL landing site is closer to the mouth of the valley, near the boundary between the heavily cratered southern highlands and the northern plains.

of a global dust storm. Importantly, although the efficiency factor is large, the dust is lifted in a manner fully consistent with the model-predicted wind stress, and the dust is then allowed to circulate in a manner fully consistent with the dynamics. Figure 3 shows the difference in the near-surface wind field and perturbation opacity after 10 hours of dust lifting (near sunrise) for the global low efficiency case and the global high efficiency case on grid 4. Dust lifting was initiated during the evening. Although the magnitude of the dust opacity is different, the patterns are similar, indicating that dust has had a limited impact on the dynamics up through this point. Also note that the wind magnitudes and directions are quite similar.

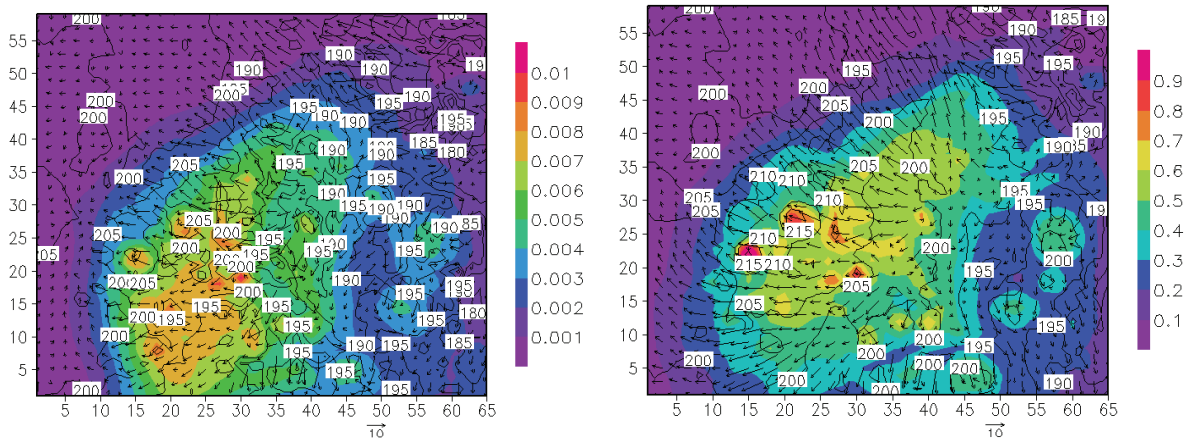


**Figure 3:** Dust opacity and near-surface winds in a slightly dusty (left) and very dusty (right) simulation at sunrise after 10 hours of active dust lifting. The similarity of the wind and dust fields indicate that dust has behaved primarily as a passive tracer during the evening period.



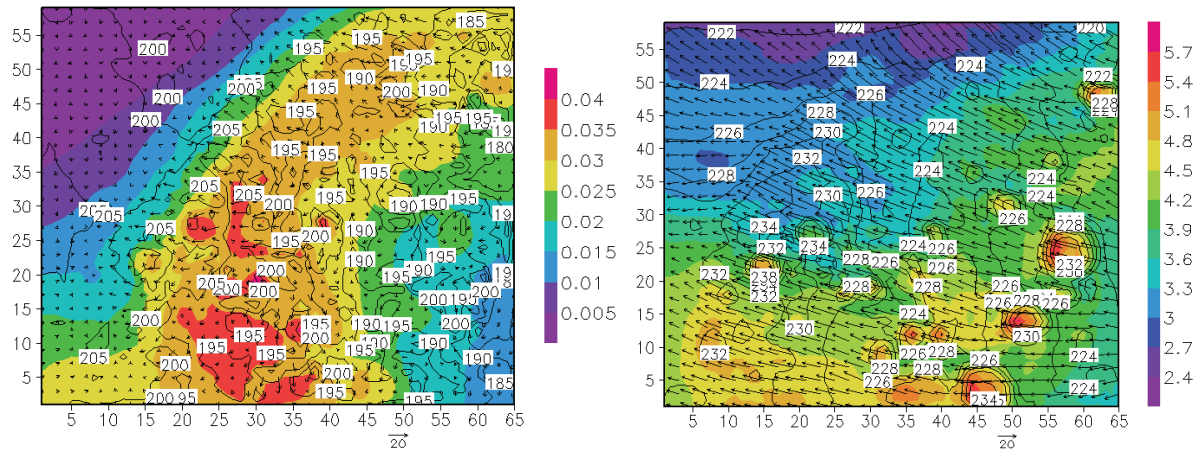


**Figure 4:** Same as Fig. 3, but 24 hours later. Wind speeds in the dust case are nearly twice that of the slightly dusty case and the dust distributions are substantially different. Dust has been actively modifying the dynamics over this period.

Figure 4 shows the same simulations 24 hours later. The winds in the globally dusty case are nearly twice as strong as those in the limited dust case. Furthermore, the influence of topography on the circulation is heavily muted in the dusty simulation. Apparently, the dust heating has become strong enough that it overwhelms the topographically-driven circulations that dominate in modest dust loading scenarios. This effect is also seen in the pressure traces from a location near the proposed landing site (Fig. 5). As dust loading increases, the diurnal tidal signal strengthens while the semidiurnal and topographic pressure signals fade.

Dust is clearly having a large impact on the local circulations and this has resulted in substantially different dust distributions. However, it is not clear whether the overall acceleration of the winds is related to the global increase in dustiness and an

overall strengthening in large-scale winds, or whether the acceleration is being produced locally due to the local dust field.

#### Local Impacts from Local Dust Changes

To assess the impact of local dust on the local circulation, the case with high dust lifting efficiency confined only to the fourth grid is analyzed. A local dust storm is produced in this situation. During the daylight hours, the dusty region is strongly heated to produce a negative pressure perturbation (Fig. 6).

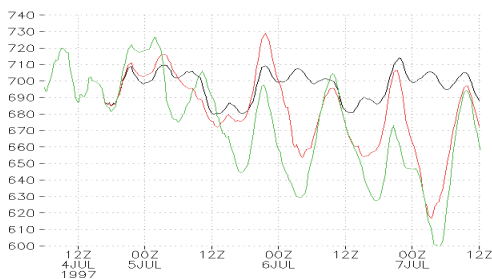


**Figure 5:** Pressure traces from a slightly dusty (black), moderately dusty (red) and highly dusty (green) simulations. As dust increases, the diurnal signal begins to dominate over topographic and semi-diurnal tidal signals.

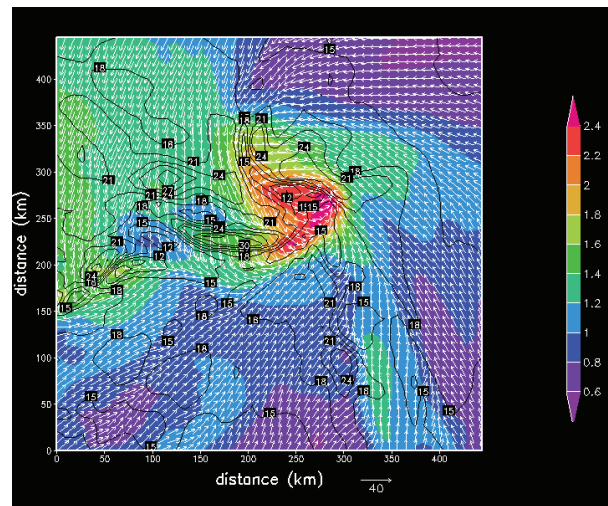


**Figure 6:** A cyclonic dust storm forms in the late afternoon in the simulation with high dust lifting efficiency operating on only the fourth grid. The structure is consistent with that seen in idealized simulations and strongly suggests that the positive feedback mechanism is active. Dust opacity (shaded) is maximum near the center of the disturbance. Spiral arm bands with strong winds (contoured) and active dust lifting are emanating from the center.

This pressure distribution then initiates the development of a cyclonic circulation with a ring of strong wind speeds and a much calmer center. Spiral arm bands where wind speed and dust lifting are maximized is also apparent. These features are exactly those predicted based on the idealized experiments [1]. The location of Mawrth Valles is also at the preferred latitude for maximum positive feedback, because solar heating is still rather strong in the subtropics and the coriolis force is strong enough to produce rotation.

A view of the entire fourth grid (not shown) shows that there are typically more than one disturbance at any given time. In this case, the storms tend to organize along a shear boundary

A vertical cross-section (through  $y=250$  km in Fig. 6) is displayed in Fig. 7. Here, two disturbances are seen with the one in Fig. 6 being the eastern most. Dust mixing ratio is maximized in the center of the storm and is lofted primarily in the deep updrafts associated with the spiral arms. Note that the storm produces an elevated dust layer in the outflow region; dust mixing ratio has a maximum value at  $\sim 8$ -13 km with the top of the dust extending to  $\sim 20$  km. Strong gravity wave activity is also present above the storm. Vortical motion is indicated by the organized flow into and out of the page (north-south) with magnitudes of  $\pm 30$  m/s. This would be sufficient to categorize this disturbance as a very strong tropical storm on Earth.

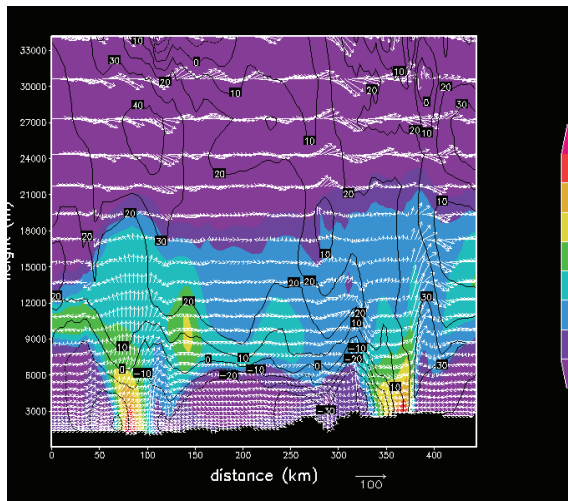


**Figure 7:** A vertical cross-section along  $y=250$  km in Fig. 6. The section slices near the center of the mature eastern disturbance and through an updraft band in the western. The rapid, deep vertical transport of dust (mixing ratio shaded g/kg) is evident. These systems produce elevated dust layers. Contour lines show the winds into and out of the page. The strong vertical motion of the western system is comparable to a strong tropical disturbance on Earth.

Surprisingly, the convective boundary layer does not appear to be deeper than in the lightly dust case (Fig. 8). However, the boundary layer of the dust simulation is generally more energetic, is locally deeper in the regions of active dust lifting and vertical transport, and is somewhat suppressed in the quiescent regions. The lower boundary layer in the quiescent regions is likely due to compensating subsidence associated with upward motion in the storms. In this sense, the boundary layer is responding exactly as it does on Earth to deep moist convection.

The dynamical storm structures that develop during the day rapidly dissipate at night and are not seen to regenerate the next sol. The reason for the dissipation is, as described in the idealized situation, due to the loss of solar heating, which ultimately provides the energy for the system. Topographic influences and wind shear then destroy the incipient vortex. It is not clear why the system does not redevelop the next sol. However, it is likely due to the limited supply of surface dust, most of which is removed during the dust storm.

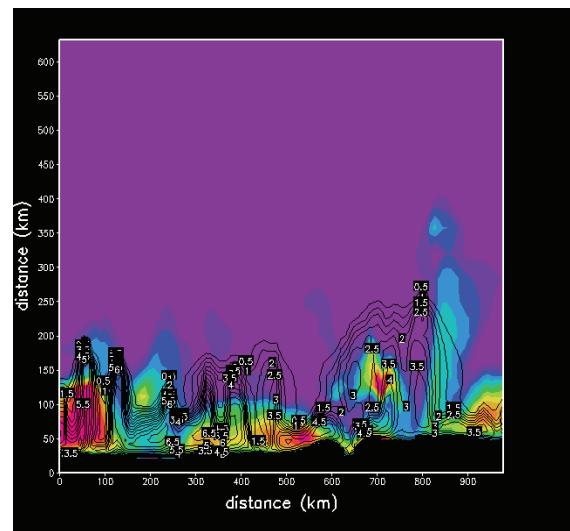


**Figure 8:** Subgrid scale turbulent kinetic energy from the dust storm simulation (shaded) and from the lightly dusty case (contoured). The dust storm case is generally more energetic and the boundary layer is locally deeper in regions of active lifting. However, the depth of the layer in the dust storm case is somewhat suppressed compared to the lightly dusty case. This behavior is likely due to compensating subsidence and response similar to that seen with deep moist convection on Earth.

**Summary:** Although much work remains to be done, it does appear that the positive dust storm feedback process does operate under realistic conditions. The Mawrth Valles simulation was chosen strictly out of convenience; the appearance of an organized storm in this simulation suggests that the underlying dynamics may be commonplace. Additional simulations at other locations need to be conducted to confirm this.

Given the ease in which local dust storms formed, it now seems more plausible that these systems are behind some of the disturbances that have been repeatably imaged from orbit. However, it is difficult to ascertain dynamics of the observed systems based solely on visual appearance. Surface stations with such storms or orbital retrievals of pressure, temperature and winds with sufficient spatial resolution to capture the storm structure are necessary.

Should a spacecraft descend into an active local dust storm, it is likely to encounter conditions that are drastically different than nominal. Likewise, robotic or human missions operating on the surface would experience very poor, possibly hazardous, weather conditions.

**References:** [1] Rafkin, S.C.R. (2009) *JGR* 114, E01009, doi:10.1029/2008JE003217. [2] Michaels, T.I. (2006) *Geophys. Res. Lett.* 33, L19S08, doi:10.1029/2006GL026268. [3] Armstrong J.C. and C.B. Leovy (2005) *Icarus* 176, 57-74. [4] Haberle, R.M., C.B. Leovy, and J.B. Pollack (1982) *Icarus*, 50, 322-367.

**DUST LIFTING, DEPOSITION, AND TRANSPORT PROCESSES IN GM3.** Wu, D.<sup>1</sup>, McConnell, J.C.<sup>1</sup>, Kaminski J. W.<sup>1</sup>, and Akingunola, A.<sup>2</sup>. <sup>1</sup>Centre for Research in Space Science and Engineering (York University, 4700 Keele Street, Toronto, ON, M3J1P3, Canada , email: wudi2004@yorku.ca), <sup>2</sup>Canadian Space Agency

**Introduction:** Previous studies of Martian dust cycle [1,2,3] have taken into account two dust lifting mechanisms: mechanical processes (wind shear) and thermal convective processes (specifically, dust devils). They suggested that thermal convective processes can maintain the background dust haze, and the mechanical processes can trigger global and local dust storms. A mechanical dust lifting process based on the terrestrial Dust Entrainment And Deposition (DEAD) model [4] has been studied for dust lifting in a Mars general circulation model GM3 (the Global Mars Multiscale Model) developed at York University. The dust emission is assumed by saltation sandblasting process as depicted in DEAD model. The threshold wind friction for saltation is calculated using a semi-empirical equation developed by Iversen and White [4,5,6]. The optimal diameter for saltation particles has been found around 110  $\mu\text{m}$ . This size of sand particle is assumed everywhere on the surface of Mars. The saltation occurs whenever friction velocity is greater than the saltation threshold friction velocity.

**The model description:** The Mars general circulation model GM3 has been developed at York University [7,8], which is built on the Canadian operational weather forecast Global Environmental Multiscale NWP Model (GEM version 3.3.0). The mechanical dust lifting, dust dry deposition, and transport of dust processes have been added into GM3 in the following simulations by running the model with horizontal resolution  $9^\circ$  by  $9^\circ$ , 102 vertical levels, time step 30 minutes, and an isothermal at rest initial state atmosphere.

The surface roughness length is assumed globally uniform,  $z_0=0.01\text{m}$ . To enhance the probability of dust lifting, the Weibull distribution is applied to the mean near surface wind before determine lifting condition. For testing, five wind bins have been adopted. Dust lifting is not allowed where the surface is ice-covered. No radiative feedback of lifted dust is taken into account.

After the vertical dust flux is obtained, dust is partitioned into four dust bins for transport both vertically and horizontally, furthermore, the gravitational settling and turbulent mix-out have been taken account for the dry deposition. We adopted four transported dust bins (Table 1, [4]) used in the DEAD model.

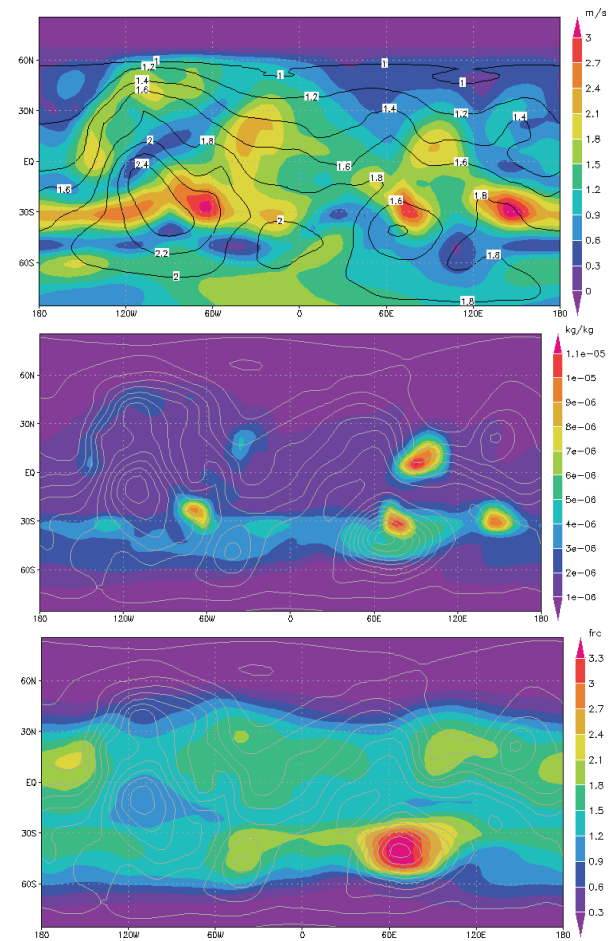


**Figure 1:** The snapshots after 30 sols simulation from Ls 270<sup>0</sup> (about Ls 286<sup>0</sup>), from top to bottom: friction velocity of wind bin 5 (shade) and threshold friction velocity for saltation (contour) in m/s, dust lifting mixing ratio for dust bin 2 near surface level, total column dust optical depth (visible). The gray contours in middle and bottom panels present topography

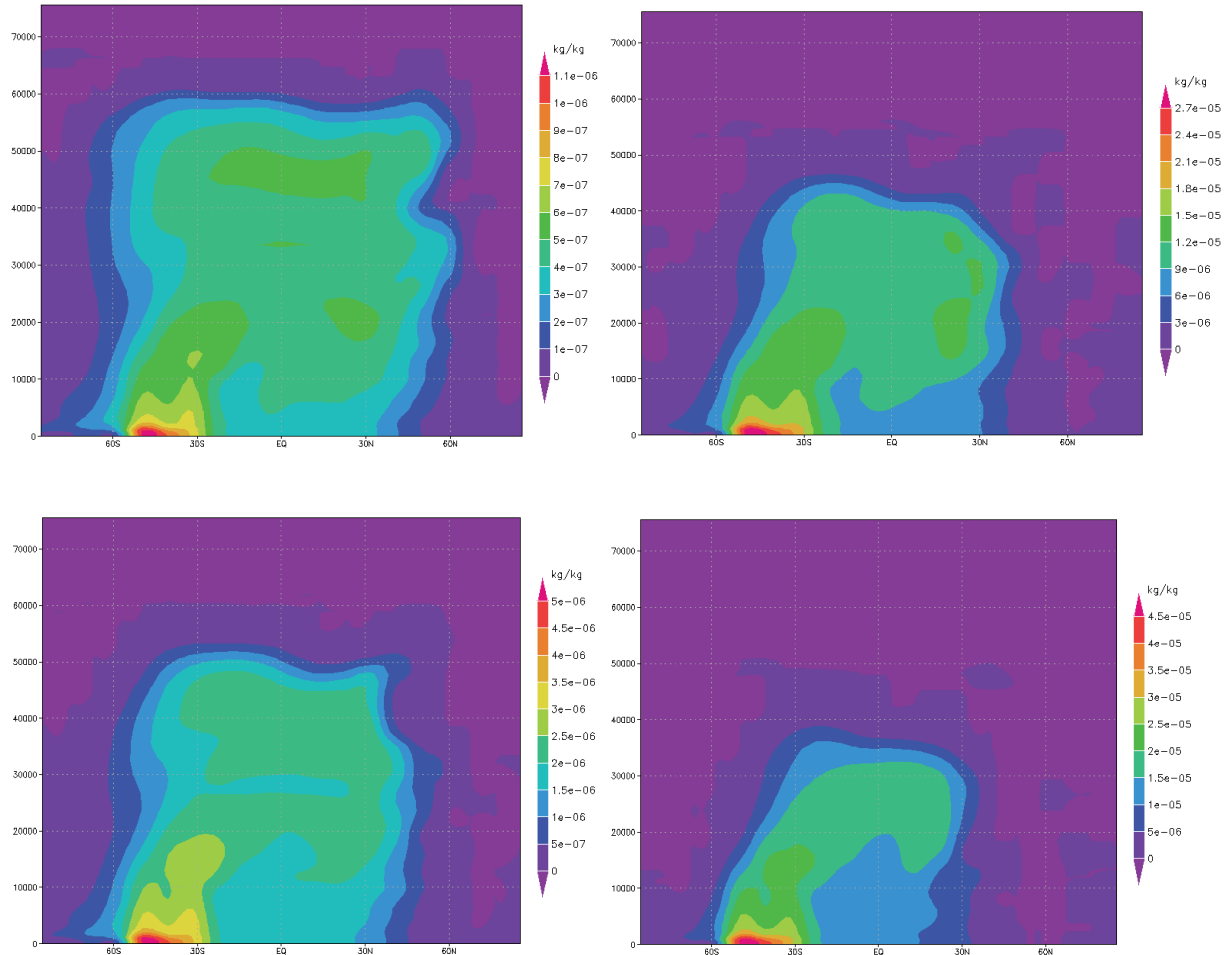


**Figure 2:** The snapshots after 30 sols simulation from Ls 270<sup>0</sup> (~Ls 286<sup>0</sup>), cross sections along longitude 65<sup>0</sup>E, from top to bottom are dust lifting mixing ratio of dust bin 1, 2, 3 and 4 respectively. The vertical levels are heights in meters.

Bin	$D_{\min}$ ( $\mu\text{m}$ )	$D_{\max}$ ( $\mu\text{m}$ )	$D_v$ ( $\mu\text{m}$ )	$\sigma_g$	$\Psi_e$ ( $\text{m}^2\text{kg}^{-1}$ )	$M_j$ (%)
1	0.1	1.0	2.524	2.0	$2.893 \times 10^3$	3.2
2	1.0	2.5	2.524	2.0	$8.350 \times 10^2$	17
3	2.5	5.0	2.524	2.0	$3.825 \times 10^2$	41
4	5.0	10.0	2.524	2.0	$1.961 \times 10^2$	38

**Table 1:** Four transported dust bins, minimum size  $D_{\min}$ , maximum size  $D_{\max}$ , volume median  $D_v$ , geometric standard deviation  $\sigma_g$  of sub-bin distribution, extinction  $\Psi_e$ , and the mass fraction of entrained and transported dust  $M_j$ , in each bin.

**Results:** The preliminary simulations show that the mechanical dust lifting and dry deposition processes from the terrestrial DEAD model can be successfully applied to our Mars GCM. Combining with the vertical and horizontal transport schemes in GM3, the results suggest that the saltation-sandblasting dust lifting scheme could account for the dust storms during the southern summer.

From Figure 1 (top) we can find that at some locations, friction velocity of wind bin 5 is greater than the threshold friction velocity for saltation, that is the lifting condition is satisfied. Figure 2 shows that the smaller dust falls out slowly, and can be transported to higher levels and longer distances.

For our further work, thermal convective process, radiative feedback, and removal mechanisms (such as condensation scavenging) will be added into GM3.

**Acknowledgments:** This work was supported by a grant from NSERC (Natural Sciences and Engineering Research Council of Canada).

**References:** [1] Newman C. E. et al. (2002) *JGR*, 107(E12), 5123. [2] Basu S. et al. (2004) *JGR*, 109, E11006. [3] Kahre M.A. et al. (2006) *JGR*, 111, E06008. [4] Zender C. S. et al. (2003) *JGR*, 108(D14), 4416. [5] Iversen J. D. and White B. R. (1982) *Sedimentology*, 29, 111–119. [6] Marticorena B. and Bergametti G., *JGR*, 100(D8) 16415-16430. [7] Moudden Y. et al. (2005) *JGR*, 110, E0400. [8] Akingunola, A. (2008) PhD thesis, York University, Canada.





**Session Seven**  
*Polar Dust and Dynamical  
Processes*

*Thursday, September 17, 2009  
8:30 AM – 10:00 AM*



## CRISM OBSERVATIONS OF ATMOSPHERIC DUST IN THE MARTIAN SOUTH POLE REGION. A.J. Brown<sup>1</sup> and M. J. Wolff<sup>2</sup> <sup>1</sup>SETI Institute, 515 N. Whisman Rd Mountain View, CA 94043, abrown@seti.org, <sup>2</sup>Space Science Institute (18970 Cavendish Rd, Brookfield, WI, 53045). Author website: <http://abrown.seti.org>

**Introduction:** CRISM has observed the planet Mars for a full Mars year, here we continue the work reported in [1-2] to document the opacity of the atmosphere in the polar regions for Martian Years 28/29.

Previous planetwide surveys of atmospheric opacity have generally omitted the areas poleward of 65 degrees due to the variability of the polar opacity and the presence of optically thick polar hood clouds during winter [2-5] although see [6] for observations of global dust storms using MOC.

CRISM has the ability to take ‘gimballed’ observations of the surface as it passes over a target, thus creating what is termed an Emission Phase Function or ‘EPF’ measurement (Figure 1) [7]. We report here on our investigations of the EPF polar observations and our attempts to model dust and ices suspended in the atmosphere and soil and ice covered surface.

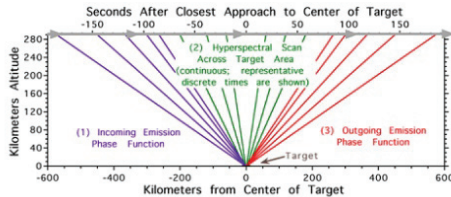


**Figure 1:** Schematic of a CRISM EPF observation

Table 1 shows all the CRISM EPF observations poleward of 55°S. Prior to  $L_s=152$ , the sun had not yet risen sufficiently high over the south polar region. CRISM is limited to daytime observations and MRO is in a ~250km circular orbit that crosses the equator south to north at 1500 local Mars standard time.

**Method:** We are using the DISORT [8] algorithm to generate a Mars model atmosphere column at one wavelength (0.696  $\mu\text{m}$ ) for each observation. We iteratively adjust three parameters (surface albedo, dust and ice opacity) in order to achieve a close fit at five points spread across the EPF (two points in the

wings and one central point). The surface albedo is assumed to be lambertian (scatters equally in all directions).

We have decided to use a four stream model, since this is suggested by Liou [9] to yield an accuracy of within 1% for ‘typical phase functions’, compared to a two stream model which introduces errors of the order of 3-10%. 16 streams is considered to give ‘close agreement’ to reality but at this stage is time prohibitive.

Earth DOY 2007	MY/ $L_s$	EPF	FRT	HRL	HRS
06 352-5	28/[152-159]	8			
006-016	[160-168]	9			
016-033	[168-176]	3		3	1
033-044	[176-183]	10	6	3	4
044-059	[183-192]	20	17	1	6
059-073	[192-200]	8	20	1	5
073-086	[200-208]	2	14		1
086-101	[208-217]	25	27		24
101-115	[217-225]	17	29	11	12
115-116	[225-234]		4	1	
132-142	[234-243]		36		3
142-156	[243-252]	27	42	5	8
156-171	[252-261]	3	37	7	2
171-185	[261-270]	12	48	4	1
185-198	[270-278]	124	30	2	2
199-212	[278-286]	43	30		
213-225	[286-295]	49	137	1	6
227-240	[295-303]	22	111	2	2
241-255	[303-312]		111	4	
255-268	[312-320]	16	66	3	4
269-282	[320-328]		34	16	4
283-296	[328-335]		49	5	13
297-311	[335-343]		18	8	4
311-348*	[343-002]				
348-004*	29/[002-012]		61	1	2
004-033*	[012-026]		43	3	
033-074*	[026-044]		39	3	2
TOTAL	$n=1599$	399	1009	84	107

**Table 1:** Totals of CRISM observations relevant to this study. Counts in italics indicate some missing geometries. Each line corresponds to the two week MRO planning cycle. DOY column gaps are when CRISM collected no data at the south pole.

\* Indicates non 14-day time periods

**Model Assumptions:** We use phase functions for water ice ‘Type 1’ (non-aphelion ice cloud) with 64 moments [10] and dust particle phase function with 64 moments derived in [11] and recommended by [12]. The dust and ice particles are assumed spherical, with a gamma particle size distribution:

$$n(r) = r^{(1-3v_{eff})/v_{eff}} \exp\left(-\frac{r}{R_{eff}v_{eff}}\right)$$

For dust:  $R_{eff} = 1.5$  microns,  $v_{eff} = 0.4$ , ice:  $R_{eff} = 2.0$  microns,  $v_{eff} = 0.1$ . Dust optical constants were from [13] and water ice optical constants were from [14]. The single scattering albedo for each atmospheric layer can then be derived.

We use an elevation corrected scheme for rayleigh molecular scattering:

$$\tau_{Rayleigh} = 1.56e^{-25} e_{scale} \sigma \left(\frac{0.305}{\lambda}\right)^4$$

Where  $\sigma$  is the column density in  $\text{cm}^{-2}$  and  $e_{scale}$  is an elevation scaling factor based on a 10km scale height [15]. We have used the MOLA heights in the center of each observation to scale the atmospheric surface pressure and assumed no barometric pressure changes with height.

Layer height (km)	Pres. (mbar)	Layer height (km)	Pres. (mbar)
0.0	6.799	41.0	1.362e-01
1.0	6.288	43.0	1.089e-01
4.0	4.950	45.0	8.686e-02
7.0	3.869	47.0	6.915e-02
9.0	3.269	49.0	5.496e-02
11.0	2.752	51.0	4.364e-02
13.0	2.309	53.0	3.462e-02
15.0	1.929	55.0	2.745e-02
17.0	1.605	57.0	2.175e-02
19.0	1.331	59.0	1.723e-02
21.0	1.099	61.0	1.365e-02
23.0	9.042e-01	63.0	1.081e-02
25.0	7.414e-01	65.0	8.559e-03
27.0	6.059e-01	67.0	6.779e-03
29.0	4.937e-01	69.0	5.369e-03
31.0	4.011e-01	71.0	4.253e-03
33.0	3.249e-01	73.0	3.370e-03
35.0	2.625e-01	75.0	2.670e-03
37.0	2.115e-01	77.0	2.116e-03
39.0	1.700e-01	79.0	1.678e-03
		179.0	1.678e-10

**Table 2:** Model Martian atmospheric layers. These are scaled for each observation according to elevation of the terrain. Pressure inversions or large variations with height are not treated. We interpolate 15 layers from this profile at 50, 40, 35, 30, 25, 20, 17, 14, 11, 9, 7, 4, 2, 1, 0.00145 and 0 km.

Starting with a Martian atmosphere with 39 2 km high layers from 1-79 km (with a base layer of 1 km and a top layer of 100 km), with 10 km scale height (Table 2) we interpolate 15 layers at 50, 40, 35, 30, 25, 20, 17, 14, 11, 9, 7, 4, 2, 1, 0.00145 and 0 km. We use MOLA heights from the CRISM DDR files to scale the atmospheric column. Dust is restricted to heights of 0-80 km, water ice clouds are restricted to 25-80 km. Both dust and water ice are assumed to be evenly distributed within these height restrictions. We use standard corrk files (produced by M.D. Smith) for CO<sub>2</sub>, (95.3%) molecules (we currently omit seasonally variable CO, H<sub>2</sub>O and CH<sub>4</sub>) and a typical ozone column at perihelion ( $L_s = 240$ ) varying from  $2.45 \times 10^{-7}$  (at 6.96 mbar) to  $7.8 \times 10^{-5}$  at 0.02mbar. We do not treat thermal radiation from the surface or within the atmosphere (this has minimal effects at  $\sim 0.7 \mu\text{m}$ ).

**Results:** Figure 2 shows a typical EPF sequence showing the projected ground coverage of each EPF segment. Ideally the images would be coincident, but due to spacecraft movement the registration of the images is not perfect. This can lead to difficulties in regions where the surface albedo is changing quickly.

Example EPF plots showing the variation versus emission angle and phase angle are shown in Figure 3.

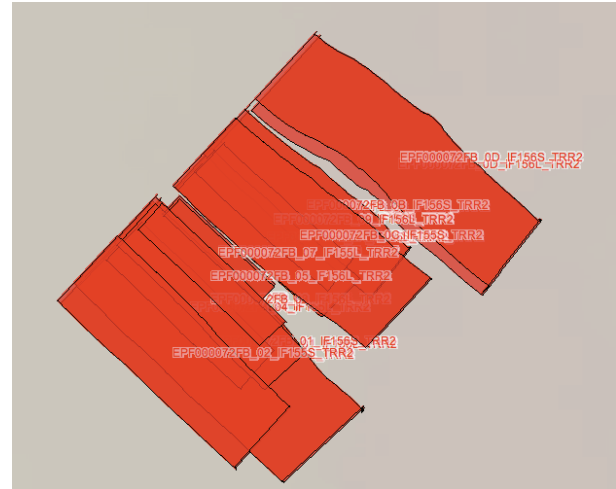


**Figure 2:** Spatial coverage of the eleven overlapping elements of CRISM EPF observation 72FB. Note the variation in spatial position and horizontal width.

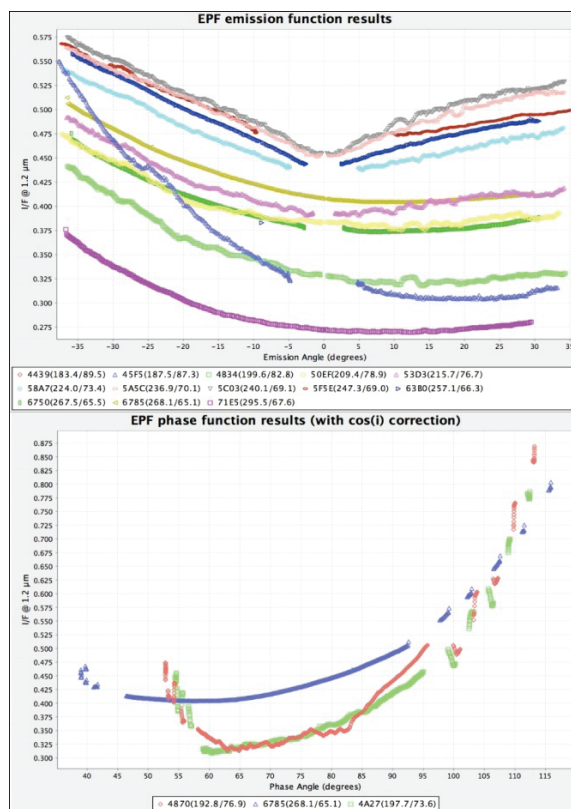


**Figure 3:** Results for polar EPFs using the CRISM channel near 1.2 microns. (above)  $I/F$  versus emission angle (negative values indicate data taken on the spacecraft 'incoming' leg) for 13 polar EPF sequences. (below)  $I/F$  versus phase angle (angle between incidence and emission vectors) for three polar EPF sequences.

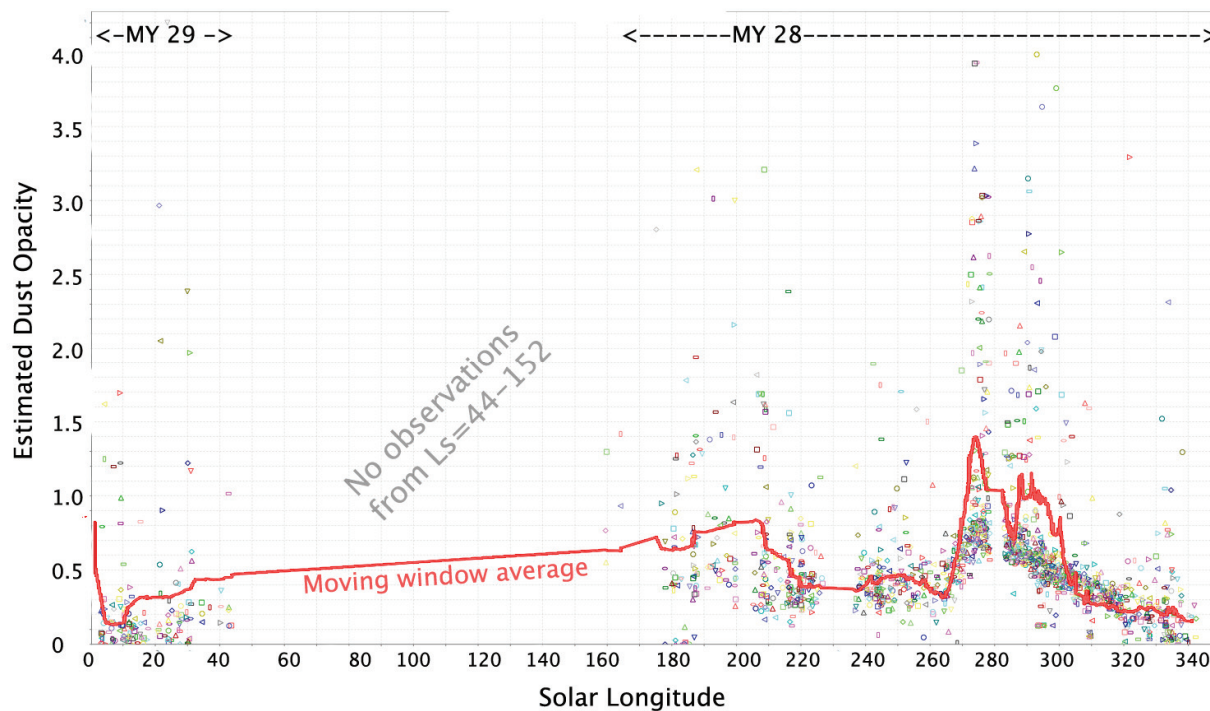


**Figure 4:**  $\tau_d$  estimates for CRISM EPF observations over the south pole (poleward of  $55^\circ\text{S}$ ).



The  $\tau_d$  results for CRISM EPF data from Mars Year 28/29 (2006-2008) are shown in Figure 4. Employing a moving window ( $n = 128$ ) average (red line) we see a background value of  $\tau_d \sim 0.3-0.5$ , which rises to a peak background of  $\tau_d = 1.4$  during the MY28  $L_s = 270-310$  dust event. The average  $\tau_d$  during the dust event rises quickly to a peak value from  $L_s = 270-280$ , and slowly returns to background levels from  $L_s = 280-320$ . Several other dust opacity excursions are also apparent, at the start of the spring recession and a small but noticeable peak from  $L_s = 240-260$ .

In order to present our surface albedo results in a familiar form, we have projected the results into a polar stereographic projection and accounted for our sparse data by using a Voronoi tessellation algorithm [16] to cover the entire pole. We have also pinned albedo results to the 0.2-0.8 range, and binned them to 0.1 increments before colour assignment. The results for 11 different periods covering the spring period of the southern polar region (each covering 20 degrees of solar longitude) are shown in Figure 5.

**Future work:** We are currently investigating using a look up table approach to speed up our processing – this will enable the use of more streams in the DISORT modeling. We also intend to utilize another wavelength (near  $0.4 \mu\text{m}$ ) to enhance the robustness of our water ice retrievals. Future work will also cover north polar FRT observations and the next year of CRISM operations.

**Conclusions:** We have derived estimates of atmospheric dust (Figure 4), surface albedo (Figure 5) and ice opacities (not shown) for the first Mars year of CRISM operations (MY28-29), which included a large dust event at  $L_s = 260-270$ . The results for this period are consistent with background dust opacities of  $\tau_d = 0.3-0.5$  for the south polar region, with average excursions to 1.4 during the MY28 dust event.

**Acknowledgements:** Our thanks to Scott Murchie (CRISM PI and the CRISM science operations team at JHU APL for their dedication to the task of obtaining this unique dataset. Our thanks to Mike Smith for providing his cook files for Martian  $\text{CO}_2$  profiles.

**References:** [1] Brown, A. et al. (2008) *LPSC XXIX* #2140 [1] Brown, A. et al. (2009) *LPSC XXXX* #1675 [3] Martin, T.Z. (1986) *Icarus* 66 2-21 [4] Colburn, D.S. et al. (1989) *Icarus* 79 159-189 [5] Smith, M.D. (2008) *AREPS* 36 191-219 [5] Cantor, B. (2001) *JGR* 106, 23653-23687 [7] Murchie, S. et al. (2007) *JGR* 112 [8] Stamnes, K. et al. (1988) *AO* 27, 2502 [9] Liou, K.-N. (1973) *JAS* 30, 1303-1326 [10] Clancy et al. (2003) *JGR* doi:10.1029/2003JE002058 [11] Tomasko et al. (1999) *JGR* 8987-9008 [12] Wolff, M. et al. (2007) *7<sup>th</sup> Mars*, #3121. [13] Wolff, M. et al. (2008) *3<sup>rd</sup> Mars Atmos. Wksp*, #9125 [14] Warren, S.G. (1984) *AO* 23, 1206-1225 [15] Pollack, J.B. et al. (1979) *JGR* 84 2929-2945 [16] Fortune, S. (1986) A sweepline algorithm for Voronoi diagrams. Proc. of 2<sup>nd</sup> Symp. on Comp. Geom. Yorktown Heights, NY, USA, p. 313-322 and <http://shaneosullivan.wordpress.com/category/voronoi/>

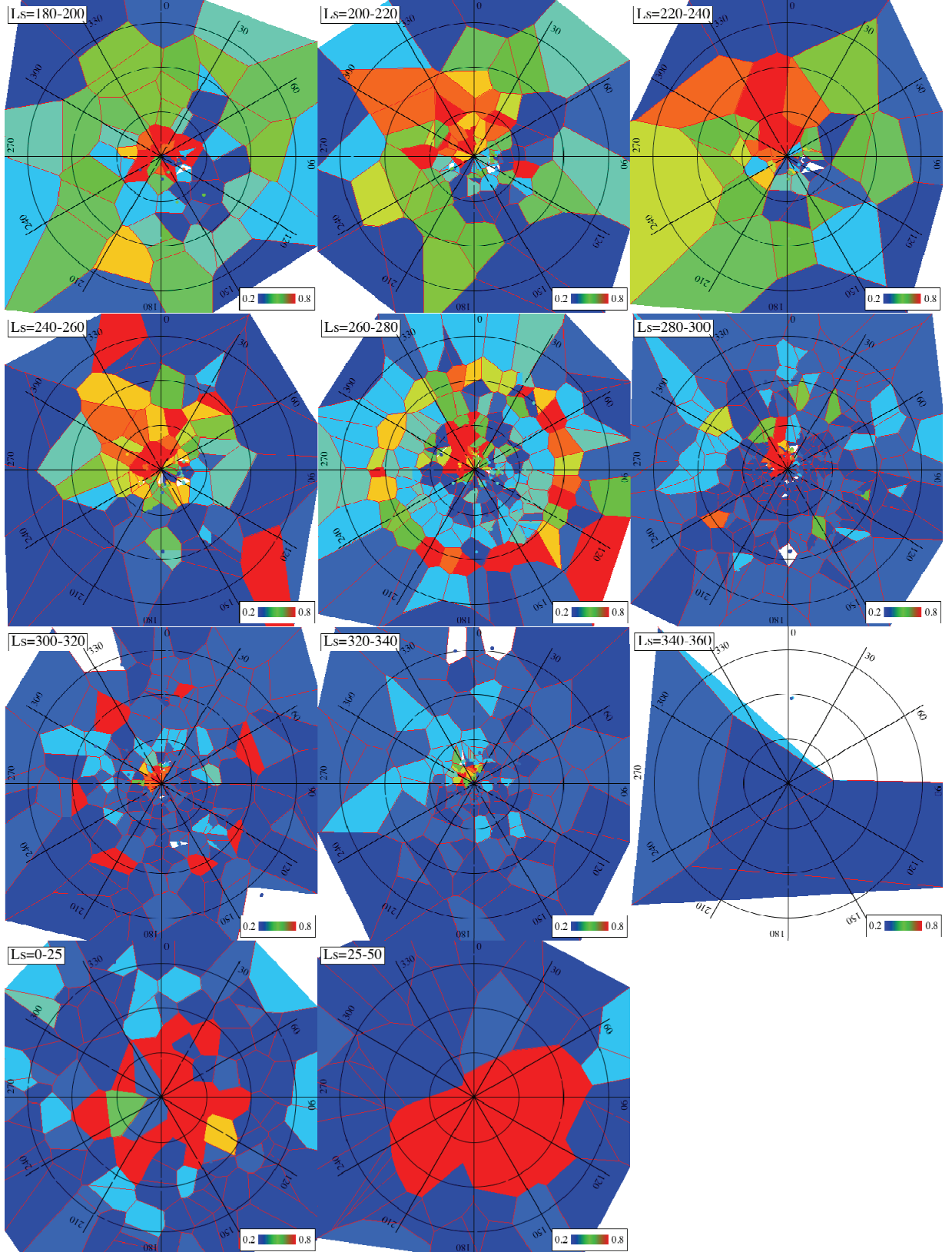


**Figure 5:** Surface albedo estimates for CRISM EPF observations covering  $L_s=280-300$  and  $L_s=320-340$ . A Voronoi tessellation scheme [16] has been used to artificially extend the influence of each point and ensure total coverage of the pole by the albedo data. Albedo values have been binned to 0.1 increments and pinned within the 0.2-0.8 range.

**EFFECTS OF GLOBAL DUST EVENTS ON THE CO<sub>2</sub> POLAR CAPS.** James<sup>1</sup>, P. B., Thomas<sup>2</sup>, P.C., and Malin<sup>3</sup>, M.C. <sup>1</sup> Space Science Institute, 4750 Walnut St., Boulder, CO 80301 (pjames@cableone.net); <sup>2</sup> <sup>1</sup>Center for Radiophysics and Space Research, Cornell University, Ithaca NY 14853; <sup>3</sup> Malin Space Science Systems, San Diego, CA.

The Mariner 9 (M9) spacecraft was inserted into orbit around Mars on November 14, 1971, and continued to acquire images and other data until October 27, 1972. The first M9 data showed an immense, planet encircling dust storm that engulfed most of the planet; the south polar cap was barely discernable beneath the dust haze. Over the next several months, as the dust cleared, M9 documented the summer recession of the south polar cap (during MY 9) to its perennial or residual configuration in late summer [1]. Figure 1 shows the residual cap in MY 9 at  $L_s = 315^\circ$ . During the subsequent Viking Mission to Mars, Viking Orbiter 2 observed the entire south polar cap recession of MY 12 (Figure 2). Comparison of the Viking and M9 observations in these two years revealed substantial differences in the residual cap between the two years [2]; the recession recorded by Viking lagged that of M9 considerably.

The next Mars orbiter that observed South Polar Cap recessions was Mars Global Surveyor (MGS) in MY 24-27. Mar Orbiter Camera (MOC) observations revealed that the residual caps in those years were very similar in extent and appearance to that observed by Viking [3]. The discovery by MOC of complex structures in the CO<sub>2</sub> surface of the RSPC [4] and of interannual variability of those features [5]

rekindled interest in the M9 observations: did the erosion of features observed within the RSPC suggest that we were observing the demise of the cap, or taken with the M9 observations did they suggest that there was a shorter term cycle of net annual deposition and erosion of CO<sub>2</sub> driven by processes unknown?

We attempt to answer this question using newly acquired data from the Mars Color Imager (MARCI) on Mars Reconnaissance Orbiter (MRO) in MY 28-29. MARCI images of the RSPC in these two years show unambiguously that the early summer observations of the cap in MY 28 resemble those of M9 while in MY 29 the cap again appears like it did in Viking and MGS observations. The main focus here is the large outlier of CO<sub>2</sub> located roughly at  $-83^\circ\text{S}$ ,  $350^\circ-30^\circ\text{W}$ . To the extent that it is possible to distinguish between seasonal and residual frost, we regard this in some sense as the last part of the seasonal cap to sublime. The reason for the "seasonal" designation is that this outlier disappears

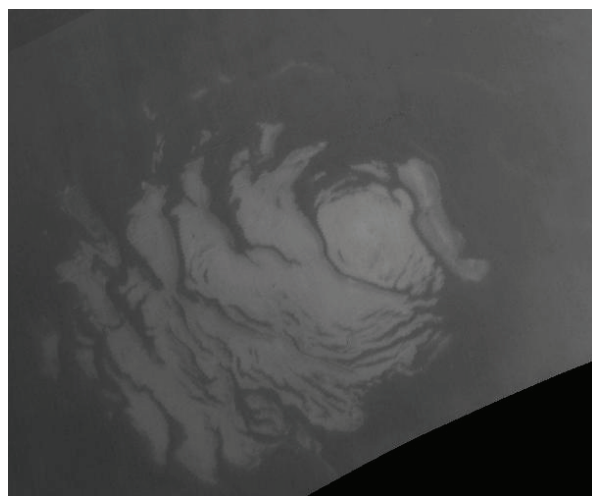


**Figure 1:** Projected Mariner 9 image 081a21 at  $L_s=315^\circ$ . Resolution is about 1 Km/px.

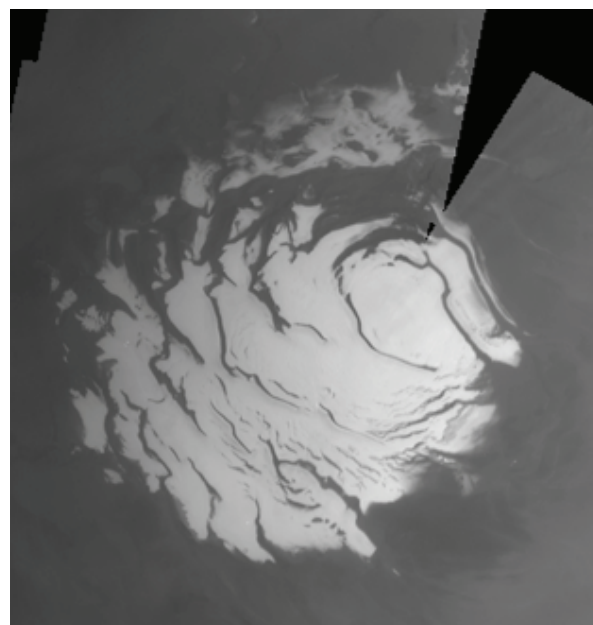


**Figure 2:** Mosaic of four Viking 358B images (07,48,57,58) at  $L_s = 315.2^\circ$ , MY12. Resolution is 0.25 Km/px, about 4x that of MARCI or M9 images.

by the end of summer in all of the Mars years that have been observed with sufficient resolution to make the distinction. The outlier disappeared before  $L_s = 320^\circ$  in MY 9 images but persists until late summer in other years, so the behavior of this feature is in some sense a paradigm for interannual variability in the late phases of cap recession.

Figure 3 displays MARCI images of the RSPC, including the outlier, for  $L_s = 293^\circ$  in MY 28 and 29; Figure 4 shows the pair for  $L_s = 313^\circ$ . The

accelerated sublimation of the outlier in MY 28 is readily apparent. The behavior of the outlier in MY 28 is qualitatively similar to that observed by M9 but has returned to its “normal” pattern in MY 29.

MY 28 is the first year since MY 9 that had both a major perihelic dust storm [6] and spacecraft observations that could resolve the outlier. We suggested previously on several occasions that large dust storms that result in elevated opacity over extended periods can accelerate the sublimation of

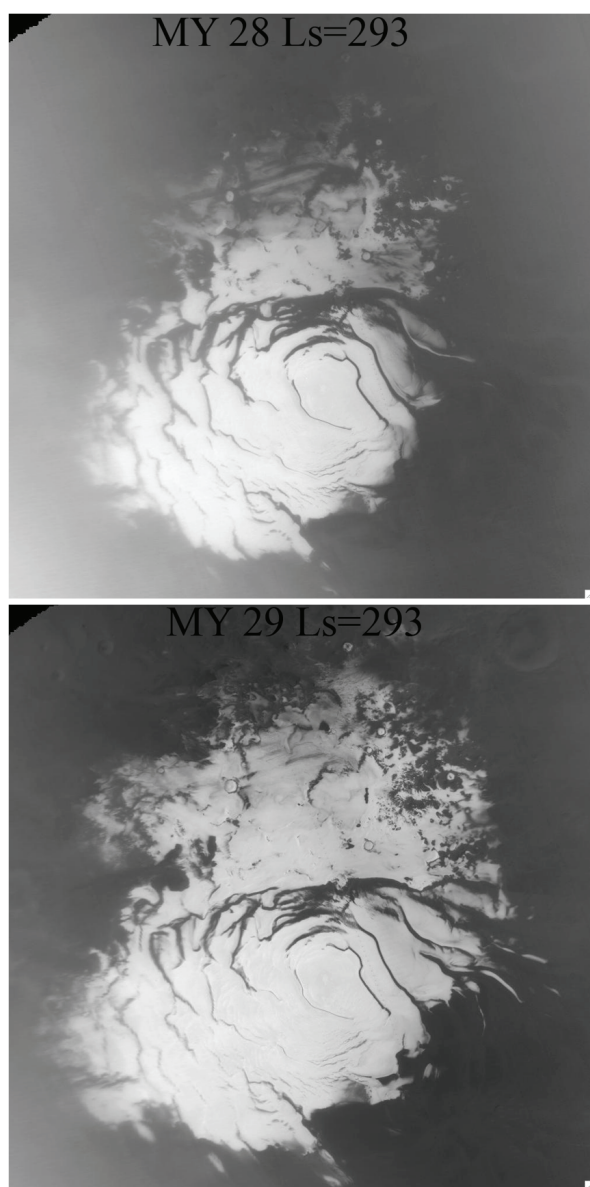


**Figure 3:**  $L_s = 293^\circ$  projections of Band 2 MARCI images from MY 28 (top) and 29. Images P10\_004870 and B10\_013691 respectively.

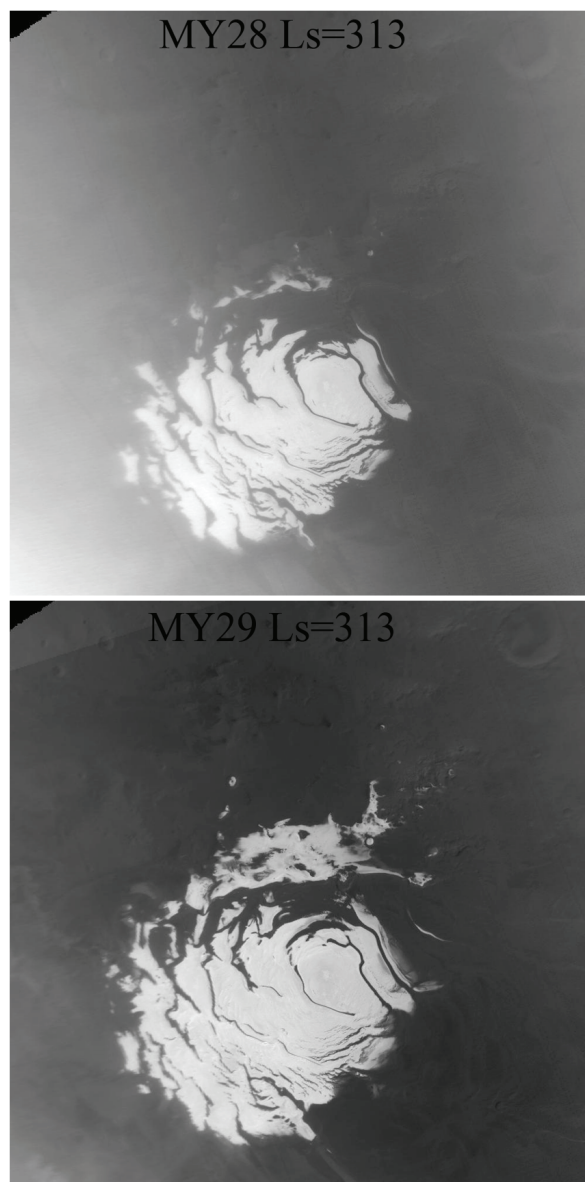


**Figure 4:** Same as Figure 3 for  $L_s = 313^\circ$ . Configurations resemble those at similar season in MY 9 and 12. Images P11\_005305 and B11\_014113 respectively.



bright CO<sub>2</sub> frost deposits by diverting insolation from the visible, where the CO<sub>2</sub> reflects strongly, to the infrared, where the CO<sub>2</sub> surface is more absorptive (Figure 5). This hypothesis explained the more rapid disappearance of the Mountains of Mitchel in MY 25, following a large dust storm, than in MY 24 that did not feature a large dust event [7]. We also investigated the effects of a perihelic storm such as that in MY 9 to ascertain if such a storm could have produced the effects observed in the RSPC in that year [8]. We hypothesized that the effects of such a storm, occurring between perihelion and solstice when insolation is maximum and most seasonal frost has sublimated, would be significant for the RSPC. We considered a storm that produced a maximum optical depth over the RSPC of 2.0 at  $L_s = 260^\circ$  and that decayed to background in 70 days. Such a storm would produce an additional 40-110 kg/m<sup>2</sup> of CO<sub>2</sub> sublimation, where the range of uncertainty is due to the range of the surface models considered (various dust and water contamination as well as grain size). This corresponds to a CO<sub>2</sub> thickness of 6-16 cm for a density of 700 kg/m<sup>3</sup>. At the time we considered that this was too small to explain the effects on the RSPC since it was thought that the CO<sub>2</sub> occurred in layers ~ 1 meter thick [9].

The amount of CO<sub>2</sub> sublimation that is equivalent to the time lag in the disappearances of the outlier in MY 9 and other years is about 100 kg/m<sup>2</sup> for an albedo of 0.7; in other words, in most years that much CO<sub>2</sub> must remain after the date of disappearance in MY 9 in order to preserve the

outlier during the remainder of summer. These two estimates depend on the nature of the CO<sub>2</sub> surface and the true optical depth history at the outlier, neither of which is well known. So although not definitive, the consistency of the two estimates strongly suggests that the simulated dust storm could have been responsible for the accelerated disappearance of the outlier in MY 9. More detailed examination of some surface features within the region of the RSPC where the interannual differences were most pronounced using the Context Camera (CTX) suggests that the CO<sub>2</sub> deposits are not as thick as was previously assumed [10]. So the circumstantial evidence to the effect that large perihelic dust storms are the cause of the changes in the RSPC observed in MY 9 and 28 now seems to be much stronger.

What are the implications for the RSPC if M9 like caps result from perihelic dust events? The rapid recovery of the cap to its usual configuration after a year with a perihelic storm (e.g. MY 29) indicates that the albedo of the CO<sub>2</sub> deposits is sufficiently high to lead to net condensation of CO<sub>2</sub> in a non-dusty year. The physical erosion and collapse of CO<sub>2</sub> deposits within the RSPC appears to steadily remove CO<sub>2</sub> to the atmosphere [11]. Although in principle the cap could be stable at the current epoch, it is difficult to envision feedback mechanisms that could result in zero net deposition averaged over a number of years. The behavior of the cap in this scenario is linked to the frequency of major dust events that remove condensate, so there could be variations in the cap over time scales of decades if the dust cycle exhibits such variation.

MARCI images show that the MY 28 residual cap was smaller than that in MY 29, with the differences occurring mainly around the periphery. Comparison of CTX observations of the “tooth” region [10] in the two years clearly shows a slower evolution in MY 29. However, the key “fork” region in MY 28 MARCI views does not resemble its appearance in MY 9. MRO observations of Mars have currently ceased due to spacecraft problems. The latest data obtained were at about  $L_s = 325^\circ$ . It is to be hoped that MRO observations will recommence before  $L_s = 350^\circ$ , October 7, 2009, so that structures within the residual cap this year can be compared to those last year.

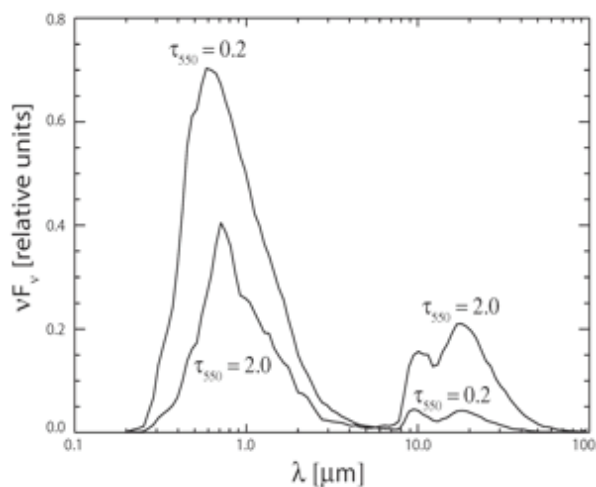


**Figure 5:** Modeled effects of dust opacity on the wavelength distribution of incident radiation.

**References:** [1] Sharp, R.P. et al. (1971). JGR 76, 357-368. [2] James, P.B. et al. (1979). JGR 84, 2889-2922. [3] Benson, J.L. and James, P.B. (2005). Icarus 174, 513-523. [4] Thomas, P.C. et al. (2000), Nature 404, 181-184. [5] Malin, M.C. et al. (2001). Science 294, 2146-2148. [6] Cantor, B.A. et al. (2008). 3<sup>rd</sup> International Mar Atmosphere Workshop, Williamsburg, VA [7] Bonev, B.P. et al., (2002). GRL 29, 13-1-13-4. [8] Bonev, B.P. et al. (2008). P&SS 56, 181-193. [9] Thomas, P.C. et al. (2005). Icarus 174, 535-559. [10] Thomas, P.C. et al. (2009). Icarus (in press). [11] Haberle, R.M. et al., (2009). Mars Polar Energy Balance Workshop, Seattle, WA.



## DUST IN THE MGS-TES LIMB SOUNDING DATA SET: DUST ADVECTION BY THERMAL TIDES, AND THE DUST-FREE WINTER POLE.

McConnochie<sup>1</sup>, T. H. Wilson<sup>2</sup>, R.J., and Smith<sup>3</sup>, M.D. <sup>1</sup>NASA Goddard Space Flight Center., Greenbelt, MD, Timothy.H.McConnochie@nasa.gov. <sup>2</sup>Geophysical Fluid Dynamics Laboratory, National Oceanic and Atmospheric Administration, Princeton, New Jersey. <sup>3</sup>NASA Goddard Space Flight Center, Greenbelt, MD.

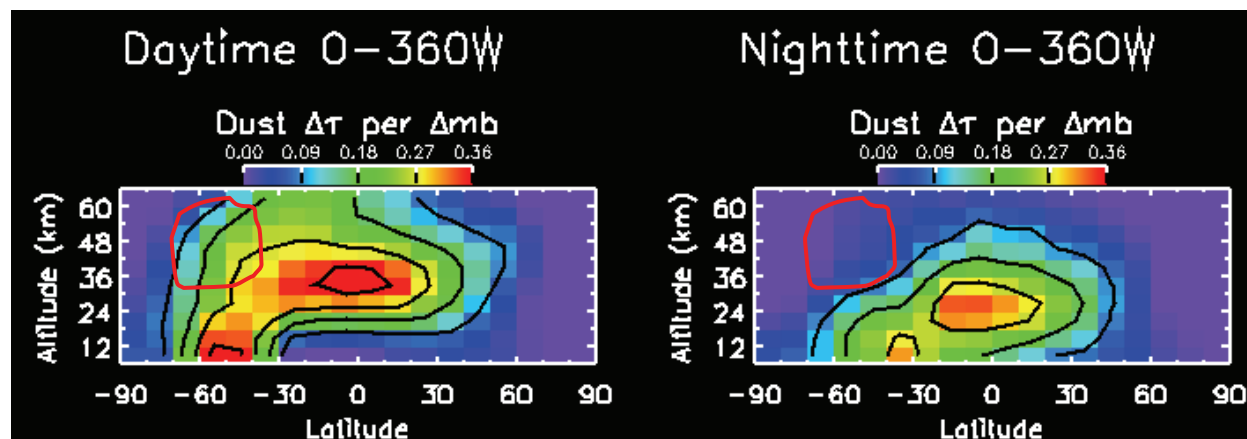


**Figure 1:** Zonal average of TES-retrieve dust mixing ratio at 2pm (left) and 2am (right), Mars Year 25,  $L_s$  197-199, during the 2001 global dust storm. Note that the absence of dust in the daytime below 20 km between  $-30^\circ$  and  $30^\circ$  latitude is a retrieval artifact. The evidence for dust advection by the diurnal thermal tide is circled in red.  $\Delta\tau$  is measured at 9.3 microns.

**Introduction:** The Mars Global Surveyor Thermal Emission Spectrometer (TES) limb sounding data set provides a global picture of the vertical distributions of aerosols at 2AM and 2PM local times in all seasons. See [1] for an overview of these results and for details of the retrieval method. Here, we focus on two interesting aspects of the dust distribution. First, we show that there is a very strong diurnal variation in the southward extent of high ( $> 20$  km) altitude dust during periods of high dust loading in southern spring and summer. We find very similar behavior in a Mars General Circulation Model (MGCM). Next, we show that the northern fall/winter polar region remains largely free of dust during periods of high dust loading over the rest of the planet. Once again, this behavior is largely captured by the MGCM, but there is an important exception at the low altitudes, where the MGCM shows a poleward leakage of dust that is not observed in the TES limb data.

**MGCM:** We have used the NASA/NOAO Mars General Circulation Model, with a cubed-sphere grid. See [2] for more details. To model the dust

distribution and its influence on the circulation, dust is treated as a radiatively active tracer with its total column opacity constrained to match the column opacity retrieved from TES nadir mode data. Where TES nadir-mode opacities do not exist, such as at night or in the winter polar latitudes, the dust opacity is unconstrained. The vertical distribution of dust is never constrained. The column opacity constraint is met by adding dust at the bottom of the atmosphere. Once again, see [2] for further discussion of this approach.

**Low altitude daytime retrieval artifacts:** Note that the TES limb aerosol retrievals give spurious results during the day below 20 km when the overlying opacity is high. Thus, in the figures presented here, the apparent absence of dust near the surface during dusty periods, and the accompanying spurious water ice signal, should be disregarded. Retrievals results at 30 km and above are not affected, even when this artifact is present at low altitudes.

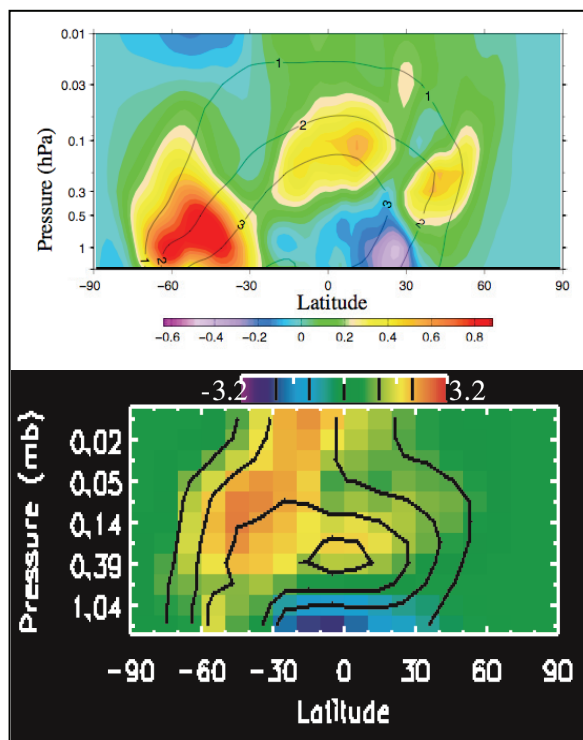


**Figure 2:** Zonal average of MGCM model (top) and TES-retrieved dust mixing ratio for Mars Year 25,  $L_s$  197-199. Unlike Figure 1, the plotted values are scaled to the visible band optical depth of a well mixed column with the given mixing ratio. The contour lines show the daytime mixing ratio and use the same contour interval in both panels. The colors show the difference between daytime and nighttime values.

**Low altitude daytime retrieval artifacts:** Note that the TES limb aerosol retrievals give spurious results during the day below 20 km when the overlying opacity is high. Thus, in the figures presented here, the apparent absence of dust near the surface during dusty periods, and the accompanying spurious water ice signal, should be disregarded. Retrievals results at 30 km and above are not affected, even when this artifact is present at low altitudes.

**Dust advection by thermal tides:** Figure 1 shows the TES-retrieved dust mass mixing ratio (expressed as the change in vertical optical depth at 9.3 microns per millibar of pressure increase with depth). The region with the most dramatic diurnal change in mixing ratio is circled in red. Figure 2 shows a comparison of the TES-retrieved dust mass mixing ratio with the dust mixing ratios from the column-opacity-constrained MGCM, in this case plotting in color the diurnal *change* in dust mixing ratio (with an

overlay – solid lines – of the daytime dust mixing ratios). Although there are differences in the details between the data and the model, both clearly show the same phenomenon of dust being present above 30 km altitude all the way to 60° S during the day, and then being absent or greatly diminished between 40° and 60° S at these altitudes at night.

These changes in dust mixing ratio imply some combination of very substantial meridional and vertical advection. Furthermore, since the TES-retrievals show this diurnal dust pattern to persist over several degrees of  $L_s$ , the daytime poleward / upward transport must be very nearly balanced by nighttime equatorward / downward transport. In other words, the diurnal tide produces no net poleward transport of dust.

**The dust-free northern winter pole:** To understand the absence of TES-observed dust at the winter pole, we must consider water ice as well as dust aerosols. We have done so in Figure 3. Figure 4 shows the temperature field, dust mixing ratios, and meridional stream function of the column-opacity-constrained MGCM for the same martian year and season (MY 24  $L_s$  250°). Note that since no TES nadir-mode opacities are available poleward of 40° in this season due to the cold surface temperatures, there are no constraints being applied to the model in this region.

Both the MGCM and the TES limb retrievals show the same dust-free polar region at high altitude, with the dust mixing falling steeply north of 30° and vanishing at about 60° in both cases. The dust free region could in principle be explained by 1) rapid downward advection in the descending branch of the Hadley cell, evident in the stream function in Figure 4; or 2) a dynamical barrier to horizontal mixing due to the polar vortex jet; or 3) scavenging or concealment of dust by coatings of water or carbon dioxide ice.

Figures 3 and 4 point towards a working hypothesis that the Hadley cell is the most important factor at high altitudes, since we observe that the regions where the dust mixing ratio falls off steeply with latitude is largely free of ice aerosols and coincides with the descending branch of the Hadley cell. A polar vortex dynamical barrier would be expected on the poleward flank of the jet, but we can see from Figure 4 that the peak winds of the jet (which coincide with the maximum temperature gradients)

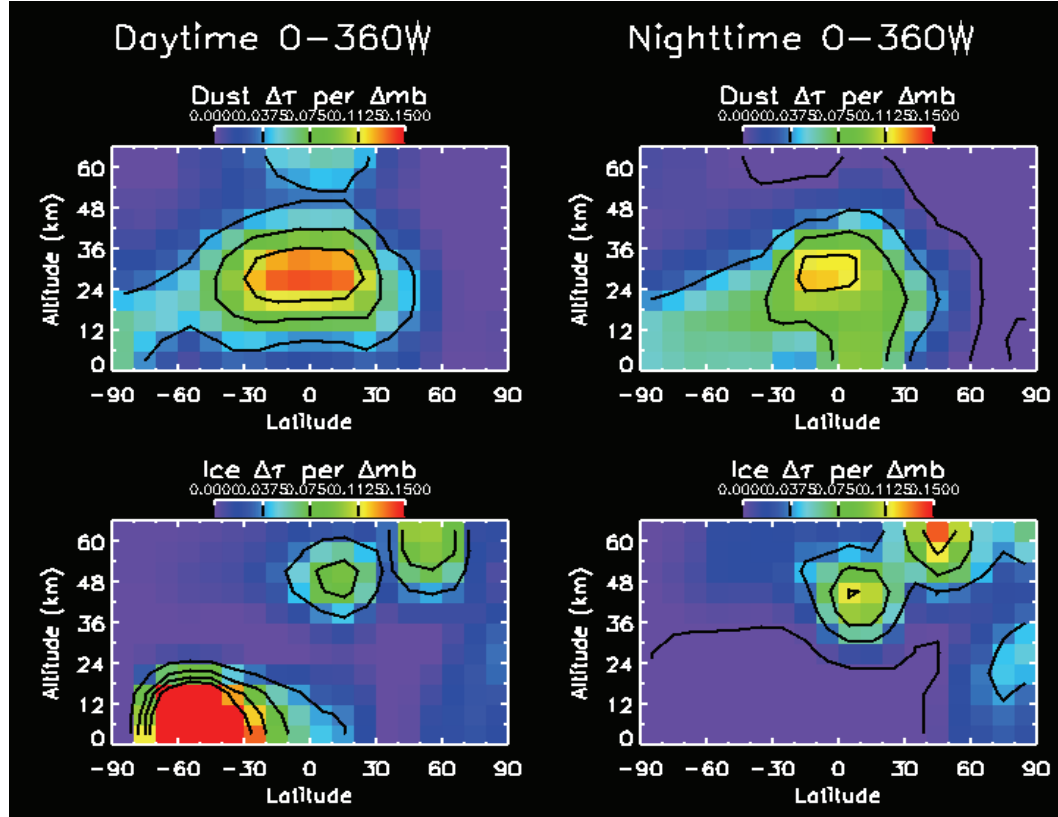


**Figure 3:** Zonal average of TES-retrieved dust (top) and ice (bottom) mixing ratio at 2pm (left) and 2am (right), Mars Year 24,  $L_s$  249-251.  $\Delta\tau$  is measured at 9.3 microns for dust and 12.1 microns for water ice.

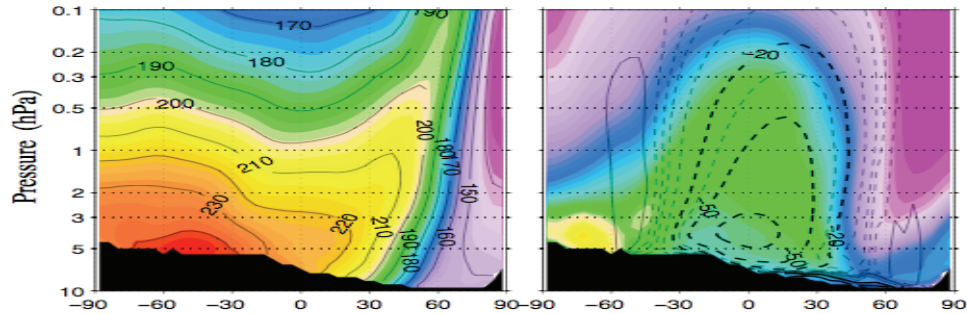


**Figure 4:** Temperature (K, at left), dust mixing ratio (right), and meridional stream function (contours, at right) for the dust-opacity constrained MGCM at Mars Year 24,  $L_s$  250.

lie north of the  $60^\circ$  latitude where the dust mixing ratio vanishes, ruling out the polar vortex as the dominant factor for the dust distribution.

Near the surface, the MGCM shows leakage of dust into to polar region while no such leakage is observed by TES. The MGCM does not consider the process

of ice coating dust particles, and so the presence of substantial ice aerosol opacity at low altitudes over the pole in the TES retrievals provides a highly plausible explanation for the discrepancy. It is not clear, however, whether the ice coatings are actually significantly enhancing the dust fall-out rate, or simply masking the spectral signature of dust.

**References:** [1] McConnochie T. H. and Smith M. D. (2008) *Third Intl. Workshop on the Mars Atmosphere*: #9114. [2] Wilson, R. J. et al. (2008) *Third Intl. Workshop on the Mars Atmosphere*: #9023.

## EFFECTS OF DUST STORMS ON WINTER POLAR WARMINGS IN THE MARTIAN MIDDLE ATMOSPHERE.

Kuroda, T.<sup>1,2</sup>, Medvedev, A. S.<sup>1</sup>, Hartogh, P.<sup>1</sup>, and Takahashi, M.<sup>3</sup>, <sup>1</sup>Max Planck Institute for Solar System Research (Max-Planck-Str. 2, D-37191 Katlenburg-Lindau, Germany, kuroda@mps.mpg.de, medvedev@mps.mpg.de, hartogh@mps.mpg.de), <sup>2</sup>Institute of Space and Astronautical Science, Japan Aerospace Exploration Agency (3-1-1 Yoshinodai, Sagami-hara, 229-8510, Japan), <sup>3</sup>Center for Climate System Research, University of Tokyo (5-1-5 Kashiwanoha, Kashiwa, Chiba, 272-8568, Japan, masaaki@ccsr.u-tokyo.ac.jp).

**Introduction:** Dust in the Martian atmosphere strongly affects the dynamics and temperature. For instance, global dust storms around the northern winter solstices significantly reduce amplitudes and increase dominant zonal wavenumbers of baroclinic waves by stabilizing the atmospheric fields [1]. By strengthening the meridional circulation, the enhanced absorption of the solar radiation by dust tends to accelerate the easterly wind above the equatorial region [2].

The global dust storm which occurred around the northern winter solstice (so-called 1977b storm) contributed to the strong increase (40-60 K) of the temperature above the North Polar region [3]. Previous studies using Martian general circulation models (MGCMs) reproduced the comparable heating due to the dust storm, and showed that the Hadley circulation strengthened, and its cell extended to high latitudes [4,5]. Partly, this can be explained by the intensified diabatic heating in the southern (summer) hemisphere that increases the meridional gradient of radiative heating [6,7]. On the other hand, inter-hemispheric solstitial circulation, at least above 40 km, is driven primarily by large-scale zonally asymmetric eddies (planetary waves and tides) [4,8]. In this study, we investigate how different type of eddies contribute to the polar warming enhancements using our MGCM [9].

**Model descriptions:** Our MGCM [10] is based on a terrestrial model developed by CCSR/NIES/FRCGC (Center for Climate System Research/ National Institute of Environmental Studies/ Frontier Research Center for Global Change, Japan). It utilizes a spectral solver for the three-dimensional primitive equations. The horizontal resolution is set at about  $5.6^\circ \times 5.6^\circ$  ( $\sim 333$  km at equator), the vertical grid consists of 30 $\sigma$ -levels with the top of the model at about 80 km. Realistic topography, albedo and thermal inertia data for the Mars surface, and CO<sub>2</sub> condensation/sublimation processes are included. Radiative effects of CO<sub>2</sub> gas (considering only LTE)

and dust, in visible and infrared wavelengths, are taken into account.

**Numerical results:** For this study, a horizontally uniform total optical depth in the visible wavelengths  $\tau = 0.5$  was specified for the “low dust” scenario, and  $\tau = 3.0$  for the planet-encircling dust storm. The vertical distribution of the aerosol mixing ratio was prescribed following the “Conrath profile” [11]:  $Q = Q_0 \exp\{0.01[1-(p_0/p)]\}$ , where  $Q_0$ ,  $p_0$  and  $p$  are the reference dust mixing ratio (that depends on the optical depth, e.g., 6.2 ppm of mass for  $\tau = 1.0$ ), pressures at the reference (600 Pa) and any given level, respectively. It corresponds to a roughly uniform mixing ratio up to  $\sim 35$  km that steeply decays above. The results to be presented are the 20-day averaged fields near the Northern winter Ls = 270°.

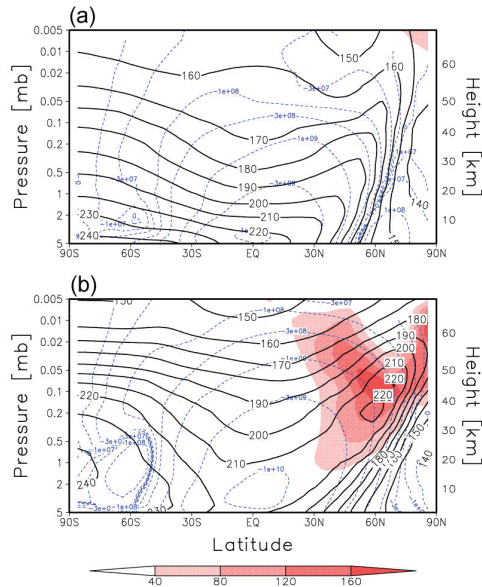
Figure 1 shows the zonal-mean temperature, mass stream function and adiabatic heating rate which is associated with the downward branch of the meridional transport cell, for the two dust opacity simulations. The enhanced adiabatic heating is mainly responsible for 40-60 K warmer winter polar air in the middle atmosphere.

Figure 2 displays the residual meridional velocities and the Eliassen-Palm (EP) flux divergences, which demonstrate the wind forcing by eddies, for both simulations. In the  $\tau = 3.0$  run, stronger absorption of the solar radiation in the southern hemisphere enhances the northward flow, and, consequently, controls the downward flux in mid- and high latitudes of the middle atmosphere. Moreover, positive EP-flux divergence appears in low latitudes, and negative one in mid- and high latitudes. From the transformed Eulerian mean (TEM) formulation [12], this clearly indicates the relation between the elevated temperature over the winter pole during dust storms and the enhanced wave forcing in the middle atmosphere [13].

To elucidate the role of different types of eddies in this process, we performed simulations with (i) a flat surface, and (ii) with the diurnal insolation cycle replaced by its mean value. Thus, generation of the stationary planetary waves (SPWs) was inhibited in the former run, and tides were excluded in the latter.

The results for the “global dust storm” scenario are plotted in Fig. 3. The differences in the simulated temperature and that from the “full physics” run (Fig. 1b) are denoted with black contour lines. They show that the winter polar air is up to 20 K colder without SPWs, and up to 25 K colder without tides. Accordingly, the adiabatic heating rates shown by the shading are smaller than in Fig. 1b. This demonstrates that both SPWs and tides contribute to strengthening the polar warmings.

Figure 4 presents the corresponding residual meridional velocities and EP-flux divergences with the flat surface and diurnal-mean insolation. It is seen that the elimination of SPWs slows down the meridional transport by  $\sim 10 \text{ m s}^{-1}$ , while has virtually no effect on the eddy forcing distributions. Meanwhile, the elimination of tides results in a dramatic reduction of the eddy forcing and the



**Figure 1:** Results of simulations for (a) the “low dust” ( $\tau = 0.5$ ) run, and (b) the “global dust storm” ( $\tau = 3.0$ ): The zonal-mean temperature [K] (solid black contours), meridional mass stream function [ $\text{kg s}^{-1}$ ] (dashed blue lines, positive values denote counterclockwise circulation), and adiabatic heating rate [ $\text{K sol}^{-1}$ ] (red shades).

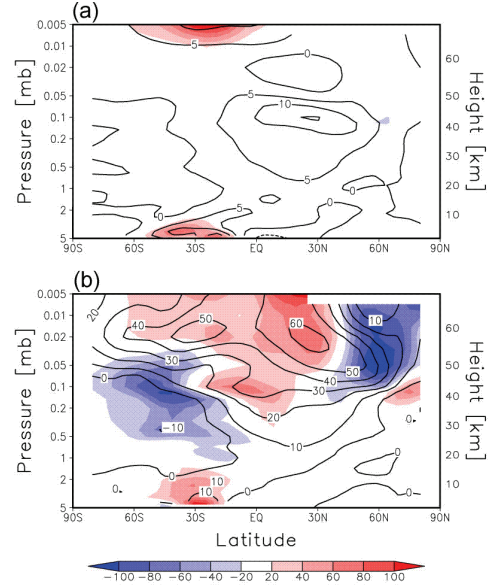


**Figure 2:** Same as Figure 1, except for the residual meridional velocities [ $\text{m s}^{-1}$ ] (black contours) and EP flux divergence [ $\text{m s}^{-1} \text{ sol}^{-1}$ ] (shades, red denotes positive values and blue denotes negative).

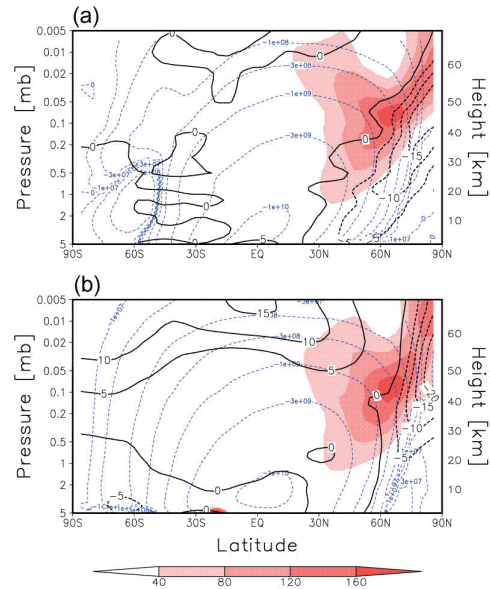


**Figure 3:** Results of the simulations for the “global dust storm” ( $\tau = 3.0$ ) with (a) a flat surface and (b) diurnal-mean solar insolation. Plotted components are the same as Fig. 1, except that the black contours denote the difference of zonal-mean temperature [K] with the “full physics” simulation in Fig. 1b.



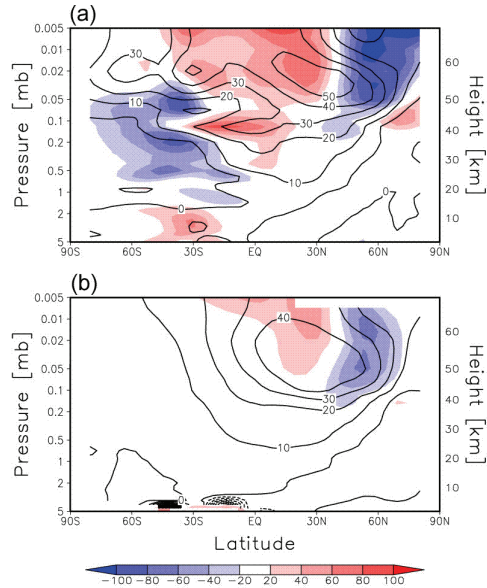


**Figure 4:** Same as Figure 3, except that the plotted components are the same as Figure 2.

meridional velocity in the summer hemisphere:  $\sim 20 \text{ m s}^{-1}$  slower residual meridional velocity and  $\sim 40 \text{ m s}^{-1} \text{ sol}^{-1}$  weaker EP-flux divergence in the winter hemisphere.

To evaluate the contribution of different waves to the eddy forcing of the meridional circulation further, we performed the temporal and spatial Fourier analysis of the 3-hourly model output. Figure 5 displays the EP-flux divergence and its spectral components calculated for the “global dust storm” run including the full physics. The EP-flux divergence for all waves (same as the shades in Fig. 2b) is shown in Fig. 5a, and the contribution of all tidal components (from diurnal to quad-diurnal for both westward and eastward propagating harmonics with zonal wavenumbers from  $s=1$  to 10, i.e., migrating and non-migrating tides) is plotted in Fig. 5b. The EP-flux divergence associated with all planetary waves (the sum of eastward and westward propagating waves with periods greater than 1 sol) is given in Fig. 5c. Shorter-scale harmonics with periods of  $\leq 1$  sol except tides represent resolved gravity waves and eddies. Their contribution is shown in Fig. 5d.

It immediately stands out that the tides, planetary waves and smaller-scale gravity waves and eddies almost equally contribute to the total forcing. The role of gravity waves grows with height, which is likely related to the enhanced dissipation by the

sponge layer near the model lid. Tidal forcing is strong in the equatorial area, and in high winter latitudes. The EP-fluxes for the migrating diurnal and semidiurnal tides are plotted with arrows in Fig. 6. The main source of the diurnal tide lies in the summer southern hemisphere, in particular over the subsolar point at around  $30^\circ \text{ S}$  (Fig. 6a). Semidiurnal tides are excited in the equatorial middle atmosphere (Fig. 6b) which corresponds to the local maximum of EP-flux divergence ( $> 50 \text{ m s}^{-1} \text{ sol}^{-1}$ ) in Fig. 5b. Increasing the dust load (from  $\tau = 0.5$  to 3.0) enhances the absorption of solar radiation by aerosol and the excitation of tides, which results in almost 3 times larger EP-fluxes in the southern hemisphere. Further propagation of the tides to high winter latitudes is less affected by the changes in the mean zonal circulation. Consequently, the tidal amplitude and the corresponding EP-flux divergence over the North Pole increased by a factor 3 in the dust storm simulation.

Among planetary waves contributing to the forcing in Fig. 5c, the most dominant are SPWs with zonal wavenumbers  $s=1$  and 2, and the eastward-propagating transient planetary wave (TPW) with  $s=1$  and 5 sols period. The amplitudes of the geopotential height as well as the corresponding squared refractive

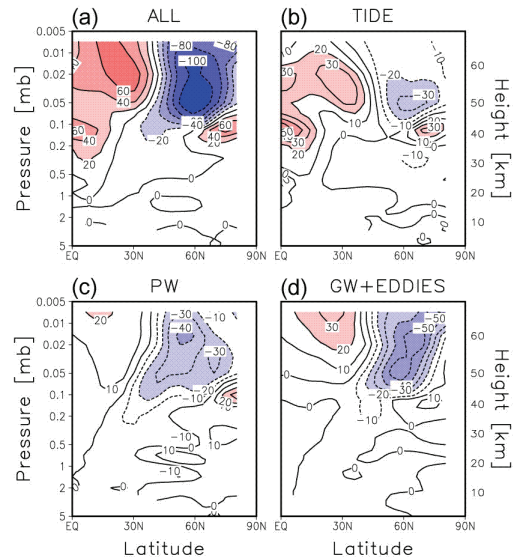


**Figure 5:** EP-flux divergence [ $\text{m s}^{-1} \text{ sol}^{-1}$ ] for the “global dust storm” ( $\tau = 3.0$ ) “full physics” simulation: (a) The total divergence; (b) contribution of tides (the sum of the diurnal to quad-diurnal components with  $s=1$  to 10); (c) contribution of planetary waves; (d) contribution of gravity waves and eddies (with  $s>10$  and periods less than a day).

indices [12], positive values of which denote regions of free vertical and meridional wave propagation, are shown in Figs. 7a, b and c for the three types of waves. It is seen that the SPW ( $s = 1$ ) dominates in the winter hemisphere during dust storms (Fig. 7a). Its amplitude increases almost tenfold compared to the  $\tau = 0.5$  simulation. This chiefly occurs due to the weakening of the westerly jet during dust storms [1], which creates favorable conditions for vertical propagation. Additionally, the near surface westerlies flowing over topography extend farther into low latitudes in times of dust storms (see Fig. 7d). Thus, SPWs are generated over larger territory. Unlike for the  $s = 1$  harmonic, the SPW ( $s = 2$ ) is weaker, and is located lower (Fig. 7b). Its amplitude and the produced forcing vary little from the  $\tau = 0.5$  run, and is negligible above 0.1 mb. The eastward-propagating TPW ( $s = 1$ ) is generated in the upper atmosphere (Fig. 7c). the TPWs are likely generated due to the barotropic instability in low latitudes, and due to baroclinic instability in high latitudes [9]. Its amplitude and contribution to the EP-flux divergence above 0.1 mb correspond to about 1/3 of those by the SPW ( $s = 1$ ).

**Conclusions:** A general circulation model of the Martian atmosphere was used to explore the changes in the meridional circulation that lead to temperature increases observed over winter poles during planet-encircling solstitial dust storms. In the absence of direct solar heating, these temperature vertical inversions have a dynamical origin, and are due to a strengthening of the overturning meridional circulation. We show that dissipating tides, planetary waves, resolved gravity waves and geostrophic eddies almost equally contribute to the forcing that causes warming in high-latitude winter middle atmosphere at times of high atmospheric aerosol content. Our results indicate for the first time the importance of resolved gravity waves and eddies in maintaining the meridional circulation in the Martian middle atmosphere, at least in high winter latitudes during dust storms. In spite of the relatively coarse horizontal resolution, the contribution of resolved gravity waves to the total eddy forcing is approximately equal to that of tides and planetary waves. We speculate that the gravity wave contribution may increase when smaller-scale waves are resolved.

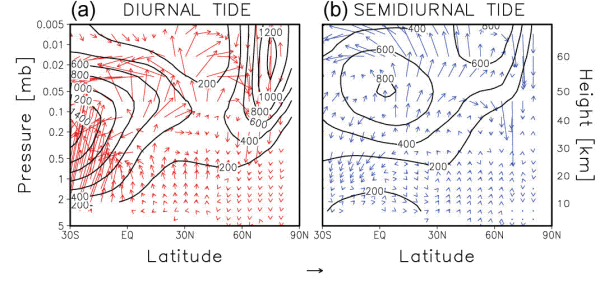


**Figure 6:** Wave geopotential height amplitudes [m] (contours) and EP fluxes [ $\text{m}^2 \text{s}^{-2}$ ] (arrows, the scale of meridional fluxes is shown in the bottom of the figure and the vertical fluxes are multiplied by 125) for (a) diurnal and (b) semidiurnal migrating tides

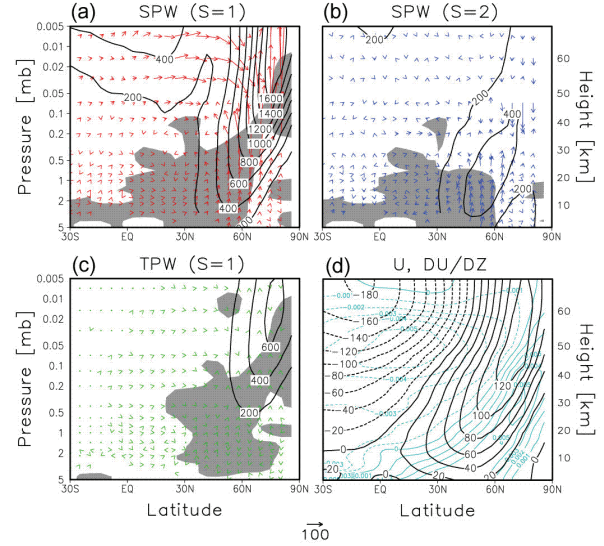


**Figure 7:** Same as Figure 6, except for (a) SPW ( $s=1$ ), (b) SPW ( $s=2$ ), and (c) eastward propagating TPW with the period of 5.0 sols and  $s=1$ . Shaded regions denote that the square of the refractive index for each planetary wave is positive. The panel (d) shows the mean zonal wind [ $\text{m s}^{-1}$ ] (black contours) and the vertical wind shear [ $\text{s}^{-1}$ ] (cyan contours).

**References:** [1] Kuroda T. et al. (2007) *GRL*, 34, doi:10.1029/2006GL028816. [2] Kuroda T. et al. (2007) *GRL*, 35, doi:10.1029/2008GL036061. [3] Martin T. Z. and Kieffer H. H. (1979) *JGR*, 84, 2843-2852. [4] Wilson R. J. (1997) *GRL*, 24, 123-126. [5] Forget F. et al. (1999) *JGR*, 104, 24155-24175. [6] Schneider E. K. (1977) *JAS*, 34, 280-296. [7] Schneider E. K. (1983) *Icarus*, 55, 302-331. [8] Medvedev A. S. and Hartogh P. (2007) *Icarus*, 186, 97-110. [9] Kuroda T. et al. (2009) *J. Meteor. Soc. Japan*, 87, 913-921. [10] Kuroda T. et al. (2005) *J. Meteor. Soc. Japan*, 83, 1-19. [11] Conrath B. J. (1975) *Icarus*, 24, 36-46. [12] Andrews D. G. et al. (1987) *"Middle Atmosphere Dynamics"*, Academic Press, 489 pp. [13] Haynes P. H. et al. (1991) *JAS*, 48, 651-678.

# **Session Eight**

## *Near Surface Environment*

*Thursday, September 17, 2009*

*11:00 AM – 3:00 PM*



## PHOENIX LIDAR OBSERVATIONS OF DUST IN THE ATMOSPHERE OF MARS.

J. Whiteway, L. Komguem, C. Dickinson, York University, Toronto, Ontario, M6J 1P3 (Whiteway@yorku.ca).

**Introduction:** The Phoenix mission [1] obtained measurements from the surface of Mars through midsummer at a latitude of 68.22°N. A unique instrument on the Phoenix spacecraft was a LIDAR [2] that detected the backscatter of pulsed laser light emitted upward into the atmosphere. It measured the vertical distribution of atmospheric dust and water ice clouds with a resolution of 10 m. The observations were carried out over an interval length of 15 minutes to one hour, usually three or more times each day during the mission. The results of the initial analysis of atmospheric dust observations are presented here.

**Measurements:** Figure 1 shows the basic lidar measurement and analysis product for the study of dust in the atmosphere of Mars. The backscatter of pulsed laser light is detected to a height of about 20 km. Analog detection is used for heights below 10 km and photon counting is used up to 20 km. The height distribution of detected backscatter signal on mission sol 48 ( $L_s = 98.57^\circ$ ) is shown in Figure 1a. The amount of scattering material in the atmosphere is proportional to the extinction coefficient. This is the fractional decrease in laser pulse energy per unit length as it propagates through the atmosphere. The extinction coefficient can also be considered as the effective cross sectional area of particulates per unit volume. This was derived from the lidar signal using the method of Fernald [3] with a constraint applied such that the extinction integrated in the vertical matches the total optical depth as measured by the Phoenix Surface Stereo Imager (SSI). Figure 1b shows the profile of extinction coefficient derived from the measurements in Figure 1a.

The profile measured on sol 48 (Fig. 1) is typical for moderate dust loading with no clouds. There is a layer of enhanced dust loading that is distributed approximately evenly to a height of 4 km above the ground. This is due to the lifting of dust from the surface and the vertical mixing by convection and turbulence during daytime within the Planetary Boundary Layer (PBL). The vertical distribution of dust provides an indication of height of the PBL, which was variable between 4 km and 6 km.

Figure 2 shows representative profiles of dust extinction coefficient from three different periods during the mission. The atmospheric dust loading reached a peak around summer solstice and then generally decreased. There is also a profile of extinction coefficient in Figure 2 from above the Australian Desert, measured with a lidar system that was equivalent to the Phoenix LIDAR. The Australian profile was obtained during wind storm conditions.

During the second half of the mission, starting 50 sols after solstice ( $L_s = 117^\circ$ ), the lidar detected a regular pattern of cloud formation each night within the planetary boundary layer. A shallow surface based cloud formed at around midnight (Mars local solar time) and a second cloud layer formed after 1 am at heights between 3 and 6 km. A contour plot of lidar backscatter coefficient from sol 99 is shown in Figure 3. The enhanced backscatter at 3 – 4 km and below 1 km indicates the outline and internal structure of the clouds that drifted above the Phoenix landing site. These clouds formed at an estimated temperature of  $-65^\circ\text{C}$ , consistent with water ice crystals [3]. For each sol in late summer the water ice clouds remained throughout the night and then dissipated when the atmosphere warmed sufficiently during daytime. As the summer progressed toward autumn, the clouds persisted longer into the morning hours and extended further toward the ground. Clouds were not detected in the afternoon or evening. The pattern of vertical streaks at the base of the 3 – 4 km cloud after 05:00 (Fig 3) is consistent with ice crystals precipitating from the cloud, and eventually sublimating in the dry air below the cloud. Later in the mission the precipitation streaks were observed to reach the ground.

**Discussion:** The Phoenix lidar measurements of atmospheric dust indicate that the planetary boundary layer (PBL) on Mars is well mixed up to a height of 4 km by the daytime turbulence and convection during summer above the northern polar region. The lidar also observed that water ice clouds form within the PBL each night in late summer and that ice crystals



SOL 48 / 22:06:08 - 22:34:22

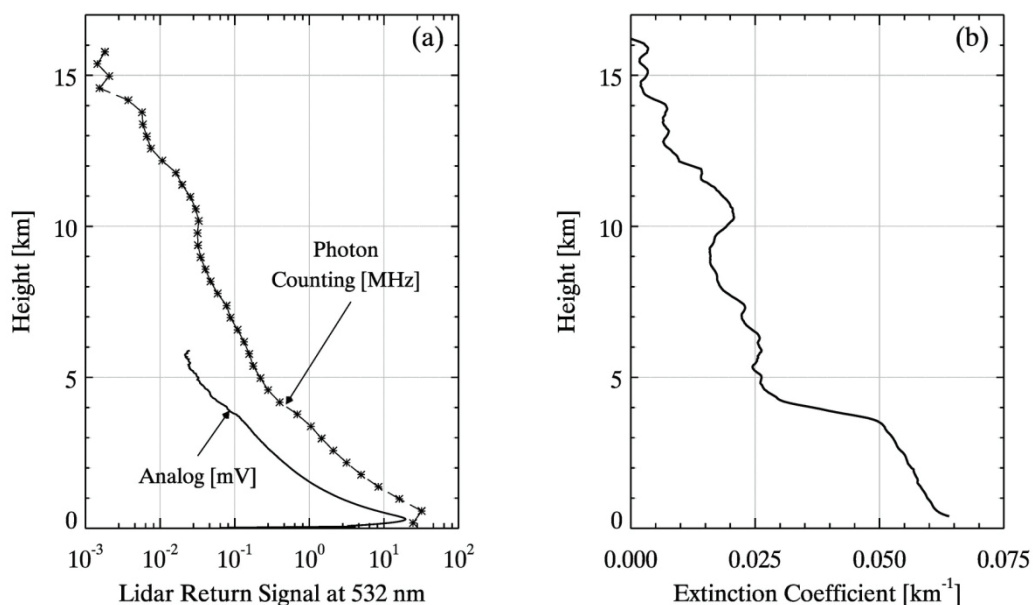


**Figure 1:** (a) Lidar backscatter signals from the atmosphere of Mars measured by the Phoenix lidar on mission sol 48 ( $L_s = 98.57^\circ$ ). (b) Dust extinction coefficient retrieved from the lidar signal on sol 48. The extinction coefficient derived from the analog and photon counting signals overlap above a height of 2 km, but only the analog signal is used below 2 km.

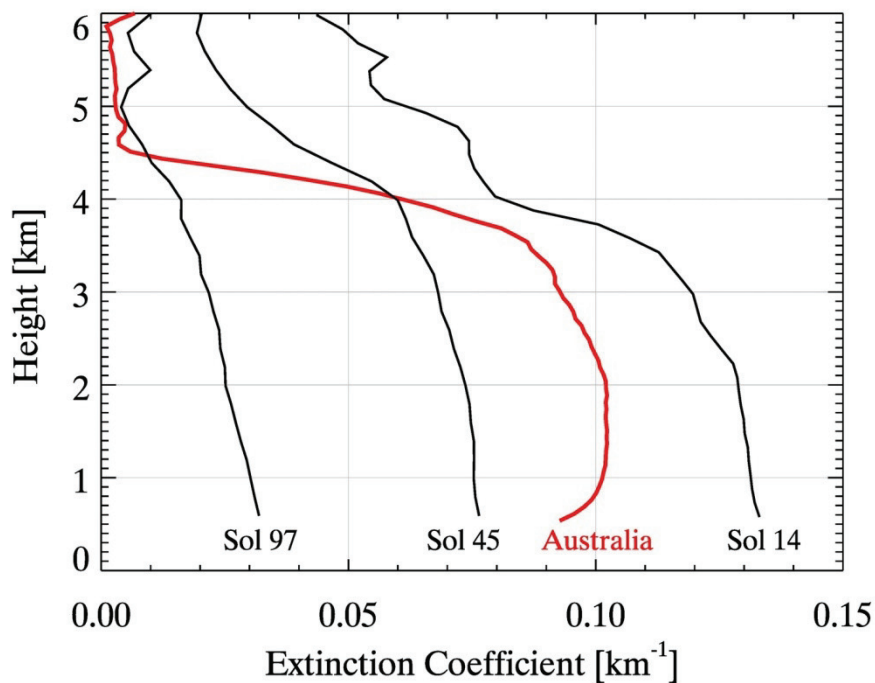


**Figure 2:** Dust extinction coefficient profiles retrieved from Phoenix lidar measurements on sols 14 ( $L_s = 82.88^\circ$ ), 45 ( $L_s = 96.95^\circ$ ), and 97 ( $L_s = 121.37^\circ$ ). For comparison, an extinction coefficient profile measured in the Australian Desert during wind storm conditions is also shown.

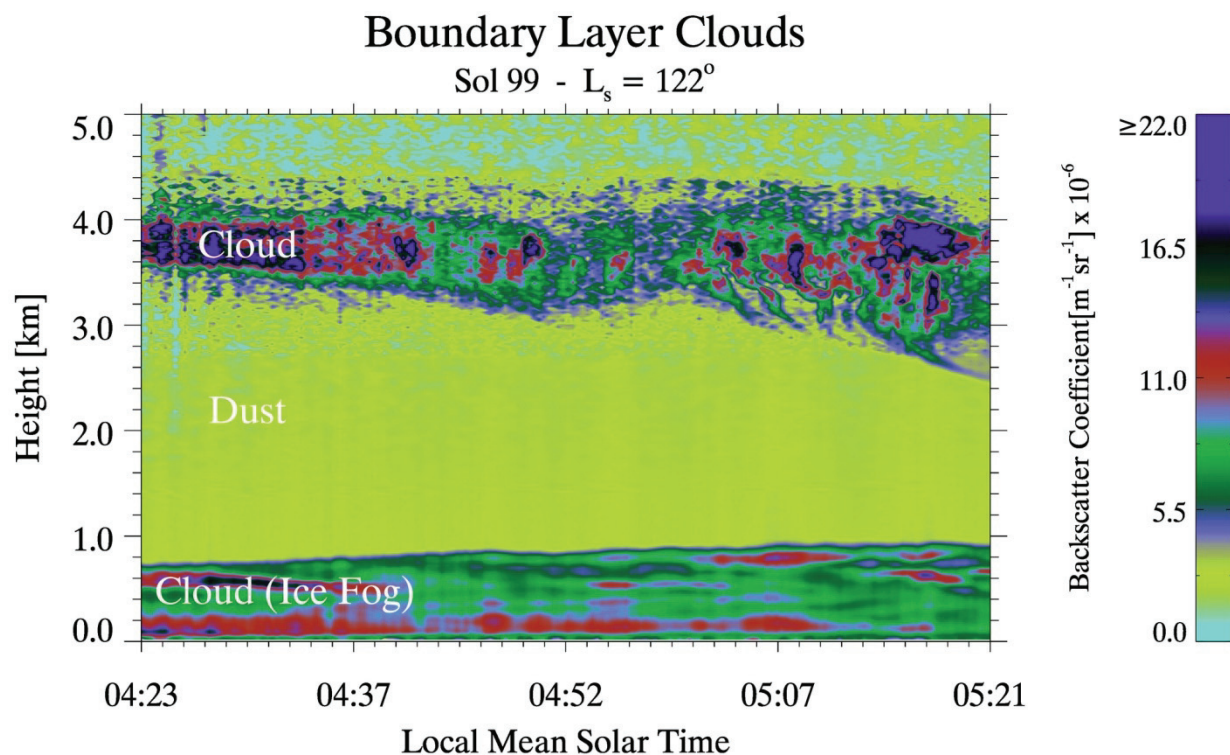


**Figure 3:** Time-Height cross section of aerosol backscatter coefficient measured on Sol 99 ( $L_s = 122^\circ$ ) showing a layer of ice fog near the surface and a cloud at 3-4 km. Backscatter coefficient is the fraction of laser pulse energy that is scattered back to the lidar receiver per unit length of propagation.

precipitate toward the surface. This process would be associated with a downward transport of the dust particles that provided the nuclei for ice crystal formation. An assessment of the amount of dust scavenging by ice crystal precipitation will require an accurate accounting of the size distribution of dust particles that nucleate ice crystal growth.

**References:** [1] Smith, P., et al. (2008), *JGR*, vol. 113, E00A18. [2] Whiteway, J., et al. (2008), *JGR*, vol. 113, E00A08. [3] Fernald, F. G. (1984), *Appl. Opt.*, 23, 652-653. [4] Whiteway, J., et al. (2009), *Science*, vol. 325

---

## PANCAM AND MICROSCOPIC IMAGER OBSERVATIONS OF DUST MOVEMENT AND MORPHOLOGY ON THE SPIRIT ROVER.

Vaughan<sup>1</sup>, A.F., Johnson<sup>1</sup>, J.R., Herkenhoff<sup>1</sup>, K.E., Sullivan<sup>2</sup>, R., Landis<sup>3</sup>, G.A., <sup>1</sup>U.S. Geological Survey, 2255 N. Gemini, Flagstaff, AZ 86004, afvaughan@usgs.gov, jrjohnson@usgs.gov, kherkenhoff@usgs.gov, <sup>2</sup>Center for Radiophysics and Space Research, Department of Astronomy, Cornell University, Ithaca, NY, rjs33@cornell.edu, <sup>3</sup>NASA John Glenn Research Center, Cleveland, OH, Geoffrey.A.Landis@nasa.gov.

---

**Introduction:** Throughout the 5 plus years of exploration by the Spirit rover, the Athena suite of instruments has been used to monitor dust movement and morphology at the Gusev landing site. Here we highlight results from observations made by the Pancam and Microscopic Imager (MI) cameras of dust accumulation and removal from the rover.

Pancam has been used to routinely monitor dust accumulation on the solar cells, the Pancam and Miniature Thermal Emission Spectrometer (Mini-TES) calibration targets, and the magnets, all of which are mounted on the rover deck. Time series movies of these dust monitoring images taken of select locations on the rover deck show dust movements that can be associated with seasonal weather patterns or specific wind events. Pancam multispectral observations of dust that has collected on the capture magnet show a steep spectral shoulder around 600 nm and a shallow 900 nm absorption consistent with nanophase ferric oxides, and similar to dust deposits on the surface [1].

The MI has been used to image particles collected on the magnets and on a portion of the solar array, allowing detailed analysis of grains and comparison with measurements made by other instruments. Dust grains of the size of typical particles suspended in the atmosphere ( $< 4 \mu\text{m}$ ) [2] are not resolved by the MI, but with continued dust accumulation on both the capture magnets and solar arrays, there is evidence that the dust is agglomerating to form larger particles (up to  $400 \mu\text{m}$ ), which has important implications for the physical process of dust entrainment.

**Cleaning Events:** The solar arrays on Spirit are subject to a continuous accumulation of dust. In addition to accumulation, the arrays are also subject to wind-related dust removal, or “cleaning events.” The arrays have had three periods of cleaning events to date, occurring in southern hemisphere early spring to early summer. The cleaning events are measured by an increase in the power produced by the solar arrays [3]. The first significant events happened around Sols 417-520, characterized by a

couple of small events starting as early as Sol 417, with a large event happening on Sol 419 (Ls=173) that removed a substantial amount of dust from the vehicle and greatly increased the solar power, with another significant event on sol 519 (Ls=234) removing more dust. Although the first of these events occurred during the same time period as the earliest appearances of dust devils at the site [4], the event has been interpreted as very strong regional wind rather than a dust devil because regional albedo patterns revealed by MOC images across the Columbia Hills changed during this time [5].

The more recent cleaning events each include a series of smaller events distributed over ~60 sols. These events each represent particularly windy episodes at Spirit’s location. The first of these took place in a series of events starting on Sol 1187 (Ls=233) through about Sol 1250 (Ls=274), just before the onset of the 2007 dust storm. The following Martian year, a major cleaning event was seen on about Sol 1900 (Ls=262). This most recent event has been of particular importance to the mission as it increased the solar power by nearly a factor of 3 and lifted several power-related constraints on the strategic plan for the rover’s potential extrication from entrapment in fine-grained deposits at its current location, “Troy.”

**Pancam Dust Monitoring:** The Pancam has been used to image the Mini-TES and Pancam calibration targets and the surrounding solar array cells that help monitor currents and voltages every ~10 sols throughout the mission. This image sequence uses 2x2 downsampled, L2, L6, and L7 filters (753 nm, 482 nm, and 432 nm, respectively), and represents the main dust monitoring science observation. Time series movies of these images were shown during the companion presentation of this work, and to illustrate cleaning events in this paper, before- and after-images of the Pancam calibration target are shown in Figure 1.

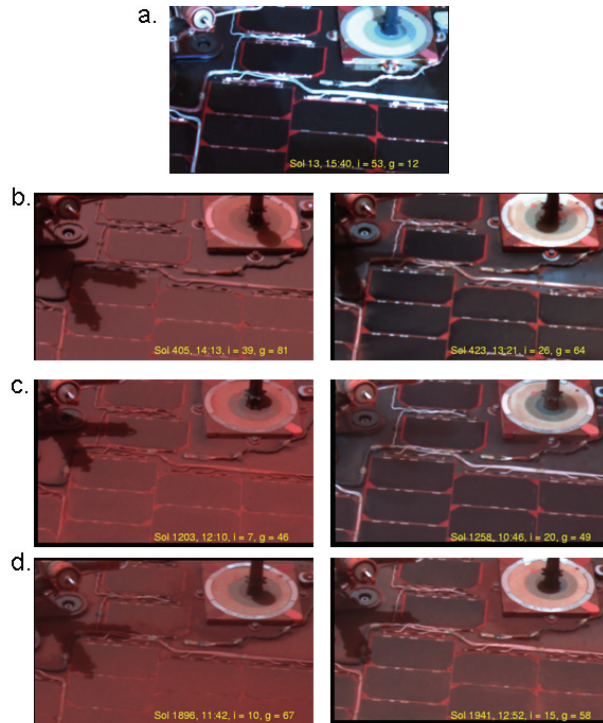


**Figure 1:** Pancam images of the Pancam calibration target and surrounding solar array cells. The yellow text on each image denotes the sol number, time of image acquisition, incidence angle ( $i$ ), and phase angle ( $g$ ). a. Image taken on sol 013 of a clean rover. b. Images taken on Sols 405 and 423 to illustrate the effects of the 420 cleaning event. c. Images taken on Sols 1203 and 1258 illustrating the cleaning events between Sols 1200 and 1250. d. Images taken on Sols 1896 and 1941 illustrating the latest cleaning events that occurred between Sols 1890 and 1950.

**Capture Magnet Dust.** The capture magnet is one of two large magnets mounted on the rover deck in front of the mast. It is the stronger of the two magnets and was designed to collect most magnetic particles from the airborne dust [6]. Pancam observations of the magnets are taken with all 13 color filters spanning the spectral range 400 nm to 1100 nm, allowing for multispectral analysis of dust deposits on the magnet. [6] Madsen, et al. (2009) reported that around Sol 600, the capture magnet became less efficient as it began collecting weak and/or non-magnetic particles. It seems reasonable to assume that at this point the capture magnet was collecting airfall dust with no strong preference for the magnetic fraction, and as such, is more representative of the global dust than simply the magnetic fraction of the dust. This can be seen in the multispectral data as well (Figure 2).

Before Sol 500, the dust spectra do not exhibit the characteristic 900 nm absorption that, along with a steep shoulder around 600 nm, represents the nanophase ferric oxide signature of the dust and is seen in all other surficial dust deposits (Figure 2a) [1]. The Sol 258 spectrum is relatively featureless in the near-infrared, and the sol 425 spectrum has a broad 800 nm absorption very similar to the clean magnet or the background. The darker portion of the dust on Sol 425 is also showing a hint of a spectral feature at 934 nm. After Sol 500, there is development of a 900 nm absorption that is present for all subsequent Pancam magnet observations (Figure 2b).

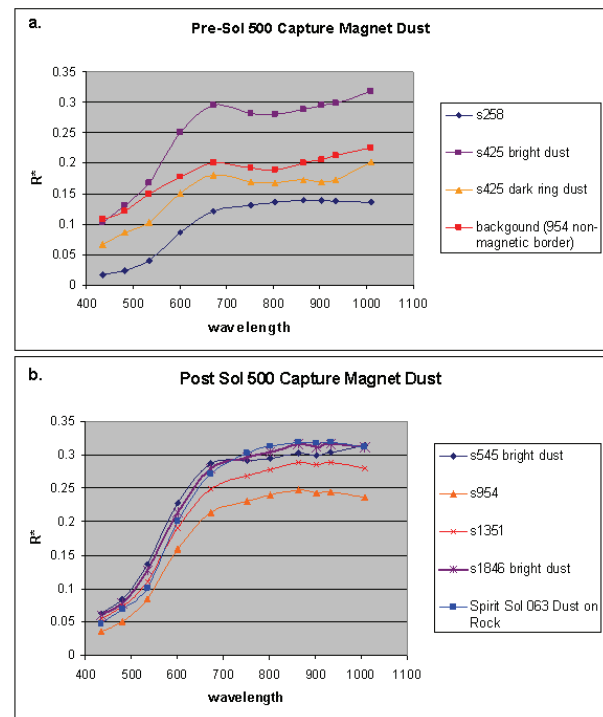


**Figure 2:** Pancam multispectral data of dust deposits on the capture magnet. a. Spectra of dust on the magnet taken before Sol 500 do not show the characteristic 900 nm absorption associated with nanophase ferric oxides, a known component of the global dust. b. Spectra of dust on the magnet taken after Sol 500 show development of the 900 nm feature. Error bars were within the area of the symbols for each spectrum except the 425 dark ring dust which had standard deviations within 0.02 at each point.



**Microscopic Imager Dust Observations:** The MI is one of the four instruments on the end of the robotic arm, and is able to reach the magnets and a portion of the solar array for imaging. Martian atmospheric dust particles are  $<4\text{ }\mu\text{m}$  in diameter [2], well below the resolution of the MI, which has a best-focus resolution of  $31\text{ }\mu\text{m}$  / pixel. The MI can resolve fine sand grains as small as about  $70\text{ }\mu\text{m}$ . Although the MI is not used as frequently as the Pancam for dust monitoring, the images are very helpful for understanding the nature of the dust.

*MI images of the Capture Magnet.* On Sol 258 there is a significant dust coating on the magnet, with one larger agglomerate that measures  $\sim 400\text{ }\mu\text{m}$  (Figure 3a). Agglomerates refer to larger particles that are resolvable and can be measured using the MI, but the individual grains comprising the agglomerate cannot be resolved, and are assumed to be dust-sized grains. The image from Sol 505 shows that the Sol 420 cleaning event removed much of the fine-grained material, and left the strongly magnetic portion of grains aligned along the magnetic rings (Figure 3b). These grains are  $\leq 100\text{ }\mu\text{m}$  in diameter. By Sol 1006 there had been considerable dust deposition, and many large agglomerates had formed, casting shadows in the image. The agglomerates range in size from  $200\text{ }\mu\text{m}$  to  $400\text{ }\mu\text{m}$  (Figure 3c). On Sol 1230, there is clear evidence that the dust is organizing and agglomerating to form larger particles (Figure 3d). This is not occurring along the magnetic rings, suggesting that this behavior has little to do with magnetism. Sol 1504 has the most dust accumulation yet seen on the capture magnet, and although individual grains are not resolved, there is a texture that is apparently caused by the clumping together of dust particles (Figure 3e).

*MI images of the solar array.* The solar array was imaged by the MI on Sol 505, after the Sol 420 wind event. The diffuse reflectance of the array is a sign of dust deposition, as a clean array would appear more like specular glass [7]. A population of well rounded, well sorted sand grains ranging from  $150\text{ }\mu\text{m}$  to  $300\text{ }\mu\text{m}$  in diameter have collected near some of the cables on the deck at a height of 68 cm from the surface (Figure 4a). It has been well documented that the easiest grain size to saltate on Mars is  $100 - 150\text{ }\mu\text{m}$ , but expected saltation heights for these particles is less well understood [8,9]. It appears that with very strong winds, it is possible for sand grains to saltate to at least 70 cm, the height of the rover deck.

The next view of the array is from Sol 1006 (Figure 4b), showing that fine-grained material had continued to collect in pockets around the cabling on the deck. The sand grains seen on Sol 505 are gone. They have either been removed entirely or have simply moved to another location on the deck. On Sol 1230 there is clear evidence of dust deposition on the array as well as the sandy material around the cables (Figure 4c). On Sol 1473, there was still significant dust on the arrays that had started to agglomerate to form larger particles. The dust had organized into clumps that were  $\sim 100\text{ }\mu\text{m}$  in size (Figure 4d).

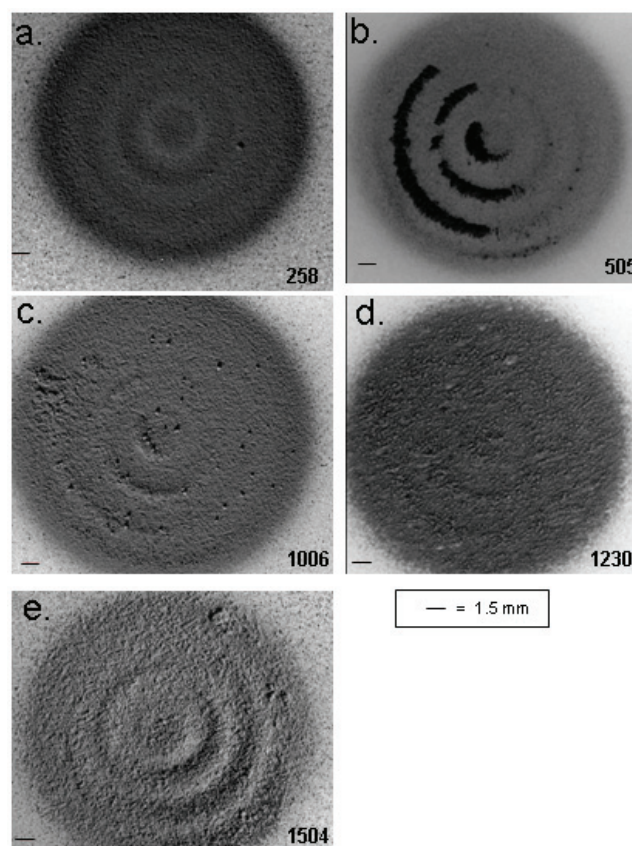


**Figure 3:** MI images of the capture magnet showing the dynamics of dust behavior throughout the mission. a. Image taken on Sol 258 shows dust accumulation and a  $\sim 400\text{ }\mu\text{m}$  agglomerate. b. Image taken on Sol 505 shows the effects of the 420 cleaning event which removed much of the fine-grained material and left behind only the strongly magnetic particles. c. Image taken on Sol 1006 shows continued dust deposition and many agglomerates. d. Image taken on Sol 1230 shows the dust agglomeration behavior. e. Image taken on Sol 1504 shows significant dust deposition and texture revealing the clumping nature of the dust.

**Implications of Dust Agglomeration:** In addition to dust agglomeration on the rover, this behavior is seen in local surface deposits investigated by the Spirit rover, and was well documented by *Sullivan, et. al. (2008)* [5]. As mentioned earlier, the easiest particle to move on Mars has been calculated to be 100 - 150  $\mu\text{m}$  sand, while actual dust size particles ( $<4 \mu\text{m}$  diameter) should be more difficult to raise [8,9]. It has been hypothesized that when saltating sand strikes the ground it kicks up dust grains that are then entrained by the wind [9], implying that wind speeds sufficient to saltate sand are also responsible for contributing dust to the atmosphere. However, there is increasing evidence that currently saltating sand is rare on Mars [10,11,12,13]. These dust agglomerates observed both in the local deposits and on the rover capture magnet and solar array that reach  $\sim 100 \mu\text{m}$  in size and larger should be easier to entrain than individual dust grains or even very dense sand grains and could help explain how dust is supplied to the atmosphere in the absence of saltating sand.

**Summary:** The Pancam and MI have been used to effectively monitor dust accumulation, removal, and morphology on the Spirit rover for almost 3 Martian years. Spirit has experienced three major cleaning events during which significant amounts of dust were removed from the vehicle. The effects of these events were observed with standard dust monitoring Pancam images. Pancam multispectral data of dust deposits on the magnets after Sol 500 are characterized by a steep shoulder around 600 nm and a shallow 900 nm feature which is consistent with nanophase ferric oxides and with bright dust deposits elsewhere at Gusev.

The MI shows various populations of grains on the rover ranging in size from dust (individual grains which cannot be resolved) to medium sand. MI images of the solar array reveal sand grains that have saltated to a height of 70 cm, implying strong winds. MI views also illustrate that the dust tends to agglomerate to form larger particles, up to  $\sim 400 \mu\text{m}$  in size. The larger dust agglomerations should be easier to entrain by wind than individual dust grains, and may represent a significant contribution to atmospheric dust loads in the absence of saltating sand.

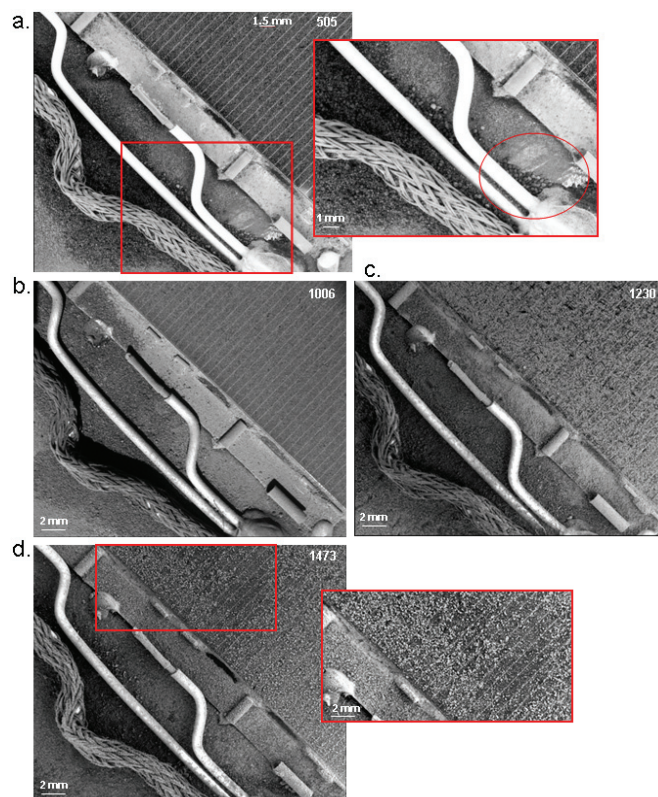


**Figure 4:** MI images of a portion of the solar array. *a.* Image taken on Sol 505. The inset shows sand grains that have collected in a pocket near some cables. *b.* Image taken on Sol 1006 shows removal of sand grains relative to Sol 505 and continued deposition of finer grained material. *c.* Image taken on Sol 1230 shows significant dust deposition on the array. *d.* Image taken on Sol 1473 shows dust agglomerates approximately  $100 \mu\text{m}$  in size.

**References:** [1] Bell, J.F. et. al. (2004) *Science*, 305, 800-806. [2] Lemmon, M.T., et al. (2004) *Science*, 306, 1753-1757 [3] Landis, G.A. (2005) *31st. IEEE Photovoltaic Specialists Conf.*, 858-861. [4] Greeley, R., et al. (2006) *JGR*, 111, E12S09. [5] Sullivan, R., et. al. (2008) *JGR*, 113, E06S07. [6] Madsen, M.B., et.al. (2009) *JGR*, 114, E06S90. [7] Landis, G.A., et al. (2006), *LPSC XXXVII*, Abstract #1932. [8] White, Bruce R. (1979) *JGR*, 84, B9, 4643-4651. [9] Greeley, R., et. al., (1992) *Mars*, 730-766. [10] Zimbelman, J.R. (2000) *GRL*, 27, 7, 1069-1072. [11] Malin, M. and Edgett, K. (2001) *JGR*, 106, E10, 23, 429-23, 570. [12] Fenton, L.K. (2006) *GRL*, 33, L20201. [13] Bourke et al. (2008) *Geomorph.*, 94, 247-255.



**SAND-SIZED DUST AGGREGATES ON MARS.** Sullivan<sup>1</sup>, R., Herkenhoff<sup>2</sup>, K., Johnson<sup>2</sup>, J., Landis<sup>3</sup>, G. and Vaughan<sup>2</sup>, A. <sup>1</sup>308 Space Sciences, Cornell University, Ithaca NY 14853 [rjs33@cornell.edu](mailto:rjs33@cornell.edu). <sup>2</sup>U.S.G.S.-Flagstaff, AZ [kherkenhoff@usgs.gov](mailto:kherkenhoff@usgs.gov), [jrjohnson@usgs.gov](mailto:jrjohnson@usgs.gov), [afvaughan@usgs.gov](mailto:afvaughan@usgs.gov). <sup>3</sup>NASA-Glenn Research Center, Cleveland, OH [geoffrey.a.landis@nasa.gov](mailto:geoffrey.a.landis@nasa.gov).

**Introduction:** Dust particles a few  $\mu\text{m}$  or less in diameter are raised into the martian atmosphere fairly routinely [1-2]. Wind tunnel experiments have shown that very strong winds are required to initiate movement of such tiny particles, but larger, sand-sized grains are easier to move [3-4]. However, there has been little evidence for sand currently moving on Mars [5-8]. It is a paradox that winds responsible for routinely raising dust into the martian atmosphere hardly affect bedforms composed of more easily moved sand-sized particles. Here we summarize portions of a recent report [9] that attempts to explain this discrepancy, and we suggest how dust-raising parameterizations in numerical simulations of the martian atmosphere might be improved in light of these results.

**MER Observations.** Dust particles suspended in the martian atmosphere typically are  $<4\ \mu\text{m}$  in diameter [10-11], much smaller than MI resolution of  $\sim 31\ \mu\text{m}/\text{pixel}$ . However, MER Microscopic Imager (MI) views show that dust mantling the surface commonly occurs as fragile, sand-sized aggregates of irregular shape, superficially resembling tiny popped corn (Figs. 1-3). The large size and low density of these aggregates should make them much easier to entrain than either  $<4\ \mu\text{m}$  air fall dust, or hard (saltation-capable) sand-sized grains [9]. We have proposed that dust aggregates like those seen in MI views are widespread across dusty regions of Mars, and that they are the primary means—the “low-hanging fruit”—for wind to raise dust directly into the atmosphere [9]. Implicit in these ideas is that once the dust aggregates are entrained, they contribute to the suspended dust load by shedding suspendable smaller grains, perhaps breaking up completely into their  $<4\ \mu\text{m}$  constituent particles. The impressions of fragility in MI images suggest that these aggregates partially or totally disaggregate back into their clay-sized constituent grains during the violence of entrainment by a passing dust devil or a strong wind event (including disintegration from high-speed impacts with the ground). Tensile strengths of martian dust aggregates likely are much less than even the tiny magnitudes of the compressive pressures of MER Mössbauer touches, which easily crush and re-mold the aggregates into extremely high-fidelity castings [9, 12-13, cf. 14]. We therefore

also have proposed that dust devils seen by *Spirit*—and by analogy dust devils elsewhere on Mars—must be raising a substantial fraction of their dust opacity by the relatively easy raising and rupturing of these fragile dust aggregates [9].

**Dust Entrainment Threshold.** Numerical simulations of martian atmosphere dynamics commonly predict wind speeds too low to directly entrain  $<4\ \mu\text{m}$  dust at the minimum shear stresses that wind tunnel experiments would suggest are necessary. Work-arounds include parameterizing dust-raising by artificially lowering the dust threshold, or lowering the threshold to that required for movement of hard sand grains. The latter

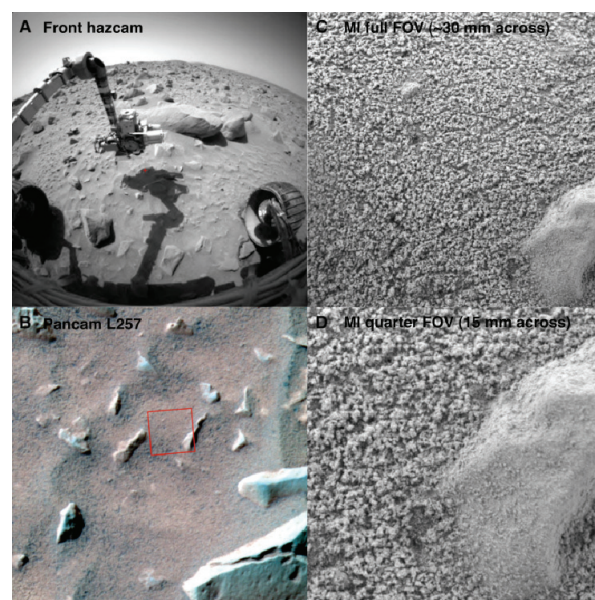


**Figure 1:** Dust mantling the surface at Gusev crater, sol 75 of *Spirit*'s mission. Panels: A = front hazcam with tiny red cross showing MI image location; B = stretched-color Pancam with red box showing MI footprint; C = stretched, full MI image view; D = quarter-frame excerpt of MI image,  $\sim 15\ \text{mm}$  across. “Popcorn” dust aggregates are large enough to affect surface texture in close-range Pancam views, verging on being individually resolved. Smaller aggregates on the pebble’s surface indicate that larger aggregates are not as stable on smooth, sloping surfaces that are also more exposed to wind. (After Fig. 18 of [9].)

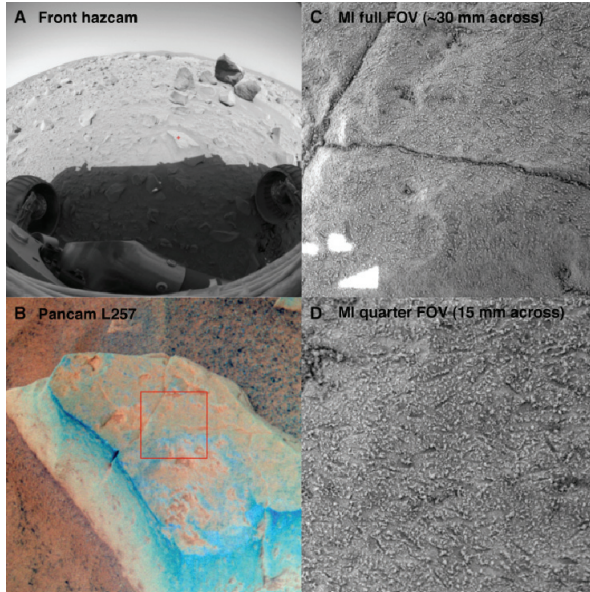


**Figure 2:** Dust mantling a rock surface at Gusev crater, sol 76 of Spirit's mission. Panel A-D arrangements are the same as for the previous figure. The MI view shows that some of the dusty color on the rock is due to relatively small but easily resolved dust aggregates distributed widely over the rock surface. Small "nick" marks in D indicate that gentle wind scouring has affected the distribution of the dust aggregates, attesting to their susceptibility to mobilization by wind. (After Fig. 19 of [9]).

approach would require loose, saltating sand to be routinely available for entrainment wherever dust is being raised on the planet. This assumption is incompatible with orbital observations indicating that sand on the martian surface, even on well-formed dunes with little dust cover, seems to rarely move at all [5-8].

For numerical atmospheric modeling, we recommend parameterizing dust-raising to involve low-density sand-sized dust aggregates like those seen in MI images at the MER landing sites (i.e., not singular  $<4\ \mu\text{m}$  air fall dust, nor hard basaltic sand). To do this, density of the dust aggregates must be estimated from visual impressions of the "popcorn"-like aggregates in the MI images. Although a precise value cannot be determined, impressions from MI images suggest that a porosity of at least 75% seems likely. With a basaltic material density of  $3000\ \text{kg/m}^3$  and 75% porosity (for a "grain" density of  $750\ \text{kg/m}^3$ ), a "grain" size of  $500\ \mu\text{m}$ , and 6.7 mb of  $\text{CO}_2$  atmosphere at  $250^\circ\text{K}$ , the threshold wind friction speed to initiate entrainment is predicted to be  $\sim 1.4\ \text{m/sec}$  using semi-empirical wind tunnel expressions [3-4]. This is around half the value for a solid, hard

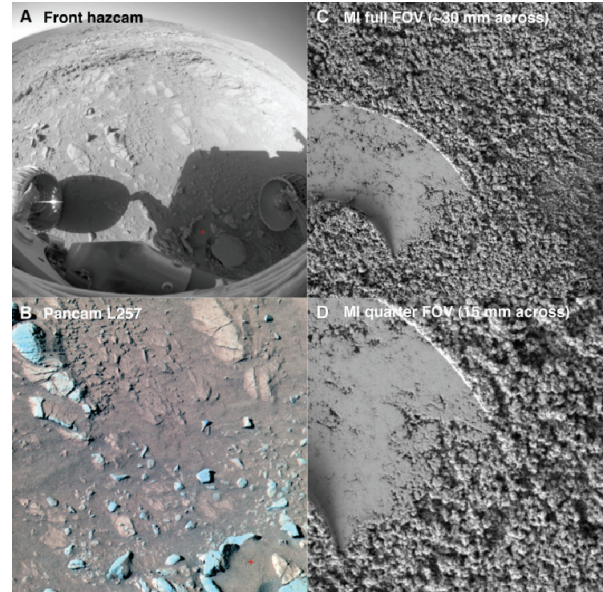


**Figure 3:** Mössbauer contact plate impression into dust mantle at Gusev crater, sol 258 of Spirit's mission. Panel A-D arrangements are the same as for the previous figure. Large, well-developed dust aggregates blanket the regolith. MI view shows where the Mössbauer contact ring touched the ground with  $\sim 1\ \text{N}$  of force, completely and easily crushing the aggregates into ultrafine, unresolved particles that allow a high-fidelity casting of the smooth metal surface of the contact plate. (After Fig. 20 of [9]).

grain of the same overall size. Fig. 4 shows how the threshold wind friction speed for dust aggregates (assuming 75% porosity) compares with values for hard grains over a sample range of MI-resolvable dust aggregate sizes. It should be kept in mind, however, that the wind tunnel experiments [3-4] involved beds of uniform particles, with "shoulder-to-shoulder" grain arrangements. In contrast, MI images show that dust aggregates commonly are found in sparser distributions, particularly on rock surfaces. In such settings, the necessary wind friction speed for entrainment would be lower still, so mobilization of at least some dust from a dusty, rock-strewn landscape should be even easier than suggested by the middle curve in Fig. 4. The lower curve in Fig. 4 employs a dust aggregate density of  $380\ \text{kg/m}^3$  from the laboratory experiments of Merrison et al. [15]. (The lower curve is dashed because the threshold expressions [3-4] were not derived from experiments using particle densities as low as  $380\ \text{kg/m}^3$ .) Merrison et al. [15] also carried out important wind tunnel experiments with hollow glass spherules to simulate both the sizes and the low densities of martian dust aggregates. They found threshold friction speed values several factors lower than for solid particles.



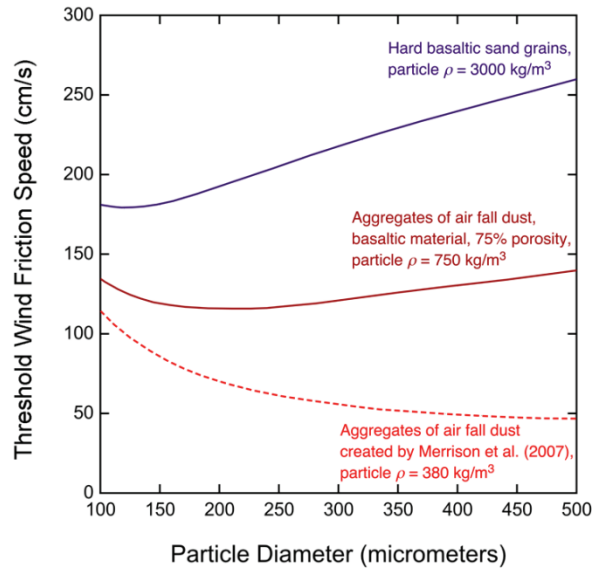


**Figure 4:** The semi-empirical relationships [3-4] for threshold wind friction speed are compared between hard basaltic sand grains, 75% porous aggregates of basaltic density air fall dust, and 380 kg/m<sup>3</sup> dust aggregates of Merrison et al. [15]. Grain size range along the X-axis is typical of, but not completely inclusive of, dust aggregate dimensions resolved in the MI images. For the middle curve, actual threshold values might be even lower due to somewhat sparser distribution of dust aggregates compared with “shoulder-to-shoulder” grain distributions typical of the particle beds of the wind tunnel experiments [3-4], and possibly higher drag coefficients for the very irregular dust aggregates compared to some (but not all) of the grains tested by [3-4]. The bottom curve is dashed and somewhat suggestive, because the realistic, low particle densities created by Merrison et al. [15] are outside the particle density range of the experiment matrix from which the semi-empirical threshold expressions [3-4] were derived.

**A Dust Particle Cycle On Mars.** The MER observations suggest that a dust particle cycle operates on Mars, in which <4 μm dust grains alternate between suspension as individual grains, and as components within very loosely-bound, much larger aggregates at the surface. How might individual dust grains migrate between these two states? Aggregate growth has been observed in wind tunnel experiments involving dust “rolling up” across the surface downwind [Rod Leach, personal communication, 1980s], and similar behavior has been observed on the MER Spirit rover deck [16]. On Mars it is unclear whether aggregate growth

might initiate earlier, between <4 μm particles “colliding” while still suspended, due to electrostatic attractions (perhaps affecting fall-out rate). Some circumstantial evidence for this comes from wind tunnel experiments in which dust aggregates were observed to form from suspended dust in a martian environmental wind tunnel [17]. We speculate that dust aggregate growth would continue on the ground, facilitated by “jostling”/rubbing/rearranging of the growing aggregates by minor wind turbulence that is otherwise too weak to move the dust aggregates enough to destroy them. This scenario suggests that on the ground, the maximum dust aggregate size at any given place and time would be a function of: (1) local dust fall-out rate; (2) time interval between disturbances (e.g., between dust devil passages, and/or regional wind events); and (3) very local aerodynamic protection characteristics of the setting (e.g., exposed, sloping rock surfaces vs. small ground patches sheltered by surrounding rocks). At the surface, then, dust aggregate size and growth rate might change with time and overall size, perhaps approaching a limiting maximum diameter governed by inherent electrostatic bond fragility and the local conditions of dust abundance (functions, in turn, of local fall-out rate and time interval since the last major wind disturbance).

**Conclusions:** On a planet where hard sand grains are found at the surface along with fragile sand-sized dust aggregates, we should expect winds to be more successful mobilizing the dust (in its weakly aggregated form) than moving the sand. This is consistent with what has been observed repeatedly from orbit (lots of dust raised, hardly any dune movements).

Dust raising therefore seems much easier than suggested by the classic Iversen & White relationships [3-4] that have been applied to hard <4 μm dust particles, or to indirect raising of these dust grains by saltation of hard, sand-size grains. But the Iversen and White relationships and their successors are still useful if the appropriate grain characteristics are applied: low density and sand-sized. When this is done, dust threshold is predicted to lower substantially.

- 
- References:** [1] Zurek, R. W. and Martin, L. J. (1993) *J. Geophys. Res.*, 98, E2, 3247-3259. [2] Cantor, B. et al. (2002) *J. Geophys. Res.*, 107, E3, doi:10.1029/2001JE001588. [3] Iversen, J. D. and White, B. R. (1982) *Sediment.*, 29, 111-119. [4] Greeley, R. and Iversen, J. D. (1985) *Wind as a Geological Process*, Cambridge, pp. 76-82. [5] Zimbelman, J. R. (2000) *Geophys. Res. Lett.*, 27, 7, 1069-1072, doi:10.1029/1999GL008399. [6] Malin, M. and Edgett, K. (2001) *J. Geophys. Res.*, 106, E10, 23,429-23,570, doi:10.1029/2000JE001455. [7] Fenton, L. K. (2006) *Geophys. Res. Lett.*, 33, L20201, doi:10.1029/2006GL027133. [8] Bourke et al. (2008) *Geomorph.*, 94, 247-255, doi:10.1016/j.geomorph.2007.05.012. [9] Sullivan et al. (2008) *J. Geophys. Res.*, 113, E06S07, doi:10.1029/2008JE003101. [10] Pollack et al. (1995) *J. Geophys. Res.*, 100, E3, 5235-5250, doi:10.1029/94JE02640. [11] Wolff et al. (2006) *J. Geophys. Res.*, 111, E12S17, doi:10.1029/2006JE002786. [12] Herkenhoff, K. E., et al. (2004) *Science*, 305, 824 – 826, doi:10.1126/science.3050824. [13] Herkenhoff, K. E., et al. (2006) *J. Geophys. Res.*, 111, E02S04, doi:10.1029/2005JE002574. [14] Pontius, D. H., and T. R. Snyder (1991) *Powder Technol.*, 68, 159 – 162, doi:10.1016/0032-5910(91)80124-2. [15] Merrison et al. (2007) *Icarus*, 191, 568-580, doi:10.1016/j.icarus.2007.04.035. [16] Vaughan et al. (2009) this meeting. [17] Merrison et al. (2004) *Planet. & Space Sci*, 52, 279-290, doi:10.1016/j.pss.2003.11.003.

**AN AERODYNAMIC ROUGHNESS LENGTH MAP DERIVED FROM MARTIAN ROCK ABUNDANCE DATA AND ITS EFFECTS ON AEOLIAN EROSION THRESHOLDS IN A MCGM.** Hébrard,<sup>1,2</sup> E., Coll,<sup>1</sup> P., Marticorena,<sup>1</sup> B., Bergametti,<sup>1</sup> G., Montmessin,<sup>2</sup> F. and Forget,<sup>3</sup> F. ([eric.hebrard@latmos.ipsl.fr](mailto:eric.hebrard@latmos.ipsl.fr)) <sup>1</sup> LISA, CNRS/INSU-IPSL-Université Paris 7 Denis Diderot, Créteil, F-94010, FRANCE. <sup>2</sup> LATMOS, CNRS-IPSL-Université Versailles St-Quentin, Verrières le Buisson, F-91371, FRANCE. <sup>3</sup> LMD, CNRS/INSU-IPSL-Université Paris 6 Pierre et Marie Curie, Paris, F-75252, FRANCE

**Introduction:** Dust storms have been reported in all seasons on Mars from ground-based and spacecraft observations, across much of the planet and ranging from small local storms covering a few tens of km<sup>2</sup> to planet encircling [1]. Simulations of these dust events using Mars Global Circulation Model (MGCM) indicates that the large quantities of dust lifted into the atmosphere during these storms can have a strong impact on the atmospheric thermal structure, the global circulation patterns and thus the climate in general [2]. Further understanding of the origin of these local and global dust storms strongly implies the description of the processes involved in dust rising and transportation from the Martian surface. Looking at observations, it is almost certain that aeolian erosion varies from one region to another depending on the ease of dust lifting from the surface [3]. Yet, until recently, there have not been enough data available in modern MGCMs to implement a spatially variable wind stress threshold map nor, for that matter, any map for any factors that are controlling (interparticle cohesion, surface roughness, etc). The aerodynamic roughness length  $z_0$  especially affect the model-calculated wind stresses and wind stress thresholds for dust lifting; a spatially varying aerodynamic roughness length field could thus affect the simulated dust cycle [4].

**Physical modeling of wind erosion threshold:** A recent physical model, applicable on large scales, has been recently designed at LISA to account for the influence of the surface characteristics on the spatial and temporal variability of dust emission in arid terrestrial environments [5,6,7,8], by including explicit parametrizations of the aeolian erosion threshold as a function

$$U(z) = \frac{U^*}{k_B} \times \ln\left(\frac{U^*}{z_0}\right)$$

$$U_t^*(D_p, z_0, z_{0s}) = \frac{U_{ts}^*(D_p, z_0, z_{0s})}{f_{\text{eff}}(z_0, z_{0s})}$$

where  $U(z)$  is the wind speed at an altitude  $z$  in the surface boundary layer,  $U^*$  is the friction velocity,  $U_t^*$  is the threshold friction velocity required to initiate particle motion,  $U_{ts}^*$  is the threshold friction velocity over a smooth surface, and  $f_{\text{eff}}$  is a coefficient expressing the efficiency of the aeolian erosion over rough surfaces using a given drag partition scheme.

Its application to simulate the Martian dust emissions requires input data concerning the surface features on Mars, in particular surface roughness data. The spatial variations of the aerodynamic roughness length  $z_0$  has not been fully investigated yet on Mars, and latest MGCM simulations have assumed a spatially uniform aerodynamic roughness length  $z_0$  value within the 0.001-0.01m range [9,10,11] estimated for the Viking and Pathfinder landing sites [12,13].

**Parametrization of the aerodynamic roughness height  $z_0$ :** We have demonstrated the possibility of using rock abundance maps [14,15] to estimate the roughness density  $\lambda$  as well as some other rock-size frequency parameters (mean diameter  $D$ , mean height  $H$ ) on Mars, and to retrieve subsequently the aerodynamic roughness  $z_0$  by using a quantitative relationships based on wind-tunnel and field measurements on Earth (Fig. 1).

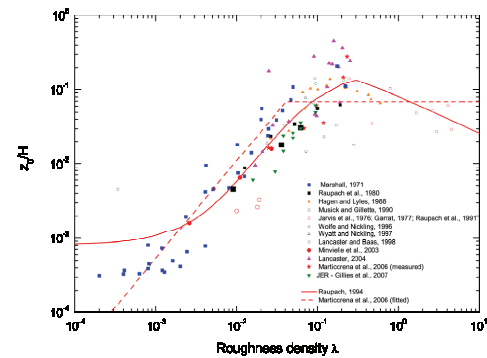


**Figure 1:** Ratio of the aerodynamic roughness length  $z_0$  to the mean roughness elements height  $H$  as a function of the roughness density  $\lambda$  [16].

Our calculations have been further validated using rock-size frequency distributions inferred from different Martian landing sites and Earth analogs [17,18]. Previous works on this topic have been mainly dedicated to better assess the quality of the landing sites [19,20,21,22]. As a consequence, the attention has been mainly focused on the bigger rocks distribution, a critical point for characterizing a landing site, that is well reproduced by their chosen

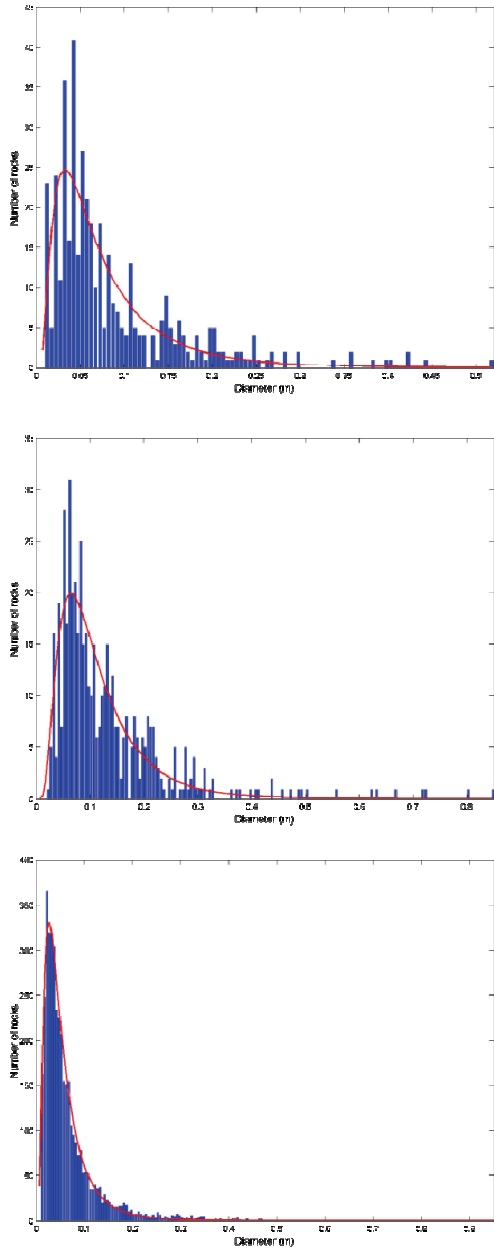


**Figure 2:** Histograms reporting the number of rocks for each size bin diameter at Viking lander 1, Viking lander 2 and Mars Pathfinder landing sites along with our fitted log-normal distributions (in red).

exponential fits to the observational data. However, surface roughness can be principally driven by the smallest rocks, and log-normal distributions seem to be better adapted to reproduce with a comparable quality the various-sized components (Fig. 2).

Compared to what has been inferred previously from the different landing sites, our results (Fig. 3) suggest that the method used here to estimate the aerodynamic roughness length  $z_0$  provides a reasonable picture of the actual conditions existing on Mars.

To extend the range of our calculations towards the poles, a mandatory task before using such maps in MGCM, we built upon the soft correlation between both the albedo and the rock abundances MGS-TES datasets (Fig. 4). We managed eventually to generate a coherent aerodynamic roughness length  $z_0$  map on the whole surface of Mars (Fig. 5).

#### Parametrization of the threshold friction velocity $U_{*c}$

Such surface roughness map can be used to compute the aeolian erosion thresholds (Fig. 6) which, associated with climatological data and surface wind velocities issued from a MGCM, can help establish the paramount importance of introducing truly representative and spatially varying aerodynamic roughness length values to identify the Martian conditions exhibiting the highest potential for dust emissions. Moreover, including such maps in

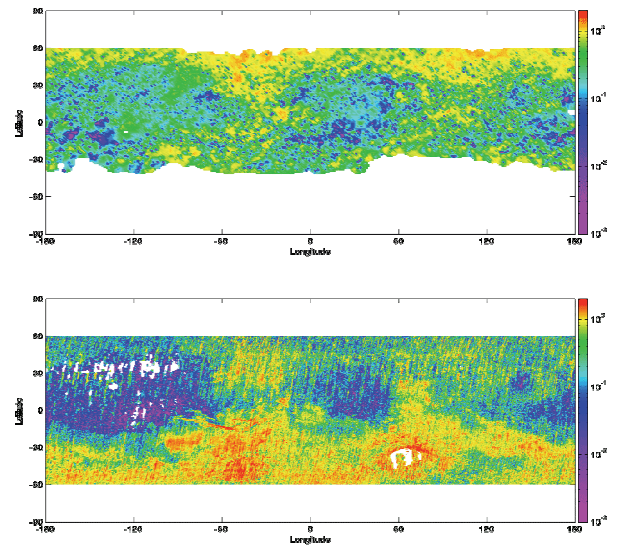


**Figure 3:** Aerodynamic roughness heights  $z_0$  (in cm) inferred from Viking-IRTM (top) and MGS-TES (bottom) rock abundance data.



future MGCM studies might certainly help to illuminate their relative importance on the Martian dust cycle and the evolution of surface dust reservoirs.

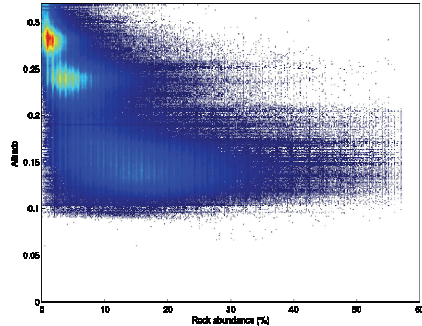


**Figure 4:** Scatterplot of MGS-TES data: albedo vs. rock abundance [15].

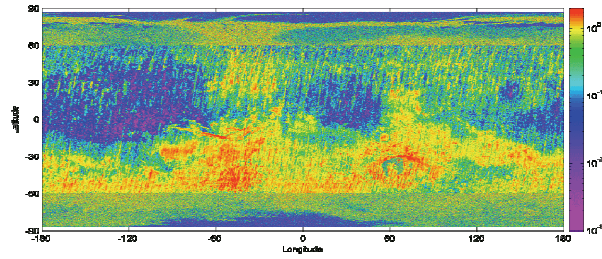


**Figure 5:** Extended aerodynamic roughness heights  $z_0$  (in cm) inferred from MGS-TES rock abundance data.

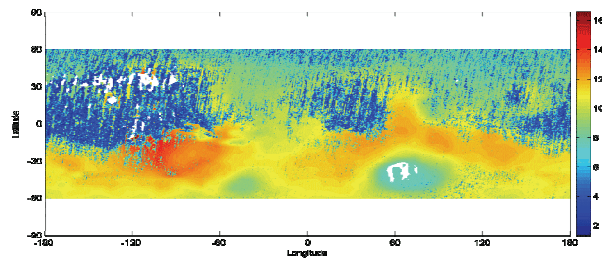


**Figure 6:** Minimal threshold wind friction velocity  $U_t^*$  (in  $\text{m.s}^{-1}$ ).

**Acknowledgment:** This work was supported by the Centre National d'Études Spatiales (CNES).

## References:

- [1] B.A. Cantor (2007). *Icarus*, 186, 60-96.
- [2] C.E. Newman, S.R. Lewis, P.L. Read, and F. Forget. (2002). *J. Geophys. Res. - Planet.*, 107, E125124.

- [3] S. Basu, J. Wilson, M. Richardson, and A. Ingersoll (2006). *J. Geophys. Res. - Planet.*, 111, E09004.
- [4] M. A. Kahre, J. R. Murphy and R. M. Haberle (2006). *J. Geophys. Res.*, 111, E06008.
- [5] B. Marticorena and G. Bergametti (1995). *J. Geophys. Res. - Atmos.*, 100, 16415-16430.
- [6] B. Marticorena, G. Bergametti, B. Aumont, Y. Callot, C. Ndoume, and M. Legrand (1997). *J. Geophys. Res. - Atmos.*, 102, 4387-4404.
- [7] B. Laurent, B. Marticorena, G. Bergametti and F. Mei (2006). *Global Planet. Change*, 52, 121-141.
- [8] B. Laurent, B. Marticorena, G. Bergametti, J. F. Léon and N.M. Mahowald. (2008) *J. Geophys. Res. - Atmos.*, 113, D14218.
- [9] L. Montabone, S.R. Lewis, and P.L. Read (2005). *Adv. Space Res.*, 36, 2146-2155.
- [10] M.A. Kahre, J.R. Murphy, and R.M. Haberle (2006). *J. Geophys. Res. - Planet.*, 111, E06008.
- [11] C.E. Newman, S.R. Lewis, P.L. Read, and F. Forget (2002). *J. Geophys. Res. - Planet.*, 107, E125123.
- [12] J.L. Sutton, C.B. Leovy, and J.E. Tillman (1978). *J. Atmos. Sci.*, 35, 2346-2355.
- [13] R. Sullivan, R. Greeley, M. Kraft, G. Wilson, M. Golombek, K. Herkenhoff, J. Murphy, and P. Smith (2000). *J. Geophys. Res. - Planet.*, 105, 24547-24562.
- [14] P.R. Christensen. (1986) *Icarus*, 68, 217-238.
- [15] S.A. Nowicki and P.R. Christensen (2007). *J. Geophys. Res. - Planet.*, 112, E05007.
- [16] B. Marticorena, M. Kardous, G. Bergametti, Y. Callot, P. Chazette, H. Khatteli, S. Le Hégarat-Masclé, M. Maillé, J.-L. Rajot, D. Vidal-Madjar and M. Zribi (2006). *J. Geophys. Res. - Earth*, 111, F03017.
- [17] N. Lancaster (2004). *Earth Surf. Process. Landforms*, 29, 853-867.
- [18] R.A. Yingst, A.F.C. Haldemann, K.L. Biedermann, and A.M. Monhea. (2007). *J. Geophys. Res. - Planet.*, 112, E06002.
- [19] M. Golombek and D. Rapp (1997). *J. Geophys. Res. - Planet.*, 102, 4117-4129.
- [20] M.P. Golombek, A.F.C. Haldemann, N.K. Forsberg-Taylor, E.N. DiMaggio, R.D. Schroeder, B.M. Jakosky, M.T. Mellon, and J.R. Matijevic (2003) *J. Geophys. Res. - Planet.*, 108, E128086.
- [21] M.P. Golombek, R.E. Arvidson, J.F. Bell, P.R. Christensen, J.A. Crisp, L.S. Crumpler, B.L. Ehlmann, R.L. Fergason, J.A. Grant, R. Greeley, A.F.C. Haldemann, D.M. Kass, T.J. Parker, J.T. Schofield, S.W. Squyres, and R.W. Zurek (2005). *Nature*, 436, 44-48.
- [22] M.P. Golombek, R.E. Arvidson, T. Heet, L. Barry, J.R. Matijevic, and A.S. McEwen (2007). *LPS XXXVIII*, Abstract #1405.

# **Lead Author List**



---

## Lead Author List

---

Barth, E. L., Southwest Research Institute, 1050 Walnut Street, Suite 300, Boulder, CO 80302 ([ebarth@boulder.swri.edu](mailto:ebarth@boulder.swri.edu)).

Brown, A.J., SETI Institute, 515 N. Whisman Rd Mountain View, CA 94043 ([abrown@seti.org](mailto:abrown@seti.org))  
Author website: (<http://abrown.seti.org>).

Clancy, R. T., Space Science Institute (P.O. Box 3370, Bald Head Island, NC 28461 ([Clancy@spacescience.org](mailto:Clancy@spacescience.org)).

Elteto, A., Laboratory for Atmospheric and Space Physics, University of Colorado, Campus Box 392, Boulder, CO 80309-0392, 303-492-1534 ([Attila.Elteto@colorado.edu](mailto:Attila.Elteto@colorado.edu)).

Esposito, F., INAF – Osservatorio Astronomico di Capodimonte – Salita Moiariello 16, 80131 Napoli, Italy. ([francesca.esposito@oacn.inaf.it](mailto:francesca.esposito@oacn.inaf.it)).

Fenton, L. K., Carl Sagan Center, NASA Ames Research Center, MS 245-3, Moffett Field, CA 94035-1000, ([lfenton@carlsagancenter.org](mailto:lfenton@carlsagancenter.org)).

Forget, F., Laboratoire de Météorologie Dynamique, Université Paris 6, BP 99, 75005 Paris, FRANCE ([forget@lmd.jussieu.fr](mailto:forget@lmd.jussieu.fr)).

Fuerstenau, S.D., NovaWave Technologies, 900 Island Dr., Redwood City, CA 94065 ([sfuerstenau@novawavetech.com](mailto:sfuerstenau@novawavetech.com)).

Gillies, J.A., Division of Atmospheric Sciences, Desert Research Institute 2215 Raggio Parkway, Reno ([jackg@dri.edu](mailto:jackg@dri.edu)).

Goetz, W., Max Planck Institute for Solar System Research, Max Planck Strasse 2, 37191 Katlenburg-Lindau, Germany ([goetz@mps.mpg.de](mailto:goetz@mps.mpg.de)).

Haberle, R.M., Planetary Systems Branch, Space and Astrobiology Division, NASA Ames Research Center, Moffett Field, CA 94035 ([Robert.M.Haberle@nasa.gov](mailto:Robert.M.Haberle@nasa.gov)).

Hale, A.S., Jet Propulsion Laboratory, Caltech, Mail Stop 169-237, 4800 Oak Grove Dr, Pasadena, CA 91109. ([Amy.S.Hale@jpl.nasa.gov](mailto:Amy.S.Hale@jpl.nasa.gov)).

Heavens, N. G., Division of the Geological and Planetary Sciences, California Institute of Technology, MC 150-21, Pasadena, CA, 91125 ([heavens@gps.caltech.edu](mailto:heavens@gps.caltech.edu)).

Hébrard, E., CNRS/INSU-IPSL-Université Paris 7 Denis Diderot, Créteil, F-94010, FRANCE., LMD, CNRS/INSU-IPSL-Université Paris 6 Pierre et Marie Curie, Paris, F-75252, FRANCE ([eric.hebrard@latmos.ipsl.fr](mailto:eric.hebrard@latmos.ipsl.fr)).

Hollingsworth, J.L., Space Science and Astrobiology Division, Planetary Systems Branch, NASA Ames Research Center, Moffett Field, CA 94035 ([jeffh@humbabe.arc.nasa.gov](mailto:jeffh@humbabe.arc.nasa.gov)).

## Lead Author List (cont.)

---

James, P. B., Space Science Institute, 4750 Walnut St., Boulder, CO 80301 ([pjames@cableone.net](mailto:pjames@cableone.net)).

Kahre, M.A., Bay Area Environmental Research Institute NASA Ames Research Center, (NASA Ames Research Center, 245-3, Moffett Field, CA, 94035, 650-604-3863 ([melinda.a.kahre@nasa.gov](mailto:melinda.a.kahre@nasa.gov))).

Kass, D.M., Jet Propulsion Laboratory, Caltech, Mail Stop 169-237, 4800 Oak Grove Dr, Pasadena, CA 91109. ([David.Kass@jpl.nasa.gov](mailto:David.Kass@jpl.nasa.gov)).

Kleinböhl, A., Jet Propulsion Laboratory, California Institute of Technology, Mail-Stop 169-237, 4800 Oak Grove Dr., Pasadena, CA, 91109 ([armin.kleinboehl@jpl.nasa.gov](mailto:armin.kleinboehl@jpl.nasa.gov)).

Kuroda, T., Max Planck Institute for Solar System Research (Max-Planck-Str. 2, D-37191 Katlenburg-Lindau, Germany ([kuroda@mps.mpg.de](mailto:kuroda@mps.mpg.de))).

Lacks, D.J., Department of Chemical Engineering, Case Western Reserve University, Cleveland, OH 44106. (216)368-4238 ([daniel.lacks@case.edu](mailto:daniel.lacks@case.edu)).

Lee, S.W., Denver Museum of Nature & Science, 2001 Colorado Blvd., Denver, CO 80205 ([Steve.Lee@dmns.org](mailto:Steve.Lee@dmns.org)).

Lorenz, R.D., JHU Applied Physics Laboratory, 11100 Johns Hopkins Road, Laurel, MD 20723 ([ralph.lorenz@jhuapl.edu](mailto:ralph.lorenz@jhuapl.edu)).

Määttänen, A., Department of Physics, University of Helsinki, P.O.Box 64, 00014 Helsinki, Finland, Finnish Meteorological Institute, Space Research Unit, P.O.Box 503, 00101 Helsinki, Finland. Presently at: LATMOS, CNRS/UVSQ/UPMC/IPSL, Réduit de Verrières, BP 3, Route des Gatines, 91371 Verrières-le-buisson Cedex, FRANCE ([anni.maattanen@latmos.ipsl.fr](mailto:anni.maattanen@latmos.ipsl.fr)).

Madeleine, J.-B., Laboratoire de Météorologie Dynamique (LMD), CNRS/UPMC/IPSL, Université Paris 6, BP 99, 4 place Jussieu, 75252 Paris cedex 05, FRANCE ([jbmld@lmd.jussieu.fr](mailto:jbmld@lmd.jussieu.fr)).

McConnochie, T. H., NASA Goddard Space Flight Center., Greenbelt, MD ([Timothy.H.McConnochie@nasa.gov](mailto:Timothy.H.McConnochie@nasa.gov)).

Michaels, T. I., Southwest Research Institute, 1050 Walnut St Suite 300, Boulder, CO 80302, USA ([tmichael@boulder.swri.edu](mailto:tmichael@boulder.swri.edu)).

Montmessin, F., LATMOS, CNRS/UVSQ/IPSL, Paris, France, ([franck.montmessin@latmos.ipsl.fr](mailto:franck.montmessin@latmos.ipsl.fr)).

Mulholland, D.P., Atmospheric, Oceanic & Planetary Physics, University of Oxford, Clarendon Laboratory, Parks Road, Oxford OX1 3PU, UK ([mulholland@atm.ox.ac.uk](mailto:mulholland@atm.ox.ac.uk), [read@atm.ox.ac.uk](mailto:read@atm.ox.ac.uk)).

Neakrase, L.D.V., School of Earth and Space Exploration, Arizona State University, Box 871404, Tempe, AZ 85287-1404, and Department of Astronomy, New Mexico State University, P.O. Box 30001, MSC 4500, Las Cruces, NM 88003-8001 ([lneakras@nmsu.edu](mailto:lneakras@nmsu.edu)).

---

## Lead Author List (cont.)

---

Newman, C. E., California Institute of Technology, MC 150-21, GPS, Caltech, 1200 E. California Blvd., Pasadena, CA 91125, USA ([claire@gps.caltech.edu](mailto:claire@gps.caltech.edu), [mir@gps.caltech.edu](mailto:mir@gps.caltech.edu)).

Ogohara, K., Earth and Planetary Sciences Division, Graduate School of Science, Kyoto University (Oiwake, Kitashirakawa, Sakyo, Kyoto, Japan ([ogohara@kugi.kyoto-u.ac.jp](mailto:ogohara@kugi.kyoto-u.ac.jp)).

Rafkin, S.C.R., Department of Space Studies, Southwest Research Institute, 1050 Walnut Street, Suite 300, Boulder, Colorado, USA, 80302 ([rafkin@boulder.swri.edu](mailto:rafkin@boulder.swri.edu)).

Spiga, A., Department of Physics and Astronomy, The Open University, Milton Keynes, United Kingdom ([a.spiga@open.ac.uk](mailto:a.spiga@open.ac.uk), [s.r.lewis@open.ac.uk](mailto:s.r.lewis@open.ac.uk)).

Sullivan, R., 308 Space Sciences, Cornell University, Ithaca NY 14853 ([rjs33@cornell.edu](mailto:rjs33@cornell.edu)).

Vaughan, A.F., U.S. Geological Survey, 2255 N. Gemini, Flagstaff, AZ 86004 ([afvaughan@usgs.gov](mailto:afvaughan@usgs.gov)).

Whiteway, J., York University, Toronto, Ontario, M6J 1P3 ([Whiteway@yorku.ca](mailto:Whiteway@yorku.ca)).

Wilson, R.J., NOAA/Geophysical Fluid Dynamics Laboratory, Princeton, NJ 08542 ([John.Wilson@noaa.gov](mailto:John.Wilson@noaa.gov)).

Wu, D., Centre for Research in Space Science and Engineering (York University, 4700 Keele Street, Toronto, ON, M3J1P3, Canada ([wudi2004@yorku.ca](mailto:wudi2004@yorku.ca)).